DISS. ETH NO. 18995

MELTING OF SUBDUCTED CARBONATED PELITES FROM 5 TO 23 GPA: ALKALI-CARBONATITES, MANTLE METASOMATISM, AND ELEMENT RECYCLING

A dissertation submitted to

ETH ZURICH

for the degree of

Doctor of Sciences

presented by

Daniele Grassi

Dipl. Natw. ETH
ETH Zürich

born on January 19, 1978

citizen of Novazzano (TI)

Accepted on the recommendation of:

examiner Prof. Dr. M.W. Schmidt	ETH Zürich
co-examiner Prof. Dr. S. Poli	Università degli Studi di Milano
co-examiner Prof Dr. G. Brey	UNI Frankfurt

2010

Science is always wrong. It never solves a problem without creating ten more.

George Bernard Shaw

Il ventaglio di possibilità si apre magnificamente come una bella ruota di pavone.

Armando Ceroni

Noi non doviamo desiderare che la natura si accomodi a quello che parrebbe meglio disposto et ordinato a noi, ma conviene che noi accomodiamo l'intelletto nostro a quello che ella ha fatto.

Galileo

Abstract

The main goal of this study is to understand what happens when carbonated sediments are deeply subducted and finally recycled into the deep mantle. In a first series of experiments at 8 and 13 GPa the melting behavior of three carbonated eclogitic pelites containing 0-1 wt% water having different X_{Ca}, Mg#, and K/Na ratios was studied at temperatures between 900 and1850 °C to define subsolidus assemblages, conditions of melting, melt compositions, and melting reactions. Subsolidus mineralogies consist of garnet, clinopyroxene, coesite or stishovite, kyanite or corundum, phengite or potassium feldspar (kfsp), K-hollandite, a Ti-phase and carbonates. At 8 GPa, the fluid-absent and dry carbonated pelite solidi locate at 950 and 1070 °C, respectively; at 13 GPa, the H_2O-present and dry solidi locate at 1150 and 1300 °C, respectively. The pressure breakdown of phengite at ca. 9 GPa and the absence of any other hydrous mineral at higher pressure changes the melting behavior in the 1.1 wt% H_2O composition from fluid-absent at 8 GPa to fluid-present at 13 GPa. Melting reactions are controlled by carbonates (magnesite and aragonite) and the potassium and hydrous phases (phengite or kfsp, K-hollandite) present at the solidus. The first melts, the compositions of which have been determined by reverse sandwich experiments, are potassium-rich Ca-Fe-Mg-carbonate melts, with extreme K_2O/Na_2O wt-ratios of up to 41 (at 8 GPa). Na remains compatible in clinopyroxene with $D_{Na}^{cpx/carbonate\,melt}$ of 10-18 at the solidus at 8 GPa. Melt K_2O/Na_2O-ratios decrease slightly with increasing temperature and degree of melting. A strong decrease occurs from 8 to 13 GPa when K-hollandite extends its stability field to as much as 200 °C above the solidus.

Further experiments on the dry composition and on the one containing 1.1 wt% H_2O, at 5.5, 6.5 and between 16 and 23.5 GPa allowed to connect the results of this thesis to the one of Thomsen (2006) investigating the 1.1 wt% H_2O composition at lower pressure (2.5-5 GPa). On the other side this series covers the pressure range of the mantle transition zone (410-660 km depth). Subsolidus mineralogies to 16 GPa contain garnet, clinopyroxene, coesite or stishovite, kyanite or corundum, phengite or kfsp ($\leq$ 8 GPa in the bulk with and without H_2O, respectively) and then K-hollandite, a Ti-phase and dolomite or Mg-calcite or aragonite + magnesite. The breakdown of clinopyroxene at $>$ 16 GPa causes a Na-rich Ca-carbonate to replace aragonite, the former then coexists with magnesite and a sodium-rich fluid. Further pressure increase leads to typical transition zone minerals such as the CAS-phase and 1 or 2 perovskites which substitute garnet at the highest investigated pressures (23.5 GPa). Melting occurs 200-350 °C below the mantle geotherm, i.e. lower than in any other natural composition, and results in alkali-rich carbonate melts. This contrasts the melting behaviour at $<$ 5 GPa where silicate melting occurs before carbonate melting (Thomsen and Schmidt, 2008b). At pressures at which cpx remains residual, the Ca-Mg-Fe-carbonate melts have extreme K_2O/Na_2O ratios, but at higher pressures, Na is repartitioned between several phases (max. 11 wt% in carbonates) and becomes as incompatible as at $<$ 3 GPa, leading to Na-rich carbonate melts with K_2O/Na_2O ratios $<$ 0.5. This leaves the pressure interval of ca. 4-15 GPa for ultrapotassic metasomatism. Comparison of the solidus with typi-

cal subducting slab-surface temperatures yields two distinct depths of probable carbonated pelite melting: at 6-9 GPa between the intersection of the silicate with the carbonate melting reaction and the phengite or kfsp stability limit, the solidus has a negative Clapeyron slope. The second melting opportunity is related to possible slab stagnation at the 660-km discontinuity which leads to thermal relaxation and partial melting of the most fertile rocks, thus recycling CO_2, alkalis and other lithophile and strongly incompatible elements back into the mantle.

To investigate the metasomatic effect that carbonate melts would produce upon migration into the mantle, highly alkaline potassic carbonate melts generated through partial melting of carbonated pelites at 8 and 13 GPa have been equilibrated with a lherzolitic mantle composition. Experiments have been run at 8 and 13 GPa, at 1100 °C-1350 °C under oxidizing and under more reducing (fO_2 = NNO-1 and IW-0.7) conditions. Under oxidizing conditions, the lherzolite is transformed into a wehrlite made of clinopyroxene, olivine and garnet coexisting with magnesite and K-rich carbonates and melt. Under more reducing conditions garnet and carbonates are replaced by phase X, diamond, and small pockets of unquenchable highly potassic melt/fluid (absent in the more reduced experiments at fO_2 = IW-0.7). These experiments suggest a scenario were alkaline carbonate melts will rise into the mantle and percolate upwards as long as the mantle remains at adiabatic temperatures. In relatively cold lithospheric mantle keels of continental shields, the carbonate melts may at least partially freeze. More likely, they react with the reduced mantle to potassium-, carbonate/diamond- and incompatible element-rich metasomatized zones, which are prime candidates to constitute the source regions of ultrapotassic magmas such as group II kimberlites and many lamproites.

The reverse sandwich experiments used to determine the exact melt compositions at near solidus conditions have been doped with over 40 trace elements including LILEs, REEs and HFSEs. Mineral/liquid partition coefficients have been determined for clinopyroxene, garnet, K-hollandite, CAS-phase, FeTi-perovskite and the K_2O-rich carbonate. The K-hollandite-carbonate melt partition coefficients are all < 0.3 except for K itself increasing then with pressure. In the Ca-rich CAS phase crystallizing at P > 20 GPa, Pb, Th and U are highly compatible with $D_{Pb} > D_{Th} > D_U > 1.5$ and $D_{Pb}/D_U = 15$. Melting in presence of this phase in the residuum leads to fractionation of these elements and to reservoirs showing different Pb isotopic flavors. Resulting estimated bulk $D^{sediment/carb.\,melt}$ based on our measured partition coefficients increase with pressure for almost all elements. Fractionation between Nb and Ta is particularly effective at the lowest pressure in the presence of cpx. At 22 GPa, the fractionation of the elements having an effect on the Pb isotopic evolution is more prominent. Calculated trace element compositions for the carbonate melts show a large enrichment in incompatible elements including LILEs and LREEs and negative anomalies for Ti, Nb and Ta (at 8 and 13 GPa) and Hf and Zr (at 22 GPa). Primitive mantle normalized patterns for the carbonate melts calculated with a simple batch melting equation show good matches with many alkaline rocks including lamproites, kamafugites and group II kimberlites confirming the presence of a sedimentary component in the source region of these rocks.

Riassunto

Questo studio è focalizzato sulla subduzione e il riciclaggio finale nel mantello profondo di sedimenti pelitici contenenti carbonati. In una prima serie di esperimenti, a 8 e 13 GPa e temperature tra 900 e 1850 °C, è stata studiata la fusione di tre differenti sedimenti caraterizzati da variabili quantità di H_2O (0-1.1 wt%), X_{Ca}, Mg# e rapporti K/Na. Questi esperimenti hanno permesso di definire le paragenesi di questi sedimenti allo stato subsolidus, le condizioni e reazioni di fusione e la composizione dei liquidi prodotti. Le fasi subsolide stabili sono granato, clinopirosseno, coesite/stisciovite, cianite/corindone, fengite/felspato alcalino, K-hollandite, una fase a titanio e carbonati. Con il crescere della pressione da 8 a 13 GPa il solidus della composizione contenente 1.1 wt% di H_2O passa da 950 a 1150 °C, quello della composizione anidra invece è localizzato a 1070 °C a 8 GPa e a 1320 °C a 13 GPa. A causa della destabilizzazione della fengite al crescere della pressione (ca. 9 GPa) e dell'assenza di una fase idrata a pressioni più alte, la fusione nella composizione contenente 1.1 wt% di H_2O passa da *fluid-absent* a 8 GPa a condizioni in cui il sistema è saturo in H_2O a 13 GPa. Le reazioni di fusione sono controllate dai carbonati (magnesite e aragonite) e dalle fasi idrate e potassiche (fengite, felspato alcalino e K-hollandite) presenti allo stato subsolido. La composizione dei primi liquidi è stata determinata attraverso esperimenti "reverse-sandwich". Questi liquidi risultano essere Ca-Fe-Mg-carbonatiti estremamente ricchi di potassio il cui valore di K_2O/Na_2O (wt%) è di ca. 41 a 8 GPa. Durante la fusione il Na si comporta da incompatibile entrando nella struttura del pirosseno. Il coefficiente di partizionamento del Na tra clinopirosseno e i primi liquidi carbonatitici $D_{Na}^{cpx/carb.\,melt}$ varia tra 10 e 18 a 8 GPa. Il rapporto K/Na diminuisce moderatamente con il crescere della temperatura e del grado di fusione, e decresce ancor più marcatamente all'aumentare della pressione dove la K-hollandite è stabile fino a 200 °C sopra il solidus.

Ulteriori esperimenti realizzati usando due differenti composizioni, una contenente 1.1 wt% di H_2O e l'altra anidra, a 5.5, 6.5 e tra i 16 e 23.5 GPa, hanno permesso da un lato di collegare i risultati di questo studio con un precedente lavoro di dottorato (Thomsen, 2006) svolto a condizioni di pressione inferiori, e dall'altro di coprire l'intervallo di pressione definito dalla zona di transizione (400-660 km). I minerali stabili allo stato di subsolido sono granato, clinopirosseno, coesite/stisciovite, cianite/corindone, fengite/felspato alcalino ($P < 8$ GPa), K-hollandite (a $P >$ 9 GPa), una fase a titanio e dolomite/Mg-calcite o aragonite + magnesite. La destabilizzazione del clinopirosseno a pressioni maggiori di 16 GPa favorisce la stabilità di un carbonato di calcio ricco in Na il quale sostituisce l'aragonite e coesiste così con magnesite e con un fluido ricco di sodio. L'ulteriore aumento di pressione porta alla cristallizzazione di minerali tipici per la zona di transizione come la fase CAS e uno o più perovskiti i quali, a $P > 23$, sostituiscono completamente il granato. La fusione avviene a condizioni di temperatura inferiori a qualsiasi altra composizione naturale. Tra i 200 e 350 °C al di sotto dell'adiabatica di mantello i liquidi risultanti sono carbonatiti ricche in alcali, in contrasto con la fusione a $P < 5$ GPa (Thomsen and Schmidt, 2008b) la quale produce magmi silicei. A condizioni di pressione dove il clinopirosseno rimane

residuale, le carbonatiti mostrano un elevato rapporto di K_2O/Na_2O. A pressioni più alte ($P > 16$ GPa) il sodio viene ripartito in quantità inferiori tra diverse fasi (massima concentrazione di 11 wt% nel carbonato), diventando, così come a pressioni inferiori a 3 GPa, altamente incompatibile. Questo causa la formazione di liquidi con un rapporto $K_2O/Na_2O < 0.5$, definendo così un intervallo per il metasomatismo ultrapotassico tra i 4 e 15 GPa. Il confronto tra la temperatura di fusione e un'ipotetica temperatura, che contraddistingue la superfice superiore dello slab, mostra due profondità alle quali, durante la subduzione, la fusione risulta essere più probabile. La prima occasione la si incontra tra i 6 e 9 GPa, nell'intervallo tra l'intersezione della linea di fusione dei carbonati con quella dei silicati a 5 GPa, e il limite superiore di stabilità della fengite a ca. 9 GPa (in questo intervallo la curva di fusione ha una pendenza di Clayperon negativa). Un'ulteriore occasione di fusione si presenta a pressioni maggiori dove lo slab stagna a 660 km. Una prolungata stagnazione causa un rilassamento delle isoterme e la fusione delle rocce più fertili favorendo così il riciclaggio nel mantello di CO_2, alcali e altri elementi altamente incompatibili.

Volendo approfondire lo studio dell'effetto metasomatico che le carbonatiti potrebbero causare durante la migrazione nel mantello, una serie di carbonatiti altamente alcaline, prodotte dalla fusione di sedimenti pelitici a 8 e 13 GPa, è stata fatta equilibrare con una composizione lherzolitica. Gli esperimenti sono stati condotti a 8 e 13 GPa, a temperaturte tra i 1100 e 1350 °C in condizioni ossidanti e ridotte (fO_2=NNO-1 e IW-0.7). In condizioni di redox ossidanti la lherzolite viene trasformata in una wehrlite caratterizzata da clinopirosseno, olivina, granato, magnesite, un carbonato di potassio e magnesio e da un liquido carbonatitico ricco di K e Na. A condizioni più riducenti il granato e i carbonati sono sostituiti dalla fase X, da diamanti e da minuscole tasche di liquido *"unquenchable"*. Questi esperimenti preliminari suggeriscono uno scenario in cui, dopo la fusione di sedimenti carbonatici le carbonatiti alcaline lasciano lo slab e percolano nel mantello fintanto che il mantello è caratterizzato da temperature adiabatiche. Sotto i cratoni continentali dove la tempersature sono più basse rispetto all'adiabatica di mantello e le condizioni fO_2 più riducenti, queste carbonatiti possono venir "congelate" formando così zone metasomatiche ricche di potassio, elementi incompatibili, diamanti e carbonati. Queste zone costituiscono molto probabilmente la regione sorgente per magmi ultrapotassici come le kimberliti del gruppo II o i lamproiti.

Gli stessi esperimenti "reverse-sandwich" utilizzati per determinare con esattezza la composizione dei primi liquidi che si formano dalla fusione di sedimenti pelitici con carbonato sono stati dopati con più di 40 elementi in traccia icludendo LILEs, REEs e HFSEs. I coefficenti di partizionamento tra minerali e liquidi sono stati calcolati per clinopirosseno, granato, K-hollandite, fase CAS, FeTi-perovskite e il carbonato ricco di potassio. I bassi valori dei coefficenti di partizionamento tra K-hollandite e carbonatite a 13 GPa suggeriscono un ruolo minore svolto da questa fase durante il frazionamento di fusione; d'altro canto a 22 GPa i coefficenti sono ca. un ordine di magnitude più elevati in accordo con stime e ipotesi precedenti. Pb, Th e U sono altamente compatibili nella fase CAS (stabile a $P > 20$ GPa) con $D_{Pb} > D_{Th} > D_U > 1.5$ e $D_{Pb}/D_U = 15$. La fusione in presenza di questa fase nel residuo comporta un alto grado di frazionamento rispetto a questi elementi generando così diversi reservoir geochimici caratte- rizzati da variabili

valori istopici di Pb. I valori dei coefficenti di partizionamento complessivi del sistema studiato aumentano con l'aumentare della pressione. Il frazionamento tra Nb e Ta è particolarmente efficace a pressioni più basse in presenza di clinopirosseno, mentre a 22 GPa il frazionamento di elementi che hanno una conseguenza sull'evoluzione isotopica del Pb è più evidente. La composizione chimica delle carbonatiti calcolata, per quel che concerne gli elementi di traccia, mostra un alto grado di arricchimento degli elementi più incompatibili (LILEs e LREEs) e un'anomalia negativa in Ti, Nb e Ta (a 8 e 13 GPa) e in Hf e Zr (a 22 GPa). Usando una semplice equazione di "batch melting", i liquidi carbonatitici calcolati, normalizzati al mantello primitivo, mostrano una buona corrispondenza con numerose rocce ultrapotassiche come lamproiti, kamafugiti e kimberliti di gruppo II, confermando la possibile presenza di sedimenti e CO_2 nelle regioni sorgente di queste rocce.

Contents

Chapter 1

Introduction

The oceanic crust including its sedimentary layer is part of the oceanic lithosphere subducting into the upper mantle and transition zone. Recycling of crustal materials into the mantle occurs through two distinct subduction related processes: first, the subducting oceanic crust partly devolatilizes, produces a mobile phase (fluid, melt or supercritical liquid, Schmidt et al., 2004; Kessel et al., 2005a,b) and thus looses part of its main and trace element inventory to the mantle wedge. Everything that has been left behind by this mobile phase will then be recycled at large depths and ultimately mix into the mantle. Such mantle heterogeneities are commonly classified by their Pb, Nd, Sr, and Hf isotopy (e.g. Eisele et al., 2002; Stracke et al., 2005), and the so-called EM-I mantle type has an important component of recycled oceanic pelitic sediments (Turner and Foden, 2001; Eisele et al., 2002). Within the geochemical element cycle, oceanic sediments are the principal subduction carrier of traces enriched in the continental crust, seawater, or manganese nodules on the ocean floor (e.g. K, Be, Sr, Th, Pb; Plank and Langmuir, 1998; Rehkämper and Nielsen 2004; Kelley et al. 2005). Subduction of sediments is the only process to recycle these lithophile elements back into the mantle.

1.1 Previuos work

Metapelites at P $>$ 2.5 GPa are eclogites composed of phengite + garnet + clinopyroxene + coesite + kyanite $\pm$ rutile (Schmidt et al., 2004). Only few studies have experimented on metapelites at $>$ 4 GPa: Domanik and Holloway (1996) to 11 GPa and they found the pressure stability limit of phengitic muscovite occuring at 8 GPa. As in K-enriched basaltic bulk compositions (Schmidt, 1996), phengite is replaced by K-hollandite ($KAlSi_3O_8$). Ono (1998) studied average shale and continental crust compositions at 6-15 GPa, 800-1400 °C, confirming replacement of phengite by K-hollandite near 9 GPa. He found, that in peraluminous compositions topaz-OH ($Al_2Si_4(OH)_2$, Wunder et al., 1993) forms near 9 GPa, which in turn reacts to phase egg ($AlSiO_3(OH)$, Eggleton et al., 1978; Schmidt et al., 1998) around 12 GPa. Phase egg is stable to 22 GPa in synthetic Al_2O_3-SiO_2-H_2O systems (Sano et al., 2003), its temperature stability in natural systems appears to be quite limited (Ono, 1998) (Fig. 1.1 a). Dobrzhinetskaya and Green (2007) confirmed the presence

of K-hollandite and topaz-OH in continental crust compositions at 9-12 GPa and achieved melting at 1100-1300 °C at 12 GPa. Irifune et al. (1994) have studied the melting of an average continental crust composition, in which all FeO was replaced by CoO, at 6-24 GPa, 1200-1800 °C. The composition is slightly peraluminous, kyanite reacting at $>$ 16 GPa to a Ca- and Al-rich silicate phase (CAS-phase). Between 21 and 24 GPa, jadeitic clinopyroxene disappears and a Na-rich calcium ferrite-type phase forms coexisting with Ca-perovskite (fig. 1.1a). In a similar peraluminous composition but with lower CaO and higher Na_2O contents Wu et al. (2009) confirmed the presence of Ca-pv at P $>$ 20 GPa still coexisting with jadeitic pyroxene up to 24 GPa. No CAS-phase was observed in the latter study. That the CAS-phase crystallizes only in CaO rich bulk composition was confirmed by Rapp et al. (2008). Finally, Sueda et al. (2004) have shown, that pure K-hollandite is stable to $>$ 50 GPa.

There are even fewer studies on impure carbonates than on pelites at P $>$ 2 GPa (Fig. 1.1 b). Although there is a large number of studies on carbonated mafic eclogites (e.g. Molina and Poli, 2000; Hammouda, 2003; Yaxley and Brey, 2004; Dasgupta et al., 2004; Dasgupta et al., 2005; Litasov et al., 2008), there is only one study on CO_2-rich pelites at $>$ 5 GPa (Domanik and Holloway, 1998), which has shown that the phengite to K-hollandite transition remains at similar pressures (8-9 GPa). In general, the stable carbonates succeed each other with increasing pressure in the sequence calcite - dolomite - magnesite (Molina and Poli, 2000, for MORB at subsolidus conditions) and Mg-calcite at the highest temperatures, the transition conditions strongly depending on bulk composition (fig. 1.1b).

The melting systematics of carbonated eclogites and peridotites at 2-9 GPa is closely dependent on the relations in the $CaCO_3$+$MgCO_3 \pm FeCO_3$ system (Buob et al., 2006). This is because mafic eclogites may be refractory at high pressures: the studies on carbonated basalts are on H_2O-free bulk compositions without significant K_2O, and Na_2O partitioning strongly into cpx but not into the melt at $>$ 3.5 GPa (Schmidt et al., 2004). Somewhat simplifying, this leads to relatively high melting temperatures of the silicate component, and thus initial melts are carbonate melts with a few wt% SiO_2 (Dasgupta et al., 2006). Thomsen and Schmidt (2008b) have shown that the relation of carbonate and silicate melting is different in phengite bearing lithologies: the addition of H_2O and K_2O lowers the silicate component melting reaction and a silicate melt is produced while high-Mg calcite is still stable. The Mg-calcite then melts at 1050-1100 °C leading to a narrow temperature interval of coexisting silicate and carbonate melt. The fluid-absent silicate solidus is expected to intersect with the carbonate melting reaction at 5-6 GPa (fig. 1.1b), the situation in a carbonaceous pelite thus becoming similar to a carbonated MORB or peridotite, i.e. carbonate melts are expected to form first.

The strategy to study a carbonaceous pelite results from two considerations: pure carbonates are extremely stable in pressure, $CaCO_3$ to $>$ 130 GPa (Ono et al., 2007), dolomite to $>$ 9 GPa (Luth, 2001) and $MgCO_3$ to $>$ 55 GPa (Katsura et al., 1991). At the same time, carbonates are refractory, the temperature stabilities of calcite, dolomite, and magnesite at 6 GPa reaching 1730, 1350, and 1650 °C, respectively (Buob et al., 2006). Thus, at typical subduction geotherms, pure carbonate sediments will not react other than for the equilibrium dolomite = magnesite + aragonite

(Buob et al., 2006; Morlidge et al., 2006). Secondly, in subducted K_2O-rich compositions to 8-10 GPa the H_2O content in phengite amounts to ca. 1/3 of the mass of K_2O, but above this pressure, hydrous minerals are limited to peraluminous bulk compositions which have small amounts of H_2O in topaz-OH (replacing kyanite) and then in phase egg. Thus, H_2O becomes the minor volatile component above 8-9 GPa. Above this pressure, the most volatile- and alkali-rich bulk compositions, and thus probably the one most easily to melt, are carbonate-rich metapelites.

1.2 Aim of the project

The idea of this study is to understand what happens to the portion of sediments which survive the pre- and sub-arc dehydration process during subduction. In other words, this project seeks to understand the mineralogical and geochemical development of carbonate bearing pelites at depths of 150-700 km (upper mantle and transition zone), and the composition of the liquids derived from carbonated sediments, which most likely migrate into the overlying mantle and create strongly reenriched metasomatic zones. These sediments produce the chemically most important anomalies in ocean island basalts (OIB), because of all lithologies possibly present in the mantle, recycled sediments are the most exotic ones. Furthermore, K_2O and CO_2 rich metasomatism, as produced by carbonaceous metapelites is at the origin of ultrapotassic magmas (Foley, 1992) such as lamproites, kamafugites or kimberlites (Wyllie et al., 1982; Wyllie, 1988; Mitchell, 1995; Mitchell, 2005), the latter containing all of the diamonds presently exploited.

A PhD thesis (Thomsen, 2006) has investigated the mineralogy and melting of carbonaceous pelites to 5 GPa (Thomsen and Schmidt, 2008a,b). The purpose of the present project is the natural succession to a now fair knowledge on the mineralogy of subducted crust to 350 km, and on melting relations of subducted sediments to 150 km. To understand the recycling of carbonated pelites from 150 km depth to below the 660-km discontinuity through an experimental determination of the mineralogy and reactions that govern the decarbonation process and its role in the metasomatic mantle reenrichment with respect to main (K_2O, CO_2) and trace elements (U, Pb, Th, Sr, Ba, Rb, Cs, etc.) is the goal of this study.

1.3 Strategy

In order to simplify the experimental investigations of such highly complex lithologies (carbonated eclogitic metapelites), the employed bulk compositions were saturated in CO_2 (carbonates), SiO_2 (coesite/stishovite) and Al_2O_3 (kyanite/corundum). The carbonated pelites were investigated at different pressures and temperatures (5.5-23.5 GPa, 900-1850 °C) defining phase relations and compositions, melting behaviour, and melt compositions. The small amount of unquenchable carbonate liquid at the solidus is really difficult to analyze, as quench phases reach from one to the other end of each melt pool. For this reason reverse sandwich experiments have been run to constrain the melt compositions. The resulting large melt pools in the reversed experiments were also used for determination of trace element distributions between minerals and carbonate melt.

The considerable pressure and temperature window in which carbonated pelites have been studied combined with trace element partitioning between minerals and carbonate melts on different compositions allowed the investigation of various aspects related to the recycling of subducted material into the mantle and to mantle metasomatism by carbonate melts.

1.4 Starting materials

Table 1.1: *Bulk starting compositions (wt%)*

	DG1	DG2	[a]AM
SiO_2 (wt%)	55.32	54.63	47.60
TiO_2	0.67	0.63	-
Al_2O_3	21.39	20.23	22.80
FeO_{tot}	5.50	4.86	9.20
MgO	4.15	2.92	2.00
CaO	4.66	5.88	6.80
Na_2O	3.36	3.20	2.40
K_2O	2.36	2.21	3.60
H_2O	[b]traces	-	1.10
CO_2	2.60	4.50	4.80
tot.	100.00	99.07	100.30
XCO_2 (molar)	n.a.	1.00	0.64
K_2O/Na_2O (wt%)	0.70	0.69	1.50
Mg#	57.1	52.4	28.3
X_{Mg} (Fe_{tot}) (molar)	0.39	0.30	0.17
X_{Ca} (molar)	0.32	0.43	0.41
Al/(Na+K+2Ca) (molar)	1.29	1.10	1.13
Al/(Na+K) (molar)	2.65	2.64	2.91

[a]Thomsen and Schmidt (2008b)

[b]subsolidus experiment at 8 GPa includes small amount of phengites

Natural marls are sedimentary rocks composed of pelitic and carbonate components (typically calcite or dolomite), e.g. carbonate-bearing clays, often with volcanic ash, greywacke and siliceous component in addition (Plank and Langmuir, 1998). Such compositions are common shelf and platform sediments and show extremely high compositional variability. The first bulk composition (AM) (tab. 1.1) used in this study is the same as in Thomsen and Schmidt (2008b) and corresponds to a modified version of a Fe-rich calcareous clay from the Antilles (Plank and Langmuir, 1998) simplified in the K_2O-Na_2O-CaO-FeO-Fe_2O_3-MgO-Al_2O_3-SiO_2-H_2O-CO_2

(KNCFMASH-CO_2) system. The other two compositions DG1 and DG2 (tab. 1.1) are synthetic carbonated pelites in the TiKNCFMASH-CO_2 system. Although the three bulk compositions are quite different, they are all SiO_2-, kyanite-(alumina) and carbonate-saturated. The AM composition is the one with the lowest X^*_{Mg} (Mg/(Mg+Fe^{2+}+Ca)) and the highest H_2O (1.1 wt%) and FeO_{tot} content. DG2 is a nominally anhydrous composition and has a lower K_2O/Na_2O and higher X^*_{Mg} than AM. DG1 is the one with the highest X^*_{Mg} and lowest X^*_{Ca} (Ca/(Ca+Fe^{2+}+Mg))and contains a small amount of H_2O absorbed from the ambience. The compositional differences were used to obtain additional information on the effect of bulk composition. The higher X^*_{Mg} and the lower K_2O/Na_2O of the DG's-compositions could represent a more "depleted" pelite which survived a first simplified devolatilisation process.

The starting materials are made of powders of SiO_2, Al_2O_3, TiO_2, MgO, Na_2SiO_3, fayalite, Kfsp and wollastonite, which were milled and grinded to < 5 μm and then mixed with $Al(OH)_3$, $CaCO_3$ and $MgCO_3$ (pure natural magnesite from Obersdorf Philipp, 1998) to introduce the right amount of H_2O and CO_2. The powders were kept in a desiccator under ambient temperature (DG1 and AM) and dried before use, or directly stored in a vacuum oven at 110 °C (DG2). The synthesis of the carbonate melts used during reversed experiments was done by mixing different amount of $MgCO_3$, $CaCO_3$, $FeCO_3$ (Siderite has been synthesized in a hydrothermal apparatus at 2000 bar and 350 °C sealing iron oxalate in a welded gold capsule 5.4 mm O.D. French, 1971), K_2CO_3, Na_2CO_3, TiO_2, SiO_2, Al_2O_3 and $Al(OH)_3$.

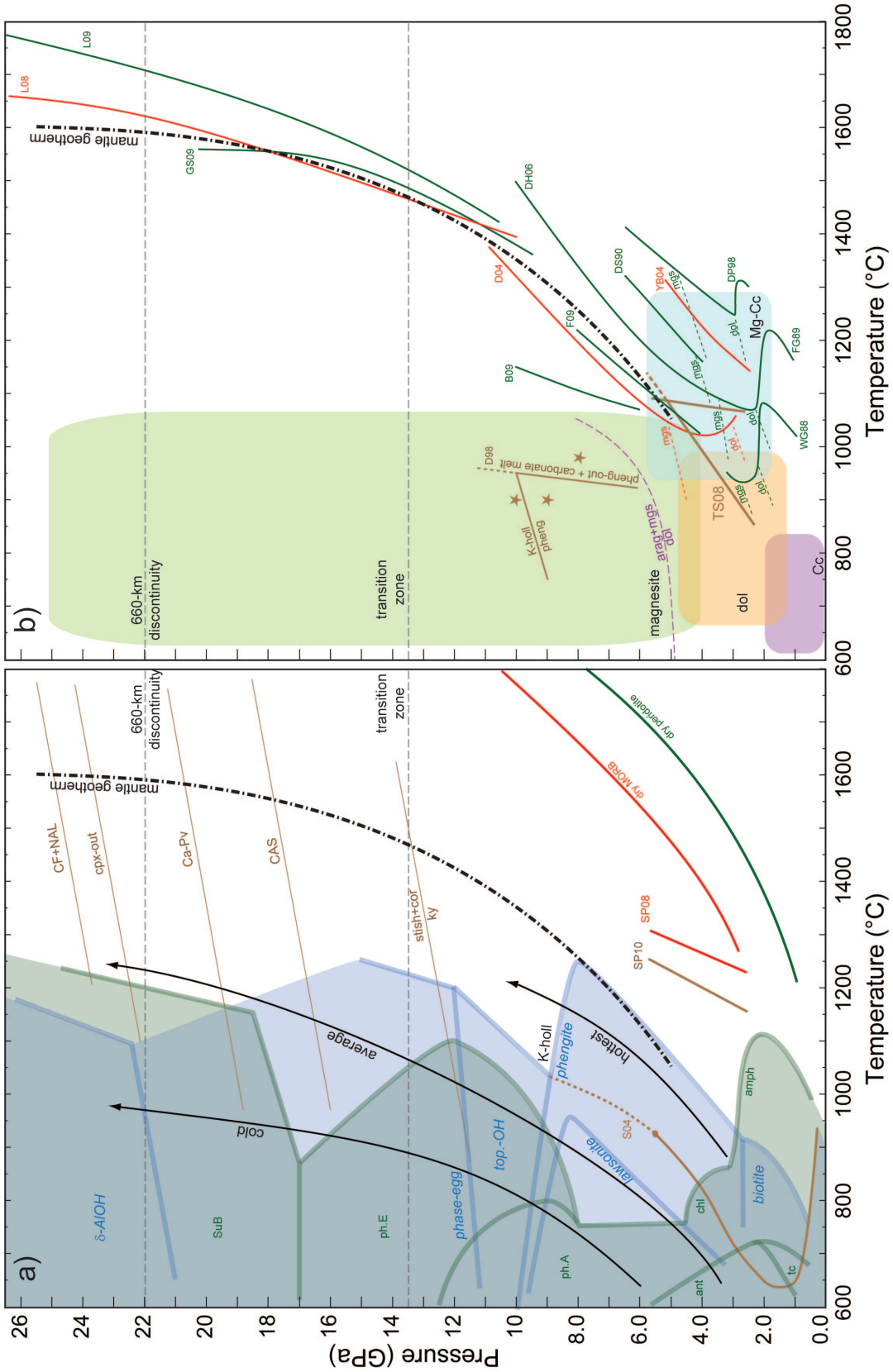
a)
b)
Pressure (GPa)
Temperature (°C)
660-km discontinuity
transition zone
mantle geotherm
cold
average
hottest
CF+NAL
cpx-out
CaPv
CAS
stish+cor
ky
δ-AlOH
SuB
ph.E
phase-egg
top.-OH
ph.A
K-holl
phengite
S04
lawsonite
chl
amph
biotite
ant
tc
SP08
SP10
dry MORB
dry peridotite
L09
L08
GS09
DH06
D04
F09
B09
DS90
YB04
DP98
FG89
WG88
TS08
Mg-Cc
magnesite
dol
Cc
arag+mgs
phengite-out + carbonate melt
K-holl
pheng

Figure 1.1: *P-T diagram for hydrous (a) and carbonated systems (b). Green lines are the solidus for different mantle materials, red lines are the solidus for basaltic compositions and brown for the pelitic. a) S04: melting and dissolution curves for potassium-rich wet sediments after Schmidt et al. (2004). SP08, SP10: solidus of a K_2O-rich basalt and of an anhydrous pelite after Spandler et al. (2008) and Spandler et al. (2010). The thin brown lines represent typical high pressure ($P > 10$ GPa) reactions in pelitic compositions after Irifune et al. (1994), Rapp et al. (2008) and Wu et al. (2009). Thick blue and green lines (and fields) show the stability of the different hydrous phases in typical peraluminous (Wunder et al., 1993; Ono, 1998; Sano et al., 2003; Dobrzhinetskaya and Green, 2007) and mantle compositions (Ulmer and Trommsdorff, 1995; Ohtani et al., 2002), respectively. The solidus for dry peridotite is after Hirschmann (2000) and the one for the dry MORB after Yasuda et al. (1994). Typical subduction paths are after Kincaid and Sacks (1997), van Keken et al. (2002) and Peacock (2003). The mantle geotherm is after Akaogi et al. (1989).*
b) Bold lines: Solidus reactions for carbonated lithologies, thin dashed lines: subsolidus reactions denote the stable carbonate phases. The slope of the solidus and melting temperatures strongly depend on the stable carbonate phase, with dolomite favoring the lowest melting temperatures. Carbonated peridotites producing carbonate liquids at > 2 GPa. WG88: Hawaiian Pyrolite + 0.3 wt% H_2O + 0.5-2.5 wt% CO_2 (Wallace and Green, 1988); FG89: Hawaiian Pyrolite + 5 wt% dolomite at ≤ 3.5 GPa (Falloon and Green, 1989); DH06: dry carbonated peridotite solidus (KLB + 2.5 wt% CO_2, Dasgupta and Hirschmann, 2007); GS09: dry carbonated peridotite solidus at 10-20 GPa (Ghosh et al., 2009). CS90, DP 98, L09: solidi in CaO-MgO-Al_2O_3-SiO_2-CO_2 system (Canil and Scarfe, 1990; Dalton and Presnall, 1998; Litasov and Ohtani, 2009). D04 and YB04: Carbonated dry basalt melting on average oceanic crust +5 wt% CO_2 (Dasgupta et al., 2004; D04) and on MORB + 30% calcite+dolomite (Yaxley and Brey, 2004; YB04). The D04 composition with X^*_{Ca}= Ca/(Mg+Fe^{2+}+Ca)=0.32 results in subsolidus dolomite and consequently in low melting temperatures, whereas the YB04 composition with X^*_{Ca}=0.44 has high Mg-calcite and melting occurs at higher temperatures. L08: solidus for simplified (CMASN) basaltic composition + CO_2 at high pressure (Litasov et al., 2008). Thick brown lines TS08: fluid-absent solidus dominated by silicates and the high Fe-Mg-calcite to carbonate melt reaction for carbonated pelite + 1.1 wt% H_2O + 4.8 wt% CO_2 (Thomsen and Schmidt, 2008b). Note that in the pelite, carbonate melts out at higher temperatures than in the D04 basaltic composition, dolomite-ankerite solid solution not forming in the low X^*_{Mg} = Mg/(Mg+Fe^{2+}+Ca) pelite. D98: phengite-out (brown-lines) and carbonate stability (stars denote the presence of magnesite in the experiments) in a fluid saturated (2.1 H_2O + 6.3 CO_2) pelite (Domanik and Holloway, 1998). The calculated fluid/melt compositions from D98 are extremly alkali- and CO_2-rich. Dashed purple curve show the experimentally determined reaction dolomite = aragonite + magnesite (Luth, 2001; Buob et al., 2006). Carbonate stability and polymorphism is very much bulk composition dependent. In general, calcite (Cc, purple field) occurs at low P-T, Mg-calcite (Mg-Cc, bright blue field) at the highest temperature, dolomite (dol, bright brown field) at increased P-T conditions and finally magnesite and aragonite at the highest pressure conditions (green field).

1.5 Organisation of the thesis

This thesis is organized as follows:

Chapter 2: *"Melting of Carbonated Pelites at 8-13 GPa: Generating K-rich Carbonate Melts for Mantle Metasomatism"*. This chapter which is presently submitted to Contibution to Mineralogy and Petrology, describes the mineralogy, melting behaviour and melt composition of the three different carbonated pelites used in this study at 8 and 13 GPa.

Chapter 3: *"The Melting of Carbonated Pelites from 70 to 700 km Depth"*. This chapter is dedicated to the fate of subducted carbonated pelites within the upper mantle and transition zone. Experiments performed with two different bulk compositions (dry and with 1.1 wt% H_2O added) between 2.5 and 23.5 GPa provide the information necessary to understand the final recycling of carbonated sediments into the mantle including CO_2, potassium and many incompatible elements enriched in sediments. This chapter is presently submitted to Journal of Petrology.

Chapter 4: *"The Role of Redox Freezing in the Generation of Highly Metasomatized Alkali- and Carbon- Rich Mantle Domains"*. In this chapter the carbonate melts previously described were let react with a peridotite at different P-T- and fO_2 conditions. Under reduced conditions, matching the mantle conditions, the carbonate melts can effectively be frozen promoting diamond nucleation and the crystallization of minerals which partly have compositions similar to the ones found as inclusions in diamonds.

Chapter 5: *"Trace Element Partitioning During Carbonated Pelite Recycling and Mantle Metasomatism by Alkali-rich Carbonate Melts at 8, 13 and 22 GPa: Sediment Signature in Mantle Components"*. This chapter reports trace element partition coefficients between minerals and carbonate melts. LA-ICP-MS measurements have been done by the Günther Group (Prof. Detlef Günther and Kathrin Hametner: Department of Chemistry and Applied Biosciences). Bulk partition coefficients have been calculated at different pressures. Resulting carbonate melt compositions calculated with a simple butch melting equation are discussed as possible metasomatic agent of the mantle.

Chapter 2

Melting of Carbonated Pelites at 8-13 GPa: Generating K-rich Carbonate Melts for Mantle Metasomatism

Daniele Grassi and Max W. Schmidt
Submitted and accepted: Contr.Min.Petr.

Abstract

The melting behavior of three carbonated pelites containing 0-1 wt% water was studied at 8 and 13 GPa, 900-1850 °C to define conditions of melting, melt compositions, and melting reactions. At 8 GPa, the fluid-absent and dry carbonated pelite solidi locate at 950 and 1075 °C, respectively; $>$ 100 °C lower than in carbonated basalts and 150-300 °C lower than the mantle adiabat. From 8 to 13 GPa, the fluid-present and dry solidi temperatures then increase to 1150 and 1325 °C for the 1.1 wt% H_2O and the dry composition, respectively. The melting behavior in the 1.1 wt% H_2O composition changes from fluid-absent at 8 GPa to fluid-present at 13 GPa with the pressure breakdown of phengite and the absence of other hydrous minerals. Melting reactions are controlled by carbonates and the potassium and hydrous phases present in the subsolidus. The first melts, which composition has been determined by reverse sandwich experiments, are potassium-rich Ca-Fe-Mg-carbonate melts, with extreme K_2O/Na_2O wt-ratios of up to 42 at 8 GPa. Na is compatible in clinopyroxene with = 10-18 at the solidus at 8 GPa. The melt K_2O/Na_2O slightly decreases with increasing temperature and degree of melting but strongly decreases from 8 to 13 GPa when K-hollandite extends its stability field to 200 °C above the solidus. The compositional array of the sediment derived carbonate melts is congruent with alkali- and CO_2-rich melt or fluid inclusions found in diamonds. The fluid-absent melting of carbonated pelites at 8 GPa contrasts that at 5 GPa where silicate melts form at lower temperatures than carbonate melts. Comparison

of our melting temperatures with typical subduction and mantle geotherms shows that melting of carbonated pelites to 400 km depth only feasible for extremely hot subduction. Nevertheless, melting may occur when subduction slows down or stops and thermal relaxation sets in. Our experiments show that CO_2-metasomatism originating from subducted crust is intimately linked with K-metasomatism at depth $>$ 200 km. As long as the mantle remains adiabatic, low viscosity carbonate melts will rise into the mantle and percolate upwards. In cold subcontinental lithospheric mantle keels, the potassic Ca-Fe-Mg-carbonate melts may freeze when reacting with the surrounding mantle leading to potassium-, carbonate/diamond- and incompatible element enriched metasomatized zones, which are most likely at the origin of ultrapotassic magmas such as group II kimberlites.

Keywords: carbonated pelites, potassium-rich carbonate melts, subduction recycling, mantle metasomatism, potassic magmatism.

2.1 Introduction

Recycling of crustal materials into the mantle occurs through two different subduction related processes: first, the subducting oceanic crust devolatilizes at least partly and produces a mobile phase (which could be a fluid, melt or supercritical liquid, Schmidt et al., 2004; Kessel et al., 2005a,b) thus loosing part of its main and trace element inventory to the mantle wedge. Whatever has been spared and left behind by this fore- and sub-arc process will then be recycled to large depths and ultimately mixed into the mantle. While H_2O is the dominant volatile component in the fore- and sub-arc (Nichols et al., 1994), this is not the case at greater depths. Beyond ca. 9 GPa, after dehydration of lawsonite and phengite, (Schmidt and Poli, 1998; Ono, 1998) only few hydrous phases remain stable, for example, topaz-OH and phase egg in peraluminous sediments (Ono, 1998) and hydrous alphabet phases in peridotite (Komabayashi et al., 2004). With depth, these hydrous phases become minor in abundance, and most of the H_2O in the subducting slab becomes stored in nominally anhydrous phases (Hirschmann et al., 2005). In contrast, carbonates, which are refractory at subarc depth (Molina and Poli 2000; Dasgupta et al. 2004; Thomsen and Schmidt, 2008a,b), maintain their stability beyond subarc depth conserving most of the CO_2 stored in the subducting lithosphere (Kerrick and Connolly, 2001; Connolly, 2005).

The strategy to study a carbonated water-poor or dry pelite results from the fact that after the reaction of phengite to K-hollandite near 9 GPa (Domanik and Holloway, 1998; Ono, 1998) hydrous minerals are limited or absent and flush melting (Poli and Schmidt, 2002) of sediments assisted by fluids derived from underlying oceanic basalts or serpentinized peridotites is limited to 9 and 6-7 GPa, respectively (Kawamoto et al., 1996; Schmidt and Poli, 1998). Furthermore, sodium becomes compatible in clinopyroxene at 3.5 GPa (Schmidt et al., 2004), leaving potassium which strongly depresses the solidus temperature of subducted sediments. Thus, the most fertile composition within the subducting oceanic lithosphere should be CO_2- and K_2O-rich, and melting reactions are expected to be controlled by carbonates and potassic phases. Although there are a

large number of studies on carbonated mafic eclogites (Yaxley and Green, 1994; Hammouda, 2003; Yaxley and Brey, 2004; Dasgupta et al., 2004,2005,2006; Litasov and Ohtani, 2009), there are only three studies on carbonated pelites at upper mantle conditions (Domanik and Holloway, 1998; Thomsen and Schmidt, 2008a,b). As has been pointed out (Dasgupta et al., 2005; Thomsen and Schmidt, 2008b), the melting systematics of peridotites and carbonated K-poor mafic eclogites at 2-7 GPa is similar to the melting relations in the simple $CaCO_3$-$MgCO_3$±$FeCO_3$ system (Irving and Wyllie, 1975; Buob et al., 2006). This is because Na_2O partitions into clinopyroxene at $>$ 3.5 GPa and somewhat simplifying, the silicate components are refractory at $>$ 3.5 GPa thus leading to initial carbonate melts with a few wt% SiO_2 (Dasgupta et al., 2004).

The relation of carbonate and silicate melting is different in K_2O-rich, phengite bearing lithologies (Thomsen and Schmidt, 2008b): the addition of H_2O and K_2O lowers the temperature of the fluid-absent silicate solidus to 900-1150 °C (2.5-5 GPa) such that at the solidus silicate melt coexists with high-Mg calcite. The latter then melts out in an almost isothermal reaction at 1050-1100 °C (2.5-5 GPa) leading to a narrow, $<$ 50 °C temperature interval of coexisting silicate and carbonate melt. We expect the fluid-absent silicate solidus with its positive Clapeyron slope of ca. 70 °C/GPa to intersect with the almost isothermal carbonate melting reaction at 5-5.5 GPa. Above this pressure, the melting relations of carbonated pelites should be similar to carbonated MORB or peridotite, in that carbonate melts form at the solidus. The scope of this study is to address the mineralogical and geochemical development of carbonated pelites after major dehydration at depths of 250-400 km, and to determine the composition of melts derived from carbonated pelites. These carbonate melts will migrate into the overlying mantle to create strongly enriched metasomatic zones possibly leading to the formation of most diverse geochemical anomalies in the mantle. Furthermore, K_2O and CO_2 rich metasomatism, as would be produced by carbonated metapelite melts is probably at the origin of group II kimberlites (Wyllie and Sekine, 1982; Wyllie, 1988; Mitchell, 1995; Mitchell, 2005) and other ultra-potassic strongly Si-undersaturated magmas. For these reasons we investigate the melting of three carbonate saturated pelites at 8 and 13 GPa, H_2O-free, and with small water contents, experimentally determine melting conditions, and reverse initial melt compositions.

2.2 Experimental procedure and analytical technique

2.2.1 Starting material

The hydrous composition (AM) used in this study is the same as in Thomsen and Schmidt (2008b) and corresponds to a Fe-rich calcareous clay from the Antilles (Plank and Langmuir, 1996) simplified in the K_2O-Na_2O-CaO-FeO-MgO-Al_2O_3-SiO_2-H_2O-CO_2 (KNCFMASH-CO_2) system. The other two compositions DG1 and DG2 are synthetic carbonated pelites in the TiKNCFMASH-CO_2 system saturated in coesite/stishovite, kyanite/corundum and carbonates. The starting materials (tab. 2.1) are made of powders of SiO_2, Al_2O_3, TiO_2, MgO, Na_2SiO_3, fayalite, K-feldspar, wollastonite, $Al(OH)_3$, $CaCO_3$, and $MgCO_3$ (pure natural magnesite from Obersdorf; Buob et al.,

2006) the latter three components to introduce the right amounts of H_2O and CO_2. The powders were mixed employing automatical mills and ground to < 5 μm. The starting materials were then kept in a desiccator and dried at 110 °C before each use (DG1 and AM), but DG1 turned out to contain a small amount of water absorbed from air, producing some minor phengite. Thus, DG2 was mixed, permanently stored in a vacuum oven at 110 °C, and did not yield any indication for the presence of H_2O.

Table 2.1: Bulk starting compositions (wt%)

	DG1	DG2	[a]AM
SiO_2 (wt%)	55.32	54.63	47.60
TiO_2	0.67	0.63	-
Al_2O_3	21.39	20.23	22.80
FeO_{tot}	5.50	4.86	9.20
MgO	4.15	2.92	2.00
CaO	4.66	5.88	6.80
Na_2O	3.36	3.20	2.40
K_2O	2.36	2.21	3.60
H_2O	[b]traces	-	1.10
CO_2	2.60	4.50	4.80
tot.	100.00	99.07	100.30
XCO_2 (molar)	n.a.	1.00	0.64
K_2O/Na_2O (wt%)	0.70	0.69	1.50
Mg#	57.1	52.4	28.3
X_{Mg} (Fe_{tot}) (molar)	0.39	0.30	0.17
X_{Ca} (molar)	0.32	0.43	0.41
Al/(Na+K+2Ca) (molar)	1.29	1.10	1.13
Al/(Na+K) (molar)	2.65	2.64	2.91

[a]Thomsen and Schmidt (2008b)
[b]subsolidus experiment at 8 GPa includes small amount of phengites

2.2.2 Experimental apparatus and sample preparation

Experiments were conducted in a 600-ton Walker-type rocking multi-anvil at 8 and 13 GPa. To improve the attainment of equilibrium and to reduce chemical zonation in the capsules the whole multi-anvil apparatus was rotated by 180 °C during the experiments (Schmidt and Ulmer, 2004). The experiments were rotated continuously during the first 30 minutes and then every 10 minutes during the remainder of the experiments lasting up to 5 days. Tungsten carbide cubes with truncation edge lengths of 8 and 11 mm in combination with prefabricated MgO-octaedra of 14 or 18 mm edge length (14/8 and 18/11 assemblies for 13 and 8 GPa, respectively) were used for the experiments. Natural pyrophyllite gaskets were employed. The furnace assemblies consist of a ZrO_2 sleeve, a stepped $LaCrO_3$ heater with inner MgO pieces, and a molybdenum disk

or ring between the furnace and the WC cubes. Pressure was calibrated based on the coesite-stishovite (Yagi and Akimoto, 1976; Zhang et al., 1996) and forsterite-wadsleyite (Morishima et al., 1994) transitions for the 14/8 assembly, and on the coesite-stishovite and $CaGeO_3$-garnet-perovskite (Susaki et al., 1985) transitions for the 18/11 assembly. Temperature was controlled by a B-type ($Pt_{94}Rh_6$/$Pt_{70}Rh_{30}$) thermocouple and no correction for the effect of pressure on the emf was applied. One or two capsules made of Au, $Au_{80}Pd_{20}$, or $Au_{50}Pd_{50}$ with 1.6 or 2 mm outer diameter (at 13 and 8 GPa, respectively) and lengths of approximately 1.5 mm were used in each experiment. Quenching was achieved by turning off the heating power and was followed by pressure unloading of about 15-20 hours. To avoid any loss of the alkali-rich quench phases of the carbonate melts, capsules were mounted longitudinally in epoxy resin and polished to the centre using a dry polish technique. The open capsules were repeatedly impregnated with low viscosity resin to avoid the loss of fragments from the quenched carbonate melts. After being prepared for analysis, all run charges were kept in a desiccator under vacuum conditions to avoid the formation of whiskers growing on the quenched carbonate melts, the former resulting in the destruction of the sample. Equilibrium in the experiments is indicated by well-crystallized grains, 120° triple junctions between phases, and a homogenous composition of the different crystalline phases throughout a particular capsule. Trends of mineral composition as a function of pressure and temperature and mass balance calculations suggest that complete equilibrium was generally reached, at least for the experiments above the solidus.

2.2.3 Analytical methods

All experimental charges were analyzed with a JEOL JXA8200 electron microprobe at ETH-Zürich with 15 kV acceleration voltages, 20 nA beam current for silicate minerals and 5 nA for carbonates and carbonate liquids. Acquisition times were 10 s for Na and K and 20 s for all other elements. Na and K were measured first to avoid diffusional losses. Beam diameters of 1 to 2 μm were used for all silicate and carbonate phases. Quenched melts were analyzed with the most defocused beam possible (3-20 μm). Secondary and back-scattered electron images from the microprobe or from a JEOL JSM6300 field emission SEM were used for textural analysis. Micro-Raman spectroscopy was necessary to identify $CaCO_3$ polymorphs (aragonite), Ti-oxides (TiO_2 with α-PbO_2 structure) and K-hollandite.

2.2.4 Reverse "sandwich experiment" melt composition determination

Carbonate melts are unquenchable and at low melt fractions form, interstitial melt pools or thin films along capsule walls (fig. 2.1), which are almost impossible to properly polish. In addition, quench phases cross the entire melt pools or films, thus measurements could not be performed with a sufficiently defocused electron beam, and contamination by residual mineral phases during the measurement could not be excluded. A focused or only slightly defocused electron beam leads to beam damage in the quench and to alkali-loss during measurement. Furthermore, the softness, heterogeneity, small size and reactivity with ambient humidity of the high-alkali carbonate quench

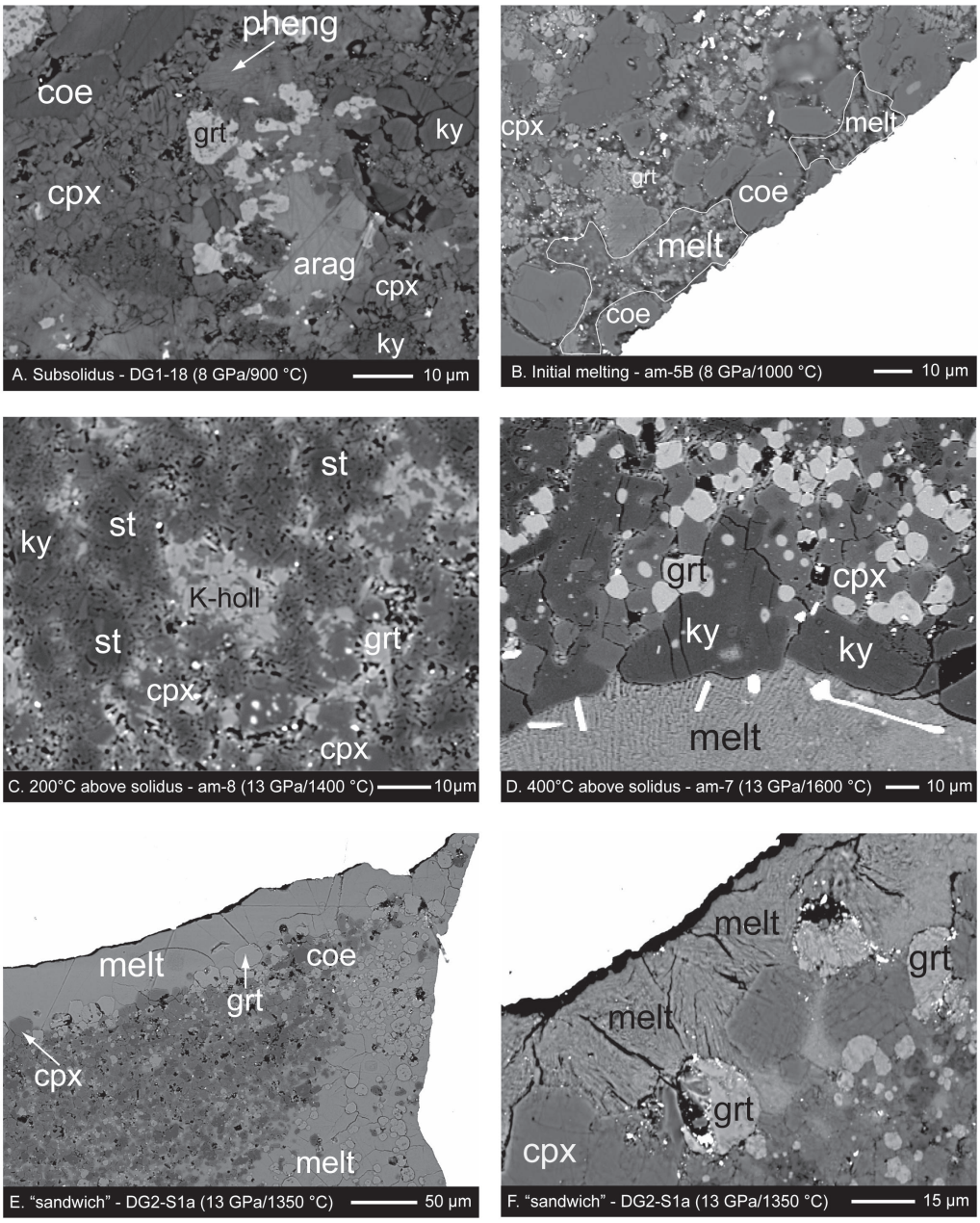

Figure 2.1: *BSE-images of run products. A. 8 GPa, 900 °C, bulk DG1; subsolidus experiment crystallizing a small amount of phengite coexisting with kfsp, grt, cpx, coe, ky, mgs, arag and a Ti-oxide. B. 8 GPa, 1000 °C, bulk AM; Initial melting with the characteristic heterogeneous and small melt pockets which in this case concentrate at the top of the capsule. C. 13 GPa, 1400 °C, bulk AM; ca. 200 °C above the solidus with K-hollandite still stable and coexisting with grt, cpx, st, ky and melt; most of the melt is concentrated along the capsule wall not visible in this image. D. 13 GPa, 1600 °C, bulk AM; Experiment ca. 400 °C above the solidus which still yields a carbonate melt ($SiO_2 < 10$ wt%) coexisting with grt, cpx, st and ky. E. and F. 13 GPa, 1350 °C, bulk DG2; sandwich experiment to reverse melt composition, large amounts of carbonate melt coexist with grt, cpx, st, ky and K-holl.*
Phase abbreviations in the figures, text and tables are: arag=aragonite; coe=coesite; cor=corundum; cpx=clinopyroxene; dol=dolomite; grt=garnet; kfsp=potassium feldspar; K-holl=K-hollandite; ky=kyanite; mgs=magnesite; pheng=phengite; stish/st=stishovite.

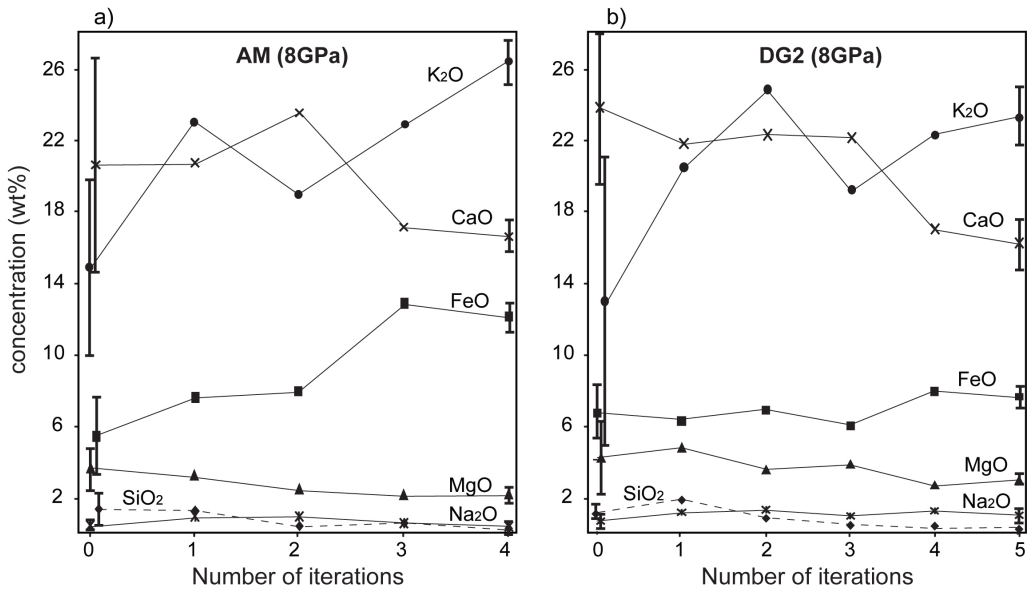

Figure 2.2: *Composition of carbonate melts produced in iterative sandwich experiments in the AM (a) and DG2 (b) composition at 8 GPa plotted versus iteration number. The composition plotted for the 0th iteration is the one measured in the normal synthesis experiment, corrected for mass balance and then added to the bulk for the first iteration. Note the large errors in particular for K and Ca which are mostly due to the heterogeneity of the quenched carbonate melts. For details of the iterative sandwich technique see text.*

material do simply not allow a satisfactory preparation and quantitative analysis of small melt pools. The preferential dissolution and mechanical loss of potassium- and sodium-rich quench during sample preparation leads to a further underestimation of the alkali concentrations which then results in artificially increased concentrations of bivalent cations (especially Ca). Melt compositions obtained under such conditions do not mass balance with the minerals, typically yielding bulks which are alkali-deficient with respect to the starting material. Thus, liquid compositions at low degrees of partial melting of the two starting materials DG2 and AM, were determined using a reverse ”sandwich” procedure (Falloon et al., 1997; Hirschmann and Dasgupta, 2007) in which the estimated melt composition from the forward experiments is mixed with the original starting material in order to obtain larger melt pools of a melt saturated in the same phases of the same composition as in the original forward experiment. These large homogeneous areas of melt (figs. 2.1e, 2.1f) then allow for analysis using a defocused beam (EMPA) or an area-scan analysis (SEM). The true melt composition at near solidus conditions is achieved after an iterative process in which the analyzed melt composition is employed as an additive to the original starting material in a cascade of consecutive experiments until mineral assemblage (garnet, clinopyroxene, coesite/stishovite, kyanite/corundum $\pm$ K-hollandite and carbonates) and mineral compositions in the final sandwich experiment are identical with those in the original melting experiment (forward experiment). Before being mixed with the original starting material the analyzed melts of the original forward experiments and of the different iterations were slightly modified according

Table 2.2: Near solidus melt compositions at 8 and 13 GPa for the hydrous (AM) and anhydrous (DG2) pelites

	AM (8/1000)			DG2 (8/1100)			AM (13/1200)			DG2 (13/1350)		
	synthesis	mass balance	reverse	synthesis	mass balance	reverse	synthesis	mass balance	reverse	synthesis	mass balance	reverse
	experiment	correction	4 iteration	experiment	correction	5 iteration	experiment	correction	4 iteration	experiment	correction	2 iteration
measurements	7		13	12		15	14		19	9		14
SiO_2 (wt%)	1.30 (0.9)	0.43	0.30 (0.1)	1.10 (0.6)	0.62	0.26 (0.1)	0.53 (0.2)	0.53	0.48 (0.2)	0.84 (0.1)	1.01	0.22 (0.1)
TiO_2	-	-	-	0.03 (0.1)	0.02	2.37 (0.4)	-	-	-	1.69 (0.2)	2.03	1.83 (0.3)
Al_2O_3	1.17 (0.4)	0.68	1.85 (0.3)	1.27 (0.2)	0.73	1.55 (0.3)	1.46 (0.3)	1.47	1.35 (0.2)	1.84 (0.1)	2.21	1.18 (0.3)
FeO_{tot}	5.45 (2.1)	4.10	12.1 (0.9)	6.67 (1.5)	3.97	7.55 (0.6)	6.64 (0.6)	6.68	9.50 (0.8)	8.73 (0.3)	9.63	7.08 (0.6)
MgO	3.60 (1.2)	5.61	2.10 (0.2)	4.22 (2.1)	4.77	2.95 (0.3)	3.32 (0.4)	3.33	2.32 (0.3)	6.39 (0.5)	6.86	5.35 (0.3)
CaO	20.59 (6.2)	10.39	16.5 (0.8)	23.90 (8.5)	15.67	16.3 (1.5)	25.48 (2.2)	20.61	25.5 (1.4)	22.29 (1.1)	26.82	26.4 (1.2)
Na_2O	0.45 (0.1)	0.20	0.65 (0.2)	0.61 (0.5)	0.18	0.95 (0.6)	4.54 (1.2)	4.57	4.8 (0.6)	4.95 (0.4)	5.96	4.71 (0.6)
K_2O	14.94 (5.1)	30.75	26.8 (1.7)	13.04 (9.2)	31.30	24.4 (2.8)	9.75 (4.1)	9.81	10.2 (1.7)	8.56 (2.1)	14.98	9.43 (1.1)
tot.	47.50	52.15	60.30	50.84	57.25	56.33	51.72	47.00	54.15	55.29	100.00	56.20
[a]Si(pfu)	0.05	0.01	0.01	0.04	0.02	0.01	0.02	0.02	0.02	0.03	0.02	0.01
Ti	-	-	-	0.00	0.00	0.05	-	-	-	0.04	0.04	0.04
Al	0.05	0.02	0.06	0.05	0.02	0.06	0.06	0.06	0.05	0.07	0.06	0.04
Fe_{tot}	0.17	0.11	0.29	0.19	0.10	0.19	0.18	0.20	0.25	0.22	0.19	0.18
Mg	0.20	0.26	0.09	0.22	0.21	0.14	0.16	0.18	0.11	0.29	0.25	0.24
Ca	0.81	0.35	0.51	0.88	0.49	0.54	0.89	0.78	0.87	0.73	0.69	0.85
Na	0.03	0.01	0.04	0.04	0.01	0.06	0.29	0.31	0.30	0.29	0.28	0.28
K	0.70	1.23	0.99	0.57	1.16	0.96	0.41	0.44	0.41	0.33	0.46	0.36
K_2O/Na_2O (wt%)	32.92	151.81	41.31	21.26	174.88	25.68	2.15	2.15	2.13	1.73	2.51	2.00
Mg#	54	70	23	54	68	42	47	47	31	57	57	57
X^*_{Mg}	0.17	0.36	0.10	0.17	0.26	0.16	0.13	0.15	0.10	0.23	0.22	0.19
X^*_{Ca}	0.69	0.49	0.57	0.68	0.62	0.62	0.72	0.68	0.71	0.59	0.61	0.67

Errors show the variability in the different analysis
[a] cations calculated on the basis of 6 oxygens.

to both, mass balance and partitioning coefficients between solid phases and melt. Secondly, the compositions of the coexisting solid solutions garnet, clinopyroxene, carbonates and K-hollandite in the iterative experiments were compared to the mineral compositions of the original forward experiments to slightly adjust the melt composition such that mineral compositions in the iterative experiments converge with those of the forward experiments. Na_2O-concentrations in the carbonate melt are limited through the saturation with jadeitic clinopyroxene. Log($D_{Na}^{cpx/carbonate\,melt}$) varies linearly with 1/T and the obtained Na_2O concentrations of the carbonate melt of the final iterative sandwich experiments are in perfect agreement with the log($D_{Na}^{cpx/carb.\,melt}$) vs. 1/T relation determined experimentally at higher temperatures (where larger melt pools allow for direct measurement of the melts in the forward experiments). The potassium content of the carbonate melt at 13 GPa is buffered by the presence of K-hollandite as SiO_2 and Al_2O_3 saturation lead to the potassium concentration as the only variable in the solution product of K-hollandite at a given pressure and temperature. At 8 GPa the K_2O concentration is not strictly buffered, but excessive K_2O contents led to the crystallization of a $K_2Ca(CO_3)_2$ carbonate. The absence of phengite and K-feldspar above the solidus at 8 GPa could have led to a slight overestimation of the total K_2O concentration and K_2O/Na_2O-ratio of the melts. Nevertheless, the low amount of melt present in the forward experiments (ca. 10 wt%) in combination with the absence of any major potassium bearing crystalline phase and a low K_2O concentration $\leq$ 0.5 wt% in both garnet and clinopyroxene, suggest a K_2O content in the carbonate melt higher than 20 wt%. Furthermore, resulting $D_K^{cpx/carb.\,melt}$ are roughly constant for temperatures to ca. 200 °C above the solidus, indicating, if any, rather an underestimation of K_2O concentrations in the carbonate liquid. The iterative procedure was stopped, when the mineral saturations and mineral compositions became identical with those in the forward experiments and the mineral and melt compositions allowed for mass balancing the original bulk composition with deviations $\leq$ 2 relative-% of each oxide component. Table 2.2 compares the composition of the initially measured melts at a temperature just above the solidus for the two pelites AM and DG2 at 8 GPa (for 13 GPa see online material) with those obtained after four and five iterative steps, respectively. In this table we also give the mass balanced optimized compositions, i.e. after adjusting the K_2O and Na_2O contents of the originally measured melt for an optimal fit. In figure 2.2 we plot the forward experiment melt composition as the 0th iteration step. As can be easily seen, neither the direct initial measurements nor the mass-balance corrected compositions are close to the true equilibrium composition as obtained by the iterative sandwich method. Differences amount to as much as 12 wt% K_2O, 7.5 wt% CaO and 6.5 wt% FeO (fig. 2.2), which catastrophically propagate into e.g. K_2O/Na_2O ratios and mass balance in the original forward experiment. For the final melt composition, uncertainties for the alkali-concentrations remain relatively high, as the heterogeneous quench of the alkali-rich carbonate melts causes individual large area analyses to vary considerably. The results from the reversals on the DG2 and AM melt compositions together with mass balance calculations have then been adopted to adjust the DG1 melt composition. Particularly useful are the partition coefficients (especially $D_{Na}^{cpx/carbonate\,melt}$) and the K_2O/Na_2O wt-ratio for the potassium and sodium concentrations. The correlation of X^*_{Ca} (bulk) vs. X^*_{Ca} (melt) and X^*_{Mg} (bulk) vs. X^*_{Mg} (melt)

is also useful to assess the consistency of analyzed and corrected melt compositions.

2.3 Results

30 experiments were performed on three different bulk compositions (tab. 2.1) at 8 and 13 GPa, and at temperatures between 900 °C and 1850 °C. Run conditions with calculated phase proportions are listed in table 2.3 and represented in fig. 2.3. Subsolidus assemblages consist of garnet, jadeitic clinopyroxene, coesite/stishovite, kyanite or corundum, phengite and/or K-feldspar (at 8 GPa) or K-hollandite (at 13 GPa), a Ti-phase, and aragonite + Fe-rich magnesite (fig. 2.1).

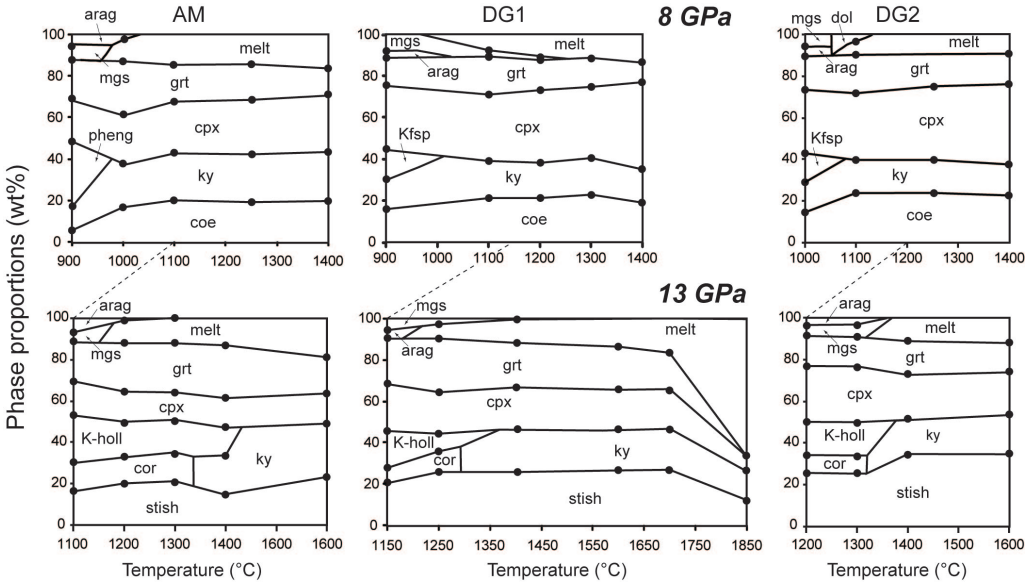

Figure 2.3: *Calculated modes in weight fractions of the observed phases for coesite/stishovite + kyanite/corundum saturated, fertile carbonated metapelites at 8 and 13 GPa. The AM bulk has 1.1 wt% H_2O and a trace of kfsp (not shown) at 8 GPa and 900 °C, DG1 has traces of H_2O and minor phengite (not shown) at 8 GPa, 900 °C, DG2 is dry. First melts are carbonate melts which become silica-rich (see Fig. 4) only at temperatures > 400 °C above the solidus. At 8 GPa the K-phase completely dissolves into the melt at the solidus while at 13 GPa, K-hollandite may coexist with carbonate melt up to 200 °C above the solidus. To 300 °C above the solidus, the melt fraction is just slightly higher than the carbonate fraction in the sediment, larger melt quantities are only produced once melting of the silicate components becomes significant (at 13 GPa for DG1 between 1700 and 1850 °C).*

Throughout the investigated P-T-range, the three bulk compositions are all coesite/stishovite-, kyanite/corundum-, garnet-, and clinopyroxene-saturated (fig. 2.3). The crystallization of a small amount of K-feldspar coexisting with phengite at 8 GPa is taken as proof that the subsolidus experiments and the melting reaction were fluid absent. The absence of graphite/diamond in the run products suggests an oxygen fugacity above the graphite-CO-CO_2 (CCO) buffer. In the following, compositions are discussed in terms of Ca:Fe:Mg-ratio which we denote as molar ratio X^*M^{2+} = M^{2+}/(Ca+Mg+Fe^{2+}). To avoid confusion, we use Mg# = 100*(Mg/(Mg+Fe^{2+})), also on a molar

Table 2.3 Experimental run conditions and calculated phase proportions (wt%)

run/bulk	P [GPa]	T [$^{\circ}$C]	time [h]	phengite	K-felspar	K-holl	aragonite	magnesite	dolomite	[a]Ti-Phase	garnet	cpx	kyanite	cor	coesite/ stishovite	carb. melt
DG1-18	8	900	24	x	15.4 (0.7)	-	2.8 (1.5)	7.9(1.0)	-	x	13.8 (1.7)	30.1 (2.8)	13.5 (1.5)	-	16.5 (0.8)	-
DG1-9	8	1100	24	-	-	-	-	3.1 (1.1)	-	x	18.2 (1.3)	31.7 (2.5)	17.4 (2.0)	-	21.6 (1.0)	8.0 (3.1)
DG1-11	8	1200	24	-	-	-	-	1.3 (0.6)	-	-	14.6 (2.6)	34.2 (3.2)	17.7 (1.8)	-	21.5 (1.2)	10.9 (3.0)
DG1-19	8	1300	24	-	-	-	-	-	-	-	13.4 (2.7)	33.1 (2.6)	18.6 (1.3)	-	22.7(0.8)	12.2 (2.5)
DG1-13	8	1400	24	-	-	-	-	-	-	-	10.0 (2.1)	40.7 (2.8)	16.4 (2.8)	-	19.1 (1.0)	13.9 (2.8)
DG2-1	8	900	24	-	xx	-	x	xx	-	x	xx	xx	xx	-	xx	-
DG2-5B	8	1000	96	-	14.1 (0.8)	-	3.3 (1.0)	6.2 (0.6)	-	x	16.2 (2.1)	31.0 (2.2)	13.9 (1.8)	-	15.3 (1.3)	-
DG2-3	8	1100	24	-	-	-	-	-	3.2 (1.3)	x	16.4 (1.6)	32.7 (2.9)	15.8 (2.0)	-	24.6 (1.2)	7.4 (3.2)
DG2-2	8	1250	24	-	-	-	-	-	-	-	16.1 (1.9)	36.2 (2.8)	15.0 (2.8)	-	22.7 (1.0)	10.0 (2.8)
DG2-4	8	1400	9	-	-	-	-	-	-	-	11.1 (3.4)	31.4 (2.5)	13.8 (1.8)	-	20.6 (0.9)	11.0 (3.1)
am-1	8	900	24	30.4 (1.9)	-	-	5.9 (0.7)	5.4 (1.1)	-	-	18.8 (2.1)	20.8 (2.3)	11.5 (1.7)	-	7.1 (0.8)	-
am-5B	8	1000	96	-	-	-	x	-	-	-	26.4 (2.4)	22.3 (2.6)	21.2 (2.9)	-	16.9 (1.0)	12.8 (1.7)
am-3	8	1100	24	-	-	-	x	-	-	-	18.3 (2.1)	24.0 (3.0)	23.1 (2.6)	-	20.4 (1.0)	14.3 (2.1)
am-2	8	1250	24	-	-	-	-	-	-	-	16.0 (1.6)	26.0 (2.4)	23.1 (1.7)	-	19.9 (1.1)	14.9 (2.8)
am-4	8	1400	9	-	-	-	-	-	-	-	11.7 (1.6)	28.0 (3.2)	24.2 (2.5)	-	19.7 (0.9)	16.2 (2.3)
DG1-8	13	1150	24	-	-	16.6 (1.0)	4.15 (0.5)	5.8 (0.8)	-	x	20.9 (1.4)	23.3(2.7)	-	8.1 (1.5)	21.2 (0.8)	-
DG1-7	13	1250	24	-	-	9.1 (0.8)	-	2.9 (1.3)	-	x	24.9(2.8)	20.1 (2.3)	-	9.8 (1.3)	25.8 (1.3)	7.5 (2.7)
DG1-15	13	1400	24	-	-	-	-	-	-	-	22.9 (1.4)	18.5 (3.1)	20.0 (2.4)	-	26.4 (0.8)	12.2 (2.6)
DG1-1	13	1600	24	-	-	-	-	-	-	-	21.0 (2.9)	18.3 (2.1)	19.9 (2.9)	-	26.6 (0.8)	14.2 (1.7)
DG1-6	13	1700	5	-	-	-	-	-	-	-	18.4 (1.4)	18.9 (3.2)	19.7 (1.4)	-	26.8 (1.1)	16.3 (1.2)
DG1-17	13	1850	1/3	-	-	-	-	-	-	-	2.3 (3.1)	5.6 (2.9)	14.2(2.9)	-	12.5 (1.0)	65.4 (1.9)
DG2-9	13	1200	96	-	-	15.3 (0.8)	3.6 (1.2)	6.9 (0.9)	-	x	17.0 (2.1)	25.5 (1.9)	-	7.9 (0.9)	23.8 (2.0)	-
DG2-11	13	1300	96	-	-	15.2 (0.9)	3.8 (1.6)	6.9 (1.0)	-	x	16.8 (2.6)	24.9 (3.0)	-	7.9 (1.3)	24.4 (1.3)	-
DG2-8	13	1400	48	-	-	-	-	-	-	-	16.7 (3.3)	18.4 (2.9)	19.3 (2.7)	-	30.7 (1.0)	14.8 (1.3)
DG2-7	13	1600	24	-	-	-	-	-	-	-	12.7 (1.8)	19.3 (2.0)	21.1 (2.5)	-	31.2 (1.2)	15.7 (1.6)
am-12a	13	1100	96	-	-	xxx	xx	x	-	-	xx	xx	-	xx	xx	-
[b]am-12d	13	1100	120	-	-	23.9 (1.1)	6.7 (0.7)	4.2 (0.6)	-	-	18.8 (3.4)	16.9 (3.0)	-	12.5 (0.4)	17.0 (1.3)	-
am-9	13	1200	96	-	-	17.2 (1.2)	-	-	-	-	25.4 (1.3)	13.6 (2.0)	-	12.4 (1.1)	19.8 (1.2)	11.9 (2.8)
am-11	13	1300	96	-	-	15.7 (0.9)	-	-	-	-	24.1 (3.4)	13.3 (2.1)	-	14.2 (1.4)	20.7 (1.3)	12.1 (3.0)
am-8	13	1400	48	-	-	13.3 (0.8)	-	-	-	-	25.6 (2.7)	14.3 (2.1)	18.8 (2.6)	-	14.7 (0.8)	13.3 (2.6)
am-7	13	1600	24	-	-	-	-	-	-	-	18.0 (2.4)	13.8 (2.0)	25.7 (1.8)	-	23.8 (1.0)	18.6 (2.3)

xxx: $>$ 20 wt%; xx: 5-20 wt%; x: $<$ 5 wt%
subsolidus experiments include H_2O and CO_2 as mass balance components. FeO adjusted for Fe-loss to the capsule for all exp. with large amount of melt
[a] TiO_2 was excluded during MB-calculations
[b] this experiment contained 3 wt% H_2O

basis, to describe Mg-Fe^{2+} variations.

2.3.1 Solidus location and melt composition

The AM composition, which has 1.1 wt% H_2O and the highest bulk X^*_{Fe} of 0.42, has the lowest solidus temperatures of 950 and 1150 °C at 8 and 13 GPa, respectively. The composition DG1 with minor absorbed H_2O has intermediate solidus temperatures of 1000 °C and 1200 °C at 8 and 13 GPa, and as to be expected, the dry DG2 composition has the highest solidus temperatures of 1075 °C and 1325 °C at 8 and 13 GPa, respectively (fig. 2.4).

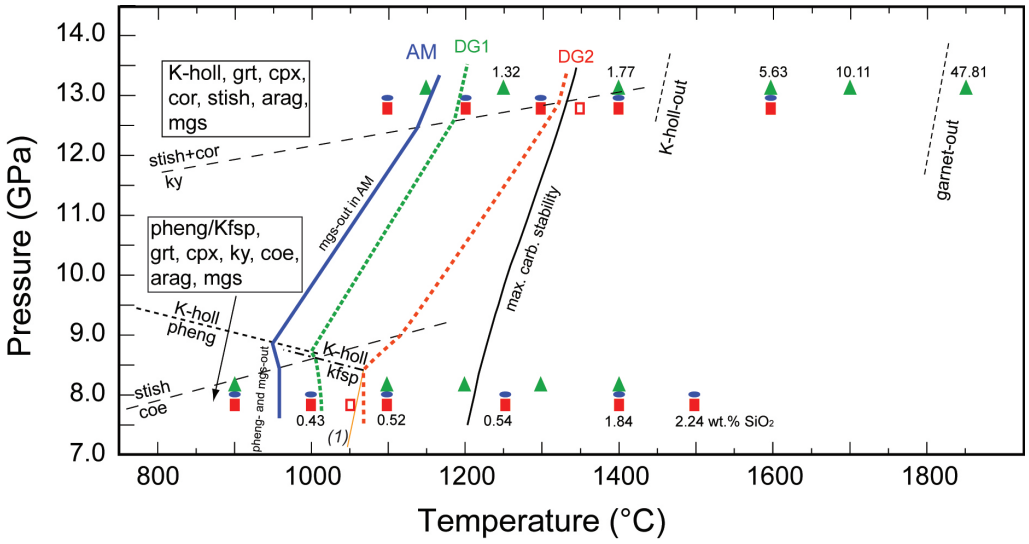

Figure 2.4: *Pressure-temperature diagram of experimental results for carbonated pelites at 8 and 13 GPa in the system TiKNCFMASH-CO_2. Blue ellipsoids (AM), red squares (DG2) and green triangles (DG1) are individual experiments. The solidus is controlled by the hydrous, alkali and carbonate phases. The AM composition, with 1.1 wt% H_2O is the one with the lowest solidus temperature, followed by the DG1 bulk with traces of water and by the dry DG2 bulk. To define the solidus for AM and DG1 middle point of run bracket temperatures (1100-1200 = 1150 °C; 1150-1250 = 1200 °C) are chosen; for DG2 at 8 GPa (1075 °C) the solidus is defined by the middle point between the first experiments containing melt (1100 °C) and a reverse experiments at 1050 °C which didn't show any sign of melt. Similarly, at 13 GPa the middle point between the subsolidus experiment at 1300 °C and the reverse experiment at 1350 °C was chosen. The change of the slope of the different solidi is drawn according to Schreinemaker rules at the intersections with coesite-stishovite reaction (Zhang et al., 1996), the decomposition-reaction of kyanite to corundum+stishovite (Schmidt et al., 1997; this study), the phengite to K-hollandite reaction (Schmidt et al., 2004), and the kfsp to K-hollandite reaction. Note that the slope and the exact position of the kfsp to K-hollandite reaction is unknown as in the simple K_2O-Al_2O_3-SiO_2-system K-hollandite replaces wadeite at 9 GPa (at 1000 °C, Yong et al., 2006). Above 8 GPa, the temperature stability of K-hollandite is strongly bulk composition dependent. At 13 GPa the AM composition with the highest K_2O content has K-hollandite coexisting with the melt to 1400 °C, i.e. 200 °C above the solidus; DG1 and DG2 have no K-hollandite above 1350 °C. Numbers at symbols refer to SiO_2 contents in the melts (in wt%, for the AM bulk at 8 GPa and for DG1 at 13 GPa).*

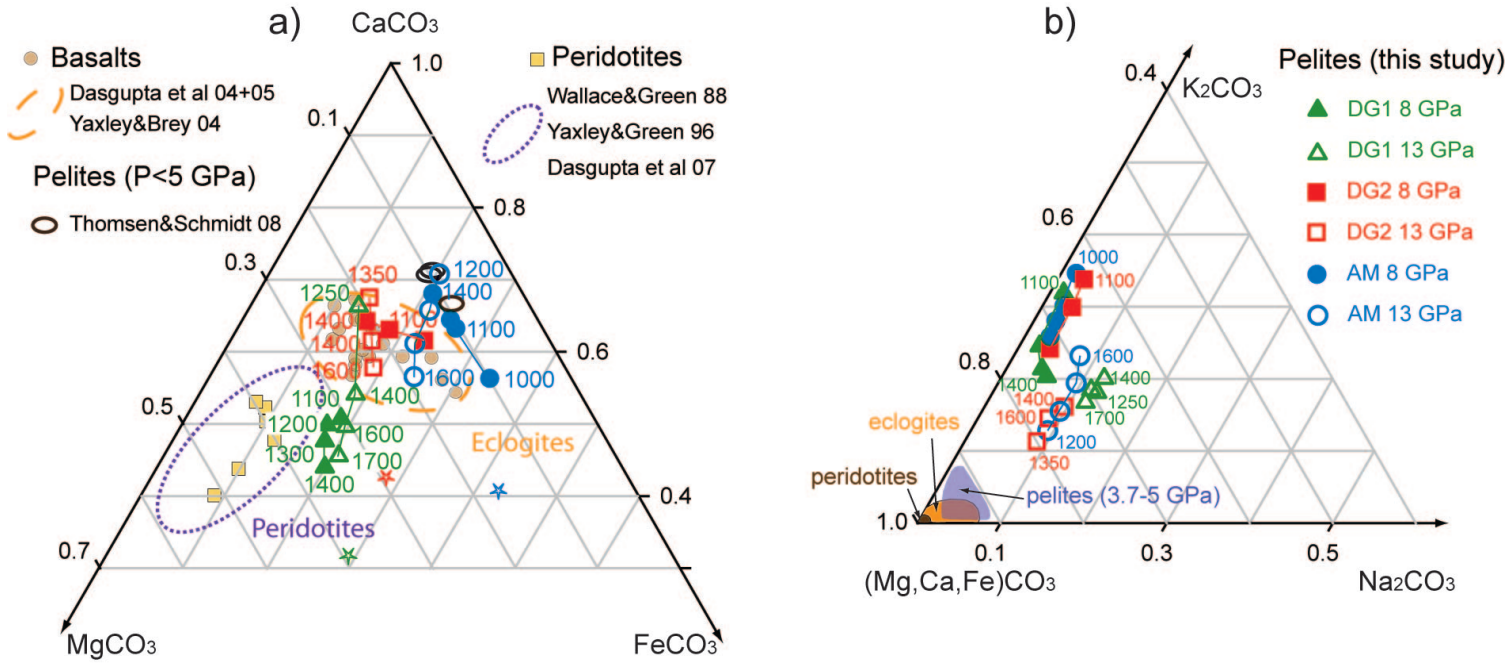

Figure 2.5: *a. Compositions of carbonate melts projected into $FeCO_3$-$CaCO_3$-$MgCO_3$ space. The carbonate melts derived from pelites overlap with the carbonate melts generated from carbonated mafic eclogites due to similar bulk X^*_{Ca} and X^*_{Mg} (data of Yaxley and Brey, 2004; Dasgupta et al., 2004,2005). Differences between the three pelites reflect bulk composition in terms of X^*_{Ca} and X^*_{Mg}. Note that for each bulk rock type, the near solidus melts plot within relatively narrow fields which are thought to stretch along the minimum cotectic line in the $FeCO_3$-$CaCO_3$-$MgCO_3$ ternary system for pelitic and basaltic bulks, while the near solidus melts from peridotitic compositions stretch along the peritectic of the ternary carbonate system (Franzolin et al., 2010). b. Compositions of carbonate melts projected in the Na_2CO_3-K_2CO_3-(Mg,Ca,Fe)CO_3 space. The carbonate melts of this study have much higher amounts of K_2O and Na_2O compared to melts from carbonated mafic eclogites (3-8 GPa, Hammouda, 2003; Yaxley and Brey, 2004; Dasgupta et al., 2004), peridotites (2-10 GPa, Wallace and Green, 1988; Yaxley and Green, 1996; Dasgupta et al., 2007; Ghosh et al., 2009), and pelites at $P < 5$ GPa (Thomsen and Schmidt, 2008b). With increasing pressure the K_2O/Na_2O-ratio decreases. The most alkali-rich melts are formed at 8 GPa just above the solidus.*

Table 2.4 Carbonate melt compositions

Run no.	AM-5B	AM-3	AM-2	AM-4	AM-9	AM-11	AM-8	AM-7	DG1-9	DG1-11	DG1-19	DG1-13
P (Gpa)/T(°C)	8/1000	8/1100	8/1250	8/1400	13/1200	13/1300	13/1400	13/1600	8/1100	8/1200	8/1300	8/1400
SiO_2 (wt%)	0.30 (0.1)	0.55 (0.3)	1.04	3.01 (0.2)	0.48 (0.2)	0.88	1.84	5.45 (0.6)	0.26	2.28	6.84	13.20
TiO_2	-	-	-	-	-	-	-	-	0.45	1.96	1.88	2.68
Al_2O_3	1.85 (0.3)	2.15 (0.4)	2.23	2.33 (0.3)	1.35 (0.2)	1.94	2.75	3.25 (0.2)	2.03	3.02	3.19	4.81
FeO_{tot}	12.1 (0.9)	9.9 (0.6)	9.10	8.44 (0.4)	9.50 (0.8)	9.99	9.76	9.8 80.5)	7.44	7.95	8.04	7.93
MgO	2.10 (0.2)	2.35 (0.3)	2.37	2.42 (0.2)	2.32 (0.3)	2.86	3.82	4.19 (0.2)	6.78	8.44	8.33	7.87
CaO	16.5 (0.8)	19.2 (1.5)	20.28	20.9 (0.9)	25.5 (1.4)	23.36	21.20	17.4 (1.1)	15.70	17.95	16.21	13.47
Na_2O	0.65 (0.2)	1.05 (0.4)	1.20	1.36 (0.5)	4.8 (0.6)	4.76	4.72	4.05 (0.4)	0.80	1.30	2.06	2.34
K_2O	26.8 (1.7)	22.5 (1.5)	20.03	17.9 (1.6)	10.2 (1.7)	12.44	15.20	16.8 (1.6)	25.13	20.42	16.55	14.20
[b]H_2O	9.40	8.89	8.41	7.97	9.88	8.98	7.21	5.41	n.a.	n.a.	n.a.	n.a.
[bc]CO_2	38.45	37.81	36.12	34.77	43.12	40.12	36.20	23.59	41.41	36.68	36.90	33.50
tot.	60.35	57.72	56.25	56.45	54.13	56.23	59.29	60.93	100.00	100.00	100.00	100.00
[a]Si (pfu)	0.01	0.02	0.05	0.14	0.02	0.04	0.08	0.23	0.01	0.09	0.28	0.52
Ti	-	-	-	-	-	-	-	-	0.01	0.06	0.06	0.08
Al	0.09	0.11	0.12	0.13	0.08	0.10	0.14	0.16	0.10	0.14	0.15	0.22
Fe_{tot}	0.44	0.38	0.35	0.33	0.38	0.38	0.35	0.34	0.27	0.27	0.27	0.26
Mg	0.14	0.16	0.16	0.17	0.16	0.19	0.24	0.26	0.43	0.51	0.51	0.46
Ca	0.77	0.93	1.01	1.04	1.30	1.14	0.97	0.78	0.72	0.78	0.71	0.57
Na	0.05	0.09	0.11	0.12	0.44	0.42	0.39	0.33	0.07	0.10	0.16	0.18
K	1.49	1.30	1.19	1.07	0.62	0.72	0.83	0.90	1.38	1.05	0.86	0.71
K_2O/Na_2O (wt%)	41.31	21.43	16.69	13.21	2.13	2.61	3.22	4.15	31.41	15.71	8.03	6.07
Mg#	24	30	32	34	30	34	41	43	62	65	65	64
X^*_{Mg} (Fe_{tot}) (molar)	0.10	0.11	0.11	0.11	0.09	0.11	0.16	0.19	0.30	0.33	0.34	0.36
X^*_{Ca} (molar)	0.57	0.64	0.66	0.68	0.71	0.66	0.62	0.56	0.51	0.50	0.48	0.44
Jd mol%	71	66	61	55	87	86	84	76	68	63	63	49
X_{pyrope}	0.12	0.13	0.13	0.14	0.16	0.15	0.16	0.15	0.27	0.39	0.45	0.39
$X_{grssular}$	0.36	0.39	0.41	0.41	0.42	0.40	0.41	0.41	0.25	0.17	0.15	0.12
$D^{cpx/melt}_{Na}$ (wt%)	17.68	9.94	8.21	6.55	2.71	2.71	2.59	2.63	12.26	7.21	4.43	2.96

The temperature differences between the three bulk compositions are mainly due to the different amounts of water present, but are also influenced by their different bulk X^*_{Mg}, X^*_{Ca} and X^*_{Fe}. While all three bulk compositions have magnesite+aragonite at subsolidus conditions, melting consumes magnesite in AM, which has a low X^*_{Mg} of 0.17 and high X^*_{Ca} of 0.41, consumes

Table 2.4 continued

Run no.	DG1-7	DG1-15	DG1-1	DG1-6	[d]DG1-17	DG2-3	DG2-2	DG2-4	reverse	DG2-8	DG2-7
P (Gpa)/T(°C)	13/1250	13/1400	13/1600	13/1700	13/1850	8/1100	8/1250	8/1400	13/1350	13/1400	13/1600
SiO_2 (wt%)	1.32	1.77	5.63	10.04	47.82	0.26 (0.1)	1.48	1.88 (0.7)	0.22 (0.1)	0.88 (0.4)	2.81 (0.5)
TiO_2	1.54	2.79	2.53	2.38	1.01	2.37 (0.4)	2.51	3.34 (0.4)	1.83 (0.3)	1.69 (0.3)	2.18 (0.3)
Al_2O_3	2.32	1.89	3.64	5.59	16.14	1.55 (0.3)	2.05	2.50 (0.3)	1.18 (0.3)	2.06 (0.2)	2.67 (0.2)
FeO_{tot}	5.17	7.18	6.97	8.15	3.75	7.55 (0.6)	6.9	6.27 (0.4)	7.08 (0.6)	8.37 (0.5)	8.8 (0.8)
MgO	4.68	5.82	6.19	7.26	5.18	2.95 (0.3)	3.89	4.8 (0.5)	5.35 (0.3)	6.06 (0.4)	6.04 (0.3)
CaO	20.72	16.10	13.97	13.76	5.68	16.3 (1.5)	18.88	20.9 (1.7)	26.4 (1.2)	23.3 (0.9)	21.0 (0.9)
Na_2O	6.24	5.95	5.30	5.50	4.01	0.95 (0.6)	1.21	1.50 (0.3)	4.71 (0.6)	5.28 (0.8)	4.66 (0.5)
K_2O	13.84	14.99	12.74	12.09	3.23	24.4 (2.8)	21.68	18.6 (2.1)	9.43 (1.1)	12.6 (1.9)	10.8 (1.8)
[b]H_2O	n.a.	n.a.	n.a.	n.a.	n.a.	-	-	-	-	-	-
[c]CO_2	44.17	43.51	43.03	35.23	13.18	43.67	42.88	40.21	43.80	39.76	41.04
tot.	100.00	100.00	100.00	100.00	100.00	100.00	100.00	100.00	100.00	100.00	100.00
[a]Si (pfu)	0.06	0.08	0.25	0.39	1.49	0.01	0.07	0.08	0.01	0.04	0.12
Ti	0.05	0.09	0.08	0.07	0.02	0.08	0.08	0.11	0.06	0.05	0.07
Al	0.12	0.10	0.19	0.26	0.59	0.08	0.11	0.13	0.06	0.10	0.14
Fe_{tot}	0.19	0.26	0.26	0.27	0.10	0.29	0.26	0.23	0.27	0.29	0.32
Mg	0.31	0.38	0.40	0.42	0.24	0.20	0.26	0.31	0.36	0.38	0.39
Ca	0.97	0.75	0.66	0.58	0.19	0.81	0.90	0.98	1.28	1.04	0.97
Na	0.53	0.50	0.45	0.42	0.24	0.08	0.10	0.13	0.41	0.43	0.39
K	0.77	0.84	0.71	0.60	0.13	1.44	1.23	1.04	0.54	0.67	0.60
K_2O/Na_2O (wt%)	2.22	2.52	2.40	2.20	0.81	25.68	17.92	12.41	2.00	2.38	2.31
Mg#	62	59	61	61	71	41	50	58	57	56	55
X^*_{Mg} (Fe_{tot}) (molar)	0.21	0.27	0.31	0.33	0.46	0.16	0.18	0.21	0.19	0.22	0.23
X^*_{Ca} (molar)	0.66	0.54	0.50	0.46	0.36	0.62	0.64	0.64	0.67	0.61	0.58
Jd mol%	89	84	83	80	65	65	58	55	79	78	78
X_{pyrope}	0.32	0.39	0.39	0.39	0.51	0.21	0.28	0.30		0.32	0.33
$X_{grssular}$	0.26	0.17	0.18	0.17	0.12	0.29	0.26	0.21		0.20	0.22
$D^{cpx/melt}_{Na}$ (wt%)	2.06	2.09	2.28	2.05	2.37	10.00	7.11	5.33	2.37	2.32	2.43

[a] cations calculated on the basis of 6 oxygens.
[b] H_2O and CO_2 content calculated from bulk and melt fraction.
[c] CO_2 content (if no H_2O) calculated by difference of 100 and the measured analytical total.
[d] cations calculated on the basis of 8 oxygens.

aragonite in DG1, which has the highest X^*_{Mg} of 0.39 and the lowest X^*_{Ca} of 0.32, leads to dolomite formation in DG2 at 8 GPa, and to exhaustion of both carbonates at the solidus at 13 GPa, a consequence of an intermediate X^*_{Mg} of 0.30 and high X^*_{Ca} of 0.43. Carbonate melts formed from the three carbonated pelites are Ca-rich magnesio- (DG1 and DG2) and ferro-carbonate melts (AM). They contain 24.4 to 26.8 wt% K_2O but only 0.65-0.95 wt% Na_2O at the solidus at 8 GPa and 9.4-13.8 wt% K_2O and 4.8-6.2 wt% Na_2O at the solidus at 13 GPa (tab. 2.4, fig. 2.5). At

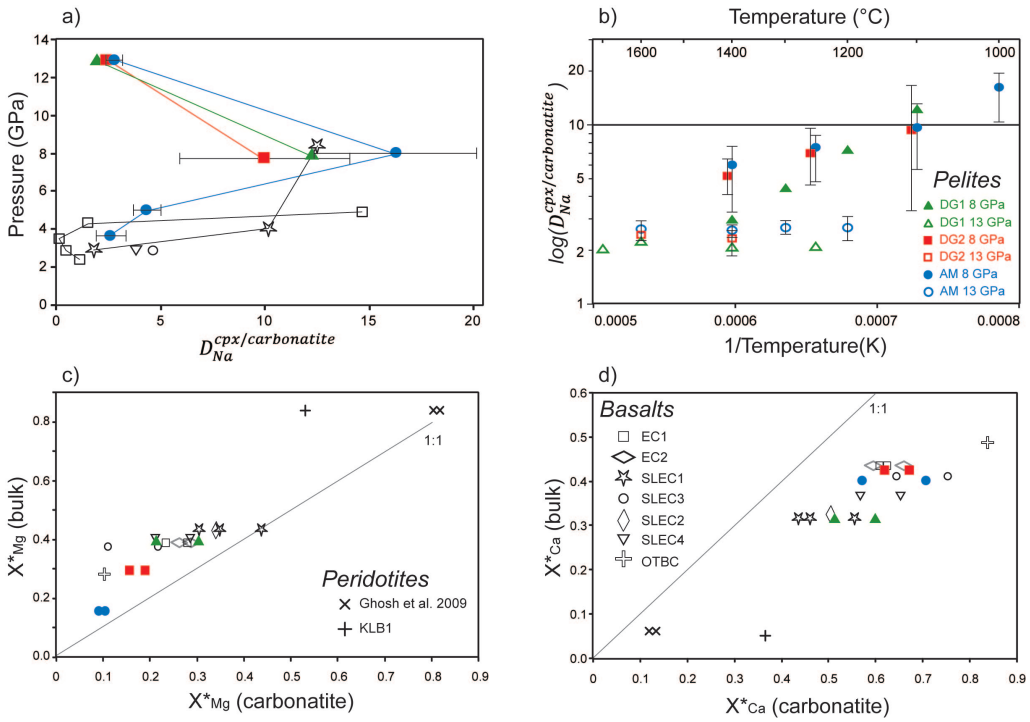

Figure 2.6: *a.* $D_{Na}^{cpx/carbonate\,melt}$ *vs. pressure showing an increase of the compatibility of* Na_2O *in cpx with increasing pressure to 8 GPa reaching a cpx/carbonate melt partition coefficient of 16, followed by a decrease down to a value near 2 at 13 GPa when approaching the upper pressure stability of cpx (15-20 GPa). Some data sets, not focused on the carbonate melt compositions have inconsistencies probably due to the analytical problem of measuring small intergranular volumes of unquenchable carbonate melts. b.* $Log(D_{Na}^{cpx/carb.\,melt})$ *varies linearly with 1/T. c. and d.* X^*_{Ca}*(melts) vs.* X^*_{Ca}*(bulk) and* X^*_{Mg}*(melts) vs.* X^*_{Mg}*(bulk) for carbonate melts generated from carbonated pelites (this work), mafic eclogites from 2.5 to 8.5 GPa (Hammouda, 2003, OTBC; Yaxley and Brey, 2004, EC; Dasgupta et al., 2004,2005, SLEC), and peridotite at 6.6-15 GPa (Dasgupta and Hirschmann, 2007; Ghosh et al., 2009). In spite of the strong pressure dependence of the carbonate melt composition, in particular in the peridotitic system, a positive correlation between bulk* X^*_{Ca} *and melt* X^*_{Ca} *and between bulk* X^*_{Mg} *and melt* X^*_{Mg} *is evident.*

8 GPa, the presence of a small amount of carbonate melt is enough to immediately dissociate the potassic mineral present, causing the observed extreme K_2O-concentrations. In contrast, at 13 GPa, K_2O-concentrations are more moderate due to an up to 200 °C wide field of coexistence of K-hollandite + carbonate melt in the H_2O-bearing compositions, and a comparatively high melt productivity exhausting both K-hollandite and carbonates in the dry composition. At 8 GPa, cpx plays a minor role in the melting reaction, whereas at 13 GPa Na_2O contents indicate a strong involvement of cpx in the melting reaction. All solidus melts are poor in SiO_2 (0.2-1.3 wt%) and Al_2O_3 (1.2-2.3 wt%), and contain considerable TiO_2 (0.45-2.37 wt%). The most distinguishing feature in comparison to basalt or peridotite derived carbonate melts are the potassium content and the K_2O/Na_2O wt-ratios at the solidus, the latter being as high as 26-42 at 8 GPa, decreasing to 2-2.2 at 13 GPa.

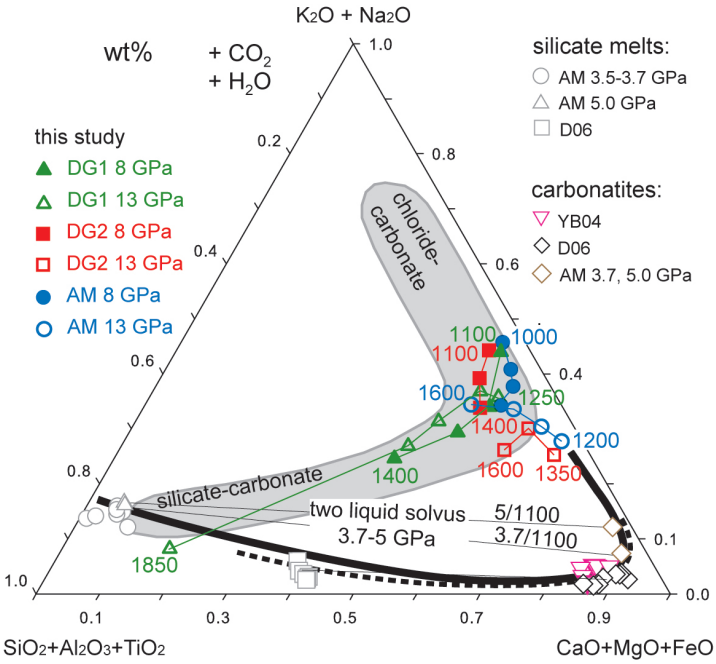

Figure 2.7: *Pseudo-ternary projection of carbonate and silicate melts after Freestone and Hamilton (1980), defining a silicate - carbonate liquid miscibility gap at 1100 °C, 3.7-5 GPa for the AM composition (Thomsen and Schmidt, 2008b) compared to the miscibility gap after Dasgupta et al. (2006) (dashed line) and the carbonate melts of Yaxley and Brey (2004). The pelite derived carbonate melts plot in the same area as carbonate-rich melt/fluid inclusions found in diamonds (Klein-BenDavid et al., 2007, grey field).*

This is due to the different K-phases present at 8 and 13 GPa and to the partitioning of Na between clinopyroxene and carbonate melt (figs. 2.6a and 2.6b). At 8 GPa, the potassic subsolidus phases phengite and K-feldspar are exhausted at the solidus and the carbonate melt becomes the major K-bearing phase. Instead, at 13 GPa, K-hollandite remains stable to as much as 200 °C above the solidus. While clinopyroxene is stable in all experiments, the partitioning of Na changes dramatically with pressure: $D_{Na}^{cpx/carbonate\,melt}$ (wt%-concentration of Na_2O in cpx divided by the wt%-concentration of Na_2O in the carbonate melt) is 10.0-16.1 at the solidus and decreases with temperature at 8 GPa. At 13 GPa, $D_{Na}^{cpx/carbonate\,melt}$ varies only between 2.1-2.7 (fig. 2.6a). The decrease of K_2O/Na_2O with pressure is also accompanied by a decrease of the total amount of alkalis in the near solidus melt from 26-28 to 15-20 wt% at 8 to 13 GPa, respectively, and consequently by increasing CaO and partly MgO.

The effect of temperature on SiO_2 and Al_2O_3 concentrations in the carbonate melts is relatively small, and up to 400 °C above the solidus SiO_2 remains at < 10 wt%, Al_2O_3 at < 5 wt%. It is only from 1700 °C to 1850 °C (13 GPa), i.e. 600 °C above the solidus, that a silicate melt resembling an alkali basalt forms, and that a silicate phase, i.e. garnet, exhausts (fig. 2.3). For the investigated pressure and temperature range a continuum from carbonate melt towards more silica-rich melts has been observed. No indication of a miscibility gap has been found (fig. 2.7), similar to the $>$ 6 GPa melting of carbonated peridotite (Brey et al., 2008). Other effects of temperature on melt composition are the decrease of CO_2 and K_2O through dilution with increasing melt fraction, and a twofold increase in Na_2O content at 8 GPa, leading to a decrease in K_2O/Na_2O with temperature. At 13 GPa the K_2O/Na_2O ratio varies only between 2.1 and 4.1 with temperature due to the different behavior of K-hollandite and clinopyroxene at this pressure.

2.3.2 Textures and Mineral compositions

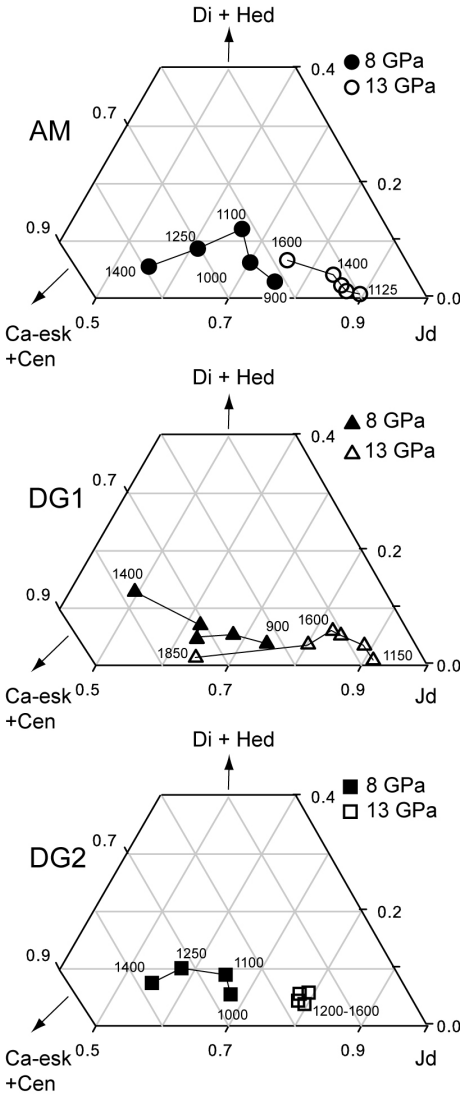

Fig. 8

Figure 2.8: *Clinopyroxene compositions in terms of jadeite (Jd) - diopside+hedenbergite (Di+Hed) - Ca-eskaloite+clinoenstatite (Ca-esk+Cen). With temperature, jadeite contents decrease from* Jd_{74-77} *(900 °C) to* Jd_{49-55} *(1400 °C) at 8 GPa. The decrease in jadeite content is compensated first by an increase of the diopside and clinoenstatite components followed by a strong increase of the Ca-eskolaite component at higher temperatures. A similar trend is observed at 13GPa, but shifted to higher jadeite of* Jd_{80-92} *at the solidus and to lower Ca-eskolaite contents. The Mg# for cpx increase with temperature and decrease with increasing pressure. Ca-Tschermaks-component is always* < 3 *mol%.*

Clinopyroxene (cpx) is stable in all experiments and forms relatively small < 15 μm long prismatic crystals. In all isobaric sections, clinopyroxenes have the highest jadeite content at the lowest temperature (fig. 2.8 and Appendix C). They then follow various trends leading to a decrease of jadeite and an increase of the diopside, clinoenstatite and Ca-eskolaite endmembers. Ca-Tschermaks component is < 3 mol% in all experiments, generally increasing with temperature. For all three compositions, subsolidus jadeite contents are 68-76 and 80-92 mol% at 8 and 13 GPa.

Upon melting at 8 GPa, jadeite contents decrease at most by 5-15 mol% to about 100-200 °C above the solidus. Then, cpx becomes omphacitic at 300-400 °C above the solidus. Upon melting at 13 GPa, jadeite contents decrease by 2-3 mol% across the solidus, and by further 2-12 mol% 300-400 °C above the solidus. The Ca-eskolaite component increases strongly with temperature from 15-20 to 30-32 mol% at 900-1200 to 1250-1400 °C (8 GPa). At 13 GPa, only the DG1

experiment at 1850 °C yielded strongly increased Ca-eskolaite of almost 40 mol%, in the other two isobaric sections at 13 GPa experimental temperatures were not high enough to achieve such an increase. Generally, Ca-eskolaite decreases with pressure, i.e. from 15-32 to 10-20 mol% from 8 to 13 GPa. K_2O concentrations in cpx vary from 0.20-1.03 wt% with the highest values found at 8 GPa at subsolidus conditions.

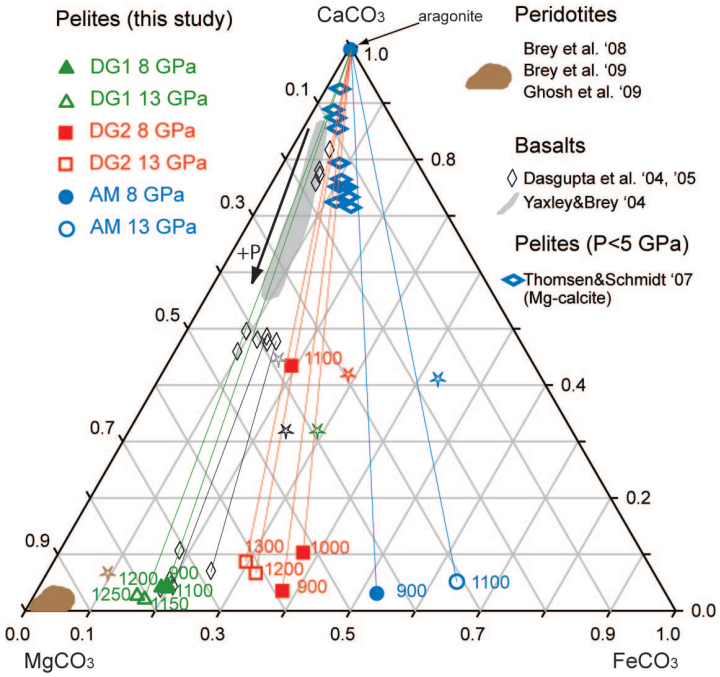

Figure 2.9: *Carbonate compositions in $CaCO_3$-$MgCO_3$-$FeCO_3$ space. The carbonates of this study are compared to carbonates from carbonated basaltic eclogites (Yaxley and Brey, 2004; Dasgupta et al., 2004,2005), peridotites (Brey et al., 2008; Ghosh et al., 2009; Brey et al., 2009), and sediments (Thomsen and Schmidt, 2008b). Note the correlation between carbonate and bulk composition, in particular of the Mg# of magnesite and the bulk. Tie-lines connect coexisting carbonate pairs, stars denote bulk compositions.*

Carbonates stable in the different experiments are magnesite, aragonite and dolomite. Aragonite and dolomite normally form 5-15 μm mostly polyhedral grains, clearly differing from magnesite, which crystallizes as small grains interstitial between larger minerals. Aragonite is almost pure containing less than 1 mol% $FeCO_3$ or $MgCO_3$ component in all bulk compositions.

The composition of magnesite (fig. 2.9 and Appendix C) reflects the Mg# of the starting materials while Ca-contents generally increase with temperature from 2 to 10 mol%. In DG1 (Mg# 57), magnesite occurs in 5 sub- and super-solidus experiments and contains 16-21 mol% siderite, comparable to what has been found in basaltic eclogites at 4-8 GPa with a Mg# of 64 (Dasgupta et al. 2004). In DG2 (Mg# 52), magnesite has 38 and 30-32 mol% siderite at 8 and 13 GPa, respectively. Finally, in AM (Mg# 28), the magnesite-siderite solid solution has 53 and 64 mol% siderite at 8 and 13 GPa, respectively. In DG2 a Fe-rich dolomite containing 19 mol% siderite component leading to an Mg# of 65.9 is formed at 8 GPa and 1100 °C (DG2). This places the reaction aragonite + ferro-magnesite (Mg# 76.5) = ferro-dolomite (Mg# 65.9) between 1000 and 1100 °C (8 GPa), which compares well with the 1100-1150 °C bracket of Luth (2001) in the pure $CaMg(CO_3)_2$ system.

Phengite (pheng) is present only at 8 GPa at subsolidus conditions in the two H_2O-bearing bulk compositions DG1 and AM as small (< 10 μm) subidiomorphic grains and has, as to be expected (Thomsen and Schmidt, 2008b), a high celadonite component of 3.68 Si pfu and an Mg#

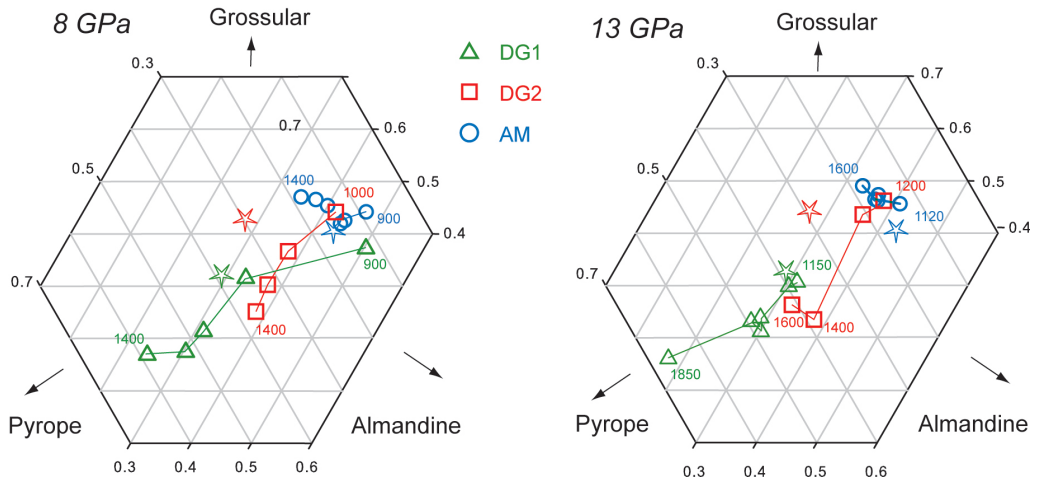

Figure 2.10: *Garnet compositions. At subsolidus conditions garnets are similar in all three compositions with only small differences in X*$_{Ca}$. The different trends with increasing temperature are strongly correlated with bulk composition (especially X*$_{Mg}$). In all compositions, garnet shows an increase in the pyrope contents and in Mg# with temperature, this behaviour being more pronounced in the bulk compositions with higher X*$_{Mg}$. With increasing pressure similar trends, slightly shifted towards higher pyrope-contents, are observed. The majorite component of garnets at 8 GPa is below detection limit, and Si is < 3.08 apfu at 13 GPa due to saturation in kyanite/corundum. Stars denote bulk compositions.*

of 61 in AM.

K-feldspar (kfsp) which occurs at 8 GPa in all subsolidus experiments forms up to 25 μm large, inclusion rich idiomorphic grains almost pure in composition with 0.3-0.4 wt% Fe_2O_3(tot) and Na_2O- and CaO-content close to the detection limit.

K-hollandite (K-holl) is the only potassium mineral at 13 GPa and forms small aggregates of prismatic grains which contains 0.3-0.7 wt% Fe_2O_3(tot), 3-6 mol% Na-hollandite, and 2-6 mol% of a Ca-component. The identity of kfsp and K-holl were confirmed by Raman spectroscopy, although in retrospect, the compositional and textural differences between the two phases as described above would be sufficient for unequivocal identification. In the pure K_2O-Al_2O_3-SiO_2 system kfsp is replaced by wadeite ($K_2Si_4O_9$) + kyanite + coesite at 6 GPa which in turn is replaced by K-hollandite at 9 GPa (at 1000 °C, Yong et al., 2006).

Wadeite has yet not been found in natural complex systems and our data indicate a direct transition from kfsp to K-hollandite. The reason for this cannot be the presence of sodium, as extensive $(K,Na)_2Si_4O_9$ solid solution exists (Yong et al., 2006), we thus speculate that Fe_2O_3 stabilizes kfsp over wadeite.

Garnet (grt) forms homogenous, mostly inclusion-free subidiomorphic 5-30 μm large crystals. Garnets at subsolidus conditions have similar X_{pyrope} (Mg/(Mg+Ca+Fe^{2+})) of 0.10-0.21, and $X_{grossular}$ (Ca/(Ca+Mg+Fe^{2+})) of 0.44-0.47 in AM and DG2 and significantly higher X_{pyrope} of 0.16-0.40, and lower $X_{grossular}$ of 0.33-0.30 in DG1, mainly reflecting the X*$_{Ca}$ of the bulk compositions (fig. 2.8). In AM, the garnet evolution with temperature is limited, over 500 °C,

X_{pyrope} increases by 0.06 and $X_{grossular}$ by 0.03. In DG2, garnet evolves over 400 °C through an increase of X_{pyrope} by 0.25 compensated by a decrease in $X_{grossular}$ by 0.20. Finally, in DG1, X_{pyrope} increases over 500 °C by 0.41 and $X_{grossular}$ decreases by 0.15.

The evolution of X_{pyrope} and $X_{grossular}$ in garnets with increasing temperature (fig. 2.10 and Appendix C) does not strongly change with pressure. Na_2O contents in garnets are 0.1-0.45 and 0.65-1.1 wt% at 8 and 13 GPa, respectively, with garnet in the AM bulk always having the lowest concentrations. Si in garnet at 8 GPa remains < 3.02 apfu, i.e. no majorite component within error, and amounts to max. 3.08 apfu in garnets from 13 GPa mainly charge compensating for Na through a coupled substitution $M^{2+}Al$ = NaSi. These Si-contents are in stark contrast to garnets from basaltic and peridotitic compositions which at similar conditions typically range from 3.05-3.20 Si pfu (Yasuda et al., 1994; Okamoto and Maruyama, 2004). Nevertheless, this finding is not surprising, as kyanite or corundum saturated compositions will always result in the minimum majorite content stable at a given pressure and temperature.

Coesite and *stishovite* form anhedral grains which are almost pure in composition with up to 0.5 wt% of FeO_{tot}, increasing with temperature. Similarly, the major impurity of *kyanite* and *corundum* is iron, which amounts to max. 1.1 and 5.1 wt% Fe_2O_3(tot) respectively, increasing with both temperature and pressure.

2.3.3 Melting reactions

The presence of kfsp coexisting with phengite at 8 GPa in both hydrous compositions AM and DG1 indicates H_2O-undersaturated, fluid-absent conditions. Similarly, complete absence of phengite in the nominally anhydrous pelite DG2 indicates that this composition is truly dry. At 13 GPa instead, H_2O previously stored in phengite in the AM bulk is likely to be present as a fluid-phase. Nevertheless, the large amounts of K-hollandite, jadeitic cpx and carbonates observed in BSE images of the subsolidus experiments at 13 GPa, which are confirmed by mass balance calculations, suggest that the presence of a small amount of fluid does not dissolve major fractions of the potassium-, sodium- or CO_2-bearing phases.

Furthermore, the presence and amount of fluid also depends on the H-solubility of other nominally anhydrous phases (Keppler and Smyth, 2006) such as stishovite dissolving up to 3000 ppm H_2O (Litasov et al., 2007) and clinopyroxene (1200 ppm H_2O in $Di_{60}Jd_{40}$, Wu et al., 2009). The reported high solubility of H in stishovite and cpx suggest that the DG1 composition at 13 GPa could be fluid-absent.

The generation of first highly potassic carbonate melt at 8 GPa is controlled by a melting out of carbonates and K-phases. The melting reaction is similar for all three bulk compositions with small differences in the amount of each phase involved in the reaction:

AM (900-1000 °C):
0.5 mgs + 0.5 arag + 2.1 pheng + 0.1 cpx = 1.0 melt + 0.9 grt + 0.5 ky + 0.7 coe (2.1a)

DG1 (900-1100 °C):
0.5 mgs + 0.3 arag + 1.7 Kfsp + 0.1 cpx = 1.0 melt + 0.5 grt + 0.3 ky + 1.0 coe (2.1b)

DG2 (1000-1100 °C):
0.9 dol + 1.7 Kfsp + 0.1 cpx = 1.0 melt + 0.7 grt + 0.2 ky + 0.9 coe (2.1c)

the coefficients being in wt-units and normalized to 1 melt. Summarized, this yields the following qualitative reaction:

1 carbonates + 2 Kfsp or phengite ($\pm$ cpx) = 1 carbonate melt + 0.3 ky + 0.9 coe + 0.7 grt

The small amount of cpx involved in the reaction and the Na_2O-content of < 1 wt% of the melts at 8 GPa indicates a minor role of cpx at the solidus. Instead, the complete destabilization of phengite or kfsp at the solidus leads to the crystallization of a large quantity of garnet, kyanite, and coesite, the amount of garnet depending on the Mg# of the bulk with the lowest Mg# producing most garnet. From 8 to 13 GPa the only mineralogical change is the presence of K-hollandite instead of kfsp or phengite, nevertheless, the situation is quite different: approaching the pressure stability of cpx, jadeite becomes essential during melting as the carbonate melts at the solidus have 4.7-6.2 wt% Na_2O. Furthermore, K-hollandite now coexists with melt over up to 200 °C. Together, this results in a decrease of the K_2O/Na_2O-ratio of the melt from 26-42 to 2-2.2, and a decrease of total alkalis from 25.9-27.5 to 14.1-20.1 wt%, from 8 to 13 GPa, respectively. Consequently, the K-phase has a lesser and jadeite a more important role in the mass balanced solidus reactions at 13 GPa:

AM (1100-1200 °C):
0.4 mgs + 0.6 arag + 0.7 -holl + 0.4 cpx = 1.0 melt + 0.6 grt + 0.1 cor + 0.4 stish (2.2a)

DG1 (1150-1250 °C):
0.5 mgs + 0.5 arag + 1.0 K-holl + 0.5 cpx = 1.0 melt + 0.6 grt + 0.1 cor + 0.7 stish (2.2b)

DG2 (1300-1400 °C):
0.5 mgs + 0.5 arag +0.7 K-holl + 0.4 cpx = 1.0 melt + 0.5 grt + 0.2 ky + 0.4 stish (2.2c)

resulting in the average reaction:

1.0 carbonates + 0.8 K-holl + 0.4 jadeite = 1 carbonate melt + 0.6 grt + 0.1 cor/ky + 0.5 stish

For the AM and DG1 compositions, there is additionally a small amount of H_2O-bearing fluid involved on the educt side. This fluid completely dissolves in the carbonate melt; its main effect is the lowering of the solidus temperature. The melting reactions for DG1 and AM bulks at 13 GPa have corundum on the product side because their solidi occur at the high pressure - low temperature side of the reaction 1 stishovite + 1 corundum = 1 kyanite (Schmidt et al., 1997).

2.4 Discussion

2.4.1 Effect of bulk composition

The differences in bulk composition are reflected in the position of the solidus and in the amount, composition and evolution of garnet, clinopyroxene, carbonates and melts as function of pressure and temperature. The subsolidus compositions of garnet mostly reflect the X^*_{Ca} of the bulk, while the garnet evolution with temperature reflects the bulk X^*_{Mg} (fig. 2.10). The Mg# of the magnesite-siderite solid solution mainly reflects the Mg# of the bulk (fig. 2.9), a lower Mg# correlating with a lower melting point of this carbonate. The higher Na_2O and lower K_2O contents of the DG bulks (3.2-3.4 wt% Na_2O, 2.2-2.4 wt% K_2O) compared to the AM composition (2.4 wt% Na_2O, 3.6 wt% K_2O) is reflected in the higher amount of cpx (30 vs. 20 wt% in the DG vs. AM bulks) and lower amount of K-hollandite (16 vs. 24 wt% in the DG vs. AM bulks) present in the experiments (tab. 2.3). Consequently, K-hollandite has the widest field of coexistence with melt in the AM bulk. Melt compositions also strongly reflect bulk X^*_{Mg} and X^*_{Ca}, as can be seen when projected into a ternary $FeCO_3$-$CaCO_3$-$MgCO_3$ diagram (fig. 2.5a). In our compositions, the effects of bulk X^*_{Mg} and X^*_{Ca} on the melting temperature cannot be isolated from those of the H_2O- and K_2O-contents, thought to dominate.

2.4.2 Melting systematics for carbonated lithologies

Compared to other studies on carbonated mafic eclogites (Hammouda, 2003; Dasgupta et al., 2004,2005; Yaxley and Brey, 2004) and on peridotites (Dasgupta and Hirschmann, 2007; Brey et al., 2008; Ghosh et al., 2009), our pelites exhibit a 100-300 °C lower solidus temperature due to the higher alkali (especially K_2O) and water (AM) content (fig. 2.11). Even if compared with recent studies on wet carbonated peridotites with high potassium and volatiles content (Brey et al., 2009; Foley et al., 2009) our solidus locates at ca. 100 °C lower temperatures due to higher potassium contents and lower X^*_{Mg}. Comparing X^*_{Ca} and X^*_{Mg} of carbonate melts of this study with those formed from carbonated eclogites and peridotites (figs. 2.6c and 2.6d), it becomes apparent that the carbonate melt X^*_{Mg} and X^*_{Ca} correlates well with the X^*_{Mg} and X^*_{Ca} of the bulk. Generally, X^*_{Ca}(melt) $> X^*_{Ca}$(bulk) and X^*_{Mg}(melt) $< X^*_{Mg}$(bulk), and this correlation could be used to predict near solidus melt compositions. The carbonate melts from our pelites have very similar X^*_{Mg} (0.09-0.30) and X^*_{Ca} (0.51-0.71) as the melts generated from basaltic eclogites (X^*_{Mg} between 0.11 and 0.43; X^*_{Ca} between 0.44 and 0.75) but clearly lower X^*_{Mg} and higher

X^*_{Ca} than peridotite derived carbonate melts which have X^*_{Mg} = 0.53-0.81 and X^*_{Ca} = 0.12-0-36 at similar pressures. Similar to melts from carbonated basaltic eclogites, melts presented in this study at 8 GPa have very low Na_2O contents due to high partition coefficient $D_{Na}^{cpx/carbonate\,melts}$ which reaches its maximum near 8 GPa (fig. 2.6a). A similar trend can be expected also for carbonated peridotitic systems, but low Na_2O contents in peridotitic cpx combined with the difficulties in obtaining accurate analysis of alkalis in carbonate melts led to unrealistic wide ranges of $D_{Na}^{cpx/carbonate\,melt}$ (fig. 2.8 in Dasgupta et al., 2005). The SiO_2 and Al_2O_3 content in the carbonate melts of this study remains below 10 wt% even at 400 °C above the solidus.

Carbonate melts derived from peridotitic and basaltic systems at similar pressure (Dalton and Presnall, 1998; Dasgupta et al., 2004; Brey et al., 2008) show much higher SiO_2 and Al_2O_3 contents up to 25-30 wt% at < 200 °C above the solidus. The most evident reason for this behaviour is the lower solidus temperature on pelitic alkali-rich systems compared to basaltic or peridotitic lithologies. Nevertheless, even in experiments run at similar pressure and temperature conditions, the silica content in alkali-rich carbonate melts derived from sediments shows considerably lower values than in other systems. Silica dissolution in carbonate melts coexisting with peridotitic or basaltic assemblages with comparatively low SiO_2-activity is apparently more effective than in carbonate melts coexisting with SiO_2-saturated solid assemblages. The principal structural unit of carbonate melts are isolated planar CO_3-units (Genge et al., 1995; Kohara et al., 1998), not dissimilar to the high concentration of isolated SiO_4-tetrahedra in depolymerized low-SiO_2 silicate melts, but contrasting high SiO_2-melts with large clusters or networks of Si-tetrahedra. We thus speculate that the high SiO_2-contents in carbonate melts of silica undersaturated systems could be a result of the higher structural similarity of carbonate melt with low Si-activity depolymerized silicate melts.

2.4.3 The carbonated pelite solidus, slab melting, and the role of thermal relaxation

A comparison of calculated subduction geotherms (Kincaid and Sacks, 1997; van Keken et al., 2002) with the solidus of carbonated pelites yields the following picture: With respect to the dry solidus (DG2) of carbonated pelite, melting is only feasible for extremely hot subduction (fig. 2.11) over a small pressure window at 7-9 GPa. While carbonated pelites might melt under these conditions, carbonated mafic eclogites or peridotites will not (fig. 2.11). In a system with 1.1 wt% H_2O, such as the AM composition, the solidus is lowered by > 100 °C, and melting could take place at temperatures close to average subduction zone conditions at pressures $>$ 7-9 GPa. The slope of the AM solidus is subparallel to a typical P-T trajectory, implying that melt would form upon crossing of the P-T trajectory, but that upon further burial, no significant further melt production would occur. At > 9 GPa, the AM composition has ca. 1 wt% free H_2O supposedly forming a H_2O-CO_2-fluid, causing the previously fluid-absent carbonated pelite to become fluid-present. It is questionable whether this fluid would be preserved in the carbonated pelite during further subduction at pressures above the phengite dehydration. If this fluid is not retained in the pelite, then, melting has either to occur immediately at the phengite decomposition reaction, or the H_2O-bearing fluid would be lost to the overlying mantle wedge. The further subducting pelite

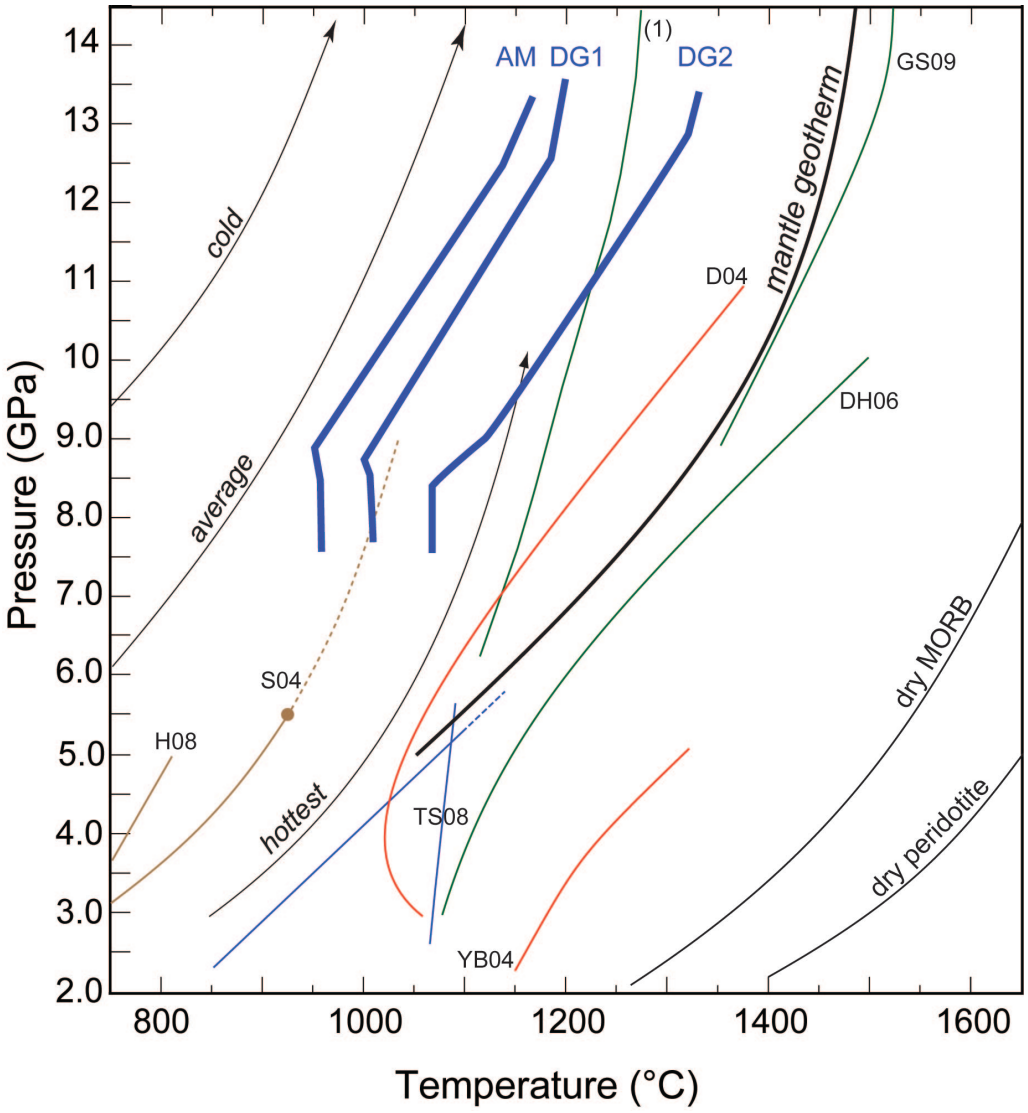

Figure 2.11: *P-T diagram showing a plausible range of subduction P-T-paths and solidi for (carbonated) pelites, basalts and peridotites. Comparison of our solidus temperatures with typical subduction paths (Kincaid and Sacks, 1997; van Keken et al., 2002; Peacock, 2003) and the mantle geotherm (Akaogi et al., 1989) yields melting of these pelites only feasible during very hot subduction or at the end of convergence when subduction halts and thermal relaxation towards the mantle adiabat may occur. (1) is the solidus of potassium-rich hydrous carbonated peridotite compiled from Ghosh et al. (2009), Foley et al. (2009) and Brey et al. (2009). K-rich carbonate melts from subducted sediments, that rise into the mantle are expected to remain in the liquid state also in the mantle at least until major reduction to diamond occurs. Lines: solidi of subducted material, brown: CO_2-free pelites, blue: carbonated pelites, red: carbonated MORB, green: carbonated peridotite. TS08: carbonated pelite (AM composition) solidus and calcite-out reaction after Thomsen and Schmidt (2008b). D04, YB04: solidi of carbonated basaltic eclogite after Dasgupta et al. (2004) and Yaxley and Brey (2004), the former bulk yields subsolidus dolomite or magnesite, the latter Mg-calcite. D06, GS09: solidi of dry carbonated peridotite after Dasgupta and Hirschmann (2006) and Ghosh et al. (2009). S04 and H08: melting and dissolution curves for potassium-rich wet sediments after Schmidt et al. (2004) and Hermann and Spandler (2008). The solidus for dry peridotite is after Hirschmann (2000) and the one for dry MORB after Yasuda et al. (1994).*

becomes thus dry and the solidus of the dry DG2 composition would apply. Cold subduction P-T-paths will not allow melting of carbonated pelites during ongoing subduction.

The precision of temperature prediction in subduction zones does not allow defining an exact depth of melting for the carbonated pelites, in particular near the slab surface, where sediments locate at least when oceanic crust enters into a subduction zone. Nevertheless, the three solidi are 150-300 °C below the mantle adiabat. Thermal relaxation of the slab towards the adiabat becomes important with the end of surface convergence, when subduction slows down or stops due to collision or changes in plate configuration, possibly leading to slab break off. Progressive temperature increase will promote at first the melting of the most fertile lithologies, i.e. hydrous and dry carbonated pelites. These melts will travel into the surrounding mantle leaving a volatile-free, potassium-poor, peraluminous restitic eclogite assemblage behind. This assemblage would be refractory and may survive within the mantle for long periods without being affected by other melting events. Our experiments were performed under closed system conditions. In nature it can be expected that, once formed, carbonate melts rapidly escape from their source rock. Thus, when the solidus reaction is completed due to carbonate exhaustion, further melting of the residual volatile free K_2O-poor eclogitic restite can only be expected when reaching the volatile free solidus of SiO_2-saturated eclogites.

2.4.4 H_2O at $\geq$ 9 GPa in CO_2-free pelites

Previous studies on SiO_2-Al_2O_3-saturated compositions at similar P-T-conditions resulted in two hydrous phases at pressure above the phengite to K-hollandite reaction at 8-9 GPa: Ono (1998) studied average shale and continental crust compositions with 6 wt% H_2O at 6-15 GPa, 800-1400 °C and found, that in peraluminous compositions topaz-OH ($Al_2Si_4(OH)_2$, Wunder et al., 1993) forms instead of kyanite upon phengite breakdown. Near 12 GPa topaz-OH reacts to phase egg ($AlSiO_3(OH)$, Eggleton et al., 1978; Schmidt et al., 1998). Although phase egg is stable to 22 GPa in synthetic Al_2O_3-SiO_2-H_2O systems (Sano et al. 2003), its temperature stability in natural systems appears to be limited to between 1300 and 1400 °C (Ono, 1998). Dobrzhinetskaya and Green (2007) confirmed the presence of K-hollandite and topaz-OH in continental crust compositions at 10-12 GPa, 1100-1300 °C. At 16-20 GPa, 1250-1300 °C, Rapp et al. (2008) obtained phase egg in a pelitic bulk composition with 8 wt% H_2O, but not in the one with 1 wt% H_2O. Even in the original synthesis by Eggleton et al. (1978), phase egg was only obtained from starting materials containing substantial quantities of water. Our subsolidus experiments at 13 GPa, which locate in the phase egg stability field, did not yield phase egg in the AM bulk with 1.1 wt% H_2O. A repetition of one experiment at 13 GPa, 1100 °C with ca. 3 wt% H_2O confirms the previous observations that phase egg only crystallizes in pelitic compositions if larger amounts of water ($>$ 5 wt%) are present. Realistically, subducting slabs at $>$ 9 GPa, contain less than the 1.1 wt% H_2O as present in our AM composition or in the 1 wt% H_2O composition of Rapp et al. (2008). Topaz-OH may be formed at the phengite to K-hollandite reaction at $<$ 1000 °C. At higher temperatures, a supercritical liquid results which is expected to mostly escape the system, leaving $<$ 0.1 wt% H_2O that may be incorporated into nominally anhydrous minerals (Keppler and Smyth,

2006; Litasov et al., 2007; Wu et al., 2009).

2.5 Evidence for subducted carbonates and K-rich metasomatism in the mantle

The analysis of melt and fluid inclusions in diamonds and other minerals found in kimberlites generated deep in the mantle (van Achterbergh et al., 2003; Kamenetsky et al., 2004; Korsakov and Hermann, 2006; Tomlinson et al., 2006; Klein-BenDavid et al., 2007; Guzmics et al., 2008) yielded compositions very similar to our experimental alkaline carbonate melts. These inclusions are extremely rich in alkalis, with generally $K_2O > Na_2O$, and also in volatiles (Cl, H_2O and CO_2), and show a strong affinity to the cationic composition of our melts, especially the carbonate rich end members (fig. 2.7). Not only fluid and melt inclusions but also many mineral inclusions in diamonds (Kamenetsky et al., 2004; Walter et al., 2008) show a correlation with the phases in which our melts are saturated (carbonates, hydrous and potassium-rich phases, K-hollandite, corundum and stishovite). Trace elements and O, C, and Sr isotopic signatures of carbonate melt inclusions in kimberlitic minerals suggest a crustal or crust-derived metasomatic provenance of these materials (van Achterbergh et al., 2002; van Achterbergh et al., 2003; Cartigny, 2005).

2.5.1 Mantle metasomatism and origin of ultra-potassic volcanism

The solidus for carbonated, wet and K_2O-rich peridotites lies at temperatures between 1100 °C and 1200 °C at oxidizing conditions from 8 to 13 GPa (Ghosh et al., 2009; Brey et al., 2009; Foley et al., 2009) which is about 200 °C below the average mantle geotherm (Akaogi et al., 1989) (fig. 2.11). With the end of surface plate convergence a decreasing burial rate of the slab results in a relaxation of subduction isotherms which in turn causes the melting of the most fertile lithologies within the slab. As temperatures increase, the carbonated pelites situated at the upper part of the slab column will melt and generate highly mobile carbonate melts (Hammouda and Laporte, 2000), in our case alkali-rich carbonate melts with $K_2O >> Na_2O$. As long as temperatures remain at $>$ 1100-1200 °C these carbonate melts will infiltrate into the overlying mantle and quickly percolate upwards, thereby concomitantly introducing large amounts of CO_2 and K_2O. The absence of any evidence for an accumulation of this kind of melts at the base of the lithosphere, where temperatures would be low enough for complete crystallization of the carbonate melts suggests that a redox reaction with the reduced mantle (Frost and McCammon, 2008; Rohrbach et al., 2009) immobilizes these carbonate melts. In fact, diamond crystallization has been shown to be favored by the catalytic behaviour of K_2CO_3-rich melt and fluid (Taniguchi et al., 1996; Klein-BenDavid et al., 2007).

The interaction between incompatible elements, potassium, and calcium with the mantle will transform the latter‘s assemblages, introducing incompatible elements, causing an increase of the clinopyroxene/orthopyroxene ratio (Green and Wallace, 1988; Thibault et al., 1992; Dalton and Wood, 1993), and the crystallization of carbonate and potassic phases such as magnesite, K-rich

carbonate, phlogopite, K-richterite and phase-X (Konzett and Fei, 2000). With increasing distance from percolation zones, this process will produce carbonated wehrlites, carbonated re-fertilized lherzolites and so-dubbed "cryptic" metasomatism (Dawson, 1984). Later melting of these metasomatic enriched mantle veins (Foley, 1992) and domains will produce alkali-rich carbonate melts with high concentrations of incompatible elements and a hybrid mantle/crust geochemical characteristics. These carbonate melts may then evolve to the different highly alkaline ultrapotassic silicate melts that form group II kimberlites, lamproites, and aillikites (Foley et al., 2009; Brey et al., 2009; Francis and Patterson, 2009). Geochemical data of many alkali rocks, associated carbonate melts, and of kimberlites and related rocks show isotopical characteristics on the mixing line between the HIMU (recycled altered oceanic crust) and EM1 (subducted oceanic crust and pelagic sediments) mantle endmembers (Faure, 2000; Becker and Le Roex, 2006). These characteristics are thought to be generated by low degree melting of a depleted mantle re-enriched through a potassic-, CO_2 and incompatible element-rich melt or fluid (Girnis et al., 2006; Becker and Le Roex, 2006; Brey et al., 2008; Agashev et al., 2008). All these characteristics coincide with our pelite derived alkaline carbonate melts. The potassium- and CO_2-dominated metasomatism initiating with the melting of carbonated pelites between 8 and 13 GPa would cover most of the important geochemical characteristics deduced for the generation of ultrapotassic and related rocks in the deep upper mantle.

2.5.2 Application for the genesis of group II kimberlites

Kimberlites are ultrapotassic, ultramafic and at the same time extremely enriched in most of the incompatible trace elements and volatile including CO_2 and H_2O. Both kimberlite groups (group I and group II) are thought to be generated at pressure higher than 5-6 GPa from a depleted mantle source re-enriched through volatile-rich melts or fluids containing high trace elements concentrations (Brey et al., 2008). Group II kimberlites differ from group I in their mineralogy, major and trace elements concentrations and isotopic composition (Mitchell, 1995; Becker and Le Roex, 2006). Trace element characteristics of group II kimberlites show an affinity to calc-alkaline mafic magmas and thus to subduction related fluids and melts (Coe et al., 2008). Moreover, their Hf, Sr, and Nd isotopic compositions with low ϵHf, ϵNd and highly radiogenic $^{87}Sr/^{86}Sr$ (Mitchell, 1995; Becker and Le Roex, 2006; Coe et al., 2008) match well with the one of ancient sediments (Rehkamper and Hofmann, 1997; Vervoort and Blichert-Toft, 1999). Compared to group I kimberlites, group II kimberlites are characterized by higher K_2O and H_2O contents, higher K_2O/TiO_2- and K_2O/Na_2O ratios (fig. 2.12) and higher CaO for a given SiO_2 concentration (Mitchell, 1995; Becker and Le Roex, 2006).

McCandless (1999) presented a model where kimberlitic magmatism was attributed to deep-seated subduction, based on age data for kimberlite magmatism combined with seismic images and thermal models of subducted slabs. Our carbonate melts generated from a phengite bearing carbonated pelite at 8 GPa is able to explain all these observed characteristics of group II kimberlites. They contain large amounts of volatiles (CO_2 and H_2O), are extremely enriched in potassium, and are characterized by sedimentary and subduction related geochemical signatures inherited from

their source and subduction history. In the clan of ultramafic ultrapotassic rocks group I kimberlites are the most enriched in CO_2 followed by group II kimberlites and by lamproites, which indicate comparatively low CO_2 contents.

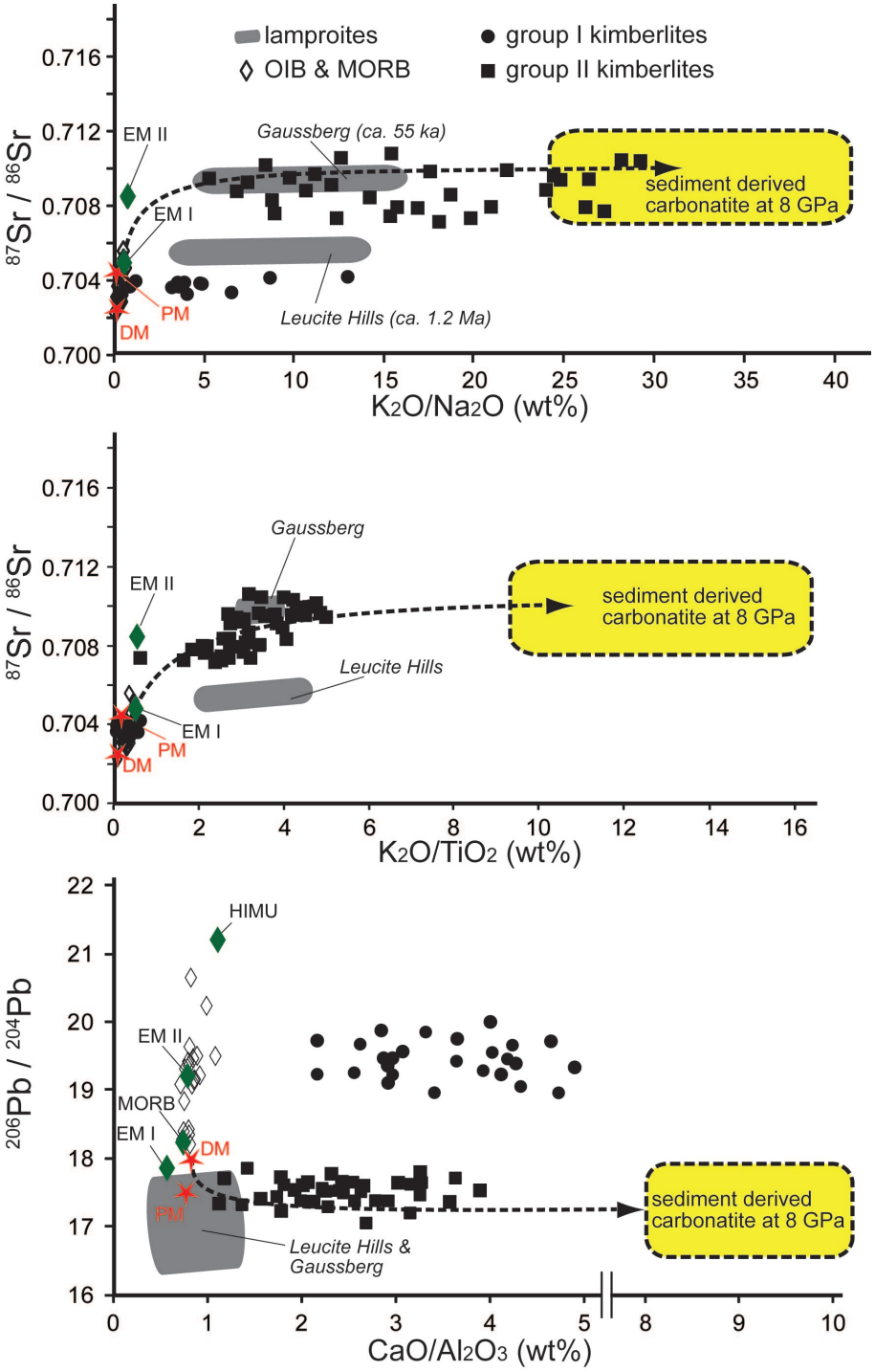

Figure 2.12:

Figure 2.12: *Major element wt-ratios vs. radiogenic isotope composition for OIB and MORB (Jackson and Dasgupta, 2008), group I and group II kimberlites (Le Roex et al., 2003; Becker and Le Roex, 2006; Coe et al., 2008) and lamproites (Gaussberg, Murphy et al., 2002; Leucite Hills, Mirnejad and Bell, 2006). The isotopic composition for the sediment derived melt used for mixing is from 1.5 Ga old sediment (after 1.4 Ga evolution for a $^{87}Rb/^{86}Sr$ ratio of 0.2) consisting of 90 wt% pelagic sediment with an initial $^{87}Sr/^{86}Sr_i$ of 0.7074 (Rehkämper and Hofmann, 1997) and 10 wt% marine carbonates with an initial $^{87}Sr/^{86}Sr_i$ of 0.706 and a Sr concentration 10 times higher than in the pelagic component (Mirota and Veizer, 1994; Plank and Langmuir, 1996). The Sr (2000 ppm) and Pb (10 ppm) concentrations of the melt employed to calculate the mixing lines are in agreement with the results of chapter 5 and with subduction related fractionation after Kelley et al. (2005). Values for the depleted mantle and primitive mantle are after Rehkamper and Hofmann (1997) and Hofmann (1988), respectively. a. and b. $^{87}Sr/^{86}Sr$ vs. K_2O/Na_2O and K_2O/TiO_2 showing a good positive correlation as was already recognized for OIB (Jackson and Dasgupta, 2008) and in particular for the EM types (Spandler et al., 2010). Note the compositions of group II kimberlites lying on the mixing line depleted mantle - sediment derived 8 GPa carbonate melts. c. $^{206}Pb/^{204}Pb$ vs. CaO/Al_2O_3 with group II kimberlites lying exactly on the mixing line depleted mantle - sediment derived 8 GPa carbonate melts.*

This observation shows a positive correlation with the CaO/Al_2O_3 wt%-ratio (fig. 2.12c) of these magmas and with the CaO content within a single rock-type (Becker and Le Roex, 2006; Coe et al., 2008). The higher amounts of CaO for a given SiO_2 content observed in group II kimberlites could thus be ascribed to the metasomatic effect of carbonate melts with higher X^*_{Ca}, as the ones generated from carbonated sediments (figs. 2.6c and 2.6d). Figure 2.12 shows the positive correlation between the potassium enrichment and the radiogenic $^{87}Sr/^{86}Sr$ isotopic composition of group II kimberlites thus linking both characteristics with a single subduction related metasomatic process involving a sedimentary source. .

2.6 Conclusion

When heating subducted carbonated pelites towards a mantle adiabat, melting results into alkaline dolomitic to ferro-magnesian carbonate melts that provide a genetic link between CO_2 and potassic metasomatism of the mantle. Residual jadeite in the pelite holds back Na and strongly fractionates the K/Na ratios, leading to an ultrapotassic character of the melts. When entering the mantle, the relatively oxidized carbonate melts will react with the relatively reduced mantle forming diamond and K_2O and CO_2 rich metasomatic zones, which are the most likely source regions for highly potassic kimberlites.

Chapter 3

The Melting of Carbonated Pelites from 70 to 700 km Depth

Daniele Grassi and Max W. Schmidt
Submitted: Journal of Petrology

Abstract

Phase assemblages, melting relations and melt compositions of a dry carbonated pelite (DG2) and a pelite with 1.1 wt% H_2O (AM) have been experimentally investigated at 5.5-23.5 GPa and 1070-1550 °C. The subsolidus mineralogies to 16 GPa contain garnet, clinopyroxene, coesite or stishovite, kyanite or corundum, phengite or potassium feldspar ($\leq$ 8 GPa in the bulk with and without H_2O, respectively) and then K-hollandite, a Ti-phase and dolomite/Mg-calcite or aragonite + magnesite at higher pressures. The breakdown of clinopyroxene at $>$ 16 GPa causes Na-rich Ca-carbonate (max. 11 wt% Na_2O) to replace aragonite, the former coexisting with magnesite and a Na-rich fluid. Further pressure increase leads to typical transition zone minerals such as the CAS-phase and 1 or 2 perovskites which completely substitute garnet at the highest investigated pressure (23.5 GPa). Melting at 5.5-23.5 GPa yields alkali-rich magnesio- (DG2) to ferro-dolomitic (AM) carbonate melts at temperatures 200-350 °C below the mantle adiabat, i.e. lower than for any other studied natural composition. Melting reactions are controlled by carbonates and alkali-hosting phases: to 16 GPa clinopyroxene remains residual, Na is compatible and the magnesio- to ferro-dolomitic carbonate melts have extremely high K_2O/Na_2O ratios, decreasing when K-hollandite expands its stability field with increasing pressure. At $>$ 16 GPa, Na is repartitioned between several phases, and becomes as incompatible as at $<$ 3 GPa, leading to Na-rich carbonate melts with K_2O/Na_2O ratios $<<$ 1. This leaves the pressure interval of ca. 4-15 GPa for ultrapotassic metasomatism. Comparison of the solidus with typical subducting slab-surface temperatures yields two distinct depths of probable carbonated pelite melting: at 6-9 GPa

the solidus has a negative Clapeyron slope between the intersection of the silicate and carbonate melting reactions at ca. 5 GPa, and the phengite or potassium feldspar stability limit at ca. 9 GPa. The second opportunity is related to possible slab deflection at the 660-km discontinuity, leading to thermal relaxation and partial melting of the most fertile lithology, thus recycling sedimentary CO_2, alkalis and other lithophile and strongly incompatible elements back into the mantle.

Keywords: carbonated pelites, subduction, alkali-carbonate melts, mantle metasomatism, element recycling

3.1 Introduction

There is consensus, that at subarc depths, H_2O is the volatile component controlling fluid- and melt-producing reactions (Schmidt and Poli, 1998, Hacker et al., 2003; Hacker, 2008). This is because high pressure, low temperature fluids have low XCO_2 (Connolly, 2005) and fluid-saturated minimum melting reactions at subarc depths result in hydrous silicate melts in pelites, basalts, and peridotites (Nichols et al., 1994; Schmidt et al., 2004; Niida and Green, 1999). Furthermore, even minimum melting in carbonated pelites yields silicate melts to 5 GPa (Thomsen and Schmidt, 2008b). However, once the subducting lithosphere is beyond typical arc depths (i.e. $>$ 4-7 GPa), the situation changes profoundly as most of the H_2O is by then expelled and because carbonates behave differently: as only a small fraction of the subducted carbonate decomposes below the arc (Kerrick and Connolly, 2001), most is transported to deeper regions (Connolly, 2005) and thus is available for melting reactions at greater depth. At pressures of 8-13 GPa, carbonated pelites melt 200-350 °C below the mantle adiabat (chapter 2). They have the lowest melting temperature of all lithologies of the subducting lithosphere, and yield potassic magnesio- to ferro-dolomitic carbonate melts over a temperature interval from the solidus to well above the adiabat, both for H_2O bearing and dry compositions (chapter 2). One can thus expect that carbonate melts are produced from carbonated pelagic or psammitic sediments at the latest when subduction slows down, stops, or when the subducted lithosphere deflects at the 660-km discontinuity and moves horizontally parallel to the discontinuity for a relatively long period. This is in contrast to K-free carbonated basalts or peridotites, which have significantly higher melting temperatures (Dasgupta et al., 2004; Yaxley and Brey, 2004; Dasgupta and Hirschmann, 2006) and are expected to melt only upon upwelling at $>$ 200 km depth when adiabatic mantle temperatures exceed the conductive geotherm (Dasgupta and Hirschmann, 2006).

Of all possible lithologies subducted into the mantle, recycled carbonated metasediments are the most fertile because of their distinct major element (K_2O, CO_2) and trace element/isotopic (e.g. Ba, Sr, Th, Pb- and Nd) composition. In this study we aim to understand the mineralogy and reactions that govern melting, and the composition of the minimum melts derived from sediments for depths ranging from the subarc region to just beyond the 660-km discontinuity.

3.2 Experimental procedure and analytical technique

3.2.1 Starting material

The bulk composition with 1.1 wt% H_2O (AM, tab. 3.1) is the same as in Thomsen and Schmidt (2008b) and corresponds to a Fe-rich calcareous clay simplified in a K_2O-Na_2O-CaO-FeO-Fe_2O_3-MgO-Al_2O_3-SiO_2-H_2O-CO_2 (KNCFMASH-CO_2) system. The dry composition DG2 (tab 3.2) is a synthetic carbonated pelite in the TiKNCFMASH-CO_2 system. Both compositions are saturated in coesite/stishovite and kyanite/corundum, and in the subsolidus with carbonates. The starting materials were made of powders of SiO_2, Al_2O_3, TiO_2, MgO, Na_2SiO_3, and synthetic fayalite, potassium feldspar and wollastonite, milled and ground to < 5 μm and then mixed with $Al(OH)_3$, $CaCO_3$ and $MgCO_3$ (pure natural magnesite from Obersdorf, Philipp, 1998) to introduce the desired amount of H_2O and CO_2. The powders were kept in a desiccator under ambient temperature (AM) or in a vacuum oven at 110 °C (DG2).

In the following, compositions are discussed in terms of Ca:Fe:Mg-ratio which we denote as molar ratio $X^*M^{2+} = M^{2+}/(Ca+Mg+Fe^{2+})$. To avoid confusion, we use $Mg\# = 100*(Mg/(Mg+Fe^{2+}))$, also on a molar basis, to describe Mg-Fe^{2+} variations.

3.2.2 Experimental procedure

Experiments up to 16 GPa were conducted in a 600-ton Walker-type rocking multi-anvil. The whole multi-anvil apparatus was rotated by 180° during the experiments in order to improve attainment of equilibrium and to reduce chemical zonation in the capsules (Schmidt and Ulmer, 2004). The experiments were rotated continuously during the first 30 minutes and then every 10 minutes during the remainder of the experiments. At higher pressures (18-23.5 GPa), a conventional 1000-ton Walker-type multi-anvil was used. Tungsten carbide cubes with truncation edge lengths of 11 (5.5-8 GPa), 8 (13 GPa) and 3.5 mm (16-23.5 GPa) were combined with prefabricated MgO-octaedra of 18, 14, and 10 mm edge length, respectively, and with natural pyrophyllite gaskets. Assemblies consisted of a zirconia insulator, a stepped $LaCrO_3$-furnace (straight for the 10/3.5 assembly), inner MgO parts and Mo end disks and rings. Details for the experiments at 8 and 13 GPa are described in chapter 2 and for the smaller 10/3.5 assembly in Stewart et al. (2006). Temperature was controlled using a B-type ($Pt_{94}Rh_6$/$Pt_{70}Rh_{30}$) thermocouple and no correction for the effect of pressure was applied. Two $Au_{80}Pd_{20}$ capsules were used in each experiment, stacked in the central part of the furnace assembly below the thermocouple. Quenching was done by turning off the heating power and was followed by pressure unloading of about 15-20 hours. The absence of graphite/diamond in the experiments suggests an oxygen fugacity above the graphite-CO-CO_2 (CCO) buffer. Capsules were mounted longitudinally in epoxy resin and polished to the centre using a dry polishing method to avoid loss of alkalis in the alkali-rich carbonates and quenched carbonates of the carbonate melts. Additionally, the open capsules were repeatedly embedded in low viscosity resin to avoid chemical and mechanical loss of quench carbonate melts. After analysis the capsules were stored in a desiccator under vacuum.

Table 3.1 Bulk (AM) and carbonate melt compositions for the hydrous system AM pelite

Run no.	[a]AM	[a]AM-19	[a]AM-07	[a]ME-110	[a]AM-24	[a]ME-110	am-5B	am-9	am-25	am-19	[b]S6a
P (GPa)/T(°C)		2.5/900	3.7/1000	5/1100	3.7/1100	5/1100	8/1000	13/1200	16/1350	18/1400	22/1500
No. Analyses		7	6	4	12	7	11	13	6	5	21
SiO_2 (wt.%)	47.60	66.9 (1.7)	64.9 (1.1)	59.2 (1.3)	0.91 (0.7)	0.62 (0.4)	0.30 (0.1)	0.48 (0.2)	0.61 (0.5)	0.3 (0.2)	0.04 (0.1)
TiO_2	-	-	-	-	-	-	-	-	-	-	-
Al_2O_3	22.80	19.0 (1.2)	20.3 (1.0)	18.4 (1.5)	0.97 (0.5)	0.87 (0.3)	1.85 (0.3)	1.35 (0.2)	0.95 (0.2)	1.2 (0.4)	0.30 (0.1)
FeO	9.20	0.72 (0.4)	1.09 (0.1)	3.06 (0.8)	8.76 (0.8)	11.9 (0.7)	12.1 (0.9)	9.50 (0.8)	6.94 (0.4)	10.5 (1.5)	9.35 (0.2)
MgO	2.00	0.07 (0.3)	0.13 (0.1)	0.50 (0.2)	3.62 (0.3)	3.76 (0.4)	2.10 (0.2)	2.32 (0.3)	3.59 (0.5)	4.5 (0.8)	6.02 (0.3)
CaO	6.80	0.70 (0.9)	0.46 (0.1)	2.45 (0.5)	30.8 (2.1)	30.1 (1.7)	16.5 (0.8)	25.5 (1.4)	25.4 (2.2)	26 (2.3)	20.1 (0.2)
Na_2O	2.40	1.71 (0.6)	1.37 (0.2)	2.44 (0.2)	4.01 (2.1)	1.97 (0.6)	0.65 (0.2)	4.8 (0.6)	7.7 (1.5)	10.5 (3.1)	19.6 (0.3)
K_2O	3.60	10.9 (1.1)	11.7 (0.9)	14.0 (0.8)	0.71 (0.2)	4.21 (0.7)	26.8 (1.7)	10.2 (1.7)	8.7 (1.3)	4.5 (0.9)	3.37 (0.2)
[d]H_2O	1.10	3.4	3.2	3.7	n.a.	n.a.	9.4	9.88	n.a.	9.5 (1.5)	n.a.
[d]CO_2	4.80	2.4	2.2	2.2	48.9 (2.4)	47.6 (4.4)	38.45	43.12	n.a.	37.0 (3.5)	n.a.
tot.	100.30	100	100	100	49.78	53.43	60.35	54.13	53.89	57.50	58.73
[c]Si (pfu)		3.02	2.95	2.81	0.03	0.02	0.01	0.02	0.02	0.01	0.00
Ti		-	-	-	-	-	-	-	-	-	-
Al		1.01	1.09	1.03	0.04	0.03	0.06	0.05	0.03	0.04	0.01
Fe_{tot}		0.03	0.04	0.12	0.26	0.34	0.29	0.25	0.18	0.25	0.19
Mg		0.01	0.01	0.04	0.19	0.19	0.09	0.11	0.16	0.19	0.22
Ca		0.03	0.02	0.13	1.17	1.10	0.51	0.87	0.82	0.78	0.53
Na		0.15	0.12	0.23	0.28	0.13	0.04	0.30	0.45	0.57	0.94
K		0.63	0.68	0.85	0.03	0.18	0.99	0.41	0.34	0.16	0.11
K_2O/Na_2O (wt%)	1.50	6.39	8.59	5.73	0.18	2.24	41.31	2.13	1.13	0.43	0.17
$D_{Na}^{cpx/carb.\,melt}$ (wt%)	-	3.10	7.32	3.58	2.20	5.43	17.68	2.61	1.67	-	-
Mg#	27.90	25.00	20.00	25.00	42.22	35.85	23.68	30.56	47.06	43.18	53.66
X^*_{Mg}	0.17	0.14	0.14	0.14	0.12	0.12	0.10	0.09	0.14	0.15	0.23
X^*_{Ca}	0.41	0.43	0.29	0.45	0.72	0.67	0.57	0.71	0.71	0.64	0.56

[a] Thomsen and Schmidt (2008b)

[b] reversed

[c] Cations calculated on the basis of 6 oxygens for carb. melts and 8 oxygens for silicate melts

[d] H_2O and CO_2 content calculated from bulk and melt fraction.

Table 3.2 Bulk (DG2) and carb. melt compositions for the nominally dry DG2 pelite

Run no.	DG2	DG2-3	reverse	DG2-27	DG2-19	[a]S5a	DG2-15
P (GPa)/T(°C)		8/1100	13/1350	16/1350	18/1400	22/1500	22/1550
No. Analyses		13	14	7	12	19	14
SiO_2 (wt%)	54.63	0.26 (0.1)	0.22 (0.1)	0.99 (0.5)	0.09 (0.1)	0.05 (0.1)	0.07 (0.1)
TiO_2	0.63	2.37 (0.4)	1.83 (0.3)	1.70 (0.2)	1.03 (0.8)	0.56 (0.1)	0.47 (0.1)
Al_2O_3	20.23	1.55 (0.3)	1.18 (0.3)	1.15 (0.4)	0.82 (0.3)	0.26 (0.1)	0.44 (0.1)
FeO	4.86	7.55 (0.6)	7.08 (0.6)	6.81 (1.2)	5.17 (1.1)	7.32 (0.2)	4.36 (0.4)
MgO	2.92	2.95 (0.3)	5.35 (0.3)	3.52 (0.8)	4.67 (0.7)	7.36 (0.6)	11.1 (1.1)
CaO	5.88	16.3 (1.5)	26.4 (1.2)	25.1 (1.7)	19.8 (4.1)	15.3 (0.2)	15.9 (2.1)
Na_2O	3.20	0.95 (0.6)	4.71 (0.6)	7.02 (1.1)	17.5 (5.1)	22.7 (0.8)	20.1 (1.1)
K_2O	2.21	24.4 (2.8)	9.43 (1.1)	8.79 (1.9)	4.03 (1.1)	3.27 (0.2)	4.97 (0.5)
[c]CO_2	4.50	43.67	43.80	44.86	46.78	43.12	42.64
tot.	99.07	56.33	56.20	55.14	53.12	56.88	57.36
[b]Si (pfu)		0.01	0.01	0.03	0.00	0.00	0.00
Ti		0.05	0.04	0.04	0.02	0.01	0.01
Al		0.06	0.04	0.04	0.03	0.01	0.01
Fe_{tot}		0.19	0.18	0.17	0.12	0.15	0.09
Mg		0.14	0.24	0.16	0.19	0.27	0.40
Ca		0.54	0.85	0.81	0.58	0.40	0.41
Na		0.06	0.28	0.41	0.93	1.07	0.93
K		0.96	0.36	0.34	0.14	0.10	0.15
K_2O/Na_2O (wt%)	0.69	25.68	2.00	1.25	0.23	0.14	0.25
$D_{Na}^{cpx/carb.\,melt}$ (wt%)	-	10.00	2.37	1.76	-	-	-
Mg#	52.10	42.42	57.14	48.48	61.29	64.29	81.63
X^*_{Mg}	0.30	0.16	0.19	0.14	0.21	0.33	0.44
X^*_{Ca}	0.43	0.62	0.67	0.71	0.65	0.49	0.46

[a] reversed

[b] Cations calculated on the basis of 6 oxygens.

[c] CO_2 content calculated by difference of 100 and the measured analytical total

3.2.3 Analytical methods

All experimental charges were analyzed with a JEOL JXA8200 electron microprobe at ETH-Zürich employing 15 kV acceleration voltages, 20 nA beam current for silicate minerals and 5 nA for carbonates and carbonate melts. Acquisition times were 10 seconds for Na and K and 20 seconds for all other elements, measuring Na and K first to avoid diffusional losses. Beam diameters of 1 to 2 μm were used for silicates and carbonates. Quenched melts, which are susceptible to beam damage, were analyzed, whenever possible, using a defocused beam (3-20 μm). Secondary and back-scattered electron images from the microprobe or from a JEOL JSM6300 field emission SEM were used for textural analysis. Micro-Raman spectroscopy was employed to identify carbonate polymorphs, potassium feldspar/K-hollandite and Ti-oxides at 8 GPa, perovskite at P $>$ 18 GPa, and to identify the structure of the Na carbonate, which is similar to calcite and dolomite.

Table 3.3 Experimental run conditions and calculated phase proportions (wt%)

run/ bulk	P [GPa]	T [°C]	time [h]	pheng	kfsp	K-holl/ K-Phase	arag	mgs	dol/ Mg-cc	Na-carb	[a] Ti-Phase/ Fe-oxide	grt	cpx	CAS	Ca-pv	Fe-pv	ky/cor	coe/ stish	carb. melt
DG2-22	5.5	1070	96	-	13.4	-	-	-	9.9	-	x	10	32.8	-	-	-	16.8	17.1	-
DG2-31	5.5	1125	72	-	-	-	-	-	-	-	-	xx	xxx	-	-	-	xx	xx	x
DG2-32	5.5	1180	48	-	-	-	-	-	-	-	-	xx	xxx	-	-	-	xx	xx	xx
DG2-30	6.5	1070	72	-	-	-	-	-	x	-	-	xxx	xxx	-	-	-	xx	xx	x
DG2-25	16	1250	96	-	-	14.3	-	4.3	-	6.1	-	21.9	15.9	-	-	-	9.8	27.6	x
DG2-27	16	1350	72	-	-	9.9	x	2.4	-	-	-	22.9	19.0	-	-	-	9.2	27.1	6.9
DG2-24	18	1200	96	-	-	xxx	-	x	-	xx	-	xxx	-	-	-	-	xx	xx	-
DG2-26	18	1300	72	-	-	15.8	-	2.6	-	13.3	-	21.9	-	-	-	-	13.1	33.3	-
DG2-19	18	1400	48	-	-	11.1	-	2.4	-		-	27.9	-	-	-	-	13.0	34.9	10.8
DG2-17	22	1350	96	-	-	14.6	-	1.8	-	9.5	-	23.6	-	-	x	x	12.9	33.6	-
DG2-28	22	1400	96	-	-	xx	-	x	-	xx	-	xx	-	xx	x	x	xx	xx	x
DG2-13	22	1500	48	-	-	8.4	-	x	-	-	-	18.7	-	28.3	-	-	x	30.4	10.9
DG2-15	22	1550	48	-	-	8.9	-	-	-	-	-	12.6	-	28.1	-	-	2.7	35.9	11.7
Dg2-29	23.5	1400	96	-	-	15.5	-	2.1	-	10.3	-	5.2	-	-	5.2	10.3	15.5	36.1	-
am-22	5.5	1070	96	29.9	x	-	-	-	10.2	-	-	21.7	20.8	-	-	-	9.9	7.6	-
am-31	5.5	1125	72	-	-	-	-	-	x	-	-	xxx	xxx	-	-	-	xx	xx	xx
am-32	5.5	1180	48	-	-	-	-	-	-	-	-	xxx	xxx	-	-	-	xx	xx	xx
am-30	6.5	1070	72	-	x	-	-	-	x	-	-	xxx	xxx	-	-	-	xx	xx	x
am-25	16	1250	96	-	-	24.3	-	2.3	-	9.1	-	29.2	-	-	-	-	12.6	22.5	x
am-27	16	1350	72	-	-	20.5	x	2.3	-	-	-	29.8	11.4	-	-	-	9.6	17.9	8.5
am-24	18	1200	96	-	-	xxx	-	x	-	xx	-	xxx	-	-	-	-	xx	xx	-
am-26	18	1300	72	-	-	25.5	-	2.5	-	9.3	-	29.8	-	-	-	-	12.2	20.7	-
am-19	18	1400	48	-	-	xx	-	x	-	x	-	xxx	-	-	-	-	xx	xxx	x
am-17	22	1350	96	-	-	26.9	-	-	-	12.2	2.1	13.0	-	-	3.0	6.0	14.0	23.0	-
am-28	22	1400	96	-	-	xxx	-	x	-	xx	-	xx	-	xx	x	x	xx	xx	x
am-13	22	1500	48	-	-	22.9	-	1.5	-	-	-	26.1	-	11.1	-	-	8.6	19.6	10.8
am-15 b	22	1550	48	-	-	xx	-	-	-	-	-	xxx	-	xxx	-	-	xx	xx	-
am-29	23.5	1400	96	-	-	29.9	-	-	-	13.0	2.0	-	-	-	5.0	11.4	13.8	24.9	-
DG2-S5a c	22	1500	50	-	-	xx	-	x	-	-	-	xx	-	xx	-	x	xx	xx	xxx
AM-S6a c	22	1500	50	-	-	xx	-	-	-	-	-	xx	-	xx	-	-	xx	xx	xxx

xxx: $>$ 20 wt%; xx: 5-20 wt%; x: $<$ 5 wt%

subsolidus experiments include H_2O and CO_2 as mass balance components. FeO adjusted for Fe-loss to the capsule for all exp. with large amount of melt

[a] grt: garnet; cpx: clinopyroxene; pheng: phengite; kfsp: potassium feldspar; K-holl: potassium hollandite; stish: stishovite; coe: coesite; cor: corundum; ky: kyanite; pv: perovskite; CAS: $CaAl_4Si_2O_{11}$ (Gautron et al., 1997); dol: dolomite; mgs: magnesite; Mg-cc: magnesium calcite; arag: aragonite; Na-carb: Na-rich carbonate; Fe-oxi: Fe oxide; Ti-Phase: Ti-oxide

[b] hole in the capsule (no melt and carbonates)

[c] revers experiments

3.3 Results

In total, 38 experiments were performed on the 1.1 wt% H_2O AM composition (fig. 3.1; this study; 8 and 13 GPa: chapter 2; $\leq$ 5 GPa: Thomsen and Schmidt, 2008b) and 24 experiments on the dry DG2 composition (this study; 8 and 13 GPa: chapter 2). Mineral proportions and run conditions for the experiments of this study are presented in table 3.3, and subsolidus mineral proportions as a function of pressure plotted in figure 3.2. Equilibrium in the different experiments is indicated by well-crystallized grains, 120° triple point junctions between phases (figs. 3.3 and 3.4) and a homogenous composition of the different minerals throughout the capsule. Mineral trends as a function of pressure and temperature also suggest that equilibrium was generally reached. This result was only achieved after prolonging run times from 24 hours to 96 hours. Runs of 24 h duration were in textural disequilibrium, and at sub- and near-solidus conditions, minerals were too small to be reliably measured by electron microprobe. Nevertheless, despite run times of 96 hours at 1400 °C (e.g. run 29 at 23.5 GPa), some phases remained small ($<$ 5 m) at subsolidus conditions, making them difficult to analyze.

3.3.1 Subsolidus phase assemblages

Subsolidus assemblages evolve with increasing pressure (figs. 3.1 and 3.2), and consist of garnet, quartz/coesite, kyanite, clinopyroxene, phengite (in the H_2O-bearing AM bulk) or potassium feldspar (in the dry DG bulk) and Mg-rich calcite (AM) or dolomite (DG2) at 2.5-6.5 GPa (figs. 3.3 and 3.4). When pressure is increased from 6.5 to 8 GPa, Mg-calcite or dolomite are replaced by magnesite + aragonite, which coexist in both compositions up to 16 GPa. At 8 GPa the stable K-phases are phengite or potassium feldspar, which are both replaced by K-hollandite at higher pressures (ca. 9 GPa, Schmidt et al., 2004; Yong et al., 2006). After the breakdown of phengite, no other hydrous phases could be detected, and in the AM composition, the presence of a H_2O-rich fluid is likely in the experiments at P $>$ 12 GPa. At 12.5 GPa (ca. 1000 °C), kyanite dissociates to stishovite and corundum (Schmidt et al., 1997). Clinopyroxene is stable to 16 GPa, and its disappearance causes Na-rich Ca-carbonate with up to 11 wt% Na_2O to replace aragonite. At 18 GPa, the subsolidus assemblage consists of stishovite, corundum, garnet, K-hollandite, magnesite and Na-rich Ca-carbonate. This assemblage changes at 22 GPa, where characteristic high pressure phases such as Ca-perovskite, FeTi-perovskite, and the CAS phase ($CaAl_4Si_2O_{11}$, Gautron et al., 1997) (Appendix C), the latter only above the solidus at T $\geq$ 1400 °C, progressively substitute for garnet. In the DG2 composition at 8 and 13 GPa, small amounts of Ti-rich phases crystallize at subsolidus conditions (Rutile II; TiO_2 with α-PbO_2 structure Simons and Dachille, 1967). In the hydrous AM composition, minute grains of an almost pure Fe-oxide are observed at 22 GPa. Throughout the investigated P-T-conditions, all experiments are SiO_2- as well as Al_2O_3- saturated.

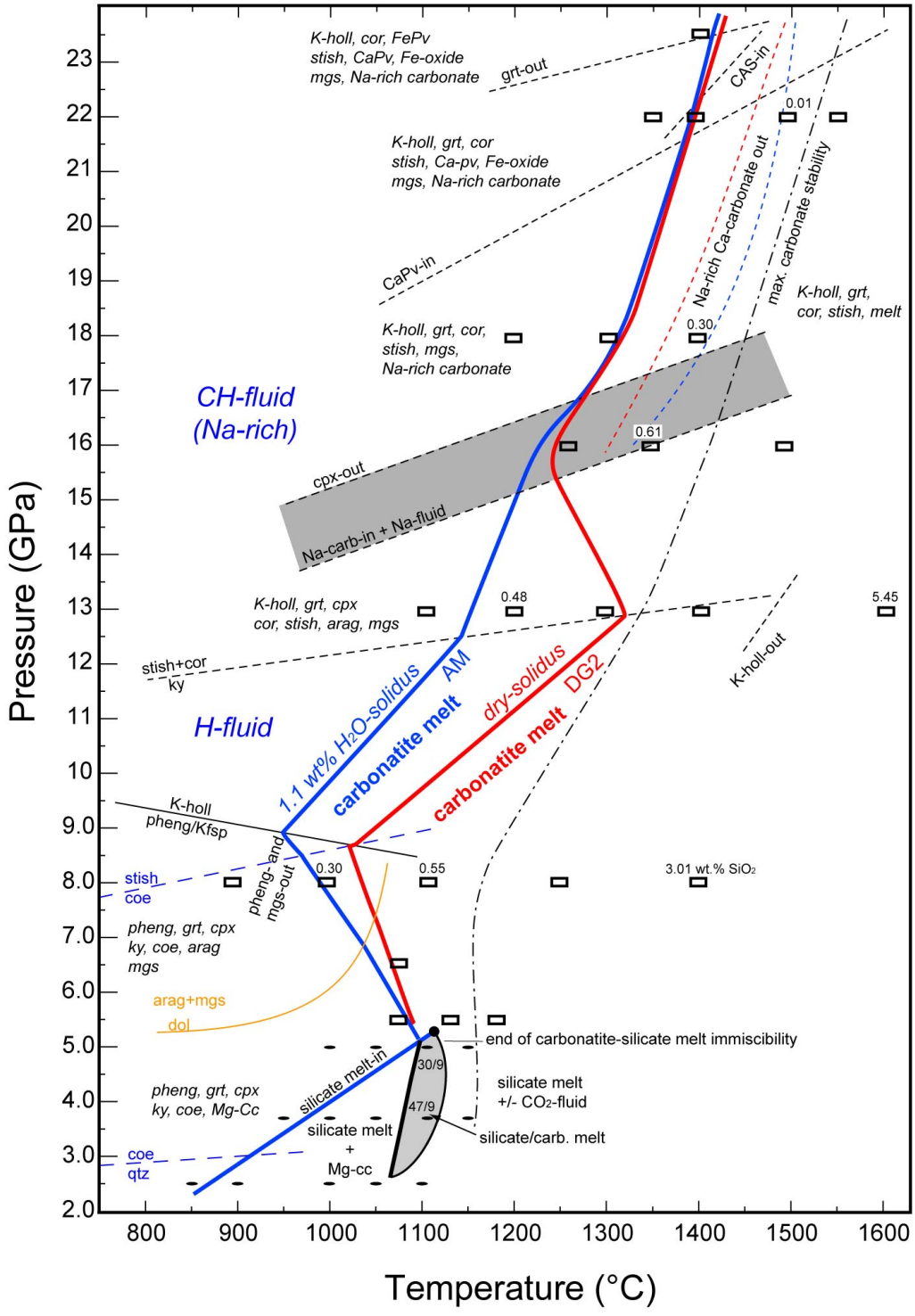

Figure 3.1: *P-T diagram compiled from the experimental results for carbonated pelites from 2.5 to 23.5 GPa in the system TiKNCFMASH-CO_2. Small black points (ellipses) are experiments by Thomsen and Schmidt (2008b). The solidus at > 9 GPa for the AM and at > 16 GPa for DG2 can be regarded as fluid-present solidus, experimentally defined by the first appearance of alkali-rich quenched carbonate melt. Numbers above experimental symbols refer to SiO_2 (wt%) contents in the melts for AM. Coesite-stishovite reaction (Zhang et al. 1996), decomposition-reaction of kyanite to corundum+stishovite (Schmidt et al. 1997; this study), phengite to K-hollandite reaction (Schmidt et al. 2004).*

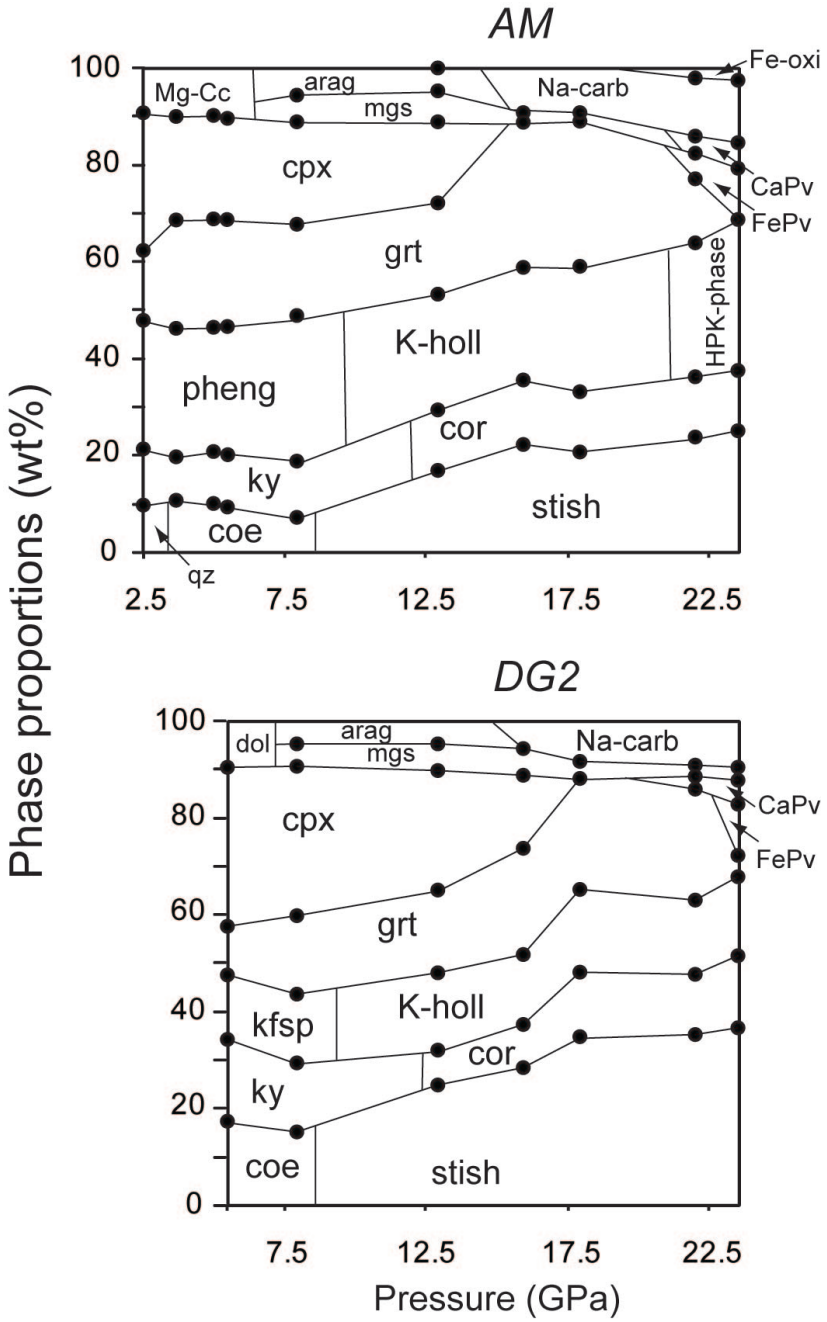

Figure 3.2: *Calculated modes of minerals (in wt%) at the solidus for the coesite/stishovite + kyanite/corundum saturated, fertile carbonated metapelites AM and DG2 as function of pressure. At P > 16 GPa some uncertainty in the mass-balance is introduced by the presence of a Na-rich fluid, dissolving significant but unknown quantities of elements. The AM bulk has 1.1 wt% H_2O and crystallizes phengite at P < 9 GPa, DG2 is dry. Different amounts of Na_2O and K_2O in the bulk are clearly reflected in the proportions of cpx and phengite/K-hollandite crystallizing at the solidus. The lower X^*_{Mg} of the AM composition is responsible for the appearance of Mg-calcite at lower pressure, whereas in the DG2 composition a Fe-rich dolomite is stable at the same condition. The increasing X^*_{Mg} of garnet and Na-carbonate with pressure leads to the disappearance of magnesite at the highest pressures in the AM composition. The highest amount of garnet is observed between 16 and 18 GPa after the cpx breakdown and before perovskite formation.*

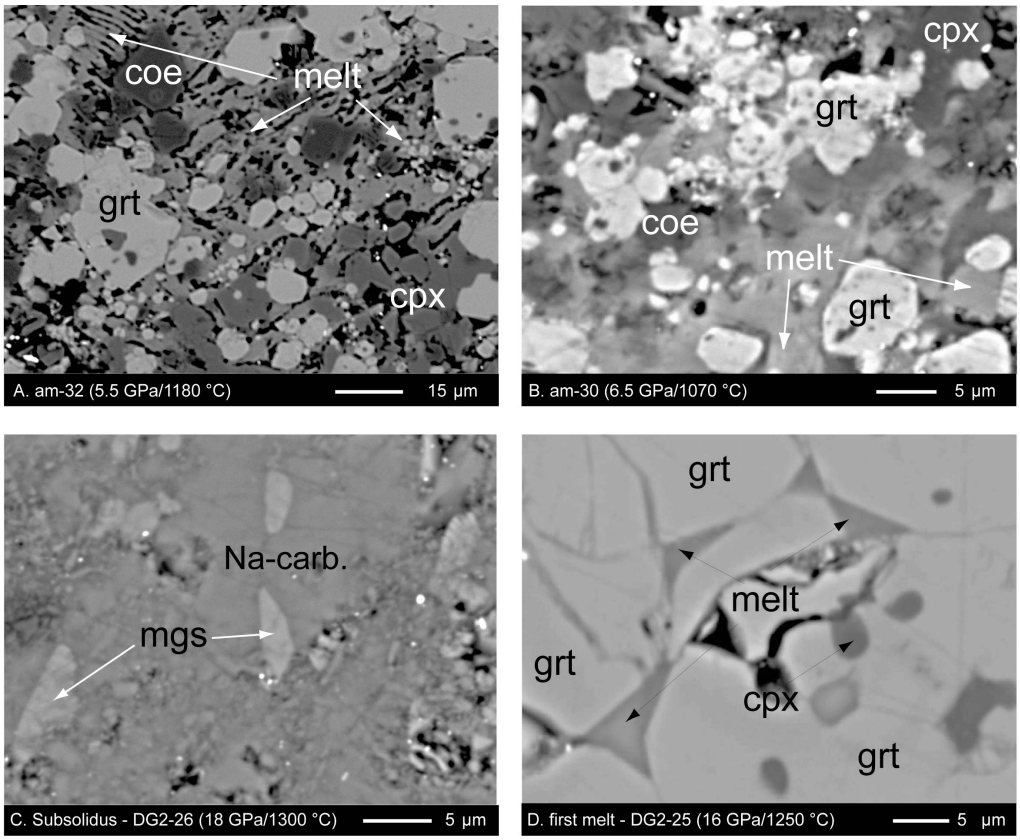

Figure 3.3: *BSE-images of run products. A: 5.5 GPa, 1180 °C, bulk AM; large amount of K-rich carbonate melt (ca. 15 wt%) coexisting with grt, cpx, coe and ky. At similar temperatures but at 5 GPa the same bulk composition produced ca. 45 wt% of silicate melt (Thomsen and Schmidt, 2008b). B: 6.5 GPa, 1070 °C, bulk AM; first small amount of potassic carbonate melt coexisting with grt, cpx, coe, ky and minor amounts of kfsp and Mg-cc (the latter not in the picture). C: 18 GPa, 1300 °C, bulk DG2; at subsolidus conditions and P > 16 GPa a Na-rich carbonate coexists with magnesite. D: 16 GPa, 1250 °C, bulk DG2; first amount of melt at 16 GPa trapped into the triple junction of garnet crystals.*

3.3.2 Mineral compositions and stability

Garnet forms homogenous, mostly inclusion-free subidiomorphic 5-30 μm large crystals (figs. 3.3 and 3.4). With increasing pressure the Mg# of garnets generally increases from 16.9 to 29.7 for AM and from 22.7 to 40.0 for DG2 (fig. 3.5). Nevertheless, discrete decreases in the Mg# of garnets are observed in both compositions at 5.5-8 GPa when magnesite + aragonite replace Mg-calcite or dolomite, and in the AM composition at 16-18 GPa when Na-rich carbonate, which contains 2-3 wt% MgO, replaces pure aragonite. Si contents in garnet remain below 3.00 Si pfu to 8 GPa, then increase slightly with pressure to 3.05 at 13 GPa and 3.25-3.30 at 22-23.5 GPa in both bulk compositions (fig. 3.5a). Na contents follow a similar trend as Si and increase with pressure from near zero at 2.5 GPa to 0.19 Na pfu (for DG2) at 23.5 GPa. As Si (and Ti) charge compensate for Na in a $(Ca,Fe,Mg)_{-1}Al_{-1}(Na,K)(Ti,Si)$ substitution, majorite component

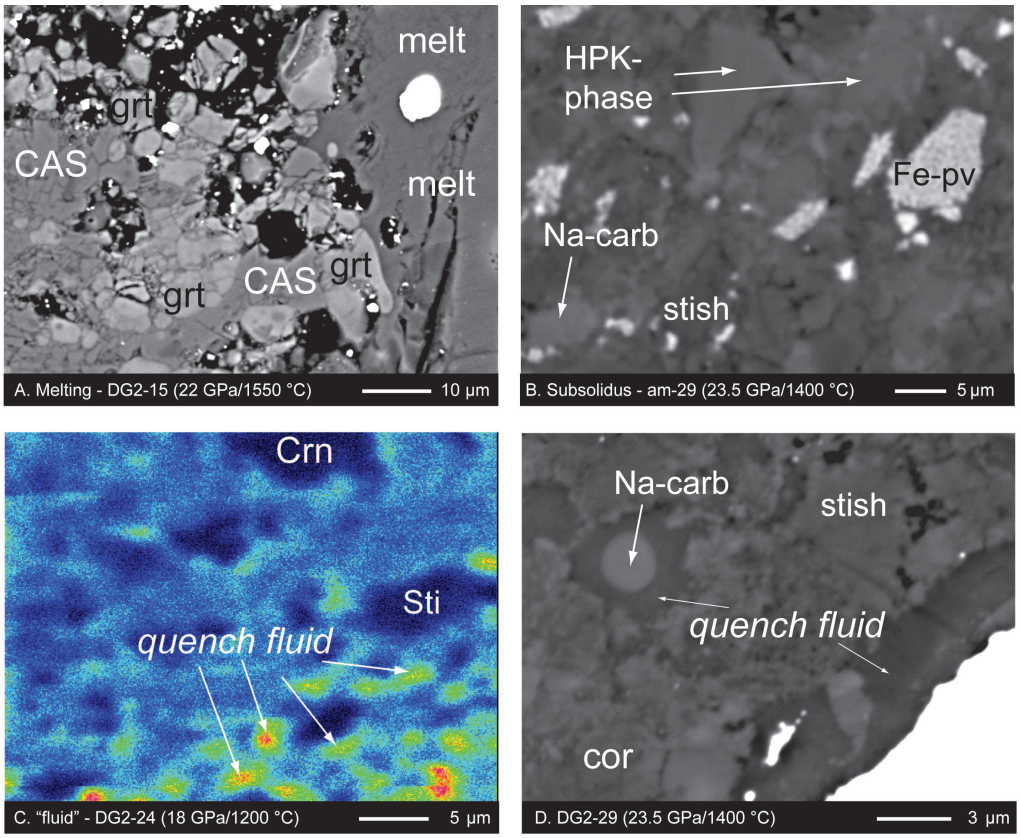

Figure 3.4: *BSE-images of run products. A: 22 GPa, 1550 °C, bulk DG2; a relatively large quantity of carbonate melts coexisting with grt and the CAS-phase (and with mgs, K-holl, stish and corundum not in the picture). B: 23.5 GPa, 1400 °C, bulk AM; near solidus experiments crystallizing Fe-perovskite coexisting with stishovite, corundum, Na-carbonate, CAS-phase, a Fe-oxide and the potassium-rich HPK-phase. C: 18 GPa, 1200 °C, bulk DG2; Na-Kα element distribution map of subsolidus high pressure assemblage coexisting with a Na-rich liquid phase. Small interstitial Na-rich patches indicate quench of a probably Na_2O-CO_2-phase and are visible throughout the entire capsule. D: 23.5 GPa, 1400 °C, bulk DG2; Na-rich carbonate with ca. 20 wt% of Na_2O (33-34 mol% Na_2CO_3) but almost no Fe and Mg (<1 mol%) interpreted as quench products from the fluid.*

resulting from tschermaks substitution is equal to (Si+Ti)-3-(Na+K), and is significant only in the lowest temperature experiments at 18-23.5 GPa, where it remains $\leq$ 10 mol%. These low majorite contents result from the presence of kyanite/corundum, which forces garnets to remain on the Al_2O_3-saturation surface, the latter representing the minimum majorite component stable at a given P-T condition. The TiO_2 concentration in garnet increases with pressure to 1.44 wt% at 8 GPa, reaching a maximum of 1.91 wt% at 18 GPa. At 22 and 23.5 GPa, Ti-concentrations in garnet are much lower (0.32-1.33 wt%). This is attributed to the presence of Ti-rich Ca- and Fe-perovskites, and the preferential partitioning of Ti in these phases relative to garnet (see below). The potassium concentration in garnet increases from 0.07 to 0.21 wt% (AM composition) as pressure increases from 2.5 to 8 GPa. The K-contents then decrease between 8 and 18 GPa, but

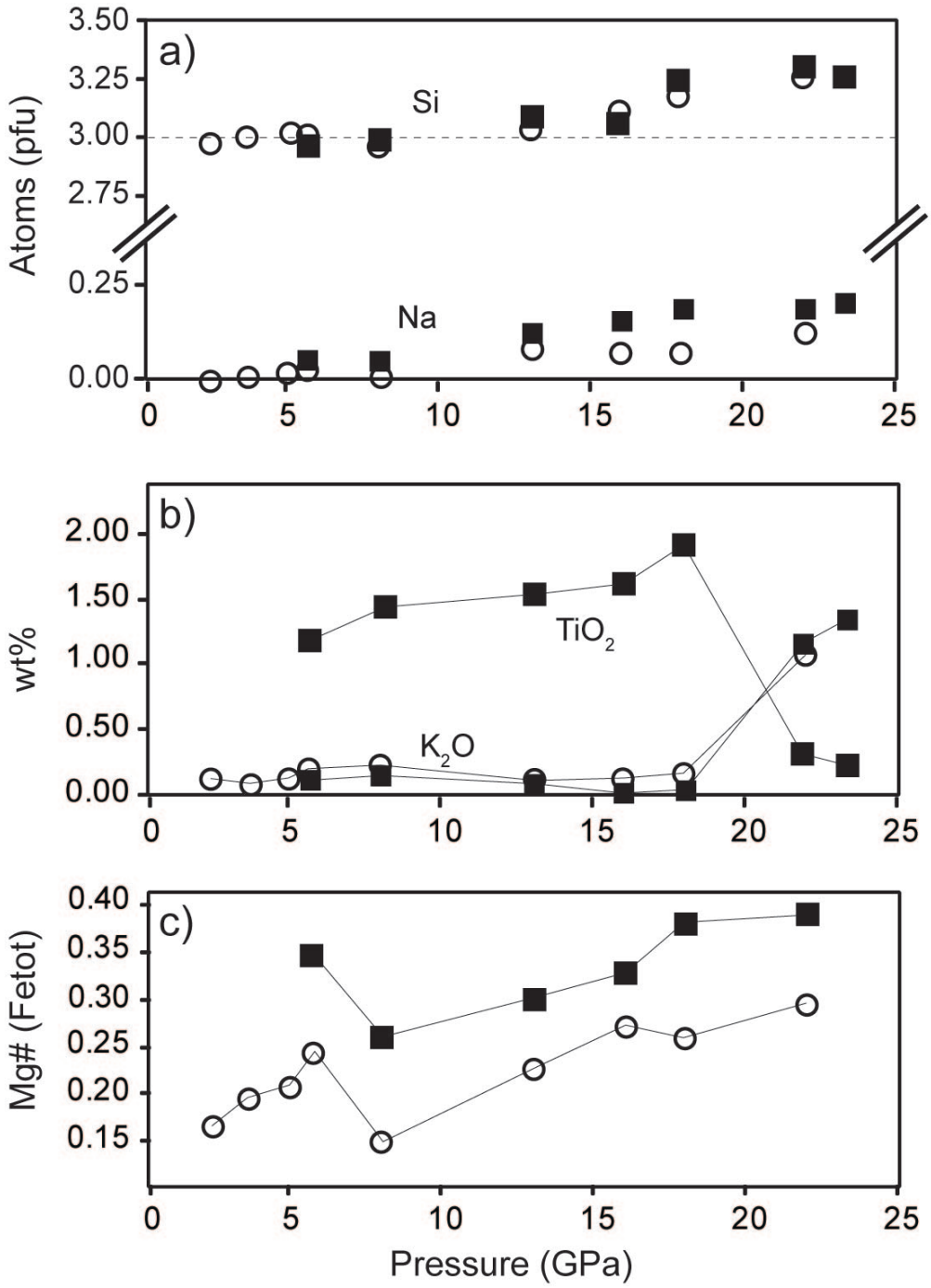

Figure 3.5: *Composition of garnet as function of pressure. At subsolidus conditions garnets in both compositions are quite similar. The increase in Si is not due to a majorite component, which remains nil in this kyanite/corundum saturated bulk compositions, but due to a charge-coupled substitution* M^{2+} *+ Al = (Na,K)+(Si,Ti). Open circles are for the AM composition; filled squares for DG2.*

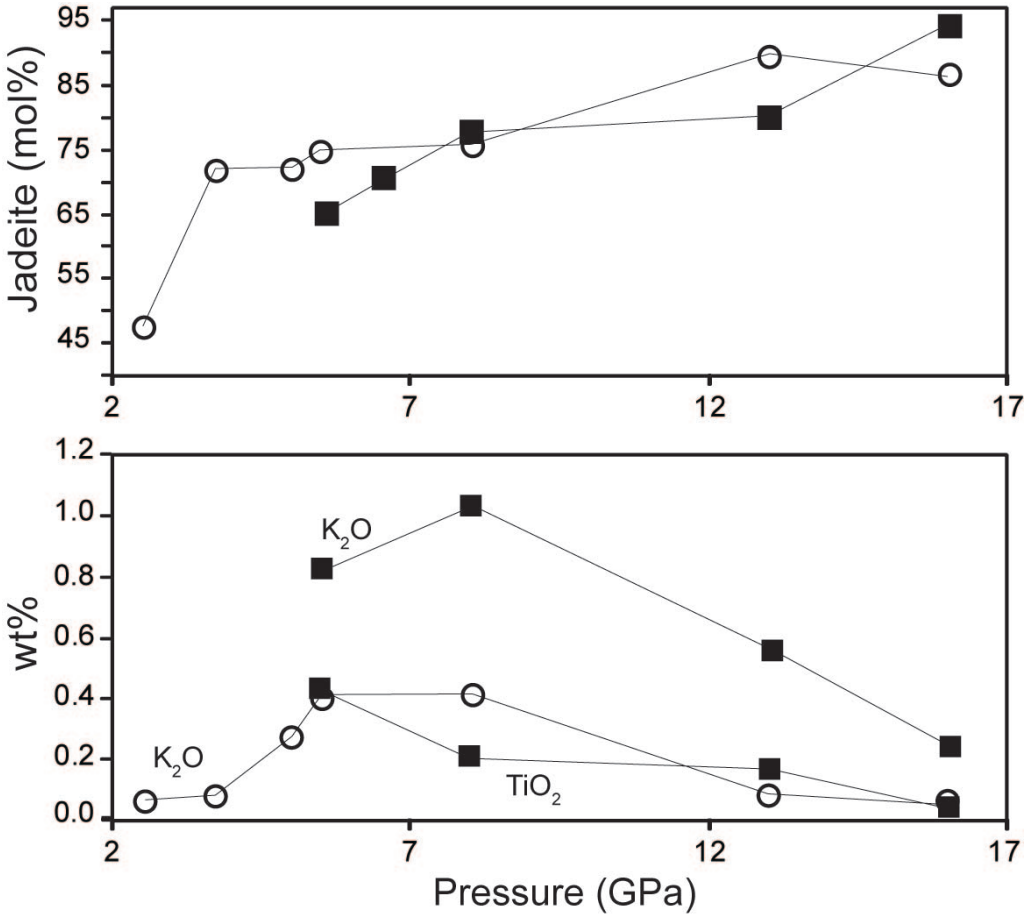

Figure 3.6: *Clinopyroxene composition as function of pressure. Notice the increasing of jadeite component with pressure and the maximum K_2O content of cpx at 8 GPa, i.e. at a pressure just below the formation of K-hollandite. Such a trend is also observed for the K-content of carbonate melts (see fig. 3.11). Open symbols: 1.1 wt% H_2O-AM composition; filled symbols: dry DG2.*

increase again at 22 GPa, reaching 1.08-1.15 wt% K_2O at subsolidus conditions, confirming the high potassium content in garnet at P $>$ 22 GPa measured by Wang and Takahashi (1999) in a K-rich basaltic composition.

At 23.5 GPa garnet has disappeared from the low X^*_{Mg} AM composition but remains present at 5-10 wt% in DG2, where it coexists with Ca- and Fe-Ti-perovskite. The transition from a garnet-bearing to a garnet-free perovskite-bearing assemblage in a Fe-rich system at 23-24 GPa has also been observed by Rapp et al. (2008). The presence of a H_2O-bearing fluid in the AM composition favors the oxidation of Fe through hydrogen loss. Together with the low Mg# and the high FeO-content, this explains the earlier disappearance of garnet and the larger amount of Fe-perovskite in the AM composition, Fe-perovskite accommodating larger amounts of Fe^{3+} than garnet (McCammon and Ross, 2003; Litasov and Ohtani, 2005).

Clinopyroxene is stable to $\leq$ 16 GPa in both compositions and forms relatively small $<$ 15 μm long prismatic crystals. In the AM composition clinopyroxene breaks down at 16 GPa where.

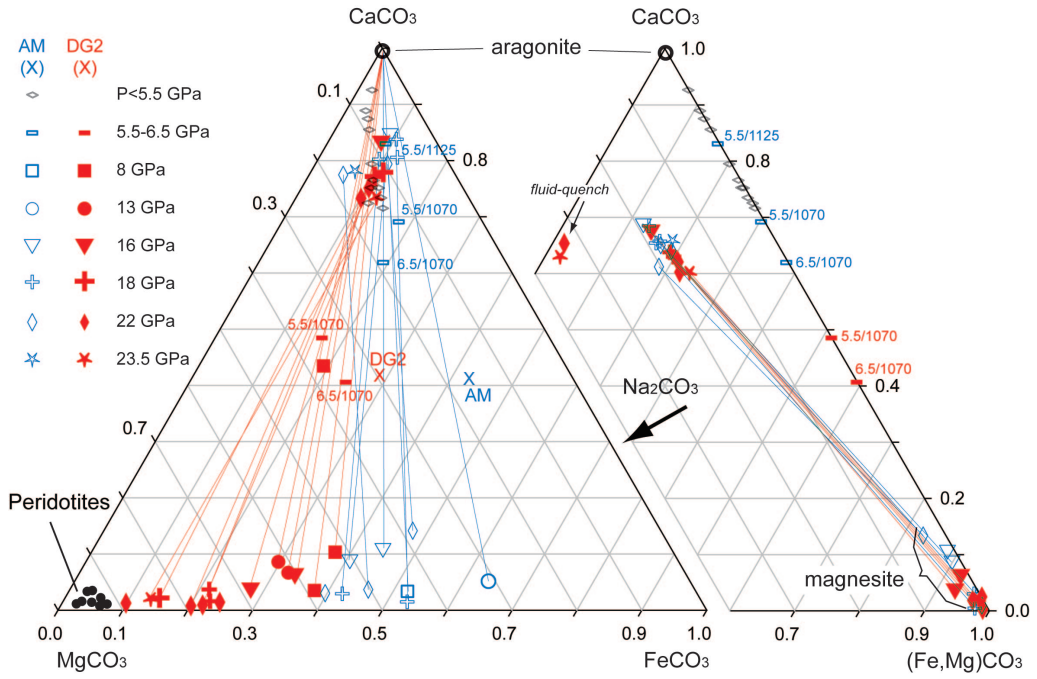

Figure 3.7: *Carbonate compositions in $CaCO_3$-$MgCO_3$-$FeCO_3$ and $CaCO_3$-Na_2CO_3-($MgCO_3$+$FeCO_3$) space. The Mg# of the magnesites increases with pressure whereas the Na-carbonates become CaO-poorer. Aragonites remain pure $CaCO_3$ in all experiments. Note the strong positive correlation between magnesite composition and the Mg# of the related bulk composition. Crosses denote bulk compositions.*

At this pressure the clinopyroxene bearing assemblage in equilibrium with carbonate melt (at 1350 °C) is replaced by a subsolidus assemblage with a Na-rich carbonate at 1250 °C. In the experiments with the anhydrous composition (DG2), clinopyroxene is always present at 16 GPa, the lowest temperature experiment having cpx and the Na-rich Ca-carbonate in the same capsule but in different zones and not in direct contact. These observations suggest that in the DG2 bulk, with its higher Na_2O content and slightly higher X^*_{Ca}, the reaction from jadeitic cpx to Na-rich carbonate takes place at slightly lower temperature/higher pressure than in the AM composition. In cpx, jadeite is the most abundant component and increases from Jd_{48} at 2.5 GPa to Jd_{72} at 3.5 GPa (Thomsen and Schmidt, 2008b) and to Jd_{90} at 13 GPa in the AM composition (fig. 3.6). At 16 GPa (AM) cpx coexisting with carbonate melt has Jd_{84}, similar to the cpx at 13 GPa. In the DG2 composition, jadeite increases from Jd_{65} at 5.5 GPa to Jd_{94} at 16 GPa (fig. 3.6). A large amount of the Ca-Tschermak component is observed only at 2.5 GPa (11 mol%), but then decreases considerably between 2.5 and 3.7 GPa and ultimately goes below the detection limit at 8 GPa. The Ca-eskolaite component does not show any particular trend with pressure, although slightly higher contents are observed at intermediate pressures (9 mol% at 3.7 GPa in AM and 4 mol% at 8 GPa in DG2). In both compositions, the amount of TiO_2 and K_2O in cpx decreases from 8 to 16 GPa (fig. 3.6). A maximum amount of K_2O (0.42 wt% in AM, 1.02 wt% in DG2) is reached at 8 GPa, 900 °C, similar to garnet which also has high K-contents at 8 GPa.

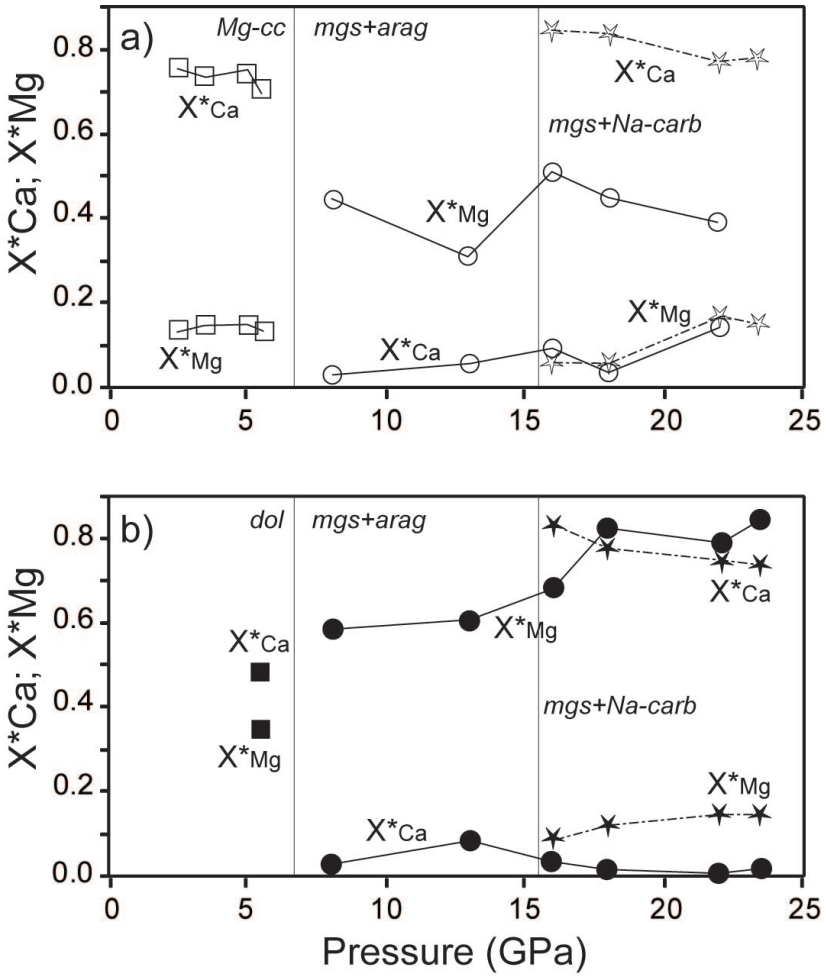

Figure 3.8: *X^*_{Ca} and X^*_{Mg} of rhomboedric carbonates crystallizing in the AM (a) and DG2 (b) bulk composition as function of pressure. Squares are for dolomite or Mg-calcite at P < 7 GPa, circles for magnesite at P ≥ 8 GPa and stars are for Na-carbonates at P ≥ 16 GPa.*

Carbonates stable in the different experiments are Mg-calcite in the AM composition (Thomsen and Schmidt, 2008b) and dolomite in the DG2 composition at P ≤ 6.5 GPa, magnesite+aragonite as long as cpx is stable in the subsolidus, and magnesite + Na-rich calcite at P ≥ 16 GPa. Mg-calcite contains up to 14 and 16 mol% siderite and magnesite at subsolidus conditions, and dolomite 17 and 35 mol% siderite and magnesite, respectively. Both are replaced by pure aragonite + magnesite, the latter with 10 mol% calcite and a Mg# of 57.9 at 8 GPa (DG2). At 16 GPa (ca. 1300 °C), Na-rich calcite (16-18 mol% Na_2CO_3, 60-68 mol% $CaCO_3$) replaces aragonite and coexists with magnesite, the latter with 4-6 mol% calcite and a Mg# 71.1 (DG2). Magnesite coexisting with Na-rich carbonate has a Mg# up to 15 points higher than when magnesite coexisting with aragonite (55.6 instead of 32.6 in the AM composition, and 71.1 instead of 57.9 in the DG2 composition) (figs. 3.7 and 3.8). In the DG2 composition at 22 and 23.5 GPa, and temperature ≤ 1400 °C a third, carbonate with ca. 20 wt% of Na_2O (33-34 mol% Na_2CO_3) but almost no Fe and Mg (< 1 mol%) has been identified (fig. 3.4D). Texturally, this carbonate forms intergranular

irregular shaped needles contrasting the rhombohedral habit of the Ca-carbonate with ca. 10 wt% Na_2O and magnesite. We interpret this additional Na-rich carbonate as quench product from the fluid, on the basis of these textures.

Phengite has been found only at P $\leq$ 8 GPa at subsolidus or near solidus conditions in the hydrous AM composition. As expected, a trend of increasing celadonite content or inverse Tschermak's substitution with pressure, from 3.1 Si pfu at 2.5 GPa to 3.68 Si pfu at 8 GPa is observed (chapter 2; Thomsen and Schmidt, 2008b).

K-hollandite contains a few wt% of Na_2O and CaO, mostly increasing with temperature and especially with pressure. In the DG2 composition (3.2 wt% bulk Na_2O) Na in K-hollandite increases steadily with pressure, while in the AM composition (2.4 wt% bulk Na_2O) Na in K-hollandite reaches a maximum at 16 GPa (0.06 Na pfu) and then remains constant with pressure. The different behaviour of sodium in the AM composition can be explained by the lower bulk Na_2O in combination with H_2O, part of the Na being more easily accommodated in a Na-rich fluid. Ca in K-hollandite increases in the DG2 composition from 0.03 to 0.08 Ca pfu at 13 to 22 GPa. In the AM composition, Ca in K-hollandite is constant at ca. 0.05 pfu. At 16 and 18 GPa, K-holl in the AM composition at the lowest temperatures shows a Si deficit up to 0.15-0.2 apfu, which may be attributed to the incorporation of small amounts of hydrogen due to the substitution of Si by Al + H on the octahedral site, as well known from stishovite (Panero et al., 2003; Panero and Stixrude, 2004; Litasov et al., 2007). The possible presence of hydrogen is also indicated by low totals (94 to 98 wt%) in some analysies.

HPK-phase: In the same hydrous AM composition but at 22 and 23.5 GPa, again at the lowest temperatures, K-hollandite was not observed but a new potassium phase (here dubbed HPK-phase) with higher Al_2O_3 contents, and K:Al:Si ratios of approximately 1:2:3 occurs. Average totals between 98-99 wt% possibly indicate the presence of some hydrogen, yielding an approximate formula of $KAl_2Si_3O_9(OH)$. Raman spectra of this phase are similar to those of K-hollandite with characteristic bands near 760 and 217 cm^{-1} (Liu and El Gorsey, 2007) suggesting some structural similarities between both potassium phases. Analyses, Raman spectra and BSE images are given in Appendix A.

Coesite is almost pure in composition, differing from *stishovite* which contains up to 2.3 wt% of Al_2O_3 and 0.77 of FeO_{tot} especially at high pressure.

Kyanite and *corundum* have FeO_{tot} contents of up to 3 wt%, SiO_2 up to 2 wt% and TiO_2 and MgO up to 0.5 wt%. These oxides describe above generally increasing with pressure and temperature.

CAS-Phase ($CaAl_4Si_2O_{11}$) (Gautron et al., 1997) is stable only at P $\geq$ 22 GPa at temperatures above the solidus (1400 °C), in agreement with Ishibashi et al. (2008) and with a simplified formation reaction 1 Ca-perovskite + 2 cor + 1 stish = 1 CAS. The CAS phase contains up to 1.4 wt% TiO_2 in the dry composition (DG2), and is an important host for alkalis, with up to 3.9 wt% K_2O and 0.7 wt% of Na_2O at the highest temperatures. The excess of SiO_2 and alkalis and the deficit of Al_2O_3 with respect to the ideal stoichiometry can be explained by a coupled substitution of the type $Al_{-3}Si_2$(Na,K) and $Ca_{-1}Al_{-1}Si$(Na,K), as already recognized by Hirose

and Fei (2002) and Zhai and Ito (2008) in K-free sodic systems.

Ca(Ti)-perovskite crystallizes at P $\geq$ 22 GPa at low temperatures, and at subsolidus conditions coexists with Ti-rich Fe-perovskite (DG2). At higher temperature, after the breakdown of the latter, Ca-perovskite contains up to 27 wt% of TiO_2 (DG2). Being Ti-rich, this Ca-perovskite is quenchable and does not transform to an amorphous substance as does near endmember Ca-perovskite (Leinenweber et al., 1995).

Fe(Ti)-perovskite is stable only at P $\geq$ 22 GPa at subsolidus conditions, and its amount increases with pressure and decreases with increasing temperature. In the hydrous composition, Fe-perovskite is almost pure in composition, with just 1.5 wt% Al_2O_3. In the anhydrous Ti-bearing system (DG2), Fe-perovskite contains up to 39 wt% TiO_2.

Oxides are Ti-oxides (rutile II, TiO_2 with α-PbO_2 structure; Simons and Dachille, 1967) at 8 and 13 GPa in the DG2 composition and an almost pure iron oxide with up to 3 wt% Al_2O_3 in the hydrous AM composition at P $\geq$ 22 GPa.

3.3.3 Melting behavior

The position and shape of the solidus from 2 to 24 GPa (fig. 3.1) depends mostly on the stability and composition of the hydrous and carbonate phases, on the presence of a fluid, and on the (in-)compatibility of alkalis with the various alkali-rich subsolidus phases such as phengite, kfsp, K-hollandite, clinopyroxene and carbonates. In the hydrous AM composition, melting is fluid-absent to 9 GPa, i.e. as long as phengite is stable (fig. 3.1). At higher pressures, the absence of any hydrous phase suggests the presence of a fluid phase; the apparent solidus is then established by the appearance of the first quenched carbonate melts. In the nominally anhydrous composition DG2, the presence of a liquid at temperatures lower than carbonate melt formation is indicated by mass balance calculations and textures at P $>$ 16 GPa, i.e. after the breakdown of cpx (16 GPa/1300 °C). Above this pressure, the apparent solidus is again defined by the appearance of the first quenched carbonate melts. We cannot discriminate between (quenched) carbonate melts in continuum with liquids at lower temperatures, and the existence of a true carbonate solidus involving two immiscible liquids.

At pressures from 2.5 to 3.5 GPa the melting out of coesite and phengite at 920 to 1000 °C is responsible for the generation of 30-35 wt% silicate melt coexisting with Mg-calcite in the H_2O-bearing AM composition (Thomsen and Schmidt, 2008b). From 3.5 to 5 GPa, a silicate melt coexists with a carbonate melt over a limited temperature interval around 1100 °C (figs. 3.1 and 3.9). At 5 GPa, the melting reaction produces a silicate and a carbonate melt through the reaction:

$$0.9\ pheng + 0.3\ coe + 0.1\ cpx + 0.3cc = 1sil.\ melt + 0.4\ carb.\ melt + 0.2\ grt + 0.1\ ky \quad (3.1)$$

For the dry composition, there are no experiments available at P $<$ 5.5 GPa, but recently Tsuno and Dasgupta (2010) showed that the solidus of a dry carbonated eclogitic pelite at 2.5-3 GPa lay at

ca. 950 °C. The first melt is a K-rich granitic melt which forms at ca. 200 °C below the solidus of a dry CO_2-free pelite (Spandler et al., 2010), and coexists with crystalline carbonates up to 100 °C above the solidus. In contrast with the melting relations at lower pressure, at 5.5 GPa the first melts are carbonate melts. The first small amounts of these carbonate melts just above the solidus appear concomitantly with the destabilization of phengite and the formation of kfsp. The formation of a carbonate melt and the progressive dilution of potassium into this melt, destabilizing phengite and then kfsp, leads to the disappearance of the classical melting reaction of the type phengite/kfsp + quartz/coesite = silicate melt + kyanite/garnet. At 5.5 GPa and 1180 °C, ca. 100 °C above the solidus, the carbonate melts are highly potassic with just minor amounts of Al_2O_3 (3 w%) and SiO_2 (4 wt%).

In the simple K_2O-Al_2O_3-SiO_2-system, kfsp is stable up to ca. 6 GPa, where it reacts to form wadeite ($K_2Si_4O_9$) (Yong et al., 2006), kyanite and coesite. Wadeite is then stable to ca. 9-10 GPa and is replaced by K-hollandite at higher pressures. In natural or more complex systems like our simplified pelitic system, wadeite has never been observed. Our experiments have shown kfsp being stable to 8 GPa, probably stabilized with respect to wadeite by Na and Fe3+. Notably, in the pressure range of 6-9 GPa, where wadeite would be stable in the simple system, the solidus is anomalously low compared to lower and higher pressures. Reaction 3.2 illustrates the melting behaviour at 8 GPa for the hydrous composition AM:

0.5 mgs + 0.4 arag + 2.1 pheng + 0.1 cpx = 1 carb. melt + 0.9 grt + 0.5 ky + 0.7 coe (3.2)

At around 9 GPa phengite reacts to form K-hollandite which is then responsible for the increased compatibility of potassium with pressure and the subsequent shift of the solidus towards higher temperatures in both compositions. With increasing pressure cpx begins to play a major role in the melting reaction, resulting in carbonate melts with a higher sodium content and lower K/Na ratio. At 13 GPa the melting reaction is

0.4 mgs + 0.6 arag + 0.7 K-holl + 0.4 cpx = 1 carb. melt + 0.6 grt + 0.1 cor + 0.4 stish (3.3)

Just before 16 GPa, a strong decrease of the solidus in the dry composition DG2 occurs concomitantly with the breakdown of cpx (16 GPa, 1300 °C) and the crystallization of a Na-rich Ca-carbonate, the latter coexisting with a Na- and CO_2-rich fluid. This transition from a fluid-absent to a fluid-saturated situation would explain the decrease in the solidus temperature of 50 °C near 16 GPa. At pressures beyond the stability of cpx, both compositions show the first appearance of carbonate melt at almost the same temperature, which then again increases with further increasing pressure. At $P > 16$ GPa, the melting reaction is dominated by the Na-carbonate and in minor amounts by K-hollandite, resulting in carbonate melts with low K_2O/Na_2O ratios, which further decreases with increasing pressure.
At 22 GPa the melting reaction 3.4 also involves the crystallization of the CAS phase:

1.2 Na-carb + 0.7 K-holl + 0.8 grt + 0.1 stish + 0.7 cor = 1 carb. melt + 2.1 CAS + 0.3 mgs (3.4)

For the melting reaction at 22 GPa, the involvement of perovskite cannot be constrained by mass balance due to its small amount at near-solidus conditions. With increasing temperature, the observed perovskites are replaced by garnet and the CAS-phase.

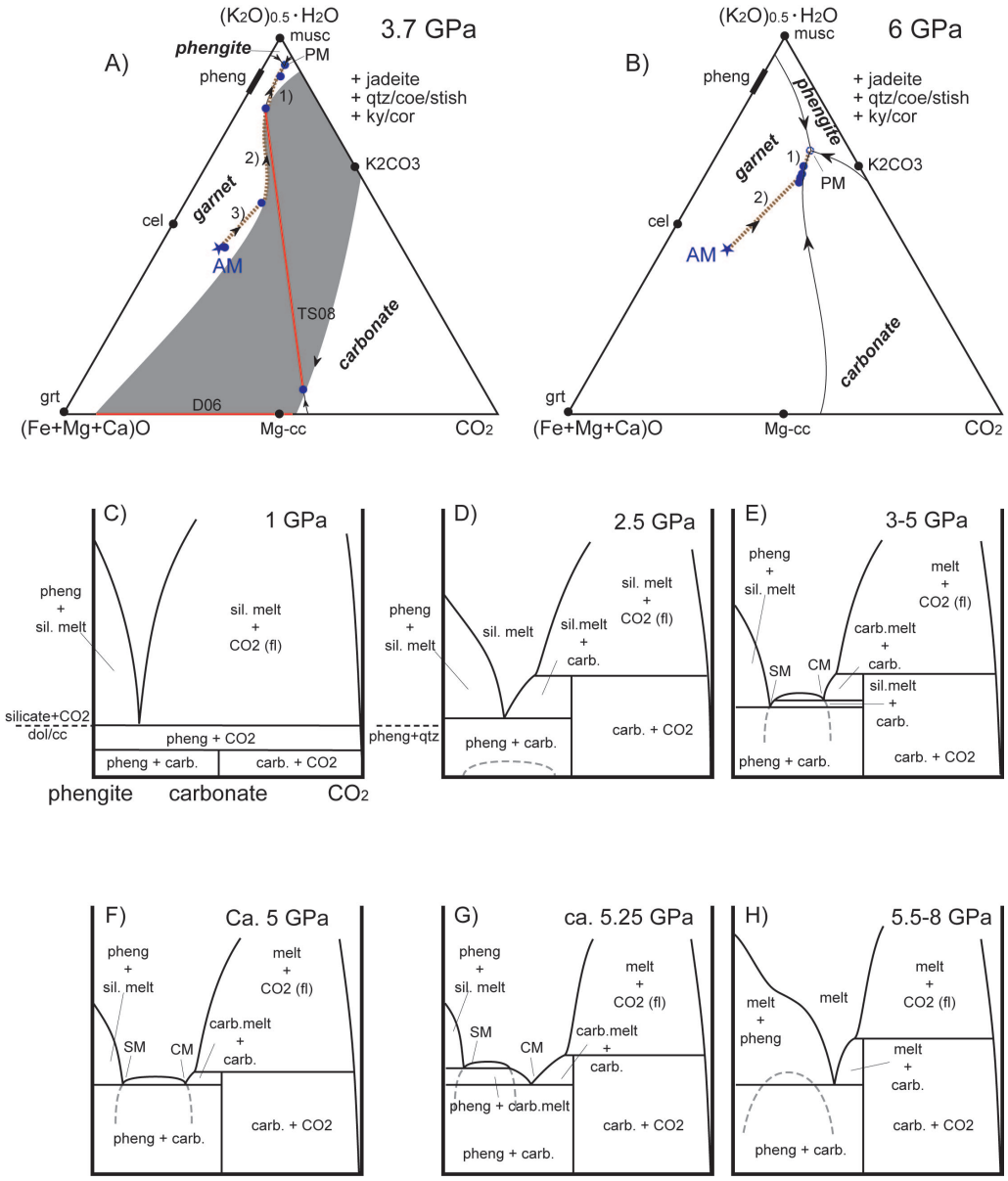

Figure 3.9:

Figure 3.9: *Principal melting topology of silicate-carbonate-CO_2 systems in projection from coesite, kyanite and jadeite into CO_2 - $(K_2O)_{0.5} \cdot H_2O$ - (Fe,Mg,Ca)O at (a) 3.7 and (b) 6 GPa with analyzed melt compositions, melt surface, peri- or cotectic points and curves. This projection would be thermodynamically valid if $(K_2O)_{0.5}$+H_2O would be a system component and if Ca+Mg+Fe^{2+} would mix ideally. Bold italic labels designate liquidus surface phases. Thick dashed brown lines represent melting paths with increasing temperature. The peritectic minimum (PM) moves from the $(K_2O)_{0.5} \cdot H_2O$ corner towards more M^{2+} + CO_2-rich compositions after the crossing of the carbonate melting reaction with the fluid-absent silicate solidus between 5 and 5.5 GPa. (a) At 3.7 GPa melt develop from the peritectic point (PM) along the garnet-carbonate cotectic until this cotectic intersects the carbonate-silicate melt immiscibility gap (grey area: immiscibility gap along the (Fe+Mg+Ca)O-CO_2 line is after Dasgupta et al. 2006 (D06)). At this pressure, carbonate melts in a monotectic yielding a carbonate liquid. The two melt compositions then evolve along the limits of this solvus (2) until in our bulk the carbonate melt is exhausted and melts proceed on the garnet liquidus surface. (b) At 6 GPa the peritectic (PM), exhausting phengite and leading to a carbonate melt which evolves along the garnet-carbonate cotectic (1) until carbonate is exhausted. At this pressure no liquid immiscibility has been observed. (c) - (h): Visualization of melting relations in pseudobinaries along phengite-CO_2 in the same system additionally projected from garnet (+cpx+ky+qz/coe). This series of pseudobinaries illustrates the main features of melting and decarbonization in sedimentary systems: (c) breakdown of carbonates before reaching the silicate solidus; (d) silicate melting leaving residual carbonate; (e) the intersection of the immiscibility gap with the silicate solidus producing a carbonate to carbonate melt monotectic and coexisting silicate (SM) and carbonate (CM) melt; (f) the precise pressure at which the silicate and carbonate melting reactions occur at the same temperature; (g) carbonate melting at the solidus and a very limited coexistence of carbonate melt with silicate melts; and (h) liquid immiscibility becomes again metastable and a continuum from carbonate melts to silicate melts forms. The stippled line indicates metastable parts of the immiscibility gap.*

3.3.4 The melting diagram of carbonated sedimentary systems

The principal melting topology of silicate-carbonate-CO_2 systems in projection from coesite, kyanite and jadeite is illustrated in figure 3.9a,b for 3.7 and 6 GPa. In an effort to simplify this projection, we have reduced (Ca,Mg,Fe^{2+})O to one component, resulting in the three component system CO_2 - $(K_2O)_{0.5} \cdot H_2O$ - (Fe,Mg,Ca)O. This projection would be thermodynamically valid if $(K_2O)_{0.5}$+H_2O were a system component (i.e. if the K/H ratio were the same in all phases, in this case mica and melt) and if Ca+Mg+Fe^{2+} mixed ideally. In addition, we plotted melt compositions at 3.7 GPa from Thomsen and Schmidt (2008b), from this study at 6 GPa, and from Dasgupta et al. (2006) at 3 GPa for the K-free MORB+CO_2 system, which forms the (Mg+Fe+Ca)O-CO_2 baseline of the ternaries.

At 3.7 GPa, a peritectic minimum (PM) occurs near the $(K_2O)0.5 \cdot H_2O$ corner, and melting takes place through a reaction pheng + coe + cc + cpx = silicate melt + grt + ky (Thomsen and Schmidt, 2008b). This minimum moves towards more M^{2+} + CO_2-rich compositions with pressure, and at 6 GPa melting occurs through the reaction pheng + cc + cpx = carbonate melt + ky + coe $\pm$ grt. From this peritectic point, melts evolve along a garnet-carbonate cotectic ((1) in fig.

3.9a,b), which from plotting the effectively measured melt compositions and from mass balance appears to be congruent in the projections of figure 3.9(a,b), yielding a melting reaction cc + grt (+ cpx) = melt (+ coe + ky).

The complexity of this system then lies in the fact that at low pressure (e.g. 2.5 GPa), only silicate melt occurs with some carbonate component dissolved, while at 8 GPa only carbonate melt occurs, and this melt gradually dissolves silicate components, reaching 5.5 wt% SiO_2 at 400 °C above the solidus temperature (fig. 3.1). At intermediate pressures (i.e., 3-5 GPa), coexisting immiscible silicate and carbonate melt (TS08) is observed (Thomsen and Schmidt, 2008b). Thus, at 3.7 GPa, the garnet-carbonate cotectic intersects the silicate-carbonate miscibility gap, and carbonates melt in a monotectic, yielding a carbonate liquid. The two melt compositions then evolve along the limits of this solvus ((2) in fig. 3.9a) until in this particular bulk composition the carbonate melt is exhausted, and melts proceed on the garnet liquidus surface ((3) in fig. 3.9a). At 6 GPa (fig. 3.9b), the first liquid near the solidus is a carbonate melt forming through the peritectic melting reaction (2), which may produce a minor amount of garnet. Again phengite is consumed first at the peritectic (PM). With increasing pressure, the next phase to be consumed is Mg-calcite along the cotectic line (1) in figure 3.9a,b as described above. When Mg-calcite melts out, the liquids leave the garnet-carbonate cotectic and evolve towards garnet on the liquidus surface. At 6 GPa, no liquid immiscibility has been observed.

The development from silicate to carbonate melt melting at the solidus can best be understood in the visualization of melting relations in figure 3.9c-h. In this series of pseudobinary sections along phengite-CO_2 (figs. 3.9a,b), projected from garnet in addition to jadeite, kyanite and coesite/quartz, leaving phengite on the left hand side of these pseudo binaries. Although these diagrams includes severe simplifications, they illustrate well the decarbonation and melting relations of carbonated pelites, which produce silicate melts coexisting with carbonates at low pressure, two melts at intermediate pressure, and carbonate melts at high pressure. The sequence of diagrams illustrates: (fig. 3.9c) the breakdown of carbonates before reaching the silicate solidus at the lowest pressure; (fig.. 3.9d) silicate melting in the presence of carbonates and a hypothetical occurrence of a metastable immiscibility gap between silicate and carbonate melts; (fig. 3.9e) the intersection of the immiscibility gap with the silicate solidus, resulting in a carbonate to carbonate melt monotectic in addition to the silicate eutectic; (fig. 3.9f) the pressure at which the eutectic and (former) monotectic occur at the same temperature. This pressure corresponds to the intersection of the silicate and carbonate melting reactions in P-T space, as occurring in the AM composition at just above 5 GPa. At higher pressures (fig. 3.9g), melting at the solidus now produces carbonate melt coexisting with silicate melt over a narrow temperature range, and (fig. 3.9h) the disappearance of stable liquid immiscibility and a continuum from carbonate to silicate melts.

The available experimental information indicates a broad, suddenly closing immiscibility gap, a narrow pressure and temperature range where carbonate melt forms first and then coexists with silicate melt, and the necessity of a large temperature increase in order to dissolve silicate components in the carbonate melt at higher pressure. In K_2O+H_2O-free systems, garnet would replace phengite at the left hand side of the pseudobinaries, and silicate melting temperatures would lie

at values above carbonate melting temperatures. In this case, topology (fig. 3.9d) would have a eutectic close to the carbonate composition and would directly continue to topology (fig. 3.9g) or (fig. 3.9h) with or without carbonate-silicate melt immiscibility. Note that at present it is unknown whether carbonate melts would have excess CO_2 with respect to the1:1 (CaO+MgO+FeO):CO_2 ratio in carbonates.

3.3.5 Melt compositions

The first melts generated at the solidus at P $\leq$ 5 GPa are silicate melts with a peraluminous potassic granite composition at 2.5 GPa, changing to slightly peralkaline phonolite melts at 3.7-5 GPa (Thomsen and Schmidt, 2008b). Between 5 and 5.5 GPa the carbonate melting reaction crosses the fluid-absent silicate solidus. At pressures above this threshold, the first melts produced are magnesio- (DG2) to ferro-dolomitic (AM) carbonate melts containing large amounts of alkalis (figs. 3.10 and 3.11).

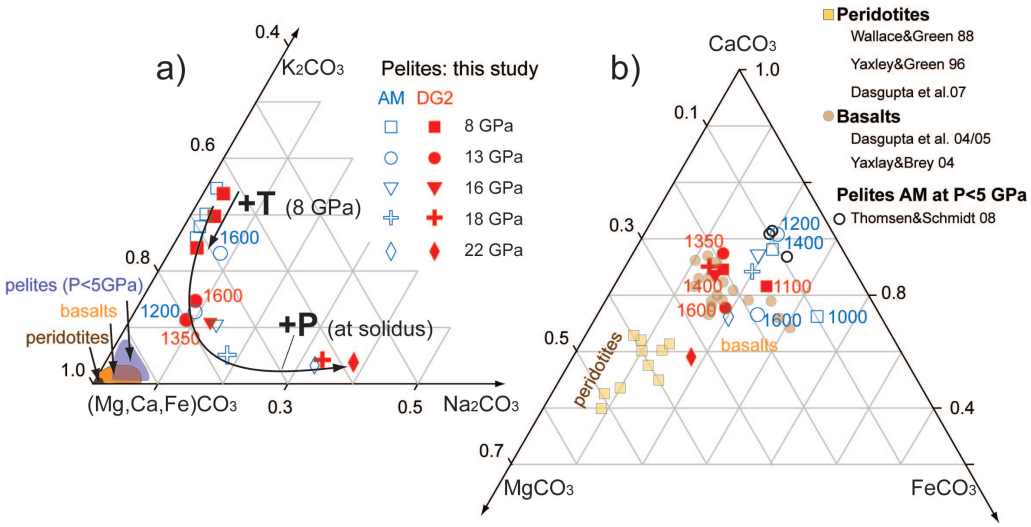

Figure 3.10: *(a) Composition of carbonate melts projected into Na_2CO_3-K_2CO_3- $(Mg,Ca,Fe)CO_3$ space. As to be expected, carbonate melts formed from pelites have higher amounts of K_2O and Na_2O than those from carbonated basalts and peridotites. From 8 to 22 GPa the potassium content decreases while the sodium content increases. (b) Compositions of carbonate melts projected into $FeCO_3$-$CaCO_3$-$MgCO_3$ space. Projected from alkalis, carbonate melts from pelites plot in the same area as carbonate melts from carbonated basalts, which have similar bulk X^*_{Ca} and X^*_{Mg}. From 16 to 22 GPa an increase of $MgCO_3$- and a decrease of $CaCO_3$-component is observed.*

At 5.5 to 13 GPa, the first melts are potassium-rich carbonate melts with a maximum K_2O-content and K/Na-ratio at the phengite or kfsp to K-hollandite reaction at 8 GPa. At 6.5 GPa, 1070 °C, the first carbonate melts in the AM composition coexists with small amounts of kfsp and Mg-cc, whereas in the DG2 composition no kfsp has been observed coexisting with the first melts. As the AM composition contains 1.1 wt% H_2O, which should destabilize kfsp with respect to the dry DG2 composition, the reason for the absence of kfsp in DG2 is most likely due to its lower

bulk K_2O-content. With further increase in pressure, melts remain carbonatitic, but gradually change from potassium-rich at 8 GPa to sodium-rich at 22 GPa (tabs. 3.1 and 3.2) due to an increasing compatibility of potassium in K-hollandite with pressure and a continuous decreasing of $D_{Na}^{cpx/carb.\,melt}$ from 8 to 16 GPa.

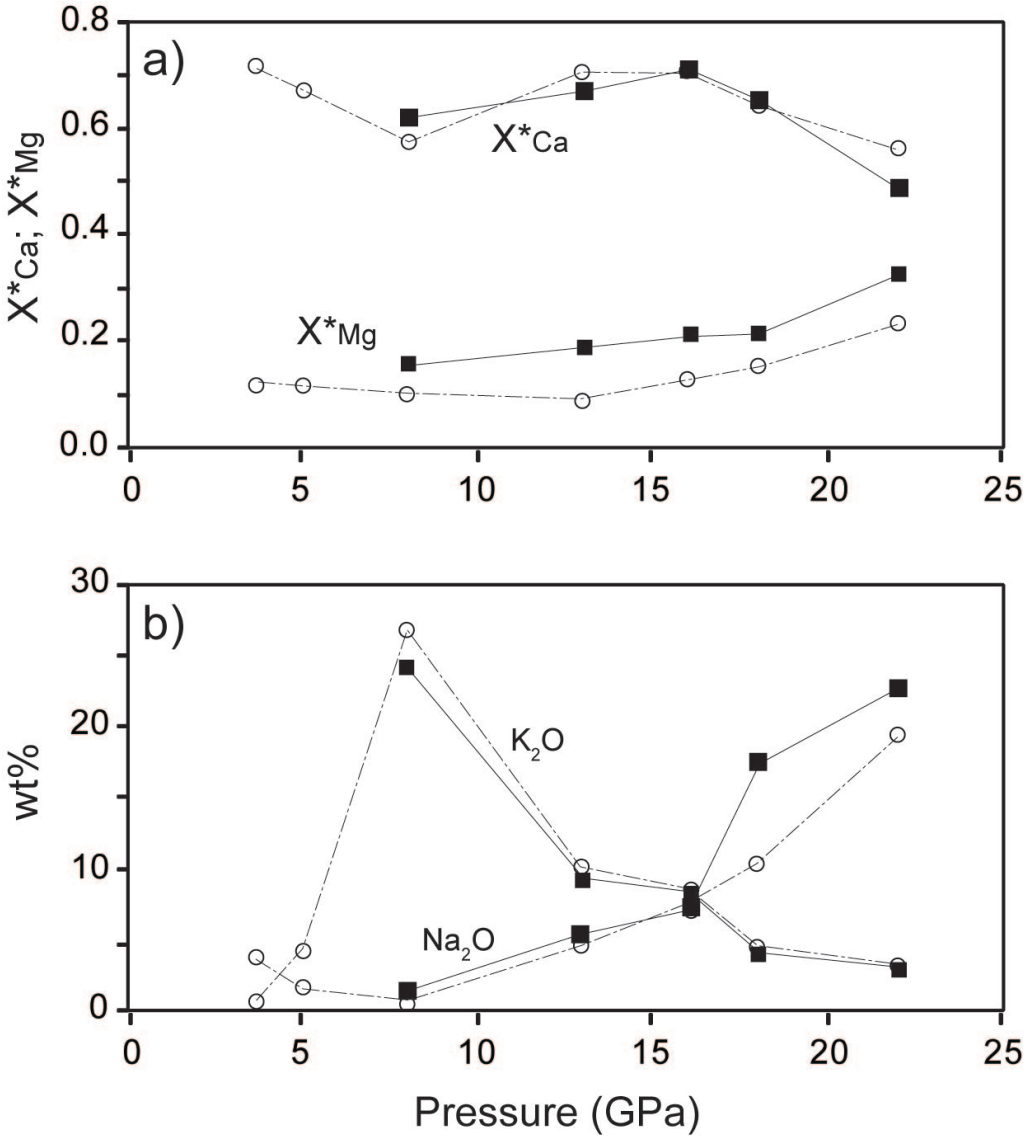

Figure 3.11: *(a) X^*_{Ca} and X^*_{Mg} as function of pressure for the pelite derived carbonate melts. (b) Melt K_2O and Na_2O contents in wt% as function of pressure. At 8 GPa carbonate melts are highly potassic but become more enriched in Na_2O with increasing pressure, in particular after the breakdown of cpx (16 GPa/1300 °C). The decrease in melt K_2O with pressure is related to the increasing stability of K-hollandite. Open circles: 1.1 wt% H_2O AM composition; filled squares: dry DG2.*

The K_2O/Na_2O wt-ratio (fig. 3.12) decreases from 41 at 8 GPa to 0.14 at 22 GPa, the K/Na-ratio in the AM composition being always slightly higher than in DG2 due to its higher bulk K_2O and lower Na_2O concentrations. At cpx-out at 16 GPa/1300 °C, melts have a K_2O/Na_2O ratio

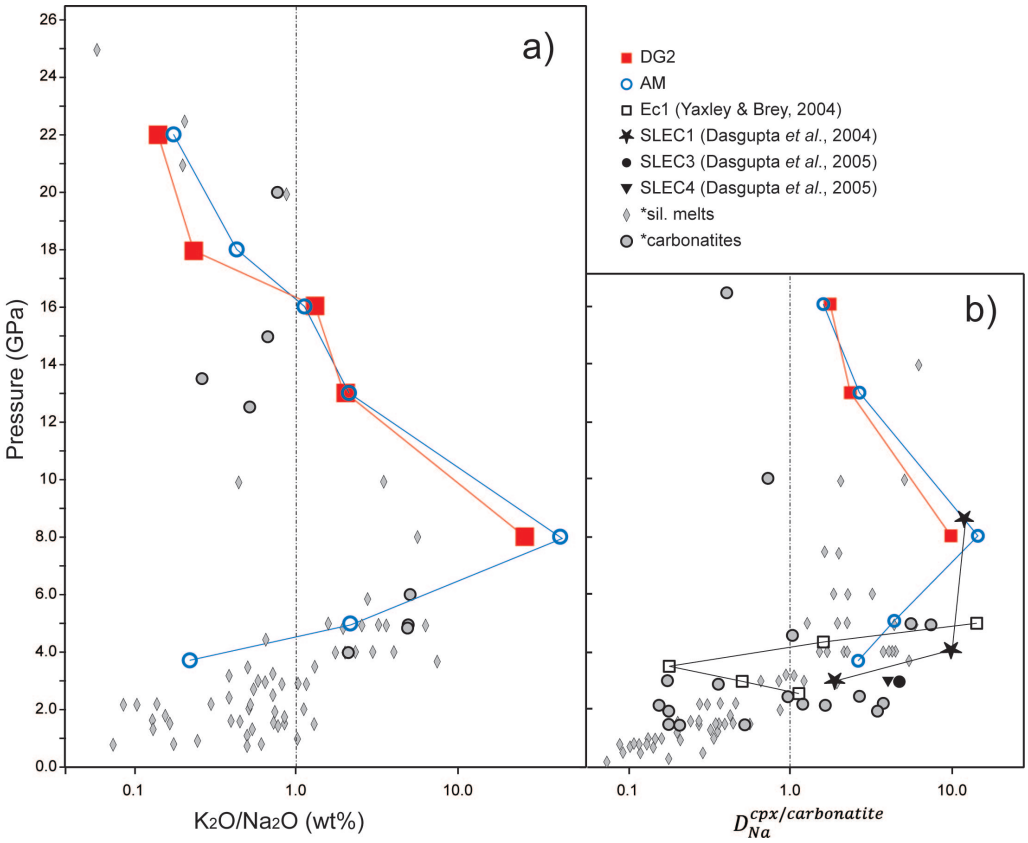

Figure 3.12: *(a) K_2O/Na_2O wt ratios vs. pressure in carbonate melts illustrating a pressure window for ultrapotassic melts and metasomatism between 5 and 15 GPa with a K_2O/Na_2O maximum near the phengite/kfsp breakdown at 9 GPa. This pressure interval correlates well with the highest sodium partitioning coefficient between cpx and melt illustrated in (b). The breakdown of jadeitic cpx at 16 GPa leads to sodic dolomite-carbonate melts at higher pressure. (b) $D_{Na}^{cpx/carb.\,melt}$ vs. pressure illustrating the increase in compatibility of Na in cpx with increasing pressure up to a cpx/carbonate melt partition coefficient of 18 at 8 GPa, followed by a decrease down to values of ca. 2-2.5 at 13 and 1.7 at 16 GPa when approaching the cpx pressure stability. Note that in some of the reported studies, the compositions of the carbonate melts were not in the focus and that Na_2O-concentrations in tiny melt pools are not reliably measurable, thus several of the plotted partition coefficients are likely to represent underestimations. Plotted silicate melt alkali ratios and cpx/silicate melt partition coefficients after data from Schmidt et al. (2004); Yasuda et al. (1994); Irifune et al. (1994); Wang and Takahashi (1999); Kessel et al. (2005); Blundy et al. (1995); Singh and Johannes (1996); Rapp and Watson (1995); Spandler et al. (2010) and Hermann and Spandler (2008); values for carbonate melt alkali ratios and cpx/carbonate melt partition coefficients after data from Wallace and Green (1988); Thibault et al. (1992); Dalton and Wood (1993); Dasgupta and Hirschmann (2006); Dasgupta et al. (2005); Dasgupta et al. (2004); Yaxley and Brey (2004); Ghosh et al. (2009); Litasov and Ohtani (2009); Ryabchikov et al. (1989); Brenan and Watson (1991); Sweeney et al. (1995) and Blundy and Dalton (2000).*

of ca. 1, defining the upper pressure limit for potassic melts and metasomatism (fig. 3.12). In both compositions X^*_{Ca} in the carbonate melt increases with pressure from 0.57-0.62 at 8 GPa to

values of 0.71 at 16 GPa. With further pressure increase, X^*_{Ca} in the carbonate melts decreases to values of 0.49-0.56 at 22 GPa. X^*_{Mg} in the AM composition shows a constant increase with pressure from 0.1 at 8 GPa to 0.23 at 22 GPa. In the DG2 composition, X^*_{Mg} is 0.16 at 8 GPa and 0.33 at 22 GPa (fig. 3.11a)

3.4 Discussion

3.4.1 Phengite and cpx breakdown and their effect on fluid presence and composition

After the breakdown of phengite in the 1.1 wt% H_2O AM composition at P $>$ 8 GPa, no hydrous phases could be detected. Phengite is replaced by K-hollandite, which coexists with garnet, cpx, stishovite, kyanite/corundum, magnesite and aragonite. The absence of any hydrous phase suggests the presence of a water-bearing, probably supercritical liquid (Kessel et al., 2005) in the AM bulk at $>$ 8 GPa. Nevertheless, a (two) carbonate to carbonate melt solidus is clearly defined by the observed textural and compositional changes.

At 16 GPa, after the breakdown of clinopyroxene at ca. 1300 °C, Na is redistributed among the Na-rich Ca-carbonate and, in minor amounts, garnet and K-hollandite. Nevertheless, for both bulk compositions, mass balance calculations for the cpx-free assemblages indicate that 30-50 wt% of the bulk Na_2O is not accounted for by the solids in all subsolidus experiments. Element distribution maps (fig. 3.4C) illustrate the presence of small Na-rich pockets ($<$ 2 μm) or thin interstitial films in both compositions. From these observations the presence of a sodium-rich CO_2 (and H_2O in AM) bearing liquid at P $>$ 16 GPa is deduced. Further indirect support for the formation of a fluid and a transition from fluid-absent to fluid-present conditions with the breakdown of cpx (16 GPa, 1300 °C) is the lowering of the solidus temperature by $\geq$ 50 °C in the DG2 bulk, but not in AM (fig. 3.1), which is already fluid-present above 8 GPa. Consequently and unexpectedly, both bulk compositions have the same solidus temperature at $>$ 16 GPa.

The transition from a cpx-bearing to a cpx-free assemblage is a continuum reaction that occurs in a basaltic composition at 15-17 GPa, at temperatures between 1400-1800 °C (Irifune et al., 1986; Yasuda et al., 1994; Ono and Yasuda, 1996; Okamoto and Maruyama, 2004). In more silica- and alumina-rich compositions (pelites or average continental crust), the transition interval is much wider, and jadeitic cpx can be stable to 24 GPa (Wu et al., 2009). Rapp et al. (2008), employing SiO_2+Al_2O_3 saturated bulk compositions with variable Na_2O content, did not find any cpx at 16 GPa, most likely because of the low CaO content (low X^*_{Ca}), the low amount of Na_2O (1.22 wt%) in the bulk with the lowest H_2O (0.99 wt%), or because of the large quantity of fluid (7.99 wt% H_2O and 2.15 wt% CO_2) in the bulk with a higher Na_2O (4.22 wt%) content. Wu et al. (2009) and Irifune et al. (1994) employed sodium-rich (4.7 and 3.9 wt% Na_2O, respectively) and H_2O poor (1-2 wt%) compositions with similar CaO content and X^*_{Ca} as in the bulk compositions of this study and found jadeitic cpx stable to 20-24 GPa. In our experiments, we located this transition near 16 GPa, the H_2O-free and more sodium-rich DG2 composition showing a slightly larger cpx-

stability field. From these considerations, we suggest that the pressure stability of clinopyroxene depends on three major bulk compositional variables: (i) the total Na_2O content of the bulk, with higher Na extending the jadeite stability field; (ii) the presence of a fluid dissolving significant amounts of sodium and thus destabilizing jadeitic cpx; and (iii), alumina saturation, which has an indirect effect on the cpx stability, by maintaining the majorite component in garnet at a minimum value and the Al-content in garnet at a maximum. This leads to a lower Na-solubility in our garnets (below 1.5 wt% at $P > 16$ GPa) compared to garnets from mid ocean ridge basalt compositions at similar conditions, (ca. 3 wt%, Okamoto and Maruyama, 2004). Thus, alumina saturation tends to stabilize jadeitic cpx and fluid-free Na-rich alumina-saturated bulk composition will have cpx stable at the highest pressures ($\geq$ 20 GPa, Irifune et al., 1994; Wu et al., 2009). Fluid- and CO_2-rich alumina-undersaturated systems will allow for partitioning of Na_2O into carbonates, fluid, and garnet; potentially leading to the lowest pressure stability of jadeitic clinopyroxene.

3.4.2 The redistribution of alkalis in subducted carbonated pelites

At high pressures, the two major alkalis Na and K are normally incorporated in different minerals and show different compatibilities as a function of pressure and temperature. The main minerals which incorporate sodium are (jadeitic) cpx at < 16 GPa and Na-rich carbonates at higher pressure. For potassium, the principal phases are phengite in hydrous compositions at < 9 GPa, kfsp at $P < 9$ GPa for dry compositions, and K-hollandite for both at higher pressures. K-hollandite may also contain some Na, its concentrations increasing with pressure and temperature. In contrast, clinopyroxene contains maximum 1 wt% K_2O, the highest concentrations being observed at 8 GPa at the lowest temperature (1.03 wt% at 900 °C for DG2), near the upper pressure stability of phengite/ kfsp. A similar behaviour is observed for garnet, which at 6.5 and 8 GPa and temperatures just above the solidus has K_2O content of up to 0.6 wt%. However, the highest potassium contents in garnet are observed at 22 GPa at subsolidus condition. At this pressure garnet, has a surprising 1.15 wt% K_2O; almost the same concentration as for sodium, yielding a total of 2.3 wt% alkalis. At 22 GPa, the CAS phase also accommodates considerable amounts of alkalis, up to 3.9 wt% K_2O and 0.7 wt% of Na_2O at the highest experimental temperature (22 GPa, 1550°C). Considering that all these phases are stable together with K-hollandite at temperatures above the solidus, an significant amount of alkalis could possibly survive the decarbonation process, e.g. during slab stagnation at the 660-km discontinuity.

Naturally occurring potassium phases at high pressures include kfsp, phengite and phlogopite, potassium richterite, phase X, and K-hollandite (for review, see Harlow and Davies, 2004). Nevertheless, potassium may be contained in minor amounts in minerals which are nominally not potassic, e.g. cpx with up to 2 wt% K_2O at 7-13 GPa (Tsuruta and Takahashi, 1998; Wang and Takahashi, 1999) and Ca-perovskite with up to 5 wt% K_2O above 20 GPa (Irifune et al., 1994; Wu et al., 2009; Okamoto and Maruyama, 2004). The major Na-rich minerals in peridotitic and basaltic compositions at high pressure are cpx to 17 GPa (Gasparik, 1996) and majoritic garnet at higher pressure, which may accommodate up to 3.0 wt% Na_2O in natural systems (Wang and Takahashi, 1999; Okamoto and Maruyama, 2004; Ghosh et al., 2009) and up to 0.9 Na pfu

(ca. 6-7 wt%) in simplified NMAS-systems at 20 GPa (Gasparik, 1996; Gasparik, 2000). Other alumina-rich phases which substitute for garnet at lower mantle depths, include the CAS-, NAL- and CF-phases, which may also accommodate large quantities of potassium and sodium. This large spectrum of alternative hosts for alkalis to be incorporated at pressures of the 660 km discontinuity suggests that a large percentage of the alkalis reaching the base of the transition zone can effectively be recycled into the lower mantle. In addition, our experiments suggest, that if melting occurs at depths near the 660-km discontinuity, the residue will acquire an increased K/Na-ratio.

3.4.3 The fate of and mass transfer from subducted carbonated pelites

In P-T space, the solidi of the investigated carbonated pelites (DG2 and AM) are mostly subparallel to typical subduction P-T-paths (fig. 3.13, Kincaid and Sacks, 1997; van Keken et al., 2002; Peacock, 2003). Nevertheless, in two particular depth ranges carbonated pelites will possibly melt forming alkali-rich carbonate melts. The first pressure range, where decarbonation through melting is plausible in warm subduction zones, is between 6 and 9 GPa. In this pressure range, carbonated pelites have a solidus with a negative Clapeyron slope strongly oblique to warm subduction P-T paths, the solidus temperatures decreasing by more than 100 °C. This is particularly true for phengite-bearing carbonated sediments which are expected during prograde metamorphism of carbonated pelites or psamnites. The fact that the pressure interval of 6 to 9 GPa terminates with the breakdown of two major hydrous phases, phengite and lawsonite (Ono, 1998; Schmidt and Poli, 1998; Okamoto and Maruyama, 2004), and that at 8-9 GPa their devolatilisation produces a water rich liquid, suggests that the solidus of the AM composition (1.1 wt% H_2O) best describes melting at these conditions. Flush melting (Schmidt and Poli, 1998) mediated by a fluid phase produced from lawsonite breakdown and rising through the sediment pile at the top of the slab column could induce carbonate melting at more moderate temperatures than indicated by our fluid-absent solidus at 8-9 GPa. The melts produced at this depth are carbonate melts with extreme K/Na ratios, as discussed in chapter 2.

The second melting interval takes place at 20-22 GPa, when the subducting slab reaches the 660-km discontinuity, where it is often deflected (Fukao et al., 2009 and references within). This melting interval is more probable in cold slabs where the carbonated sediments could have survived the first melting interval between 6 and 9 GPa. If such slabs remain at constant depth long enough to relax towards adiabatic temperatures, melting would occur in carbonated pelites. The carbonate melts forming at this pressure are sodium-rich and have K_2O/Na_2O wt-ratios ≤ 0.5. Gasparik and Litvin (2002) showed that between 20 and 24 GPa, an alkali-rich carbonate melt may coexist with typical mantle assemblages even at 100 °C below the mantle adiabat. Based on their experiments and on evidence from inclusions in diamonds (Wang and Sueno, 1996; Wang and Gasparik, 2000), they suggested a sodium-rich metasomatism by carbonate melts at the base of the transition zone, a scenario for which our study identifies the most likely source.

The two melting scenarios at 6-9 and 20-22 GPa, as discussed above, the observation of a mobile Na-rich CO_2-liquid phase forming at the cpx breakdown near 16 GPa, 1300 °C, and the fact that our solidi occur at the lowest temperature of any carbonated natural material, render subducted

carbonated pelites the prime candidates for supplying metasomatic agents at depth beyond the sub-arc regime. In addition, phengite breakdown, also occurring in CO_2-free lithologies at the same pressure of 8 GPa, provides an additional source of liquid production.

The pressure interval from an eclogite cpx-grt-stish-assemblage at $\leq$ 16 GPa first to a cpx- and then garnet-free perovskite-bearing assemblage defines the behaviour of the subducted sedimentary material when it reaches the 660-km discontinuity. In a pyrolitic system, this transition takes place at lower pressures than in a basaltic composition (24-25 and 25-27 GPa, respectively, Irifune and Ringwood, 1993; Litasov and Ohtani, 2005). Our experiments show that this transition in a carbonated pelitic system occurs at even lower pressures for the same temperatures (ca. 1400 °C). The loss of carbonates through melting at moderate temperatures upon slab deflection at the 660-km discontinuity, combined with the transition to a Ca- and Fe-perovskite-bearing assemblage at lower pressures than in the peridotitic mantle will remove any density barrier for sediments (Irifune and Ringwood, 1993; Irifune et al., 1994; Wu et al., 2009), and promote the subduction of sediments into the lower mantle.

3.4.4 A possible manifestation of transition zone carbonated sediment melting

Below eastern Asia, the subducted pacific slab travels westwards within the mantle transition zone just above the 660-km discontinuity (Fukao et al., 2001; Zhao et al., 2004). This observation led to the suggestion that some intraplate volcanoes like Changbai and Wudalianchi could be regarded as essentially very deep rooted, back-arc intraplate volcanoes (Zhao et al., 2009). The fast convergence velocities of 7-10 cm/yr (Taura et al., 2001) should allow for the preservation of carbonates in sediments transported into the transition zone. Travelling further westward at constant depths causes a relaxation of the isotherms, and an increase in slab temperatures, which may lead to partial melting of carbonated pelites. Low -velocity seismic anomalies in the upper mantle beneath the Changbai and Wudalianchi volcanoes above the subducted Pacific slab (Duan et al., 2009; Zhao et al., 2009) could be associated with ascending magmas generated by melting in the transition zone (Duan et al., 2009).

Our experiments show that alkalic magnesio- to ferro-dolomitic carbonate melts can be generated from carbonated pelites at these depths, at temperatures far below the mantle adiabat. The addition of small amounts of these volatile-rich, highly-oxidized melts to the transition zone mantle would cause a dramatic decrease in the melting temperature of peridotite (Taylor and Green, 1988; Brey et al., 2008), yielding magmas which may ascend to the surface. Contribution of this slab-derived component in the magmas of the Changbaishan volcanic province is consistent with carbon isotope analyses (Hahm et al., 2008) and trace elements characteristics (Sui et al., 2007).

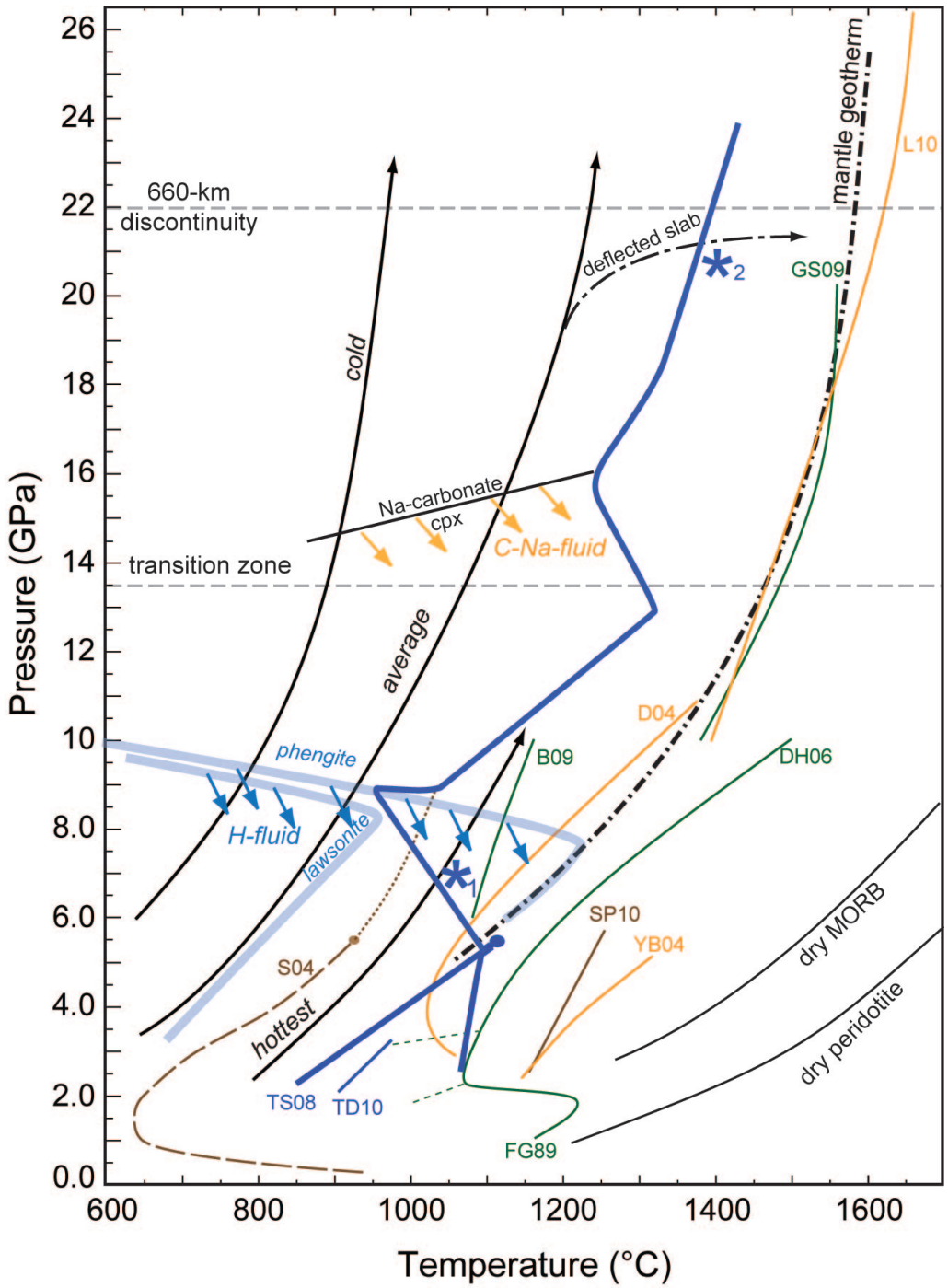
Pressure (GPa)
Temperature (°C)
660-km
discontinuity
transition zone
cold
average
hottest
deflected slab
mantle geotherm
L10
GS09
Na-carbonate
cpx
C-Na-fluid
phengite
H-fluid
lawsonite
S04
TS08
TD10
B09
D04
DH06
SP10
YB04
FG89
dry MORB
dry peridotite
*1
*2

Figure 3.13:

Figure 3.13: *P-T diagram showing a plausible range of subduction P-T-paths and the solidi for carbonated pelites, basalts and peridotites. For natural progradly subducting carbonated pelites or psammites, the solidus corresponds to that of the AM composition to pressures of the phengite-out, at which H_2O-bearing fluid is liberated and almost all H_2O lost from the bulk. At $>$ 9 GPa, the carbonated pelite solidus corresponds then to that of the dry DG2 composition. At the cpx-breakdown, a Na-rich CO_2-fluid is liberated and may cause mantle metasomatism. Typical subduction paths (Kincaid and Sacks, 1997; van Keken et al., 2002; Peacock, 2003) yield melting of these pelites feasible at 6-9 GPa for hot subduction, when P-T paths intersect with the solidus that has a negative Clapeyron slope in this pressure range (blue star with nr. 1). If a slab deflects and proceeds horizontally just above the 660-km discontinuity, thermal relaxation towards the mantle geotherm (Akaogi et al., 1989) would cause melting (blue star nr. 2). Similar, at the end of convergence when subduction slows down and thermal relaxation occurs, carbonate melts may form at any pressure. Carbonate melts from subducted sediments that rise into the mantle are expected to remain in the liquid state in the mantle as long as oxidizing conditions are maintained. Lines: solidi of subducted material, brown: CO_2-free pelites, blue: carbonated pelites, orange: carbonated MORB, green: carbonated peridotite. TS08: carbonated pelite (AM composition from 2.5 to 5 GPa) solidus and calcite-out reaction after Thomsen and Schmidt (2008b). TS10: solidus for a nominally dry carbonated eclogitic pelite after Tsuno and Dasgupta (2010). D04, YB04: solidi of carbonated basalts after Dasgupta et al. (2004) and Yaxley and Brey (2004), the former bulk resulting in dolomite or magnesite, the latter in Mg-calcite. L10: solidi of carbonated basalt simplified in the CaO-MgO-Al_2O_3-SiO_2-CO_2 system after Litasov and Ohtani (2010). FG89: Hawaiian Pyrolite + 5 wt% dolomite at $\leq$ 3.5 GPa (Falloon and Green, 1989). DH06, GS09: solidi of dry carbonated peridotite at high pressure after Dasgupta and Hirschmann (2006) and Ghosh et al. (2009). B09: solidus of a H_2O- (2.22 wt%) and CO_2- (3.63 wt%) rich peridotite after Brey et al. (2009). S04: melting and dissolution curves for potassium-rich wet sediments after Schmidt et al. (2004). SP10: solidus of dry pelite after Spandler et al. (2010). The solidus for dry peridotite is after Hirschmann (2000) and the one for the dry MORB after Yasuda et al. (1994). The stability fields for lawsonite and phengite are after Schmidt and Poli (1998).*

3.4.5 Mantle metasomatism

The presence of small amounts of carbonate melts in the mantle has been proposed to explain several aspects of mantle petrology, chemistry, dynamics and evolution. Under oxidized conditions and in the presence of alkalis, some carbonate melt is expected to be present in a CO_2-bearing upper mantle at temperatures near or even below a typical mantle adiabat (Dasgupta and Hirschmann, 2007; Ghosh et al., 2009; Brey et al., 2008; Foley et al., 2009). Dasgupta et al. (2007) suggested that many alkaline OIB could be produced by ca. 1-5 % partial melting of a fertile peridotite source with 0.1-0.25 wt% CO_2. Presnall et al. (2002) pointed out that silicate melting initiated by CO_2 + H_2O may be responsible for a geochemical signature in MORB similar to the one attributed to small-degree melts. The presence of carbonate melts or of mantle domains metasomatized by carbonate melts has also been invoked to explain the origin of several highly enriched, ultrapotassic magmas such as kimberlites, orangeites, lamproites, and other alkaline rocks (Brey et al., 2008; Girnis et al., 2006; Dixon et al., 2008).

A carbon-rich mantle, convenient to explain many aspects of the deep Earth, requires an efficient process to return the highly incompatible carbon liberated with magmas back into the mantle. For this, subduction is the only known process and most of the CO_2 is buried with carbonated sediments and altered oceanic crust (Alt and Teagle, 1999; Plank and Langmuir, 1998; Bonatti et al., 1974). Compared with other carbonated components of the subducting lithosphere (basalts and peridotites), pelites contain much larger concentrations, as well as substantial quantities of alkalis and incompatible, lithophile elements. At depths beyond the subarc regime, carbonated pelites have by far the lowest melting point, which, combined with their position on top of the subducting stratified oceanic lithosphere, renders them the easiest to melt and consequently the most efficient rock type in the carbon recycling process. Consequently, if melting temperatures were to be reached at depths greater than 170 km (5.5 GPa), carbonated pelites are bound to melt first, generating relatively exotic liquids with an enriched and distinctive signature. Therefore, melting and metasomatism through alkali-rich carbonate melts carrying crustal and sedimentary signatures provides an extremely efficient method to recycle CO_2, alkalis and many incompatible elements back into the mantle.

Some intraoceanic magmas have trace element and isotopic compositions suggesting the involvement of an enriched component similar to sediments or upper crustal material in the source region. This component is known as EM 1 and EM 2 mantle "endmember" (Chauvel et al., 1992; Hofmann, 1997; Eisele et al., 2002). Geochemical modeling suggests that mixing of a depleted mantle component with a sedimentary component (ca. 5-10 wt%) can explain the particular trace element enrichment and the radiogenic composition of the EM mantle type (Chauvel et al., 1992; Eisele et al., 2002). In particular, when comparing the isotopic signature of OIBs to their major element composition (Jackson and Dasgupta, 2008; Spandler et al., 2010), potassium enrichment, including K_2O/TiO_2 and K_2O/Na_2O ratios, correlate with $^{87}Sr/^{86}Sr$-ratios and CaO/Al_2O_3 with $^{206}Pb/^{204}Pb$ ratios. Jackson and Dasgupta (2008) suggested an enrichment of TiO_2, K_2O and K_2O/TiO_2 in the source of both EM 1 and 2 mantle reservoirs. Assuming that low SiO_2, high CaO and high CaO/Al_2O_3 ratios are related to CO_2 enrichment (fig. 3.14a,b), they pointed out that in EM 2 type mantle metasomatism through a CO_2-rich melt or fluid is more likely than in the EM 1 source. The carbonate melts of this study are extremely alkali-rich (potassic to 16 GPa, sodic above), with high K_2O/TiO_2, CaO/Al_2O_3 and $K_2O/\ Al_2O_3$ ratios (fig. 3.14c) and K_2O and TiO_2 contents, in contrast to silicate melts generated from CO_2-free sediments (fig. 3.14c). Mixing of sediment derived carbonate melts with a depleted mantle source (Rehkamper and Hofmann, 1997) results in compositions which fit well with EM 2 OIBs rather than EM 1 OIBs (fig. 3.14d). In order to fit EM 1 type compositions, a sediment-derived melt with lower Sr concentrations, and thus lower bulk $^{87}Sr/^{86}Sr$ after mixing, and/or higher potassium concentrations, is needed. Such a melt is most likely a sediment-derived silicate melt or supercritical liquid.

The low degree of melt resulting from carbonated pelites implies a much higher enrichment of trace elements than in the unmelted source and requires addition of much less sediment-derived material than in any bulk mixing model. Addition of < 2 wt% carbonate melt has the same effect as mechanical mixing with 5-10 wt% bulk sediment. Metasomatism through small amounts of

alkali-rich carbonate melts is physically easy to achieve and strongly increases the alkali content of the mantle source. Considering all these aspects we suggest that metasomatism through alkalic dolomitic carbonate melts as derived from carbonated eclogitic pelites in this study is ideal to explain the EM 2 mantle reservoir, including its major element characteristics and sedimentary component.

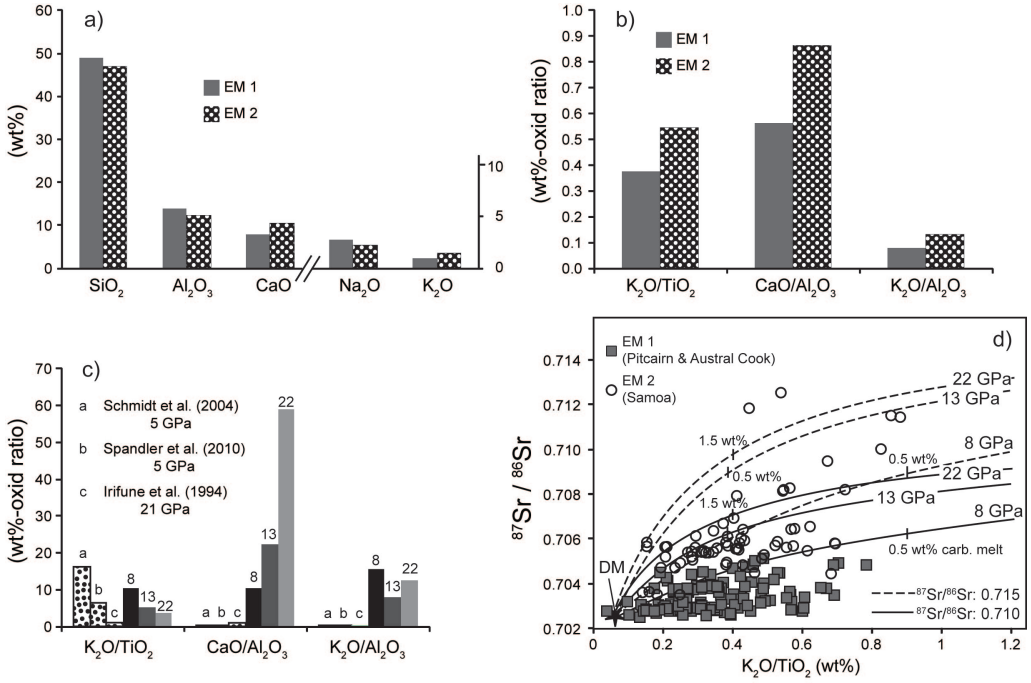

Figure 3.14: *(a) and (b): Histograms showing the major element compositional differences in (a) wt% and (b) wt-ratio between EM 1 and EM 2 type OIBs (data from Jackson and Dasgupta, 2008). The involvement of carbonate melts is more likely for EM 2 type OIBs due to lower SiO_2 and Al_2O_3 concentrations combined with higher CaO and CaO/Al_2O_3 values. (c) Same histogram as in (b) showing a positive correlation between EM 2 type OIBs and sediment derived carbonate melts, and EM 1 type OIBs and sediment derived silicate melts (Irifune et al., 1994; Schmidt et al., 2004; Spandler et al., 2010). (d) K_2O/TiO_2 vs. $^{87}Sr/^{86}Sr$ showing the difference between EM 1 type (red squares) and EM 2 type OIBs (blue circles), with EM 2 type having a higher $^{87}Sr/^{86}Sr$ ratio for a given K_2O/TiO_2 value. Data are from the GEOROC database (http://georoc.mpch-mainz.gwdg.de/georoc/). The Sr concentrations (1000-2000 ppm) of the melt employed to calculate the mixing lines are in agreement with own results (chapter 5). Values for the depleted mantle are after Rehkamper and Hofmann (1997). The isotopic compositions for the sediment derived melts used for mixing are 0.710 (continuous lines) and 0.715 (dashed lines) covering a wide spectrum of possible compositions for pelagic sediments mixed with marine carbonates (Rehkamper and Hofmann, 1997; Plank and Langmuir, 1998; Brand et al., 2009).*

3.5 Conclusion

- Comparison of the solidi for carbonated pelites with typical subduction P-T-paths yield two distinct depth ranges for melting: (i) At 6-9 GPa, related to an increased incompatibility of

potassium lowering the solidus of carbonated pelites, and possibly to the presence of fluids from the pressure breakdown of lawsonite and phengite, whose stability intersects typical subduction P-T paths at 8-9 GPa. These fluids, flushing through the sediment pile, promote the formation of carbonate melts. (ii) At the base of the transition zone, above the 660-km discontinuity, melting is related to a possible deflection and subsequent thermal relaxation of the slab, and thus of the carbonated sediments. With time, an increasing temperature necessarily induces their melting, producing highly mobile Na-rich carbonate melts.

- Given the low melting point, the position on the top of the slab column and the dynamics of subducting slabs, it is likely that much of the CO_2 trapped in pelitic rocks will be liberated during melting within the upper mantle and transition zone, unless a cold slab directly passes through the 660-km discontinuity to continue into the lower mantle.

- Of all subducted rock types, carbonated pelites have the lowest melting point, and are by far the most efficient in recycling CO_2, alkalis and incompatible elements back into the upper mantle and transition zone.

- Metasomatism through alkalic dolomitic carbonate melts derived from carbonated sediments is able to explain some of the features of EM 2 mantle reservoir, including its major element characteristics and sedimentary component.

- The alkali- and Ca-rich, relatively oxidized carbonate melts will be in chemical disequilibrium with the overlying olivine(-polymorph)-saturated, reduced mantle and thus a large variety of (redox-)reactions can be expected upon melt-infiltration.

Chapter 4

The Role of Redox Freezing in the Generation of Highly Metasomatized Alkali- and Carbon-rich Mantle Domains

Abstract

Highly alkaline potassic carbonate melts generated through partial melting of carbonated pelites at 8 and 13 GPa have been equilibrated with lherzolitic mantle to understand the metasomatic effect that this kind of melt would produce upon migration into the mantle. For this, a lherzolite has been mixed with various carbonate melts at 50:50 to 70:30 wt-ratios and reacted at pressures of 8 and 13 GPa and temperatures of 1100-1350 °C at reducing and oxidizing conditions. A first set of experiments constrains the basic aspects caused by this kind of metasomatism. In each experiment, the lherzolite was transformed into a wehrlite made of clinopyroxene and olivine coexisting with garnet, magnesite and a K-rich carbonates/melt under oxidizing conditions and with phase X and diamond (± small pockets of unquenchable highly potassic melt/fluid) under more reducing conditions (fO_2=NNO-1; fO_2=IW-0.7). The experiments suggest a scenario in which our low viscosity alkaline carbonate melts will rise into the mantle upon melting and percolate upwards as long as the mantle remains at adiabatic temperatures which are above the solidus of K-rich carbonated peridotites. In relatively cold and reduced lithospheric mantle keels of continental shields, the carbonate melts may freeze and react with the reduced mantle to potassium-, carbonate/diamond- and incompatible element-rich metasomatized zones, which most likely constitute the source regions of ultrapotassic magmas such as group II kimberlites and many lamproites.

Keywords: potassic carbonate melts, mantle metasomatism, redox freezing, diamonds

4.1 Introduction

Previously, we have investigated the melting of subducted carbonated pelites from pressures corresponding to subarc depths to the 660-km discontinuity (2.5-23.5 GPa, Thomsen and Schmidt, 2008b; chapter 2 and 3). At $\geq$ 8 GPa, i.e. beyond sub-arc depths, alkali-rich carbonate melts form at temperatures 300 °C below the mantle geotherm and similar to those expected for an average subduction regime. Thus, sediment derived carbonate melts are likely to form and infest the mantle, at latest when the sediment carrying subducted slab relaxes thermally to near-mantle temperatures. The sediment derived alkali- and Ca-rich, low X^*_{Mg}, relatively oxidized carbonate melts will be in thermal and chemical disequilibrium with the surrounding high X^*_{Mg}, olivine-polymorph saturated, reduced mantle. This disequilibrium will lead to reactions affecting the redox state, the mineral assemblage, the chemical characteristics and the fertility of the metasomatized mantle. Interactions between a mantle assemblage and Ca-carbonate melts have already been experimentally investigated at pressure below 4 GPa (Thibault et al., 1992; Dalton and Wood, 1993; Sweeney, 1994). These studies have shown that the reaction of a Ca carbonate melt with a mantle assemblage will increase the clinopyroxene/orthopyroxene ratio and transform a harzburgite into a lherzholite or wehrlite.

There are numerous studies which have investigated potassium-enriched mantle, in particular the stability of phlogopite, K-richterite, and phase X (a high pressure potassium phase) in coexistence with olivine (e.g. Sudo and Tatsumi, 1990; Luth, 1997; Konzett and Ulmer, 1999; Konzett and Fei, 2000). In mantle compositions, phlogopite is replaced by K-richterite near 6.5 GPa which in turn is succeeded by phase X near 13 GPa. Typical melting temperatures of K-enriched CO_2-free mantle are around the adiabat for K-richterite and ca. 200 °C higher for phase X (Konzett and Fei, 2000) bearing assemblages. Other experiments have dealt with CO_2-enriched mantle, resulting in melting temperatures in excess of the adiabat at $<$ ca. 250 km depth and near the adiabat at higher pressure equivalents (Dasgupta et al., 2004; Yaxley and Brey, 2004; Dasgupta and Hirschmann, 2006; Brey et al., 2008; Ghosh et al., 2009) which led to a model where the first melts to form within upwelling mantle are low viscosity carbonate melts (Dasgupta and Hirschmann, 2006).

There is general agreement, that kimberlites and also other K-rich, strongly Si-undersaturated rocks like kamafugites, lamproites and aillikites (Francis and Patterson, 2009) stem from a K_2O and/or CO_2 enriched source (Canil and Scarfe, 1990; Girnis et al., 1995; Ulmer and Sweeney, 2002; Foley, 2008). Group II kimberlites and in particular the MARID suites show ample evidence of a K_2O+CO_2 rich source mantle and contain K-richterite and phlogopite bearing xenoliths. Nevertheless, there is little information on how a K_2O and CO_2 bearing mantle comes upon us (especially if a single metasomatic process is considered), and there is even less experimental verification that the above minerals would be the ones forming from likely K_2O- and CO_2-rich metasomatic agents.

The idea of this study is thus to investigate the generation of the K_2O- and CO_2- enriched mantle within the frame of a single metasomatic process through sediment derived carbonate melts

containing large amounts of both oxides. The aim is to understand, how the sediment component is recycled back into the mantle, what redox equilibria occur during this process, and what geochemical reservoirs could be expected to form in the mantle.

4.2 Experimental procedure and analytical technique

4.2.1 Starting material

The lherzolitic composition LHZ (tab. 4.1) used in this study corresponds to an average lherzolite (Maaloe and Aoki, 1977) in the TiO_2-Na_2O-CaO-FeO-MgO-Al_2O_3-SiO_2 (NCFMASH) system. The starting materials is made of powders of SiO_2, Al_2O_3, TiO_2, MgO, Na_2SiO_3, fayalite, and wollastonite, which were milled and grinded to <5 μm. The powders were kept in a desiccator under ambient temperature or in a vacuum oven at 110 °C. The carbonate melts was mixed from different amounts of $MgCO_3$ (pure natural magnesite from Oberdorf Philipp, 1998), $FeCO_3$ (synthesized in cold seal pressure vessels at 2000 bar and 350 °C sealing iron oxalate in a welded gold capsule, French, 1971), $CaCO_3$, K_2CO_3, Na_2CO_3, TiO_2, SiO_2 and Al_2O_3.

Table 4.1: Composition of the starting materials used in this study

	LHZ	LHZ-S2a	LHZ-S2a red1-3	LHZ-S4a	LHZ-S1e	S2a	S1e	S4a
SiO_2 wt%	44.23	22.53	31.21	29.66	23.56	0.84	2.89	0.53
TiO_2	0.09	0.90	0.57	0.06	0.78	1.70	1.47	-
Al_2O_3	2.10	2.04	2.06	1.85	3.69	1.97	5.29	1.36
FeO	8.29	8.15	8.20	8.36	8.88	8.00	9.48	8.48
MgO	42.27	24.03	31.33	29.44	23.70	5.79	5.13	3.78
CaO	1.90	12.10	8.02	10.10	9.75	22.30	17.59	26.49
Na_2O	0.32	2.68	1.74	1.73	0.98	5.05	1.63	4.56
K_2O	-	6.02	3.61	4.86	10.28	12.04	20.56	14.58
H_2O	-	traces	traces	traces	traces	-	-	traces
CO_2	-	19.00	11.40	13.39	17.98	38.00	35.97	40.17
tot.	99.20	97.45	98.15	99.47	49.60	95.69	100.00	100.00
X^*_{Ca}	0.03	0.23	0.14	0.18	0.20	0.61	0.55	0.69
X^*_{Mg}	0.88	0.64	0.75	0.71	0.66	0.22	0.22	0.14
Mg#	90	84	87	86	83	56	49	44

LHZ is an average lherzolite (Maaloe and Aoki, 1977). S2a, S1e, S4a: carbonate melts derived from carbonated pelite at 8 and 13 GPa (chapter 2). LHZ-S2a: bulk starting material used at 13 GPa/1350 °C consisting of 50 wt% LHZ + 50 wt% S2a. LHZ-S2a (red1-3): bulk starting material used in the more reduced experiments at 13 GPa/1350 °C consisting of 70 wt% LHZ + 30 wt% S2a. LHZ-S4a: bulk starting material used in the experiment at 13 GPa/1220 °C (66.6 wt% LHZ + 33.3 wt% S4a). LHZ-S1e: bulk starting material used in the experiment at 8 GPa and 1100 °C (50 wt% LHZ + 50 wt% S2a).

4.2.2 Experimental procedure

Experiments were conducted in a 600-ton Walker-type rocking multi-anvil. The whole multi-anvil apparatus was rotated by 180 °C during the experiments in order to improve the attainment of equilibrium and reducing the chemical zonation in the capsules (Schmidt and Ulmer, 2004). The experiments were rotated continuously during the first 30 minutes and then every 10 minutes during the reminder of the experiments.

Tungsten carbide cubes with a truncation edge length of 11 (8 GPa) and 8 mm (13 GPa) in combination with prefabricated MgO-octaedra of 18 (18/11 assembly) or 14 mm (14/8 assembly) edge length, respectively, were used in the different experiments. Natural pyrophyllite gaskets and MgO-graphite-zirconia and MgO-$LaCrO_3$-zirconia assemblages with stepped furnaces were employed for 8 and 13 GPa respectively; further details can be found in chapter 2.

Temperature was controlled using a B-type ($Pt_{94}Rh_6$/$Pt_{70}Rh_{30}$) thermocouple and no correction for the effect of pressure was applied. Two capsules were placed in each experiment into the central thickened part of the furnace. Quenching was done by turning off heating power and was followed by pressure unloading of about 15-20 hours. After the experiment, capsules were mounted longitudinally in epoxy resin and polished to the centre by dry polishing to avoid alkali-loss in the alkali-rich carbonates and quench products of the carbonate melts. The open capsules were repeatedly embedded in low viscosity resin to avoid chemical and mechanical loss of quench carbonate melts. When not analyzed, the capsules were always kept in a desiccator under vacuum conditions.

4.2.3 Oxygen fugacity

Most of the experiments were run in $Au_{80}Pd_{20}$ capsules resulting in assemblages consisting of carbonates, carbonate melts and garnet containing significant amounts of ferric iron which combined with the absence of graphite/diamond suggests an oxygen fugacity above the graphite-CO-CO_2 (CCO)-buffer.

In order to investigate the effect of the reducing conditions to be expected in the mantle, oxygen fugacities during the reaction between carbonate melts and a mantle assemblage were buffered by pure Ni°- and Fe°-capsules or by adding small pieces of Ni° metal employing again $Au_{80}Pd_{20}$ capsules in two experiments at 13 GPa and 1350 °C. In these more reduced experiments, magnesite was not observed. The presence of much less and small patches of quenched CO_2 rich melts or fluid was only detected in the Ni°-capsule experiments. In the Fe°-capsule experiments there was no sign of any CO_2-fluid or melt. This suggest that most (NNO-buffer) or all (IW-buffer) carbon was reduced to graphite or diamond. For these experiments, oxygen fugacity was calculated from the reactions 2 Ni° + O_2 = 2 NiO in the experiment with a Ni°-capsule and 2 Fe° + O_2 = 2 FeO in the experiments with a Fe°-capsule using the X_{Ni} and X_{Fe} in the (Ni/Fe,Mg)-periclase, respectively. Resulting oxygen fugacities are 1 log unit below NNO-buffer for the experiment in the Ni°-capsule and ca. 0.7 log unit below the IW-buffer for the experiment in the Fe°-capsule.

4.2.4 Analytical methods

All experimental charges were analyzed with a JEOL JXA8200 electron microprobe at ETH-Zürich with 15kV acceleration voltage, 20 nA beam current for silicate minerals and 5 nA for carbonates and carbonate melt quench. Acquisition times were 10 s for Na and K and 20 s for all the other elements, measuring Na and K first to avoid diffusional losses. Beam diameters of 1 to 2 μm were used for all silicate and carbonate phases. Quenched melts, which exhibited beam damage, were analyzed, whenever possible, using a defocused beam (3-10 μm). Secondary and back-scattered electron images from the microprobe or from a JEOL JSM6300 field emission SEM were used for textural analysis.

4.3 Results

In these kind of experiments (tab. 4.2) two types of starting materials (tab. 4.1), one with a lherzolitic composition (LHZ) and the second (S2a, S4a and S1e) being a potassium-rich carbonate melt, identical to those generated from carbonated pelites at 8 and 13 GPa, were mixed together (50:50 to 70:30 wt%) and reacted at 8 and 13 GPa and 1100-1350 °C. The experiments were run with different capsule material ($Au_{80}Pd_{20}$, Ni° and Fe°) causing different oxidation states.

Table 4.2: Summary of the experimental run conditions, phase assemblages and calculated oxygen fugacity

Run	T[°C]	P[GPa]	time [h]	capsule	log fO_2 [ΔNNO]	assemblage
LHZ-S2a	1350	13	48	$Au_{80}Pd_{20}$	-	grt, cpx, ol, mgs, K-carb, melt
LHZ-S2a red	1350	13	72	Ni°	-1.1	cpx, ol, phase X, NiMg-peri., melt
LHZ-S2a red2	1350	13	72	[a] $Au_{80}Pd_{20}$++	-0.8	cpx, ol, phase X, NiMg-peri., melt/fluid
LHZ-S2a red3	1350	13	72	Fe°	ca. -5.5	cpx, ol, phase X, FeMg-peri.
LHZ-S4a	1220	13	72	$Au_{80}Pd_{20}$	-	grt, cpx, ol, mgs, K-carb, Fe-oxide
LHZ-S1e	1100	8	72	$Au_{80}Pd_{20}$	-	grt, cpx, ol, mgs, K-carb, FeTi-phase

[a] some Ni° metal flakes were added to the starting material to control the oxygen fugacity.

Experiments at 13 GPa and 1350 °C under different fO_2

In the more oxidized experiments LHZ-S2a in a $Au_{80}Pd_{20}$ capsule the lherzolite transformed into a carbonated wehrlite which coexists with an extremely alkali-rich carbonate melt (tab. 4.3-4.8). The stable minerals are garnet, clinopyroxene, olivine, magnesite and a potassium rich carbonate ($(K,Na)_2(Mg,Ca,Fe)(CO_3)_2$) (fig. 1.1). All C is present as carbonate (magnesite or K_2Mg-carbonate) or carbonate melt and diamond has not been observed. Comparison of the melt composition before and after the experiments (tab. 4.7) shows an increase of the Na_2O and MgO content as well as an increase of X^*_{Mg} but maintain comparatively low TiO_2, SiO_2 and Al_2O_3 contents.

Table 4.3: Composition of the silicate phases, carbonates, oxides and liquid phases

Run	Phase	SiO_2 wt%	TiO_2	Al_2O_3	FeO	[b]NiO	MgO	CaO	Na_2O	K_2O	[a]CO_2	Total
LHZ-S2a	ol	39.87	0.18	0.54	12.11	-	45.78	0.71	0.28	0.21	-	99.68
	cpx	54.09	0.12	1.14	3.05	-	16.46	22.65	1.10	0.22	-	98.82
	grt	38.89	4.66	7.54	12.90	-	10.01	22.50	0.27	0.24	-	97.00
	mgs	0.16	0.01	0.02	4.33	-	44.61	1.82	0.10	0.07	48.89	51.11
	K-carb	0.04	0.01	0.04	1.06	-	16.11	3.17	6.28	29.43	43.87	56.13
	melt	0.26	0.05	0.11	2.30	-	10.52	20.98	9.99	12.78	43.01	56.99
LHZ-S2a red1	ol	38.83	0.06	0.56	4.56	14.52	40.86	0.77	0.15	0.42	-	100.72
	cpx	53.73	0.04	1.89	1.45	1.64	15.75	22.27	1.10	0.89	-	98.76
	phase X	41.82	0.02	0.61	2.95	4.13	24.81	0.15	3.03	20.60	-	98.11
	Ni-Mg-peri	0.96	0.01	0.20	9.90	39.36	48.59	0.33	0.44	1.07	-	100.86
LHZ-S2a red2	ol	35.97	0.31	0.31	0.77	28.82	33.41	0.59	0.22	1.12	-	101.51
	cpx	53.20	0.20	3.62	0.33	3.28	14.23	20.77	1.95	0.98	-	98.56
	phase X	43.55	0.14	1.41	0.58	8.14	24.49	2.30	2.56	15.38	-	98.56
	Ni-Mg-peri	0.15	0.05	0.21	1.30	55.32	44.01	0.04	0.26	0.36	-	101.70
	melt/fluid	0.14	0.02	0.02	0.06	1.55	0.22	0.03	0.19	55.54	42.22	57.78
LHZ-S2a red3	ol	40.25	0.24	0.51	14.37	-	44.75	1.41	0.34	0.35	-	102.21
	cpx	52.12	0.40	1.76	5.00	-	20.37	17.95	1.31	1.09	-	100.01
	phase X	43.64	0.41	0.86	11.94	-	24.32	4.22	3.35	11.30	-	100.03
	Fe-Mg-peri	0.04	0.61	0.25	53.07	-	47.97	0.19	0.88	0.18	-	103.20
LHZ-S4a	ol	39.41	0.00	0.07	8.95	-	48.31	0.76	0.15	0.25	-	97.90
	cpx	53.00	0.05	0.88	3.62	-	17.22	21.68	1.17	0.37	-	97.99
	grt	38.50	0.66	8.83	16.56	-	8.50	22.93	0.40	0.51	-	96.90
	mgs	0.67	0.04	0.16	5.24	-	43.81	2.08	0.07	0.40	47.54	52.46
	K-carb	0.12	0.08	0.00	2.11	-	16.06	2.03	6.21	29.61	45.89	56.11
	oxide	1.87	0.02	0.43	64.39	-	29.98	1.19	0.97	0.21	-	99.08
LHZ-S1e	ol	39.80	0.07	0.21	14.73	-	44.44	0.32	0.02	0.25	-	99.85
	cpx	51.83	0.22	1.48	4.34	-	16.35	19.99	0.99	0.93	-	96.13
	grt	39.94	2.07	18.08	11.46	-	15.12	10.72	0.16	0.70	-	98.26
	mgs	0.04	0.00	0.03	7.34	-	43.24	1.79	0.10	0.87	46.59	53.41
	K-carb	0.39	0.0574	0.3665	3.42	-	12.86	3.48	1.74	33.01	44.68	55.32
	Ti-phase	4	42.44	0.4848	30.58	-	10.99	1.9	0.2292	0.9076		91.5317

[a] CO_2 content calculated by difference of 100 and the measured analytical total.
[b] NiO assimilated from the capsule or from the metal flakes.

Garnet is Fe- and Ti-rich, with a Fe^{3+}/Fe_{tot} of 0.84 and coexists with a Na_2O-poor (< 2 wt%) clinopyroxene.

In two more reducing experiments using Ni$^{\circ}$ either as capsule or as metal pieces mixed into the starting material within an $Au_{80}Pd_{20}$-capsule a different result is obtained. In these more reduced experiments the assemblage consists of olivine, cpx, a (Ni,Mg)-periclase, the potassium rich phase X (Luth, 1995) (tab. 4.3) and very few and small alkali- and CO_2-rich patches of quenched material

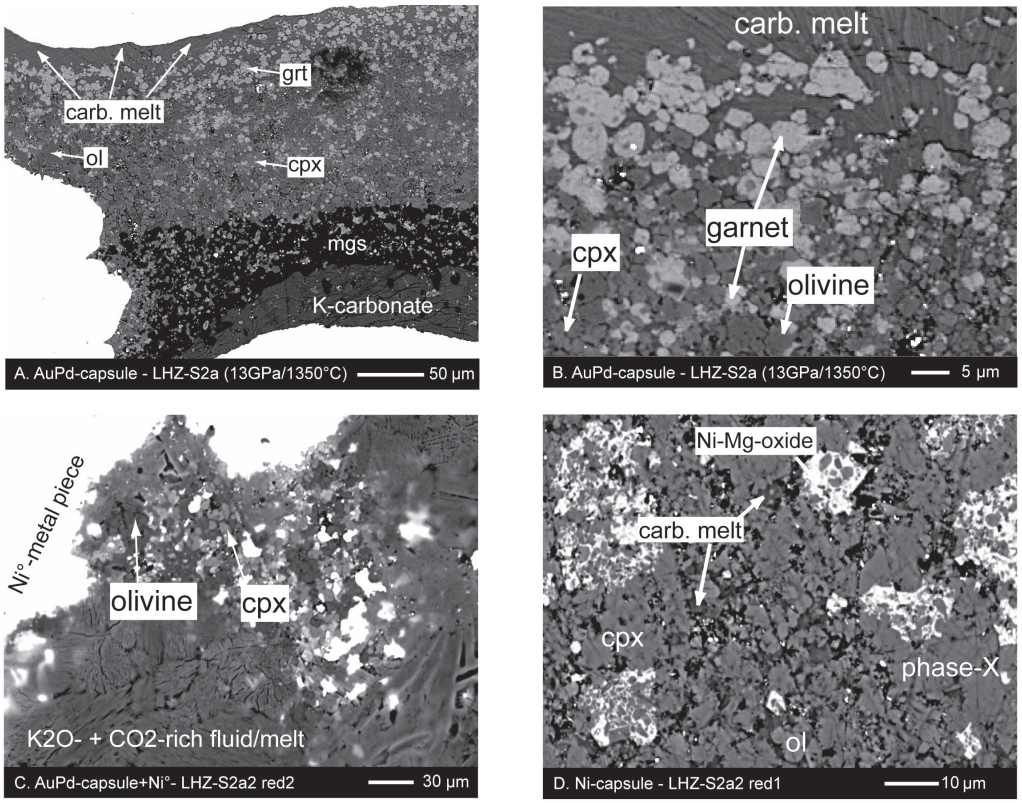

Figure 4.1: *BSE-images of run products at the same pressure and temperature of 13 GPa and 1350 °C but at different oxygen fugacity. A: LHZ-S2a in $Au_{80}Pd_{20}$-capsule constraining oxidized conditions. The alkali-rich carbonate melt (top of the capsule) coexists with grt, cpx, ol, mgs and a potassium-rich carbonate; B: details of A showing the carbonate melt concentrated at the top of the capsule; C: LHZ-S2a red2; experiments in $Au_{80}Pd_{20}$-capsule with small flakes of Ni°-metal added. In this more reduced experiment the melt is extremely potassium rich and has a more fluid-like character. D: LHZ-S2a red1; this experiments run in a Ni°-capsule results in an assemblage consisting of ol, cpx, phase X, Ni-rich Mg-periclase and some small patches of carbonate melt.*

(fig. 4.1). No K-carbonate or magnesite could be observed. Considering the quite high Ni-content in olivine and in the (Ni,Mg)-periklase (tab. 4.3) on one side and the almost complete absence of carbonates and metallic iron Fe° on the other, we suggest a redox reaction of Ni° with the CO_2 in the carbonates and carbonate melt of the type Ni° + CO_2 = NiO + C°. The reduction of the carbonates to elemental carbon leads to a strong decrease in the amount of carbonate species and thus in the amount of liquid and thus to a redox freezing. With a much reduced liquid fraction present, potassium and to a lesser extend sodium partition into phase-X. The redox conditions are most likely also leading to the destabilization of garnet due to the absence of ferric iron and to the low Al_2O_3 of the bulk. A fO_2 of about 1 log unit below the NNO-buffer for both experiments was calculated (see above).

In the most reduced experiment run in a Fe°-capsule yielding a calculated oxygen fugacity

of 0.7 log unite below the IW-buffer no carbonates (magnesite and k-carbonate) and no CO_2-rich fluid or melt could be observed. The stable phases are olivine, clinopyroxene, phase X and a (Fe, Mg)-periclase. In this experiment all the carbon has been reduced through the redox reaction Fe° + CO_2 = FeO + C° leading to the absence (freezing) of the added alkali-rich carbonate melt.

Oxidized subsolidus experiments at 8 (1100 °C) and 13 GPa (1220 °C)

In two experiments at temperatures below the solidus, one at 8, 1100 °C and the other at 13 GPa, 1220 °C, the similar assemblage as for the oxidizing supersolidus experiments has been observed. In these runs the lherzolite is transformed into a carbonated wehrlite with olivine coexisting with clinopyroxene, garnet, magnesite, a K_2Mg-carbonate and a small amount of a Fe- and Ti-rich oxide. The high CaO content of the carbonate melt added to the lherzolitic composition increases the CaO/MgO ratio of the bulk and leads to the crystallization of a large volume of clinopyroxene replacing orthopyroxene.

4.3.1 Mineral compositions

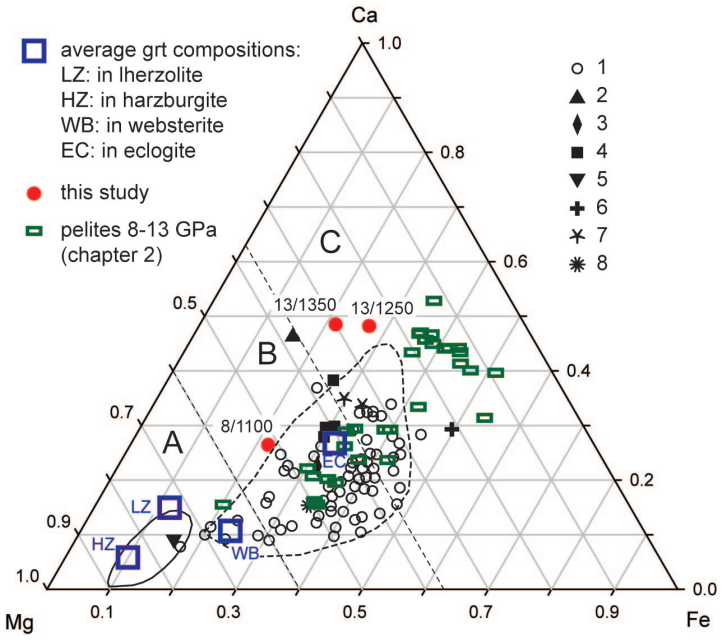

Figure 4.2: *Ternary diagram for garnets from E-type paragenesis in macrodiamonds from Mir and Udachnaya pipes (1), microdiamonds from Aykhal (2), Udachnaya (3), Sytykanskaya (4), Mir (5), Yubileynaya (6), Komsomolskaya, majoritic (7) and normal (8). Data source: Sobolev et al. (2003). Data for pelites at 8-13 GPa are from this study (chapter 2); the averaged garnet compositions found as inclusions in diamond in different paragenesis are after Stachel and Harris (2008). Group boundaries A, B and C limited by dashed lines are from Coleman et al. (1965). Figure modified after Sobolev et al. (2003).*

Garnet crystallizes only in the more oxidized experiments and is strongly andraditic with up to 1.09 Fe^{3+} pfu (tab. 4.4). In the Ca-Mg-Fe_{tot} ternary diagram (fig. 4.2) our garnets show higher Ca contents, up to 1.93 pfu at 13 GPa, compared to other garnets found as inclusions in macro- and microdiamonds. In fact, our garnets, despite being crystallized in a lherzolite, correlate much

better with the compositions of garnets thought to belong to the eclogitic series than with the ones belonging to ultramafic series in diamond inclusions.

Table 4.4: garnet and clinopyroxene composition

	LHZ-S2a grt	LHZ-S4a	LHZ-S1e	LHZ-S2a cpx	LHZ-S2a red1	red2	red3	LHZ-S4a	LHZ-S1e
SiO_2 wt%	38.89	38.50	39.94	54.09	53.73	53.20	52.12	53.00	51.83
TiO_2	4.66	0.66	2.07	0.12	0.04	0.20	0.40	0.05	0.22
Al_2O_3	7.54	8.83	18.08	1.14	1.89	3.62	1.76	0.88	1.48
FeO	12.90	16.56	11.46	3.05	1.45	0.33	5.00	3.62	4.34
NiO	-	-	-	-	1.64	3.28	-	-	-
MgO	10.01	8.50	15.12	16.46	15.75	14.23	20.37	17.22	16.35
CaO	22.50	22.93	10.72	22.65	22.27	20.77	17.95	21.68	19.99
Na_2O	0.27	0.40	0.16	1.10	1.10	1.95	1.31	1.17	0.99
K_2O	0.24	0.51	0.70	0.22	0.89	0.98	1.09	0.37	0.93
CO_2	0.00	0.00	0.00	0.00	0.00	0.00	0.00	0.00	0.00
tot.	97.00	96.90	98.26	98.82	98.76	98.56	100.01	97.99	96.13
[a]Si pfu	3.05	3.02	2.97	1.98	1.97	1.95	1.86	1.95	1.95
Ti	0.28	0.04	0.12	0.00	0.00	0.01	0.01	0.00	0.01
Al	0.70	0.82	1.58	0.05	0.08	0.16	0.00	0.04	0.07
Fe^{3+}	0.71	1.09	0.34	0.07	0.04	0.01	0.07	0.11	0.14
Fe^{2+}	0.13	0.00	0.38	0.02	0.00	0.00	0.15	0.00	0.00
Ni	-	-	-	-	0.05	0.10	-	-	-
Mg	1.17	0.99	1.68	0.90	0.86	0.78	1.08	0.94	0.92
Ca	1.89	1.93	0.85	0.89	0.87	0.82	0.69	0.85	0.81
Na	0.04	0.06	0.02	0.08	0.08	0.14	0.09	0.08	0.07
K	0.02	0.05	0.07	0.01	0.04	0.05	0.05	0.02	0.04
C	0.00	0.00	0.00	0.00	0.00	0.00	0.00	0.00	0.00
tot.	8.00	8.00	8.00	4.00	4.00	4.00	4.00	4.00	4.00
Mg#(Fe^{2+})	90	100	82	98	100	100	100	100	100
Mg#(Fe_{tot})	58	48	70	91	95	99	88	89	87

[a] cations calculated on the basis of 12 oxygens for garnet and 6 oxygens for cpx.

Clinopyroxenes are almost diopsidic with small amounts of Al (0.15 apfu) and alkalis (up to 0.21 apfu) and an Mg# of 88-99. In the pyroxene quadrilateral (fig. 4.3a) our pyroxenes show a strong affinity with peridotitic pyroxenes found as inclusions in many diamonds. These pyroxenes have lower Fe (Mg#: 85-97) content compared to eclogitic pyroxene (Mg#: 60-85) and higher Ca values (0.69-0.89 apfu) compared to pyroxenes in equilibrium with a carbonated peridotite (0.53-0.71 apfu) (Dasgupta and Hirschmann, 2007a; Ghosh et al., 2009) at similar pressures. Alkali content strongly correlates with alumina (fig. 4.3b), suggesting minor Ca-Tschermaks component similar to what is observed in peridotite xenoliths in kimberlites and in pyroxene inclusions in diamonds of many localities (Wang and Gasparik, 2001). As observed previously (Harlow, 1997 and Tsuruta; Takahashi, 1998) clinopyroxene can constitute an important host for potassium. The clinopyroxenes of this study confirm this observation and show values up 0.95 wt% K_2O at 8 GPa and up to 1.09 wt% at 13 GPa under more reduced conditions (tab. 4.4).

Olivines of this study are extremely CaO-rich (up to 1.41 wt%) (tab. 4.5) due to the high amount of CaO added through the carbonate melt. Fosterite component varies between 84 mol%

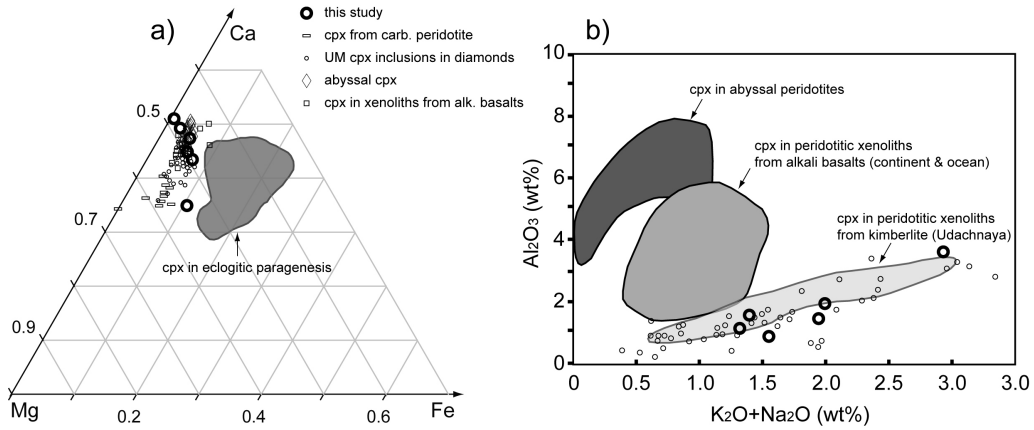

Figure 4.3: *a) Cpx compositions plotted in terms of Ca-Mg-Fe. Small circles represent ultramafic cpx inclusions in diamonds from various region of the world after Meyer (1987). The data for abyssal peridotite are from Johnson et al. (1990), for the xenoliths in alkali basalts from Hauri et al. (1993) and Coltorti et al. (1999), and for the cpx in carbonated peridotite at high pressure from Dasgupta and Hirschmann (2006) and Ghosh et al. (2009). The shaded area represents the composition of cpx in eclogitic paragenesis. b) Variation of Al_2O_3 vs. Na_2O+K_2O (wt%) in cpx from various tectonic setting. The data for peridotitic xenoliths from Udachnaya kimberlite pipe are from Shimizu et al. (1995). Both figures modified after Wang and Gasparik (2001).*

and 89 mol% in the oxidized experiments and between 66 and 81 mol% in the more reduced experiments. The latter showing then up to 30 mol% Ni-olivine component in the experiments run in the Ni° capsule.

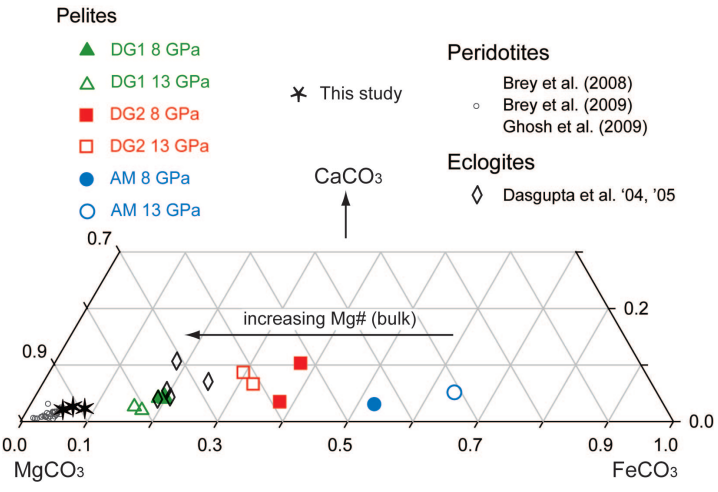

Figure 4.4: *Magnesite composition in $CaCO_3$-$MgCO_3$-$FeCO_3$ space synthesized in this study compared to carbonates from carbonated eclogites (Dasgupta et al., 2004 and Dasgupta et al., 2005), peridotites (Ghosh et al., 2009; Brey et al., 2008; Brey et al., 2009) and sediments (chapter 2). Note the strong positive correlation between magnesite composition and the Mg# of the related bulk composition.*

The *carbonates* stable in the 5 different experiments are magnesite (with 5 to 8.5 mol% siderite and 2.7 to 3.1 mol% calcite) and a potassium rich carbonate (tab. 4.6) with a general formula $(K,Na)_2(Mg,Ca,Fe)(CO_3)_2$ analoque to the Na carbonate nyereite found in the Na-carbonatites of Oldoinyo-Lengai (McKie and Frankis, 1977). Pure $K_2Mg(CO_3)_2$ has been synthesized at 25 MPa,

Table 4.5: Olivine and phase-X composition

	LHZ-S2a ol	LHZ-S2a red1	red2	red3	LHZ-S4a	LHZ-S1e phase X	LHZ-S2a red1	red2	red3
SiO_2 wt%	39.87	38.83	35.97	40.25	39.41	39.80	41.82	43.55	43.64
TiO_2	0.18	0.06	0.31	0.24	-	0.07	0.02	0.14	0.41
Al_2O_3	0.54	0.56	0.31	0.51	0.07	0.21	0.61	1.41	0.86
FeO	12.11	4.56	0.77	14.37	8.95	14.73	2.95	0.58	11.94
NiO	-	14.52	28.82	-	-	-	4.13	8.14	-
MgO	45.78	40.86	33.41	44.75	48.31	44.44	24.81	24.49	24.32
CaO	0.71	0.77	0.59	1.41	0.76	0.32	0.15	2.30	4.22
Na_2O	0.28	0.15	0.22	0.34	0.15	0.02	3.03	2.56	3.35
K_2O	0.21	0.42	1.12	0.35	0.25	0.25	20.60	15.38	11.30
CO_2	0.00	0.00	0.00	0.00	0.00	0.00	0.00	0.00	0.00
tot.	99.68	100.72	101.51	102.21	97.90	99.85	98.11	98.56	100.03
[a]Si pfu	0.99	0.99	0.96	0.99	0.98	1.00	2.04	2.06	2.03
Ti	0.00	0.00	0.01	0.00	-	0.00	0.00	0.01	0.01
Al	0.02	0.02	0.01	0.01	0.00	0.01	0.04	0.08	0.05
Fe^{3+}	0.00	0.00	0.00	0.00	0.00	0.00	0.00	0.00	0.00
Fe^{2+}	0.25	0.10	0.02	0.29	0.19	0.31	0.12	0.02	0.46
Ni	-	0.30	0.62	-	-	-	0.16	0.31	-
Mg	1.70	1.55	1.33	1.64	1.79	1.66	1.80	1.73	1.68
Ca	0.02	0.02	0.02	0.04	0.02	0.01	0.01	0.12	0.21
Na	0.01	0.01	0.01	0.02	0.01	0.00	0.29	0.23	0.30
K	0.01	0.01	0.04	0.01	0.01	0.01	1.28	0.93	0.67
C	0.00	0.00	0.00	0.00	0.00	0.00	0.00	0.00	0.00
tot.	3.00	3.00	3.00	3.00	3.00	3.00	5.73	5.48	5.42
X^*_{Ca}							0.00	0.06	0.09
Mg#(Fe_{tot})	85	77	65	81	89	83	94	99	78

[a] cations calculated on the basis of 4 oxygens for olivine and 7 oxygens for phase X.

300 °C by Simons (1983) and at 250 MPa by Taniguchi et al. (1996). It has been investigated by powder diffraction by Simons (1983) and found to be structurally analogous to nyerite. Our high pressure potassic carbonate could thus be regarded as KMg-nyerite. Compared with magnesite in equilibrium with a lherzolite (Dasgupta and Hirschmann, 2006; Brey et al., 2008 and Ghosh et al., 2009) (fig. 4.4) our magnesites show a slightly higher content of siderite and a lower Mg# of 83-87 (compared to 90 in lherzolites) reflecting the slightly lower bulk Mg#. The Mg# of the KMg-nyerite varies between 87 and 96 and the X^*_{Ca} is 0.08-0.12. The sodium content of the KMg-nyerite is much higher at 13 GPa (up to 6.3 wt%; 0.47 Na pfu) than at 8 GPa (1.75 wt%, 0.14 Na pfu), as the added carbonate melt is more Na-rich at 13 GPa.

Phase X is the high pressure breakdown product of potassium amphibole (Luth, 1995) with a general formula $K_{2-x}Mg_2Si_2O_7H_x$ with x = 0-1. This phase is present in the experiments at reduced conditions at 13 GPa (fig. 4.1). In these experiments phase X is the major host for potassium (up to 20 wt%) and has the highest Na-content of all minerals (up to 3 wt% compared to up to 1.95 wt% in cpx) (tab. 4.3-4.5). The approximate composition is $(K,Na)_{1.2}(Mg,Ni,Fe)_2Si_2O_7H_{0.8}$, leading to an x in the above formula of about 0.8. In the more reduced experiments phase X substitutes the KMg-nyerite which hosts the potassium at oxidizing conditions.

Table 4.6: K-carbonate and magnesite composition

	LHZ-S2a	LHZ-S4a	LHZ-S1e	LHZ-S2a	LHZ-S4a	LHZ-S1e
	K-carb			mgs		
SiO_2 wt%	0.04	0.12	0.39	0.16	0.67	0.04
TiO_2	0.01	0.08	0.06	0.01	0.04	0.00
Al_2O_3	0.04	0.00	0.37	0.02	0.16	0.03
FeO	1.06	2.11	3.42	4.33	5.24	7.34
NiO	-	-	-	-	-	-
MgO	16.11	16.06	12.86	44.61	43.81	43.24
CaO	3.17	2.03	3.48	1.82	2.08	1.79
Na_2O	6.28	6.21	1.74	0.10	0.07	0.10
K_2O	29.43	29.61	33.01	0.07	0.40	0.87
CO_2	40.99	45.89	44.68	48.89	47.54	46.59
tot.	56.13	56.11	55.32	51.11	52.46	53.41
[a]Si pfu	0.00	0.00	0.02	0.00	0.02	0.00
Ti	0.00	0.00	0.00	0.00	0.00	0.00
Al	0.00	0.00	0.02	0.00	0.01	0.00
Fe^{3+}	0.00	0.00	0.00	0.00	0.00	0.03
Fe^{2+}	0.03	0.07	0.12	0.10	0.12	0.13
Ni	-	-	-	-	-	-
Mg	0.92	0.92	0.80	1.83	1.78	1.74
Ca	0.13	0.08	0.15	0.05	0.06	0.05
Na	0.47	0.46	0.14	0.01	0.00	0.01
K	1.44	1.46	1.75	0.00	0.01	0.03
C	2.00	2.00	2.00	2.00	2.00	2.00
tot.	5.00	5.00	5.00	3.92	3.91	3.89
X^*_{Ca}	0.12	0.08	0.14	0.03	0.03	0.03
Mg#(Fe_{tot})	0.96	0.93	0.87	0.35	0.34	0.24

[a] cations calculated on the basis of 6 oxygens.

The *oxides* present in our experiments (tab. 4.3) are a Ni-rich (up to 55 wt% NiO) or Fe-rich Mg-periclase in the reduced experiments, a Mg-rich iron-oxide at 13 GPa/1220 °C and a Mg-, Fe-rich titanium oxide at 8 GPa/1100 °C, the latter being too small to be quantitatively analyzed by electron microprobe.

4.3.2 Melt compositions and location of the solidus

A relative large quantity of melt has only been found in one experiment at 13 GPa/1350 °C under oxidized condition (fig. 4.1). This melt (tab. 4.7) is an alkali-rich carbonate melt containing about 20 wt% CaO, 10 wt% MgO (X^*_{Ca} of 0.56 and X^*_{Mg} of 0.39) and having very low SiO_2, Al_2O_3 and TiO_2 concentrations. If we compare this melt with the melt originally added to the lherzolite (S2a) and derived from the carbonated pelites at the same pressure and temperature conditions, Na_2O and MgO are increased by 4.9 and 4.8 wt%, respectively, while FeO, SiO_2, Al_2O_3 and TiO_2 contents have decreased, CaO and K_2O remaining relatively constant (tab. 4.7 and fig. 4.5). In the other two experiments at the same P-T-conditions but at more reduced conditions (red1 and red2) small patches of quenched carbonate melt or almost pure quenched potassium and CO_2 rich

fluid have been detected (tab. 4.7 and fig. 4.1). In the Fe°-capsule experiments yielding an oxygen fugacity of 0.7 log unite below the IW-buffer no CO_2-fluid or melt has been detected.

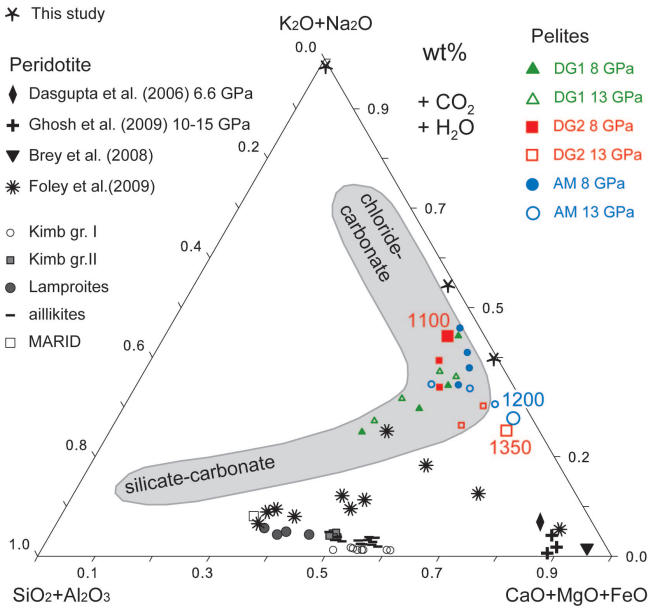

Figure 4.5: *Pseudo-ternary projection of carbonate and silicate melts after Freestone and Hamilton (1980). The melts generated from carbonated pelites at pressures between 8 and 13 GPa (chapter 2) are compared with the same melts equilibrated with a lherzolite at 13 GPa and 1350 °C. Melts produced from carbonated peridotite (Ghosh et al., 2009; Brey et al., 2008; Dasgupta and Hirschmann, 2007a) and K-rich peridotite (Foley et al., 2009) are also plotted in the same diagram, with the latter defining a continuum towards compositions similar to typical values for kimberlite (group I and II) (Mitchell, 1995), lamproites, aillikites (Francis and Patterson, 2009) and MARID's. Grey area defines the composition of several carbonate-rich melt/fluid inclusions found in diamonds (Klein-BenDavid et al., 2007)*

Figure 4.5 illustrates the compositions of carbonate melts generated from carbonated peridotites which are much more SiO_2 and Al_2O_3-rich and alkali-poor compared to the carbonate melts as produced in this study. Our melts are much more similar to the fluid and melt composition found as inclusions in diamonds from different localities, demonstrating that this kind of melts/fluid can be in equilibrium with an alkali and volatile rich mantle assemblage and is present during diamond formation.

Solidus location

The experiments of this study show that under oxidized condition the solidus of an alkali and carbonate rich lherzolite, with just traces of water (< 0.2 wt%) present, lays at temperature far below the mantle adiabat (fig. 4.6), e.g. at ca. 1300 °C at 13 GPa. This result is in agreement with the solidi as determined by Ghosh et al. (2009), Foley et al. (2009) and Brey et al. (2009). Ghosh et al. (2009) demonstrated that the presence of potassium (0.4 wt%) in H_2O-free carbonated peridotite can produce low fraction of ultrapotassic melts at very low temperature, the true solidus (suggested by lack of potassium during mass blance calculation) locating at temperatures near 1200 °C between 10 and 20 GPa. Brey et al. (2009) showed that in a volatile rich lherzolite, 3.63 wt% CO_2 + 2.22 wt% H_2O, the solidus is located between 1100 and 1200 °C at 10 GPa and below

Table 4.7: Melt composition on the three experiments at 13 GPa/1350 °C

	S2a	LHZ-S2a	LHZ-S2a red1	LHZ-S2a red2
SiO_2 wt%	0.84	0.26	0.87	0.14
TiO_2	1.70	0.05	0.03	0.02
Al_2O_3	1.97	0.11	0.05	0.02
FeO	8.00	2.30	0.92	0.06
NiO	0.00	0.00	1.19	1.55
MgO	5.79	10.52	6.23	0.22
CaO	22.30	20.98	17.66	0.03
Na_2O	5.05	9.99	10.51	0.19
K_2O	12.04	12.78	21.62	55.54
[b]CO_2	42.31	43.01	40.93	42.22
tot.	100.00	100.00	100.00	100.00
[a]Si pfu	0.04	0.01	0.03	0.01
Ti	0.06	0.00	0.00	0.00
Al	0.10	0.00	0.00	0.00
Fe	0.29	0.08	0.03	0.00
Ni	0.00	0.00	0.04	0.05
Mg	0.38	0.62	0.35	0.01
Ca	1.04	0.89	0.72	0.00
Na	0.43	0.76	0.78	0.02
K	0.67	0.64	1.05	2.91
X^*_{Ca}	0.61	0.56	0.65	0.14
X^*_{Mg}	0.22	0.39	0.32	0.83
Mg#	56	89	92	87

[a] cations calculated on the basis of 6 oxygens.

[b] CO_2 content (if no H_2O) calculated by difference of 100 and the measured analytical total.

1100 °C at 6 GPa. This temperatures have also been confirmed by Foley et al. (2009) at P $<$ 7 GPa in a extremely K_2O-rich (1.74 wt%) wet (0.63 wt% H_2O) carbonated (3.17 wt% CO_2) lherzolite. Our experiments at the most reducing conditions at 13 GPa didn't contain any carbonate melt thus indicating that under reducing conditions (below IW-buffer) all carbon is reduced to diamond (or graphite) shifting the solidus for a carbonated peridotite ($H_2O < 0.2$ wt%) to higher temperatures also in the presence of high amounts of alkalis.

4.4 Discussion

4.4.1 The diamond record

Most diamonds originating from pressures beyond the cratonic lithosphere ($>$ 7-8 GPa), contain majoritic garnets which composition matches eclogites rather than peridotites (Stachel, 2001). As asthenospheric and transition zone diamonds are almost exclusively derived from eclogitic para-

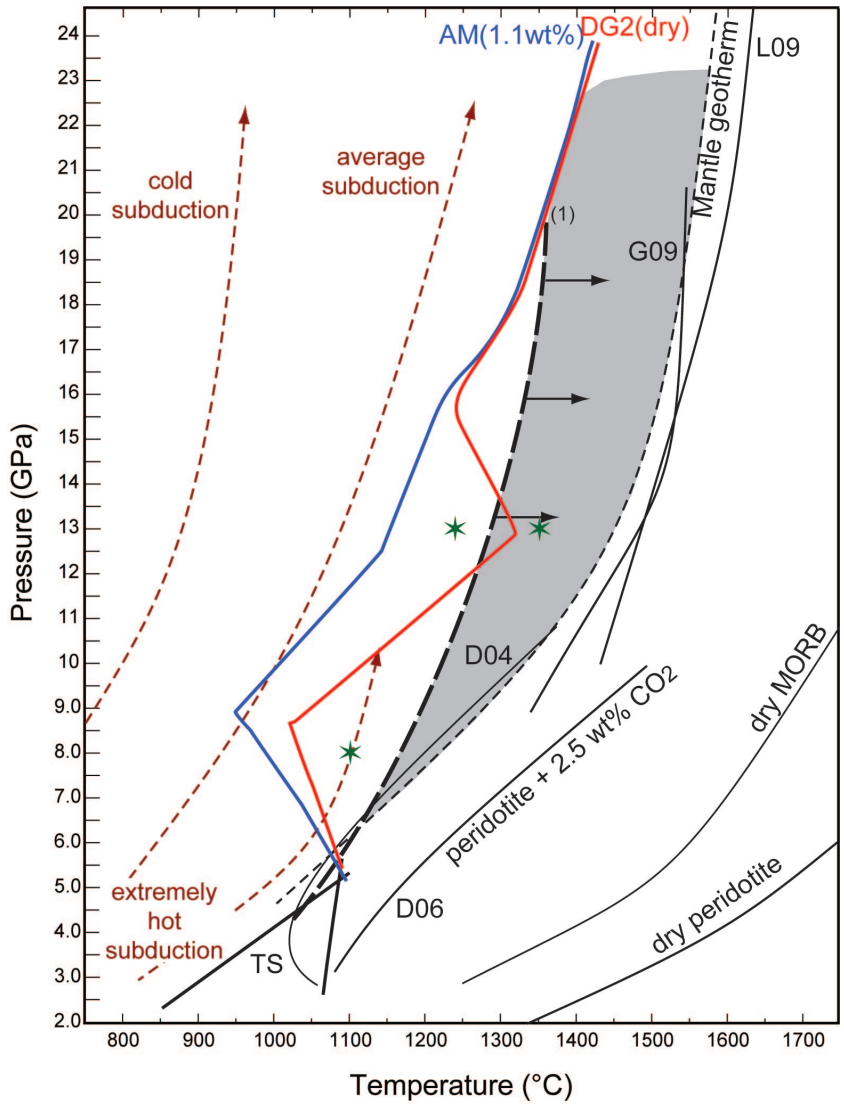

Figure 4.6: *P-T diagram showing various subduction P-T-paths and different solidi for (carbonated-) pelites (chapter 3), eclogites and peridotites. Comparison of solidus temperatures with typical subduction (dashed lines with arrows; Kincaid and Sacks, 1997) and normal mantle geotherm (Akaogi et al., 1989; thin dashed line) yields melting of carbonated pelites feasible in a very hot subduction or at the end of convergence when subduction slows down or stops and thermal relaxation occurs. The solidus of potassium-rich hydrous carbonated peridotite (1), modified after Ghosh et al. (2009), Foley et al. (2009) and Brey et al. (2009), is expected to move towards higher temperatures (small arrows) with increasing reducing conditions. The grey field represents the conditions where an alkalis-rich carbonate melt can infiltrate and percolate in the mantle under adiabatic and oxidized conditions. Lines: solidus of different subducted material between 2 and 24 GPa. TS: carbonated pelites (AM composition) solidus and cc-out reaction after Thomsen and Schmidt (2008b). D04, L09: solidi of carbonated eclogites after Dasgupta et al. (2004) and Litasov et al. (2008), respectively. D06, G09: solidus of dry carbonated peridotite after Dasgupta and Hirschmann (2006) and Ghosh et al. (2009), respectively. The solidus for dry peridotite is after Hirschmann (2000), and the one for the dry MORB after Yasuda et al. (1994). Stars represents P-T-conditions of the experiments of this study.*

geneses, Stachel (2001) suggested that E-type diamonds crystallize through redox reactions from relatively oxidized carbonated subducted crust, possibly involving mantle derived reduced fluids. Isotopically, some diamonds have extremely light carbon (Deines et al., 1991), which probably translates into an involvement of originally organic carbon. A direct origin of diamonds from organic matter was rejected by Cartigny et al. (2001) in favor of distillation processes involving methane and CO_2- fluids, but this subject remains open to debate (Stachel, 2001). It was experimentally shown that diamonds may form through reduction of carbonate melts (Arima et al., 2002) and thus diamonds might directly testify for the metasomatizing event in the mantle. Among the eclogite derived diamonds, there is a series of exotic ones, in particular from the Juina area in Brazil (Walter et al., 2008) that may not directly stem from MORB-eclogite but from carbonate melts of subducted crust (Walter et al. 2008) or from carbonate melts related to sedimentary eclogites. Inclusions ranging from K-hollandite, CAS phase, stishovite to kyanite/corundum are all minerals characteristic for aluminous pelites at high pressure (Irifune et al., 1994; see also chapter 2 and 3). Whether some diamonds can truly be traced back to subducted sediments is still matter of debate, nevertheless, crustal derived signatures in mineral inclusions and isotopes are evident and a mineralogical characterization as eclogite-derived does not necessary imply that the eclogites were always mafic in composition.

4.4.2 Oxidation state of the mantle

The oxygen fugacity in the uppermost asthenosphere is thought to be near QFM-2 (Ballhaus, 1993). Studies based on garnet peridotite from xenoliths of cratonic lithosphere as well as theoretical consideration suggest a general decrease of fO_2 with increasing pressure/depth in the earth mantle (fig. 4.7b) reaching values near the IW-buffer at 8 GPa and values between -2 to 0 log units below the IW-buffer at 13 GPa along a cratonic geotherm (Frost and McCammon, 2008 and citations within). The presence of a metal phase in the Earth deep mantle constrains the fO_2 to values below the iron-wustite equilibrium (Lauterbach et al., 2000; Rohrbach et al., 2007). In an ongoing study Rohrbach et al. (2009) have shown that carbonates (magnesite) and Fe$^\circ$ cannot coexist at pressures of the transition zone (14-23 GPa). In a metal saturated mantel, as expected for P $>$ 10-12 GPa, any carbonates will be unstable and reduced to elemental C (fig. 4.7a) unless the amount of carbonate exceeds the buffering capacity of the metal (Fe$^\circ$, Ni$^\circ$) thus allowing for oxidized carbonate-bearing mantle assemblages.

4.4.3 Redox-freezing, melting of potassium- and CO_2- metasomatized mantle

Our experiments show that under oxidizing conditions reaction of sediment derived carbonate melts with mantle assemblages at 13 GPa results in a $K_2Mg(CO_3)_2$-carbonate and less calcic, more sodio-magnesium carbonate melts which do not solidify at adiabatic temperatures (at 13 GPa). These experiments correspond to a natural situation where the metasomatizing carbonate melt imposes its intrinsic oxygen fugacity on the mantle, as expected to happen in the immediate vicinity of the sediment source. The absence of a carbonate reservoir at the infra-lithospheric

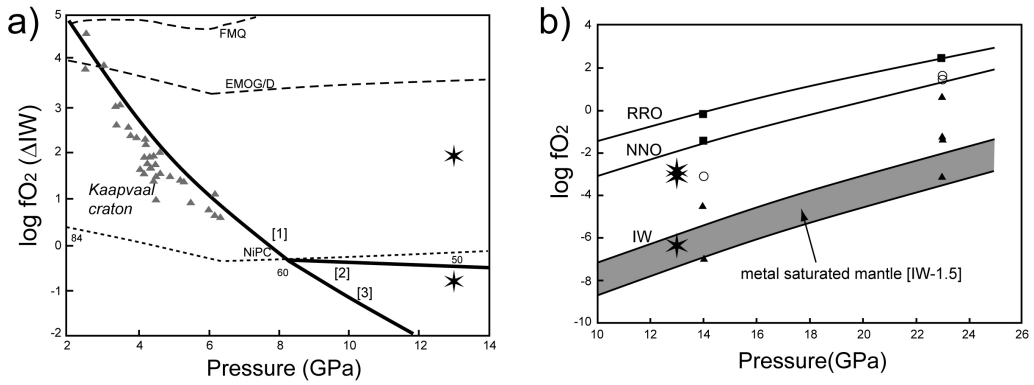

Figure 4.7: *a) Log $fO_2(\Delta IW)$ vs. P diagram after Frost and McCammon (2008) showing the increasing fugacity with depth along a cratonic geotherm. At 13 GPa an oxygen fugacity between 0 and 2 log unit below the IW-buffer is expected. (for the explanations of the different lines the reader is referred to Frost and McCammon, 2008). b) Carbonate speciation in natural peridotite as function of fO_2, P and T (modified after Rohrbach et al., 2009). Squares: magnesite stable; triangles: all carbonate reduced; circles: magnesite plus diamond present. Experiments were performed in Fe°, Ni°, Ni/Au, Re° and C capsules at 14 GPa, 1450 °C and 23 GPa, 1600 °C. fO_2 monitored with Ir° redox sensor is reported relative to Fe°-FeO (IW)-, Ni°-NiO (NNO)- and Re°-ReO_2 (RRO)-buffers (after Campbell et al., 2009). The data of this study (stars) at 13 GPa confirm the prediction of Rohrbach et al. (2009).*

thermal boundary layer however suggests that a mechanism for demobilizing the sediment-derived carbonate melts is acting within the mantle. Experiments under more reducing oxygen fugacity (NNO-1) corresponding to a situation, where volumetrically dominating, metal bearing mantle partly imposes its oxygen fugacity on the infiltrating carbonate melt, let most of the carbonate melt/carbonate disappear, and resulted in phase X coexisting with (Ni,Mg)-periclase, olivine, and cpx. Under even more reduced oxygen fugacities at or below the iron-wüstite (IW)-buffer, at conditions of fugacities similar to the one expected under a cratonic lithosphere at P $>$ 8 GPa, carbonate melts disappear in favor of diamond with the whole carbon-rich melt being effectively redox-frozen. In other words the low viscosity oxidized carbonate slab melts will percolate into the mantle along silicate grain boundaries where the dispersed iron of the mantle is situated. Most probably, only a few 100 to 1000 of meters are necessary to reduce the carbonate melts through reaction with the dispersed metal, they then will freeze and be immobilized. This redox freezing process will lead to the crystallization of diamonds which has been shown to be favored by the catalytic behaviour of a highly potassic carbonate-rich medium (Palyanov et al., 2007; Klein-BenDavid et al., 2007).

The few experiments of this work confirmed that the reaction of calcium-rich carbonate melts with a mantle assemblage causes the destabilization of orthopyroxene (opx) and the crystallization of clinopyroxene (cpx) as shown previously (Green and Wallace, 1988; Thibault et al., 1992; Dalton and Wood, 1993). The increased cpx/opx ratio transforms a typical lherzolite into a wehrlite, producing carbonated and potassium rich wehrlitic veins within the mantle, a process facilitated by the low density and viscosity and good wetting properties of carbonate melts (Dobson et al.,

1996; Hammouda and Laporte, 2000). The metasomatic alkali- and CO_2-rich mantle domains will remain stable as long as the redox and thermal conditions are stable. A new tectonic event or a new metasomatic episode (e.g. a plume, extensional tectonics, delamination of the lithosphere, etc) could in a later stage be responsible for a change of the redox conditions and thus promote redox melting through oxidation of the previously metasomatized mantle, giving origin to strongly alkaline and CO_2-rich magmas (Foley, 1992; Pilet et al., 2008). Such a magma would then be at the origin of different potassic melts such as group II kimberlites (Brey et al., 2009), lamproites, and kamafugites or aillikites (Francis and Patterson, 2009) (fig. 4.8).

Figure 4.8: *Cartoon illustrating the situation of subduction at the end of convergence. Successive and related relaxation of the isotherm leads to the melting of the most fertile lithologies responsible for potassium and CO_2 mantle metasomatism. With increasing temperatures the carbonated pelites at the top of the slab will start to melt generating alkalis-rich ($K_2O>>Na_2O$) carbonate melts which will infiltrate into the mantle and quickly percolate upwards reacting with the surrounding rocks (stage 1). The interaction of the oxidized carbonate melts with the highly reduced mantle promotes diamond crystallisation and leads to the freezing within the mantle of the CO_2-rich metasomatic agent (redox freezing). Before being reduced and frozen the carbonate melts also transform the mantle assemblage introducing a large volume of incompatible elements. Moreover, carbonate melts cause an increase of the clinopyroxene/orthopyroxene ratio and the crystallisation of carbonate phases (magnesite and K-rich carbonate). The successive melting (in a later stage 2) of these metasomatic reenriched mantle domains produces again alkalis-rich carbonate melts featured by mixed geochemical characteristics. The Melting event during stage 2 can be caused by increased mantle temperatures (plume or extensional tectonic) or by oxidation of the mantle (redox melting). The whole process, freezing and melting, could take place more than once during the subcratonic mantle evolution. On their way to the surface these melts react again with the surrounding mantle fractionating and assimilating minerals, evolving to highly alkaline and alkaline-associated rocks (kimberlites, orangeites, lamproites, aillikites, etc) found in various localities. (b) Stage 1: Reaction between potassium-rich carbonate melts and previously depleted sublithospheric mantle crystallizing magnesite, K-rich carbonate and increasing the cpx/opx ratio; the process produces carbonated wehrlites, carbonated reenriched lherzolites and a cryptic metasomatism in the surrounding mantle with increasing distance from percolation veins. The freezing of the carbonate melts due to the reaction with metal present along grain boundaries promote the formation of diamonds. (c) Stage 2: Melts generated by remelting of previously metasomatized alkalis and CO_2-rich mantle react with depleted lithospheric mantle producing again reenriched metasomatic (modal and cryptic) assemblages. Through assimilation and dissolution processes in their way to the surface, these melts evolve to magmas which are at the origin of alkaline, ultrapotassic or carbonatite volcanism/magmatism.*

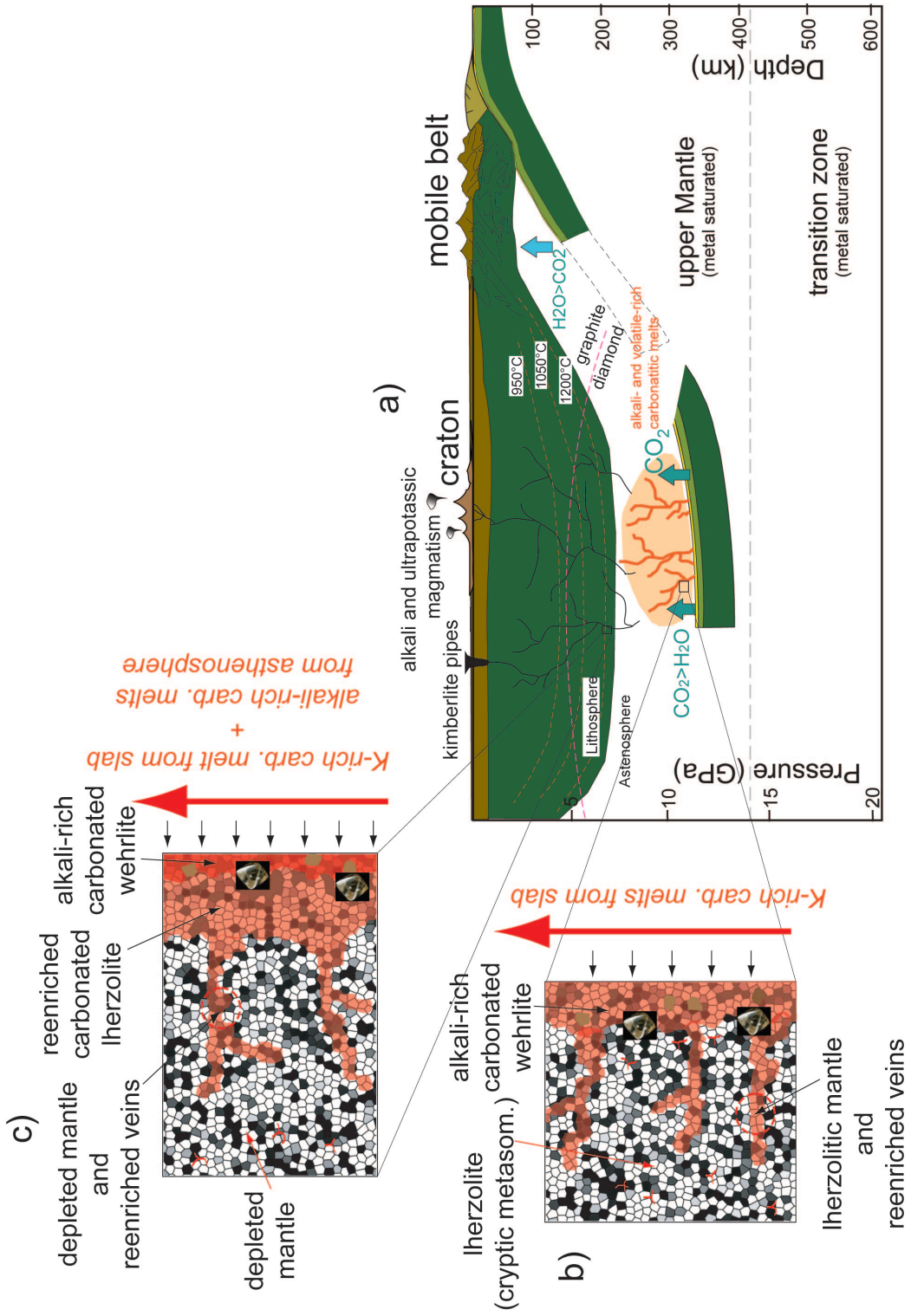
a)
mobile belt
craton
alkali and ultrapotassic magmatism
kimberlite pipes
Depth (km)
100
200
300
400
500
600
upper Mantle
(metal saturated)
transition zone
(metal saturated)
H2O>CO2
graphite
diamond
alkali- and volatile-rich carbonatitic melts
CO2
950°C
1050°C
1200°C
Lithosphere
Asthenosphere
CO2>H2O
Pressure (GPa)
5
10
15
20
K-rich carb. melts from slab
b)
lherzolite (cryptic metasom.)
alkali-rich carbonated wehrlite
lherzolitic mantle and reenriched veins
K-rich carb. melt from slab
+
alkali-rich carb. melts from asthenosphere
c)
depleted mantle and reenriched veins
reenriched carbonated lherzolite
alkali-rich carbonated wehrlite
depleted mantle

4.5 Conclusion

This study has shown that highly alkaline carbonate melts escaping from a subducted slab will undergo different reactions with the surrounding mantle depending on the local fugacity during this metasomatism. Under strongly reducing conditions as present in the mantle, these melts can effectively be redox frozen and promote diamond nucleation and the crystallization of minerals that would be characterized as ”eclogitic”, having compositions similar to the ones found as inclusions in many diamonds around the world.

Chapter 5

Trace Element Partitioning During Carbonated Pelite Recycling and Mantle Metasomatism by Alkali-rich Carbonate Melts at 8, 13 and 22 GPa: Sediment Signature in Mantle Components

Daniele Grassi and Max W. Schmidt
LA-ICP-MS measurements: Prof. Detlef Günther and Kathrin Hametner

Abstract

Subducted carbonated eclogitic pelites are the lithology with the lowest melting temperature at depths beyond major subarc dehydration. Melts generated at pressures $>$ 5 GPa are alkali-rich Ca-carbonate melts and are efficient metasomatic agents for adjacent mantle domains. Partition coefficients between residual minerals and such carbonate melts were determined at 8, 13, and 22 GPa at 1100-1500 °C. Compared to previous partitioning studies, clinopyroxene has higher jadeite contents (52-82 mol%) resulting into a larger compatibility for LILE and high D_{Ta}/D_{Nb} ratios. In garnet the compatibility of REEs increases from incompatible LREE (D_{La}=0.007 at 8 GPa) to slightly compatible Lu (D_{Lu}=0.93 to 3.45 at 8-22 GPa), DHFSE's increase with pressure from slightly incompatible at 8 GPa to highly compatible at 22 GPa always with $D_{Hf} > D_{Zr}$. K-hollandite-carbonate melt partition coefficients at 13 GPa are all $<$ 0.3 except for K itself. At 22

GPa Rb, Ba, K, Ta, and Pb become then slightly compatible in K- hollandite. At the same pressure (22 GPa), FeTi-perovskite has high D-values for HFSEs ($D_{HFSE} > 10$) as known for Ti-rich minerals. In the CAS phase, Pb, Th and U are compatible ($D_{Pb} > D_{Th} > D_U > 1.5$ with D_{Pb}/D_U = 15) leading to a strong fractionation of these elements during melting processes. Resulting bulk Dbulk residue/carbonate melt calculated from the measured partition coefficients increase with pressure for almost all elements. Bulk D_{Ta}/D_{Nb} ranges from 3 to 10^3, fractionation being particularly effective in the presence of clinopyroxene. At 22 GPa, i.e. for carbonated sediment melting in the transition zone, element fractionation strongly effects the Pb isotopic evolution. Primitive mantle normalized calculated carbonate melt trace element compositions show strong enrichment in incompatible elements including LILE and LREE and relative negative anomalies for Ti and Ta at 8 and 13 GPa and Hf, Zr, Ti and Ta at 22 GPa with absolute values close to mantle concentrations. Primitive mantle normalized patterns for the melt at 8 GPa are similar to ultrapotassic rocks and worldwide lamproites confirming the presence of a sedimentary component in the source region of these rocks. The melting of re-enriched mantle domains containing small amounts of our carbonate melts can produce the typical trace element signature observed in the South African kimberlites. The isotopic evolution of mantle contaminated by carbonate melts derived from carbonated pelites yields reservoirs which added to any known mantle compositions covers most of the compositions identified as the EM flavors of OIBs.

Keywords: trace elements, partitioning coefficients, carbonated pelites, carbonate melts, mantle metasomatism, ultrapotassic magmatism

5.1 Introduction

Carbonated pelites at pressures > 5-7 GPa, i.e. beyond the major dehydration occurring at subarc depths, are the lithology with the lowest solidus temperature (chapter 2 and 3). Combined with their position on the top of a stratigraphic slab column, this renders them the first lithology of the subducting oceanic crust to melt during crustal recycling into the mantle from 170 to $\geq$ 670 km depth. The high concentration of alkalis in carbonated pelitic or psammitic sediments is then reflected in the composition of the resulting alkali-rich calcic to dolomitic carbonate melts. When melting such sediments, carbonates disappear from the residue within a short temperature interval of less than 50-100 °C, nevertheless, melts stay carbonatitic even to temperature up to 400 °C above the solidus (chapter 2). Compared to silicate melts, carbonate melts have much lower viscosities and better wetting properties (Green and Wallace, 1988). Thus, they are extremely mobile (Hammouda and Laporte, 2000), will infiltrate the mantle and may percolate over long distances in very short time. Their particular physical characteristics allow carbonate melts to transport their distinct trace element and isotopic signature into large mantle domains which are then subsequently recognized as sediment component enriched mantle EMI and II.

An involvement of a distinct kind of subducted material has been recognized in the source region of many oceanic basalts (Hofmann and White, 1982; Weaver, 1991a,b), continental alkaline

rocks (Ulmer and Sweeney, 2002; Murphy et al., 2002; Becker and Le Roex, 2006; Gaffney et al., 2007) and some MORB (Rehkamper and Hofmann, 1997). In particular the extreme isotopic composition (e.g. low μ, low $^{206}Pb/^{204}Pb$, high $^{87}Sr/^{86}Sr$) and trace elements characteristics (e.g. low Nb/U, Nd/Pb) of pelagic material has been invoked by Chauvel et al. (1992), Eisele et al. (2002) and Weaver (1991a) to explain the singular EMI signature, i.e. low $^{206}Pb/^{204}Pb$, unradiogenic Nd ($^{143}Nd/^{144}Nd$), slightly radiogenic Sr ($^{87}Sr/^{86}Sr$), and high $^{207}Pb/^{206}Pb$ and $^{208}Pb/^{206}Pb$ combined with high Ba/Nb-, Sr/Nd- and low Ce/Pb- and Nb/U-ratios. Murphy et al. (2002) have used these characteristics to decipher the origin of the Gaussberg-lamproites, which are thought to derive from melting of sediments subducted into the transition zone where their remained isolated for a long time before melting.

Previous experimental studies on trace element partitioning between minerals and carbonate melts were conducted on typical mantle minerals (Klemme et al., 1995; Sweeney et al., 1995; Blundy and Dalton, 2000; Girnis et al., 2006; Brey et al., 2008; Dasgupta et al., 2009) and showed that extraction of only 0.1 wt% of carbonate melt would remove 30-60 % of many incompatible trace elements (Dasgupta et al., 2009). Furthermore, experimental studies have demonstrated that carbonate melts from basaltic or sedimentary eclogitic sources may form at pressures above 3 GPa (Hammouda, 2003; Dasgupta et al., 2004; Yaxley and Brey, 2004; Thomsen and Schmidt, 2008b; chapter 3). Eclogitic assemblages are quite different from typical mantle rocks in their mineralogy, mineral composition and phase abundance. Garnets are more calcic than in peridotitic bulk compositions and pyroxenes are omphacitic to jadeitic (Al- and Na-rich) compared to diopsidic clinopyroxene in mantle assemblages. In peraluminous and alkali-rich sedimentary eclogites, the situation is even more complex due to additional kyanite or corundum, which keeps the majorite component in garnet to a minimum, and especially because of the different potassic phases such as phengite, kfsp and K-hollandite which host large amounts of mostly LIL trace elements including Rb, Sr, Ba, K, Pb, La, Ce and Th.

The partitioning of trace elements between sedimentary rocks and silicate melts at pressure higher than 5 GPa has been investigated by Irifune et al. (1994), Aizawa et al. (1999) and Rapp et al. (2008) confirming the role of a sediment derived melt in the genesis of the typical EM signature. Nevertheless, at $>$ 5 GPa, carbonate bearing pelitic sediments melt at temperatures lower than carbonate free sediments, in particular above 8 GPa, where the destabilization of phengite would leave an almost dry residuum. A melting study on dry metapelites at 3-5 GPa (Spandler et al., 2010) indicates that at higher pressures the dry pelite solidus would be far above the mantle adiabat rendering melting of such a lithology unlikely. It is thus a carbonate melt of carbonated pelites that is more likely to transfer a sedimentary signature into the mantle. For this reason, this study investigates the trace element partitioning during carbonated pelite melting and in particular the partition coefficients between the potentially residual phases garnet, jadeite, K-hollandite, CAS-phase, FeTi-perovskite and near solidus carbonate melts at 8, 13 and 22 GPa. From these, we derive bulk partitioning coefficients and quantify and qualify the metasomatic effect of alkali-rich carbonate melts on the mantle and on its isotopic characteristics.

5.2 Experimental procedure and analytical technique

5.2.1 Starting material

The starting materials used in this study (tab. 5.1) are two carbonated pelites AM and DG2 (Thomsen and Schmidt, 2008b; chapter 2) mixed with various alkali-rich carbonate melts in equilibrium with these carbonated pelites in order to increase melt abundances in the charge. The hydrous composition AM corresponds to a Fe-rich calcareous clay from the Antilles simplified in the K_2O-Na_2O-CaO-FeO-MgO-Al_2O_3-SiO_2-H_2O-CO_2 (KNCFMASH-CO_2) system. The composition DG2 is a nominally anhydrous synthetic carbonated pelite in the TiKNCFMASH-CO_2 system; both are saturated in coesite/stishovite, kyanite/corundum and carbonates. The starting materials are made of powders of SiO_2, Al_2O_3, TiO_2, MgO, Na_2SiO_3, fayalite, K-feldspar and wollastonite, which were milled and grinded to < 5 μm and then mixed with $Al(OH)_3$, $CaCO_3$ and $MgCO_3$ to introduce the desired amount of H_2O and CO_2. The powders were kept in a desiccator under ambient temperature or in a vacuum oven at 110 °C. Carbonate melts are synthesized by mixing different amount of $MgCO_3$, $FeCO_3$, $CaCO_3$, K_2CO_3, Na_2CO_3, TiO_2, SiO_2 and Al_2O_3. The magnesite is a natural one from Oberdorf (Philipp, 1998), siderite has been synthesized in a hydrothermal apparatus at 2000 bar and 350 °C, sealing iron oxalate in a welded gold capsule 5.4 mm O.D., following the procedure from French (1971). To the carbonate melt compositions, a mix of 43 trace elements (TX7: Li, Rb, Cs, Be, Sr, Ba, Sc, Y, La, Sm, Dy, Yb, Lu, Ti, Zr, Hf, V, Nb, Ta, Mo, W, U, Th, In, Co, Ni, Cr, Zn, Cd, B, Ga, Ge, Bi, Sn, Pb, Ce, Pr, Nd, Eu, Gd, Tb, Er and Mn) was added resulting in a concentration between 50 and 150 ppm for each element after the final mixing of the carbonate melt with the pelitic composition in 1:1 and 2:1 ratios.

Table 5.1: Composition of the starting materials used in this study

	DG2	AM	am-S3b	DG2-S1a	am-S4b	DG2-S2a	am-S6a	DG2-S5a	trace 4
SiO_2 (wt%)	54.63	47.60	16.93	28.46	19.05	18.80	16.22	18.42	12.88
TiO_2	0.63	-	-	1.31	-	1.39	-	0.94	1.13
Al_2O_3	20.23	22.80	8.63	11.05	9.60	8.11	8.10	7.59	16.35
FeO	4.86	9.20	7.94	5.81	8.86	7.20	10.43	8.31	6.69
MgO	2.92	2.00	2.06	4.17	3.34	5.01	4.00	5.99	5.01
CaO	5.88	6.80	16.78	11.24	16.17	17.51	12.27	9.97	12.67
Na_2O	3.20	2.40	1.63	2.47	5.45	4.59	12.82	15.17	14.10
K_2O	2.21	3.60	19.23	11.57	9.87	9.13	6.01	4.09	3.35
CO_2	4.50	4.80	26.54	23.46	27.39	27.95	28.38	28.94	27.44
tot.	99.07	100.30	100.10	99.54	100.10	97.45	98.61	99.42	99.63

Carbonated pelites DG2 and AM are the same as in chapter 2 and 3.

5.2.2 Experimental procedure

Experiments at 8 and 13 GPa were conducted in a 600-ton Walker-type rocking multi-anvil (Schmidt and Ulmer, 2004). To improve equilibration and avoid too much zonation within the capsule, the

whole multi-anvil apparatus was rotated by 180 °C during the experiments, continuously during the first 30 minutes and then every 10 minutes during the reminder of the experiments. For the two experiments at 22 GPa a traditional 1000-ton Walker multi anvil was used. Tungsten carbide cubes with a truncation edge length of 11, 8, and 3.5 mm in combination with prefabricated MgO-octaedra of 18, 14, or 10 mm edge length and with natural pyrophyllite gaskets were used for the experiments at 8, 13, and 22 GPa, respectively. For the experiments at 8 and 13 GPa, the procedure has been described in chapter 2. The smaller 10/3.5 assembly is already fully described in Stewart et al. (2006). Temperature was controlled using a B-type ($Pt_{94}Rh_6/Pt_{70}Rh_{30}$) thermocouple and no correction for the effect of pressure was applied. Capsules were placed in the center of the furnace, and quenching was done by turning off heating power, followed by pressure unloading of about 15-20 hours. After the experiment, capsules (Au or $Au_{80}Pd_{20}$ depending on temperature (tab. 5.2)), were mounted longitudinally in epoxy resin and polished to the centre by dry polishing methods to avoid any loss of alkalis from the alkali-rich equilibrium carbonates and from the quench of the carbonate melts. During polishing, the open capsules were repeatedly impregnated with low viscosity resin to avoid any mechanical loss of quench carbonate melts. After being analyzed the capsules were kept in a desiccator under vacuum.

Table 5.2: Summary of the experiments

Run	capsule	P [GPa]	T [°C]	t [h]	assemblage
am-S3b	Au	8	1100	72	grt, cpx, ky, coe, melt
DG2-S1a	$Au_{80}Pd_{20}$	8	1350	48	grt, cpx, ky, coe, melt
am-S4b	Au	13	1220	72	grt, cpx, K-holl, stish, cor, carb, melt
DG2-S2a	$Au_{80}Pd_{20}$	13	1350	48	grt, cpx, K-holl, stish, cor, melt
DG2-S5a	$Au_{80}Pd_{20}$	22	1500	72	grt, CAS, K-holl, stish, cor, pv, mgs, melt
am-S6a	$Au_{80}Pd_{20}$	22	1500	72	grt, CAS, K-holl, stish, cor, melt
trace 4	$Au_{80}Pd_{20}$	22	1500	48	grt, CAS, K-holl, stish, cor, Na-carb, melt

5.2.3 Analytical methods

Electron microprobe

All experimental charges were first analyzed with a JEOL JXA8200 electron microprobe at ETH-Zürich with 15 kV acceleration voltage, 20 nA beam current for silicate minerals and 5 nA for carbonates and carbonate liquids. Acquisition times were 10 s for Na and K and 20 s for all other elements, measuring Na and K first to avoid diffusional losses. Beam diameters of 1 to 2 μm were used for all silicate and carbonate phases. Quenched melts, which exhibit beam damage, were analyzed using a defocused beam (3-20 μm).

Laser ablation-ICP-MS

Trace element analyses were obtained with laser ablation inductively coupled plasma mass spectrometry (LA-ICP-MS) at the Laboratory for Inorganic Chemistry, ETH Zurich. A 193 nm ArF

Excimer laser (Gunther et al., 1997) was coupled to an ELAN 6100 DRC ICP-MS. The laser operated at 17 J cm^{-2} using repetition rates between 5 and 10 Hz and crater sizes between 4 and 20 μm. Using helium as carrier gas, the laser aerosol produced in a standard cell was transported into the ICP. NIST 610 was used as external reference material. Internal standardization required for element concentration calculations employed major element concentrations (Al and Na) as determined by EPMA (for a detailed description of the technique, see Guillong et al. 2005). The background was acquired for 30 s followed by 15-40 s signal acquisition depending on the pit diameter used during the analysis. The data reduction and concentration calculation is based on the protocol described by Longerich et al. (1996).

5.3 Results

The phase relations and melting reactions of the dry and H_2O-bearing carbonated pelites have been fully defined in chapter 2 and 3. In these studies, the exact melt composition at near solidus conditions was determined through a reverse "sandwich" procedure (Falloon et al., 1997), in which a thick layer of carbonate melt, with the supposed composition derived from measurements of low melt fractions, is equilibrated with the carbonated pelite in question. This technique produces large homogeneous areas of melt as necessary for analysis using a defocused electron beam (EMPA) or a large laser beam diameter (LA-ICP-MS). The obtained melts at 8 and 13 GPa were in equilibrium with garnet, clinopyroxene, coesite/stishovite, kyanite/corundum, K-hollandite (only at 13 GPa), and in part with carbonate(s). At 22 GPa the carbonate melt coexists with garnet, CAS-phase, stishovite, corundum, K-hollandite, $\pm$ FeTi-perovskite, $\pm$ magnesite.

5.3.1 Mineral and melt major element composition

The minerals and melts obtained from the "sandwich" experiments (fig. 5.1) all have similar composition to the ones described in chapter 2 and 3 defining a SiO_2 and Al_2O_3 saturated eclogitic (8 and 13 GPa) or higher pressure (22 GPa) assemblage in equilibrium with highly alkalic Ca-carbonate melts.

Garnet forms subidiomorphic, 10-30 μm large and mostly inclusion-free crystals. Excess Si is low, at 8 GPa garnets have ca. 3.00 Si pfu, at 13 GPa $\leq$ 3.07 Si pfu, but reach 3.22 Si pfu at 22 GPa. Nevertheless, Si+Ti-Na-K remains below 3 in all experiments, the excess tetravalent cations thus compensating for alkalis. This lack of majorite component results from the coexistence of garnet with kyanite or corundum, resulting in maximum Al-contents. The most important component at 8 and 13 GPa is grossular which varies between 32 and 48 mol% depending on the bulk composition and temperature. At 22 GPa garnets coexist with the Ca-rich CAS-phase and have lower grossular-contents (13 mol%), and an increased almandine component (25 mol%) in the AM composition or pyrope component (24 mol%) in the DG2 composition. Mg# varies between 23 and 50 increasing with pressure, the DG2 composition crystallizing garnet with higher Mg content due to a higher bulk Mg# (52.4). In spite of the large compositional variability, the measured garnets can be

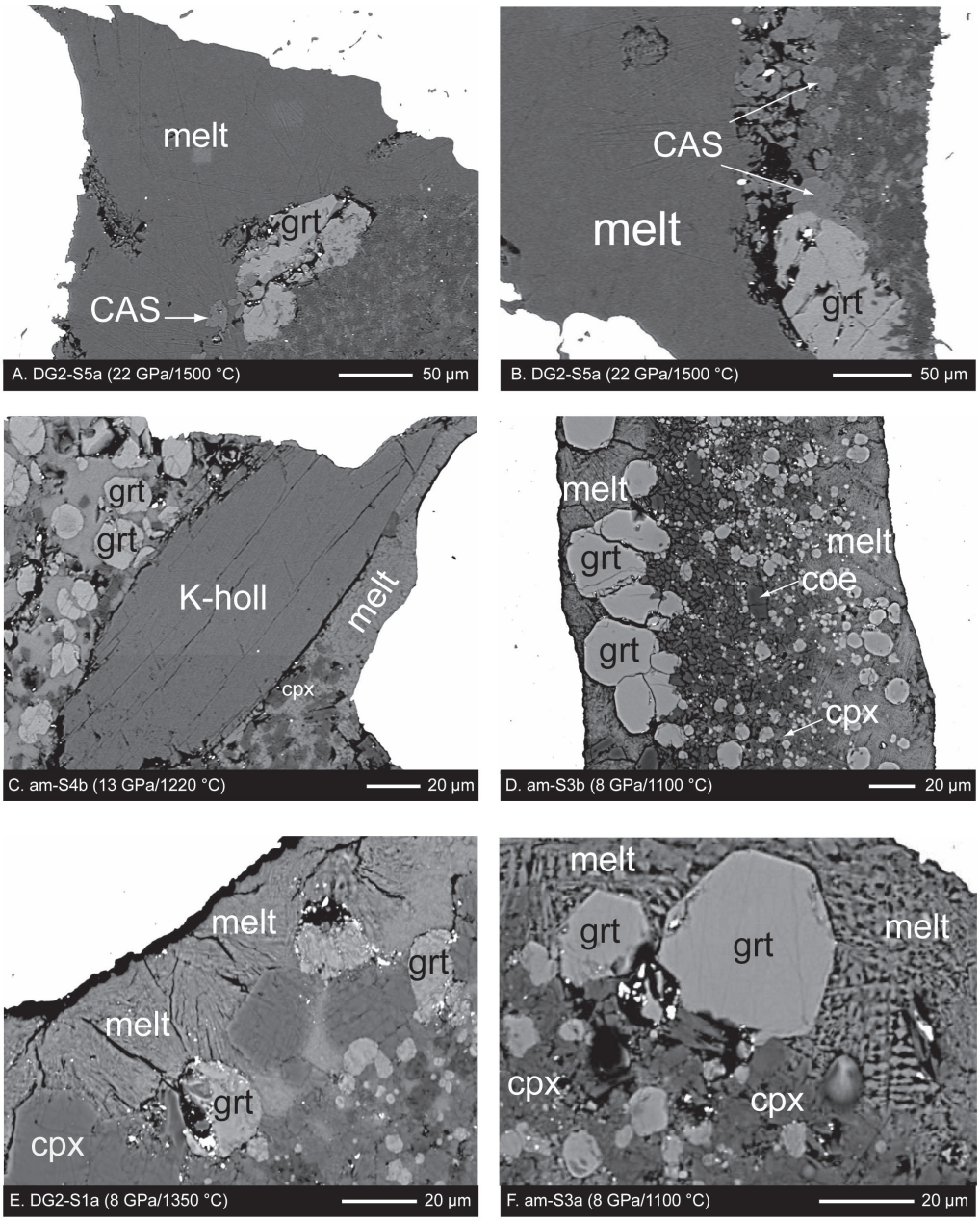

Figure 5.1: *BSE-images of run products. A: DG2-S5a (22 GPa/1500 °C); large garnet crystal in direct contact with Na-rich carbonate melts. B: DG2-S5a (22 GPa/1500 °C); large garnet crystal coexisting with smaller CAS crystals (ca. 10-20 µm) and with carbonate melt. Characteristically, large crystals form at the interface of the carbonate melt layer and the pelite layer. C: am-S4b (13 GPa/1220 °C); large K-hollandite crystal coexisting with garnet and small cpx aggregates. D: am-S3b (8 GPa/1100 °C); various garnet crystals coexisting with small aggregates of coesite, kyanite, and cpx. In this experiment, the amount of melt is large (ca. 40 wt%) and allows good measurements. E: DG2-S1a (8 GPa/1350 °C); 15-20 µm large cpx crystals, just sufficient in size to be measured by LA-ICP-MS coexist with garnet and carbonate melt. Note the quench features visible at this magnification in the carbonate melt and generally present in all quenched carbonate melts. F: am-S3b (8 GPa/1100 °C); large garnet crystal coexisting with small cpx and heterogeneous quenched carbonate melt.*

classified as eclogitic. Major differences with eclogitic garnet of basaltic origin are (i) the lower Na-solubility in our garnets (below 1.5 wt% at P $>$ 16 GPa) compared to ca. 3 wt% in basaltic compositions (Okamoto and Maruyama, 2004), (ii) the lower Si-contents contrasting garnets from basaltic compositions which at 8-18 GPa typically have 3.1-3.30 Si pfu, and (iii) the lower Mg# which varies between 49 and 75 for garnet from basaltic bulk compositions (Yasuda et al., 1994; Okamoto and Maruyama, 2004).

Clinopyroxenes form tabular 5-15 μm large grains which were often too small to be analyzed by La-ICPMS. Trace elements concentrations in cpx could be obtained only from 1 experiment with 57 mol% jadeite component (DG2-S1a). Cpx are extremely sodium- and alumina-rich with a jadeite component varying between 57 and 71 mol% at 8 GPa and between 80 and 82 mol% at 13 GPa. The Ca-Tschermak and Ca-eskolaite component are below the detection limit and Al(IV) below 0.05 apfu. Compared to eclogitic cpx from basaltic compositions the cpx of this study have much higher jadeite component (between 17 and 44 mol% at 6-15 GPa in basaltic compositions) and a lower Mg# (between 57 and 73 in our cpx and 72 to 81 in basaltic compositions) (Yasuda et al., 1994; Okamoto and Maruyama, 2004; Dasgupta et al., 2004).

K-hollandite forms elongated prismatic crystals up to 100 μm long and 40 μm wide (am-S4b). At 13 GPa, the Na-hollandite component is small ($<$ 4 mol%) but increases up to 12 mol% at 22 GPa.

CAS-phase crystallizes only at 22 GPa and contains large amount of alkalis, i.e. ca. 1.7 wt% K_2O and ca. 1.0 wt% Na_2O. Crystal sizes vary between 10 and 30 μm.

Carbonates coexisting with carbonate melt have a large compositional variability ranging from pure aragonite to Ca-poor and Fe-rich magnesite.

Table 5.3: Carbonate melt compositions

	am-S3b 8/1100	DG2-S1a 8/1350	am-S4b 13/1220	DG2-S2a 13/1350	am-S6a 22/1500	DG2-S5a 22/1500	trace 4
SiO_2 (wt%)	1.13	1.89	0.48	0.22	0.04	0.05	0.06
TiO_2	-	3.35	-	1.81	-	0.56	0.33
Al_2O_3	2.66	2.51	1.31	1.18	0.30	0.26	0.21
FeO	7.61	6.27	10.96	7.08	7.35	7.32	5.35
MgO	3.19	4.80	2.62	5.35	7.02	7.36	6.04
CaO	20.74	21.88	25.59	26.36	18.08	15.33	17.46
Na_2O	1.18	1.10	4.72	4.71	19.57	22.74	22.67
K_2O	22.96	20.62	12.05	9.43	3.37	3.27	2.90
$^a CO_2$	n.a.	37.59	n.a.	43.87	n.a.	43.12	44.99
tot.	59.47	100.00	57.73	100.00	56.72	100.00	100.00
K_2O/Na_2O (wt%)	19.48	18.82	2.55	2.00	0.17	0.14	0.13
X^*_{Ca}	0.67	0.65	0.68	0.67	0.54	0.49	0.58
X^*_{Mg}	0.14	0.20	0.10	0.19	0.29	0.33	0.28

^{a} CO_2 content calculated (if no H_2O) by difference of 100 and the measured analytical total

Melts measured in this study are alkali-rich Ca-carbonate melts (tab. 5.3). The K_2O/Na_2O

wt-ratio decreases with increasing pressure from ≥ 20, with ca. 20 wt% K_2O and $Na_2O < 1$ wt% at 8 GPa, down to values of ca. 0.13 with ca. 20 wt% Na_2O and ca. 3 wt% K_2O at 22 GPa. Si_2O and Al_2O_3 contents are always below 1.3 and 2.8 wt%, respectively, TiO_2 varies between 0.3 and 3.4 wt% depending on the coexisting phases and pressures. X^*_{Ca}- (0.49-0.71) and X^*_{Mg}- values (0.10-0.33) are similar to the ones found for melts generated from carbonated basaltic eclogites, which yield X^*_{Ca} 's of 0.44-0.75 and X^*_{Mg} 's of 0.11-0.43 (Hammouda, 2003; Yaxley and Brey, 2004; Dasgupta et al., 2004, 2005). These values are clearly different from peridotite derived carbonate melts, which have low X^*_{Ca} 's of 0.12-0-36 and higher X^*_{Mg} 's 0.53-0.81 (Dasgupta and Hirschmann, 2007; Brey et al., 2008; Ghosh et al., 2009).

5.3.2 Mineral/melt partition coefficients

Trace element concentrations in the analyzed garnet, clinopyroxene, K-hollandite, CAS-phase, and FeTi-perovskite are listed in the Appendix D. Resulting partitioning coefficients are then shown in fig. 5.2 and 5.3 and also listed in table 5.4 and in the Appendix D.

Cpx / carbonate melt

The partitioning of trace elements between cpx and the alkali-rich Ca-carbonate melts could only be measured in one experiments at 8 GPa (DG2-S1a) due to small cpx grain sizes in the other experiments. The measured cpx are slightly larger than 10 μm and thus could only be analyzed with a 4 μm beam diameter resulting in detection limits above the concentrations in cpx of several elements. The obtained partition coefficients are plotted in figure 5.2a and compared with the results of previous studies from different systems (Klemme et al., 1995; Sweeney et al., 1995; Blundy and Dalton, 2000; Adam and Green, 2001; Green and Adam, 2003; Dasgupta et al., 2009). $D^{cpx/carbonate\,melt}$ values for REEs, Hf and Sr of this study are comparable to those obtained by Dasgupta et al. (2009) for a peridotitic system, while those for LILE are more similar to the data of Green and Adam (2003) for omphacitic cpx in equilibrium with an aqueous fluid. The difference between our data and the work of Dasgupta et al. (2009) for LILE are most likely due the more jadeitic character of our cpx, allowing for the incorporation of larger amounts of LILE on the larger Na-site M2. The obtained differences in the partition coefficients between Nb (D_{Nb} = 0.008) and Ta (D_{Ta} = 11.79) are much more extreme than those previously obtained (D_{Nb} of ca. 0.2 and D_{Ta} of ca. 10 in Green and Adam (2003); D_{Nb} and D_{Ta} both with values of ca. 0.001 in Dasgupta et al. (2009), leading to an extreme fractionation of these elements in the derived melts. One possible explanation might be related to the larger incompatibility of Ta compared to Nb in carbonate melts (Veksler et al., 1998).

Garnet / carbonate melt

Garnet/carbonate melt partition coefficients from the different pressures are plotted in figure 5.2b and compared with available experimental data from other systems (Green et al., 1992; Sweeney et al., 1992; Sweeney et al., 1995; Brey et al., 2008; Dasgupta et al., 2009). Similar to previous

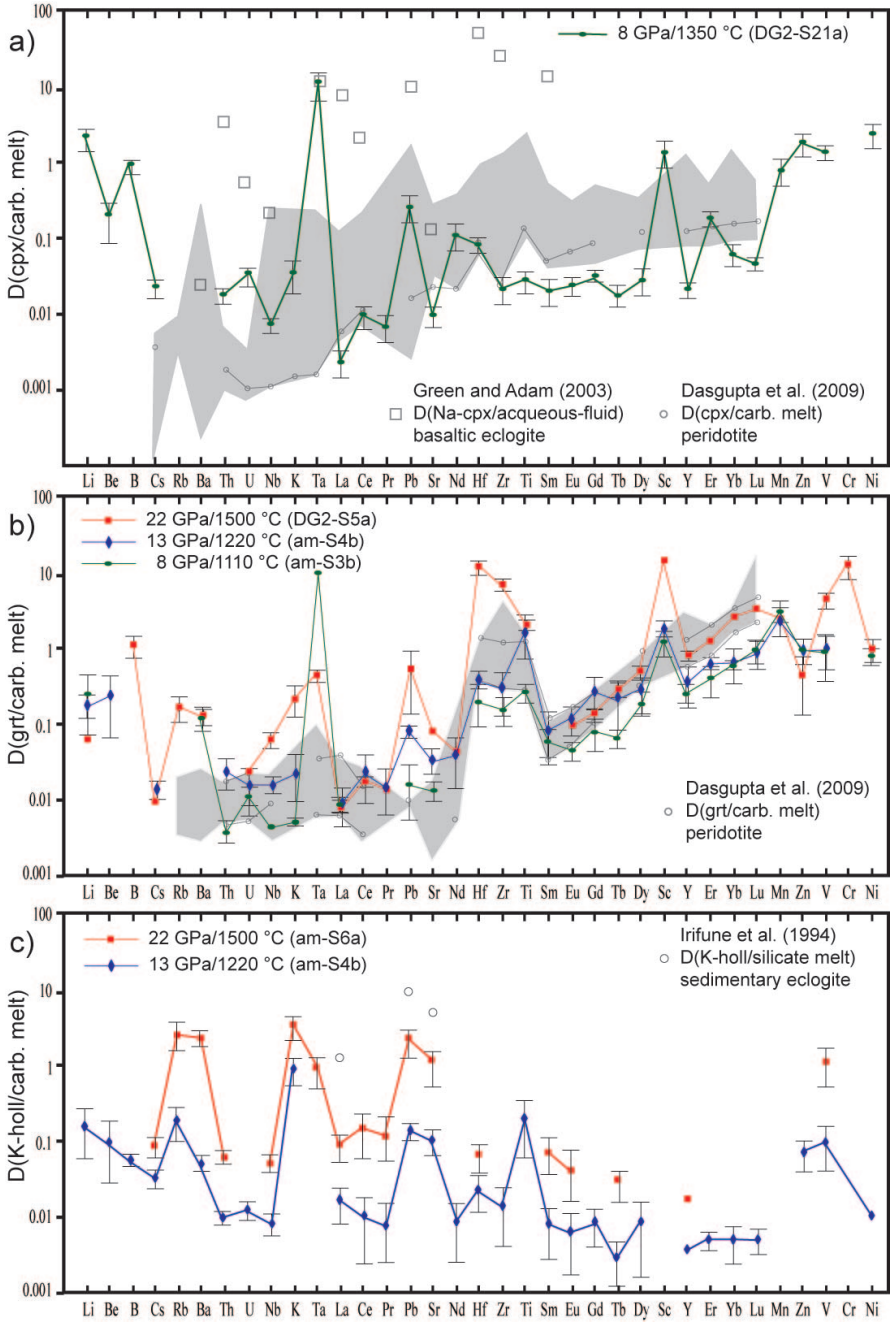

Figure 5.2: *Trace element partition coefficients between a) clinopyroxene, b) garnet and c) K-hollandite and carbonate melt as measured in this study. a) Data for comparison are from Dasgupta et al. (2009) for diopsidic cpx/carb. melt and from Green and Adam (2003) for omphacitic cpx/fluid. The grey area envelopes cpx/carb. melt partition coefficients from Klemme et al. (1995), Sweeney et al. (1995), Blundy and Dalton (2000) and Adam and Green (2001). b) Garnet/carb. melt partition coefficients composing the shaded area are from Green et al. (1992), Sweeney et al. (1992, 1995) and Brey et al. (2008). The extremely high partition coefficients of Ta and the following extreme fractionation of Nb/Ta in cpx and garnet at 8 GPa are unusual and need further confirmation.*

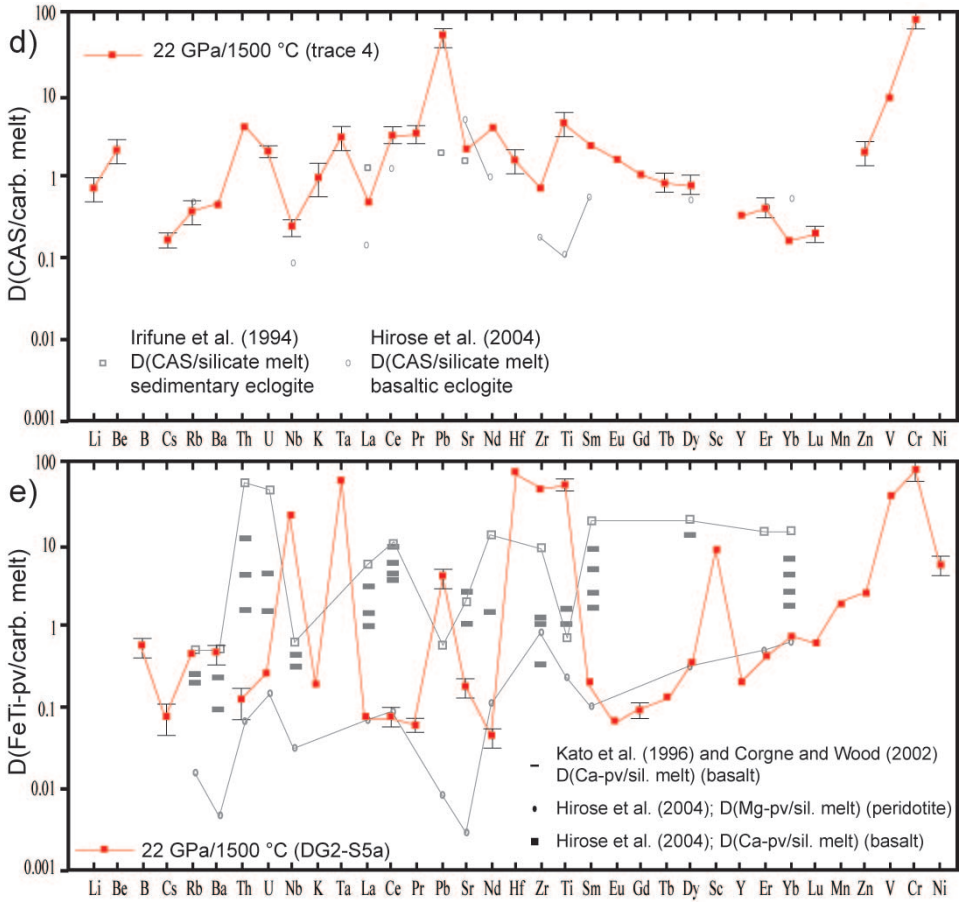

Figure 5.3: *Trace element partition coefficients between a) CAS-phase and b) FeTi-perovskite and carbonate melt obtained in this study. Data for comparison for perovskite labeled "Ca-pv (basalts)" are from Kato et al. (1996) and Corgne and Wood (2002) and are for mineral/silicate melt pairs, not for carbonate melts. Similar, the few partition coefficients available for the CAS-phase are from experiments with the CAS phase in equilibrium with silicate melts.*

work, D-values for REE show a steady increase from highly incompatible La (D_{La}=0.005 at 8 GPa) to slightly compatible Lu (D_{Lu}=0.994-3.448 at 8 to 22 GPa). Similar to what was deduced by Dasgupta et al. (2009) from data at 6.6-8.6 GPa, the compatibility of HFSE including Zr, Hf and Ti increases with increasing pressure, from fairly incompatible at 8 GPa to moderately compatible at 13 GPa and highly compatible at 22 GPa. At 8 and 13 GPa $D_{Ti} > D_{Hf} > D_{Zr}$ but this changes to $D_{Hf} > D_{Zr} > D_{Ti}$ at 22 GPa. Particularly interesting are D_{Ta} and D_{Nb} with D_{Ta}/D_{Nb} ratios being 5 and 103 at 22 and 8 GPa, respectively, resulting in strongly negative Ta anomalies in the carbonate melt, in particular at 8 GPa. D_{Pb} in our garnet is much higher than the previously measured 0.006-0.02 at 6.6-8.6 GPa (Dasgupta et al., 2009) and increases with pressure from 0.017 at 8 GPa to 0.56 at 22 GPa.

K-hollandite / carbonate melt

Figure 5.2c illustrates the trace element partition coefficients between K-hollandite and the alkali-rich carbonate melt (K_2O/Na_2O wt% ratio of about 3 and 0.14 at 13 and 22 GPa, respectively). All measured trace element partition coefficients $D^{K-holl/carbonate\,melt}$ at 13 GPa are < 0.3 and thus residual K-hollandite is not expected to leave a strong signature at this pressure. Ds for REE are 0.017 to 0.005 for D_{La} to D_{Lu}. HFSE and LILEs have somewhat higher partition coefficients with D_{Rb} and D_{Sr} above 0.1 and a D_{Sr}/D_{Nd} ratio of about 12. With increasing pressure the compatibility of potassium in K-holl increases (chapter 3); this behaviour is also observed for all other elements measured at 22 GPa including Rb, Ba, Pb and Sr which at 22 GPa reach partition coefficients above 1. Irifune et al. (1994) determined partition coefficients for La, Pb and Sr between K-hollandite and silicate melt at $P > 16$ GPa which are much higher than those of K-hollandite and carbonate melt, but which show similar D_{Pb}/D_{Sr} and D_{La}/D_{Pb} ratios.

CAS / carbonate melt

The element partition coefficients between CAS-phase and carbonate melt (fig. 5.3a) show a steady decrease of the REEs with the LREEs (D_{Ce} = 3.55) more compatible than the HREEs (D_{Lu} = 0.198). The highest partition coefficients are observed for Pb (30.75) and Th (3.72). The low D_{Nb} (0.12) leads to extreme D_{Th}/D_{Nb} and D_{Pb}/D_{Nb} ratios. In general our partition coefficients are similar to previous data by Irifune et al. (1994) and Hirose et al. (2004) for silicate melts. The high compatibility of Pb, U and Th in this phase leads to a strong fractionation of these elements during partial melting, resulting melts having higher U/Pb and lower Th/U ratios than the source rock. Such a melt would eventually evolve to more radiogenic Pb compositions than the unmelted source.

Fe(Ti)-perovskite / carbonate melt

Trace element partition coefficients between FeTi-perovskite and carbonate melt (fig. 5.3b) show a strong increase of the REEs from La to Lu, from D_{La} = 0.091 to D_{Lu} = 0.704. The HFSE including Hf, Zr, Nb and Ta show extremely high partitioning coefficients between 26 and 87, analogous to what is well known for Ti-rich phases such as rutile and sphene. Our data for REE partitioning are comparable to those from Hirose et al. (2004) for Mg-perovskite in equilibrium with a silicate melt (fig. 5.3b). The 2-3 orders of magnitude higher partition coefficients of HFSE for FeTi-perovskite than for Mg-perovskite can be attributed to the Ti-enrichment and to the carbonatitic character of our melt, the latter in general accommodating limited amounts of high valence cations.

5.3.3 Crystal chemistry and lattice strain modeling

In order to evaluate the effect of the crystal chemistry on the partitioning of trace elements between minerals and melt, the lattice strain theory (Blundy and Wood, 1994; Wood and Blundy, 1997) is

one of the most useful tools available. This theory allows the fitting of the partition coefficients (D_i) by using a near-parabolic equation (5.1)

$$D_i = D_0 \exp\left(\frac{-4\pi E N_A \left[\frac{r_0}{2}(r_i - r_0)^2 + \frac{1}{3}(r_i - r_0)^3\right]}{RT}\right) \tag{5.1}$$

where r_i is the radius of the cation, E the Young's modulus of the crystallographic site, r_0 the radius of the site, and D_0 the strain free partition coefficient of cations with radius r_0. N_A is the Avogadro's number, R the gas constant and T the temperature in K. In the following three subsections we apply the strain model to partitioning between cpx, garnet, and perovskite and their related equilibrium carbonate melt.

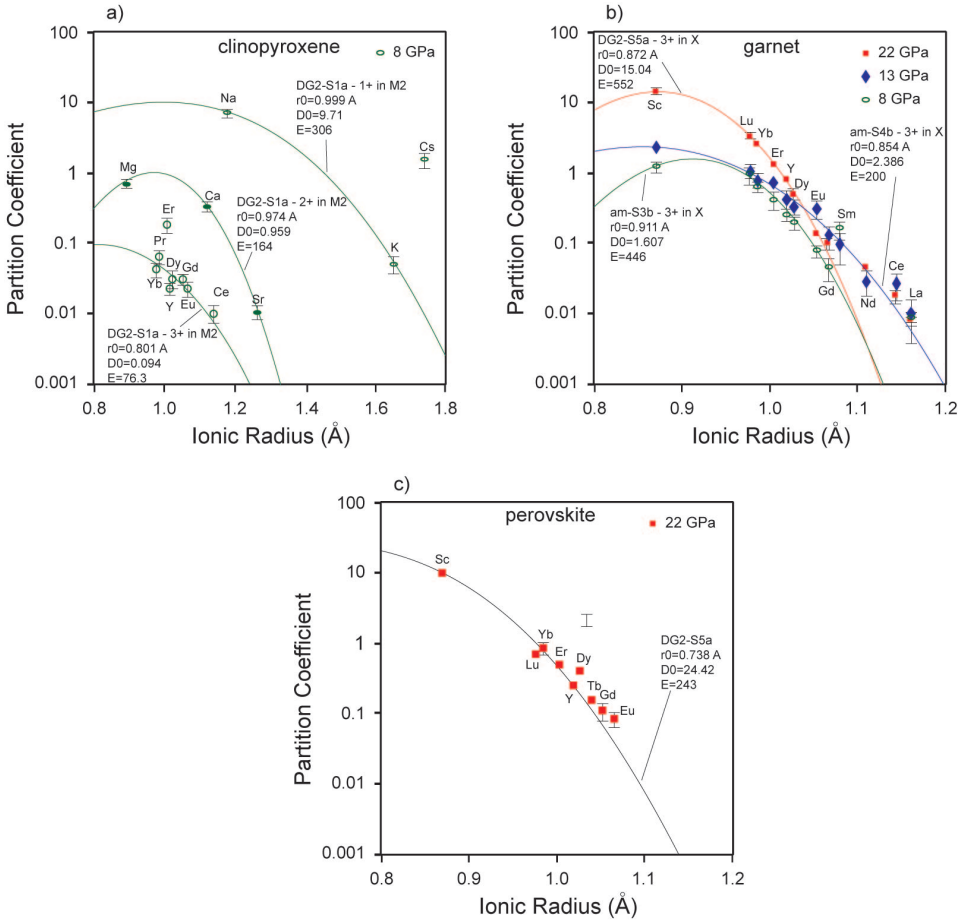

Figure 5.4: *Onuma type parabolas for mineral/carbonate melt partition coefficients as a function of ionic radius. a) mono-, di-, and tri-valent cations incorporated into the M2 site of cpx at 8 GPa. Note the spread on the tri-valent cations not allowing fitting a well constrained parabola. The small crystal size < 15-20 micron allowed only for ablation pit diameters of 4 micron yielding relatively poor results. b) tri-valent cations in the X site of garnet at different pressures. Note the changes in parabola width and D_0 and r_0 with pressure. c) Same plot for Ca-perovsikite/melt partition coefficients of tri-valent cations (MREE and LREE + Y + Sc) entering the Ca-site. Best-fit parabola have been calculated using the lattice strain model of Blundy and Wood (1994). The VIII-fold coordinated ionic radii are from Shannon (1976).*

Clinopyroxene

The lattice strain model was applied to the mono-, bi-, and tri-valent cations entering the M2 site (fig. 5.4a) of cpx (experiment DG2-S1a, 8 GPa, 1350 °C). The tri-valent REE and Y do not define a nice parabola, probably due to analytical difficulties related to the small size of the cpx-crystals. Fitted values for E (164 GPa) and D_0 (0.959) for the bivalent cations are in good agreement with the results of Dasgupta et al. (2009) at 8.6 GPa; on the other hand, the resulting r_0 (0.974) of our experiments is a bit lower than the one of Dasgupta et al. (2009). Our fitted values for mono-valent cations are completely different from those obtained by Blundy and Dalton (2000) for cpx/carb. melt pairs (E of 93; r_0 from 1.25 to 1.30 and D_0 between 0.28 and 0.36). In this work we obtain much larger values for D_0 (9.71) and E (306 GPa) and smaller values for r_0 (0.999) due to the more jadeitic (Na-rich) character of our cpx.

Garnet

Figure 5.4b shows the Onuma parabolas for the trivalent cations (REEs, Y and Sc) entering the dodecahedral site X in garnet at 8 (am-S3b), 13 (am-S4b) and 22 GPa (DG2-S5a). The increasing compatibility of the smaller tri-valent cations with increasing pressure is reflected in the fitted D_0 values which increase from 1.6 to 15.0 from 8 to 22 GPa. The fitted data for the Young's modulus E are between 200 and 552 GPa and for r_0 between 0.854 and 0.911 with the experiments at 13 GPa showing the lowest values. Compared to Dasgupta et al. (2009) (E from 577 to 739; r_0 from 0.905 to 0.911 and D_0 between 4.35 and 10.01) our experiment at a similar pressure of 8 GPa shows a slightly larger value for r_0 and lower values for E and D_0 probably due to a the higher amount of grossular component in our garnet and by the low content of alkalis in their melt. Van Westrenen and Draper (2007) developed a thermodynamical model capable to predict r_0, D_0 and E values through lattice strain modeling. Predicted r_0 and E values, which largely depend on the crystal site properties fit well within error, but their model fails to predict D_0 which differ from our fitted values by a factor thousand?!. This discrepancy is attributed to the large difference between our alkali-rich carbonate melt and the anhydrous silicate melts on which the D's of their study are based.

Perovskite

The partition coefficients for the REE in perovskite (fig. 5.4c) suggest that the LREEs behave differently from the MREE and HREE and do not show a steadily increasing compatibility. Such a behavior was already observed by Hirose et al. (2004) for Mg-perovskite, who suggested partitioning into a different and bigger site for the LREEs in the Mg-perovskite structure. Our fitted parabola values are 0.738 for r_0, 24.42 for D_0 and 243 GPa for E. The D_0 and E values are in good agreement with the one obtained by Hirose et al. (2004) for Ca-perovskite, on the other hand the fitted value for r_0 is clearly lower than previously obtained values for Ca- as well as for Mg-perovskite (Corgne and Wood, 2002; Hirose et al., 2004). At present, it remains open whether this

discrepancy in the r_0 may be attributed to the high Ti-contents, and the large quantity of ferrous and ferric iron, or is caused by an insufficient quality of the data.

5.3.4 Bulk partition coefficients for high pressure pelitic residues in equilibrium with carbonate melts

For each pressure, bulk partition coefficients were calculated using average mineral/melt partition coefficients in combination with mineral modes from chapter 2 and 3 at near-solidus conditions (tab 5.4 and fig. 5.5). Despite repeated experiments, we were not able to crystallize all minerals at all pressures large enough for measurement by LA-ICP-MS. Thus, the cpx/carbonate melt partition coefficients at 8 GPa were also employed at 13 GPa; and the missing K-hollandite/carbonate melt partition coefficients at 22 GPa were estimated from the data at 13 GPa considering an increased compatibility of all elements with pressure (tab. 5.4). Residual carbonate was not considered as the melt fraction increases rapidly at the solidus until all carbonate is exhausted, leading to complete decarbonation of the sediments.

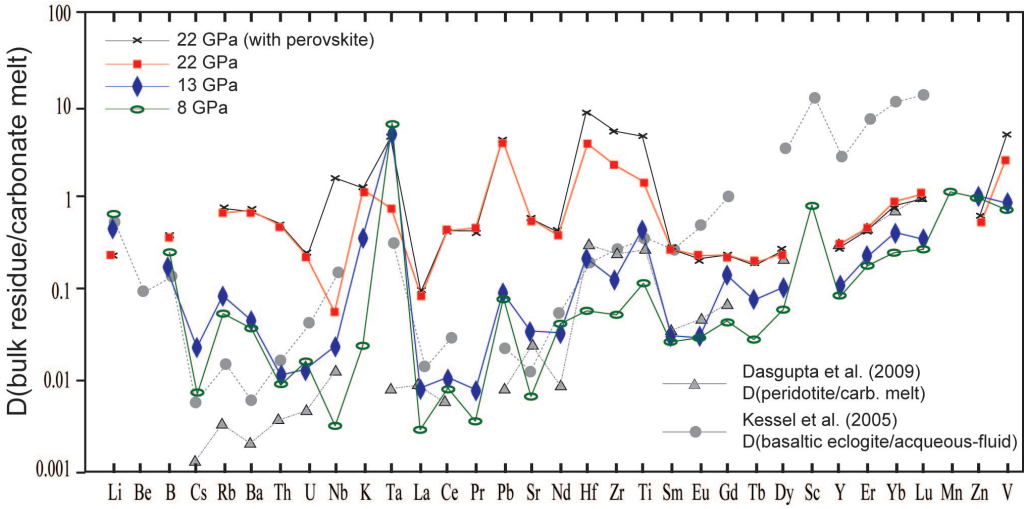

Figure 5.5: *Bulk partition coefficients calculated in this study for silica and alumina saturated eclogitic sediments in equilibrium with highly alkaline carbonate melt at 8, 13 and 22 GPa. The data are compared with the bulk partition coefficients applicable to carbonate melt generated from garnet lherzolite at 6-9 GPa after Dasgupta et al. (2009) and with the bulk partitioning coefficients between a basaltic eclogite and supercritical liquid at 6 GPa after Kessel et al. (2005). Bulk Ds of this study for the most incompatible elements (LILE) are similar to the values obtained by Kessel et al. (2005), on the other hand values for REE + Y are comparable with the data of Dasgupta et al. (2009).*

The calculated bulk partition coefficients $D^{bulk\,residue/carbonate\,melt}$ (fig. 5.5) at 8 and 13 GPa result in generally incompatible LILE and HFSE with partition coefficients mostly between 10-1 and 10-2 reaching the lowest values for Nb and La (tab. 5.4). For the REE, bulk partition coefficients increase steadily from highly incompatible La to slightly incompatible Lu. Notably high relative bulk residue/carb. melt partition coefficients are obtained for Ta, Hf, Zr, Ti and

Table 5.4: Average mineral/melt partitioning coefficients and calculated bulk Ds

P[GPa]	8		13		22				8	13	22	22 pv
Mineral	grt	cpx	grt	K-holl	grt	K-holl	CAS	Fe(Ti)pv	bulk	bulk	bulk	bulk
hline Li	0.258	2.393	0.187	0.161	0.067		0.720		0.697	0.452	0.236	
Be	2.130	0.207	2.130	0.100	2.130		2.171		0.702	0.668	0.979	
Na_2O	0.155	9.621	0.212	0.094	0.088	0.061	0.042	0.042	2.537	0.475	0.047	0.045
MgO	1.216	0.898	1.351	0.009	1.303	0.001	0.049	0.535	0.617	0.439	0.412	0.383
K_2O	0.031	0.046	0.029	1.665	0.006	4.234	0.509	0.016	0.023	0.340	1.172	1.167
CaO	0.782	0.236	0.519	0.025	0.473	0.068	0.719	0.031	0.301	0.173	0.247	0.219
Ti	0.235	0.101	0.940	0.544	2.559		2.690	64.497	0.120	0.418	1.322	4.840
V	1.164	1.282	2.044	0.103	4.923	1.101	6.006	45.614	0.686	0.809	2.493	4.793
FeO	2.139	0.322	2.112	0.049	2.333	0.032	0.265	5.145	0.750	0.666	0.775	0.959
Co	2.358	0.628	1.504	0.008	2.641	0.188		3.574	0.881	0.534	0.829	0.912
Ni	1.126	2.433		0.011	1.058			6.363	0.972	0.702	0.341	0.654
Zn	1.604	1.915	2.544	0.072	0.475		2.020	2.833	0.984	1.045	0.544	0.661
Ga	2.629	5.353	5.118	0.978	14.500	8.897	61.797	34.738	2.185	2.493	14.334	14.947
Rb		a0.02	0.173	0.198	0.173	2.436	0.384	0.505	0.058	0.091	0.736	0.752
Sr	0.014	0.010	0.037	0.107	0.082	1.156	2.004	0.210	0.007	0.033	0.577	0.562
Y	0.250	0.023	0.324	0.004	0.856	0.017	0.334	0.241	0.082	0.098	0.299	0.270
Zr	0.145	0.022	0.437	0.014	7.467		0.437	53.982	0.050	0.133	2.268	4.991
Nb	0.005	0.008	0.073	0.008	0.066	0.049	0.174	26.449	0.003	0.024	0.054	1.552
Sn		4.710	12.901	0.272	12.901	0.272			5.148	4.513		
Cs	0.006	0.021	0.037	0.034	0.010	0.087		0.089	0.007	0.020		
Ba	0.117	a0.02		0.053	0.134	2.267	0.682	0.515	0.041	0.047	0.717	0.733
La	0.007	0.002	0.016	0.017	0.008	0.088	0.507	0.091	0.003	0.008	0.089	0.088
Ce		0.010	0.024	0.011	0.018	0.142	3.553	0.090	0.010	0.011	0.487	0.451
Pr	0.006	0.007	0.015	0.008	0.014	0.111	3.461	0.071	0.004	0.007	0.466	0.430
Nd		0.105	0.052	0.009	0.047		3.700	0.139	0.043	0.033	0.500	0.464
Sm	0.062	0.022	0.086	0.008		0.080	1.951	0.233	0.024	0.030	0.290	0.278
Eu	0.073	0.024	0.081	0.006	0.104	0.040	1.543	0.080	0.028	0.029	0.234	0.216
Gd	0.121	0.031	0.424	0.009	0.142		1.541	0.106	0.045	0.129	0.253	0.235
Tb	0.076	0.018	0.242	0.003	0.310	0.030	0.868	0.151	0.028	0.073	0.208	0.193
Dy	0.130	0.075	0.303	0.009	0.519		0.812	0.403	0.059	0.101	0.273	0.263
Er	0.453	0.189	0.645	0.005	1.323		0.472	0.480	0.187	0.217	0.461	0.422
Yb	0.742	0.062	1.287	0.005	2.737		0.079	0.834	0.242	0.383	0.829	0.751
Lu	0.926	0.046	1.066	0.005	3.448		0.198	0.704	0.294	0.317	1.054	0.935
Hf	0.116	0.084	0.757	0.024	12.696	0.066	1.647	86.737	0.057	0.237	3.974	8.306
Ta	11.437	11.789		0.185	0.473	0.928	3.170	70.210	6.533	5.158	0.779	4.710
Pb	0.017	0.275	0.086	0.142	0.564	2.262	30.746	4.009	0.076	0.095	4.601	4.454
Th	0.014	0.019	0.025	0.010	0.025	0.059	3.720	0.141	0.009	0.012	0.488	0.452
U	0.023	0.037	0.016	0.013	0.024		1.861	0.302	0.016	0.013	0.260	0.255

[a] Green and Adam (2003)

cpx at 13 GPa is taken from 8 GPa; missing data for K-holl at 22 Gpa are guessed from 13 GPa; Mass Fraction: 8 GPa (0.31 grt, 0.26 cpx, 0.24 ky, 0.19 coe); 13 GPa (0.29 grt, 0.15 cpx, 0.19 K-holl, 0.14 ky, 0.23 stish); 22 GPa (0.29 grt, 0.26 K-holl, 0.12 CAS, 0.10 cor, 0.22 stish); 22 GPa mit pv (0.25 grt, 0.26 K-holl, 0.11 CAS, 0.06 pv, 0.10 cor, 0.22 stish). The partitioning between coe/stish and ky/cor are assumed to be zero for trace elements. Major elements partitioning are taken from ems analysis.

Sc. With pressure increasing to 22 GPa, the general compatibility of the LILE, HFSE and LREE increases by one order of magnitude. For the HREE this increase is much lower, leading at 22 GPa to fairly flat REE-patterns. At 22 GPa, a Fe-Ti rich perovskite formed in the residue of the Ti-bearing DG2 composition. From the Ti-concentration of the coexisting solid phases, it can be expected that this Fe-Ti-rich perovskite forms in the residue of sediments with approximately $>$ 0.5 wt% TiO_2. This perovskite increases the bulk partition coefficients 2- to 6-fold for Hf, Zr, Ti, and Ta, and 30-fold for Nb, and thus has primarily the effect of sharpening the characteristic subduction signature. The generally high compatibility for some HFSE such as Hf, Zr, and Ti is attributed to the generally low solubility of HFSE in carbonate liquid (Veksler et al., 1998; Chakhmouradian, 2006). Characteristic for our results is the outstanding compatibility of Ta at 8 and 13 GPa even in the absence of any particular Ti-rich host-phase. Ta and Nb are strongly fractionated in all our experiments: $D_{Nb/Ta}^{Bulk\,residue/carb.\,melt}$ is $5{\cdot}10^{-4}$, $5{\cdot}10^{-3}$, $6{\cdot}10^{-2}$ and $3{\cdot}10^{-1}$ at 8, 13 and 22 GPa, the latter with or without residual perovskite. Such a fractionation would yield an explanation for the negative Ta anomalies and high Nb/Ta ratios observed in several highly enriched magmas related to subduction processes (Munker, 1998; Prouteau et al., 2000).

Figure 5.5 also compares bulk partition coefficients of lherzolite/carbonate melt at 8.6 GPa (1265-1470 °C Dasgupta et al., 2009) and of basaltic eclogite/supercritical fluid at 6 GPa (1200 °C, Kessel et al., 2005) with our data at 8 GPa (1100-1350 °C): Large similarities exist for our and the Dasgupta et al. (2009) data set for the REE, which are less fractionated in a carbonatitic system than in the aqueous system by Kessel et al. (2005). On the other hand, the behaviour of LILEs in the eclogitic sediment/carbonate melt system correlates better with the eclogitic basalt/supercritical silicate liquid system by Kessel et al. (2005), probably due to more comparable amounts and compositions of garnet and cpx in the residuum at 6 to 8 GPa.

5.4 Discussion

5.4.1 Carbonate melt metasomatism as function of pressure

Melt compositions were calculated using the bulk partition coefficients of table 5.4 and a simple batch melting equation with 8 % partial melting (F = 0.08) simulating the situation after complete melting out of carbonates in a carbonated sediment containing ca. 3 wt% CO_2. Such a choice is justified by the short melting interval of 50-100 °C necessary for carbonates to disappear above the solidus (chapter 2 and 3). From the melting reactions defined in these studies, it can be deduced that carbonate fraction and melt fraction would change proportionally to at least 10-15 wt% CO_2 at all pressures, above this concentration a different melting equation would apply. The trace element composition of the simulated sediment is from Plank and Langmuir (1998) (Antilles Fe-cc clay), completed for missing elements (including for example Zr, Hf, Nb and Ta) by concentrations from Othman et al. (1989) for pelagic sediments. Furthermore, Kelley et al. (2005) showed that dehydration during subduction may lead to a strong fractionation of Pb, U and Th. For this reason we assumed that 65 wt% of Pb and 25 wt% of U were lost at sub-arc depths.

As to be expected from the bulk partition coefficients, the most enriched carbonate melt is generated at 8 GPa, the least enriched at 22 GPa (fig. 5.6a and Appendix D). The grade of melt-enrichment roughly anti-correlates with the number of phases present in the residuum. At 8 GPa the only phases retaining significant amounts of trace elements are garnet and cpx. At 13 GPa the residue comprises K-hollandite in addition, and at 22 GPa K-hollandite, CAS-phase, and perovskite, which, combined with the absence of cpx, changes the behaviour of several elements drastically. The strong negative Ta anomaly at 8 and 13 GPa is due both to the high compatibility of Ta in cpx and to the extremely low solubility of Ta in carbonate melts (Veksler et al., 1998). Although the absence of cpx at 22 GPa reduces the negative Ta anomaly in the carbonate melt, the formation of Fe-Ti-rich perovskite re-increases the anomaly to an amplitude similar to 8 and 13 GPa. The bulk residue/carbonate melt partition coefficients of Ta remain thus much higher than that of Nb, but at 22 GPa are accompanied by a negative Nb anomaly if Fe-Ti rich perovskite is residual (fig. 5.6a). The increased negative anomaly of the HFSEs including Hf, Zr and Ti with pressure is mostly caused by the increased compatibility of these elements in garnet (fig. 5.2b), again, this anomaly will be amplified when Fe-Ti-rich perovskite remains residual. At 22 GPa Hf and Zr are considerably more compatible in garnet than Ti, resulting in a weak negative Ti-anomaly compared to melts at lower pressures. Furthermore, the CAS-phase strongly retains Pb, Th and U (in this sequence; tab. 5.4), thus lowering the mobility of these elements.

The characteristic signature of the carbonate melts at 8 GPa with negative Ti-, Nb- and Ta anomalies, high primitive mantle normalized Hf/Ti- and Th/Nb-ratios, positive primitive mantle-normalized Nb/Ta-ratios and high K and Pb concentrations match well with many ultrapotassic rocks (fig. 5.6b) including lamproites (Murphy et al. 2002; Mirnejad and Bell, 2006), and some Italian kamafugites, shoshonites and leucitites (Peccerillo et al., 1988; Peccerillo, 2005; Avanzinelli et al., 2009). The presence of a sedimentary component in the source regions of these rocks was postulated by many authors (Ringwood et al. 1992; Murphy et al. 2002). Our data corroborate this interpretation and furnish details on the possible nature of this sediment component and a simple mechanism how to transport this sediment signature including potassium and CO_2 into the mantle source region of such alkaline magmas.

The two enriched mantle types EM I and EM II are commonly explained by adding different amounts of oceanic crust including a small sedimentary component (pelagic or more terrigenous) to an average mantle composition (Hofmann and White, 1982; Weaver, 1991a,b; Chauvel et al. 1992; Eisele et al. 2002). These enriched mantle reservoirs are characterized by similar trace element abundances with high LILE/HFSE- and LREE/HFSE-ratios (Weaver, 1991a). Higher Ba contents and related higher Ba/Th and Ba/Nb-ratios distinguish the EM I from the EM II signature, the latter is thought to originate from a more Ba-depleted sediment type. The comparatively low Ba-concentration of the sediments used in this study should thus be more suitable to produce a signature more similar to EM II than EM I (Weaver, 1991b). Nevertheless, comparing our melts with the EM I and EM II mantle types (figs. 5.6a,c) (Weaver, 1991a; Hofmann, 1997; Lustrino and Dallai, 2003), both carbonate melt patterns at 8 and 13 GPa match quite well with the EM I signature, especially for the HFSE except of Ta. On the other hand the melt at 22 GPa with no

perovskite in the residuum is more similar to the EM II enriched mantle.

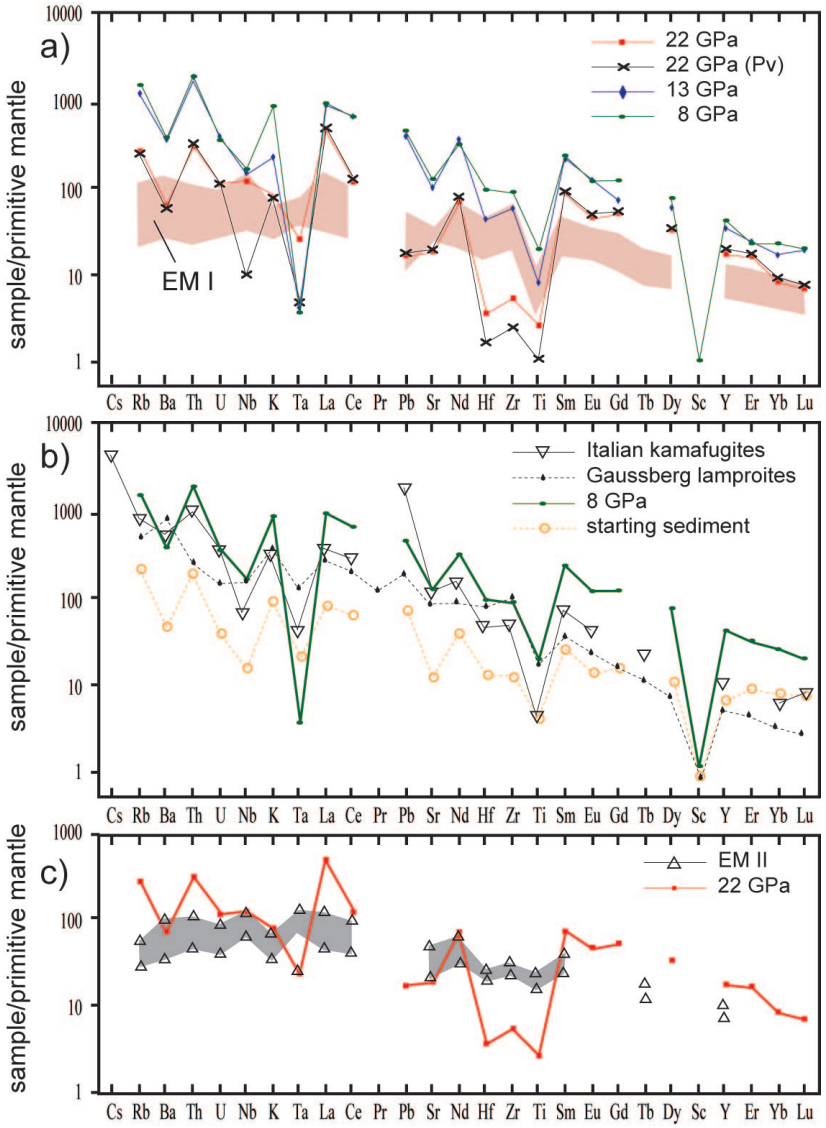

Figure 5.6: *Calculated trace element patterns for alkaline carbonate melts generated from silica and alumina saturated eclogitic carbonated sediments at 8, 13 and 22 GPa. The synthetic carbonate melt compositions at the different pressures were calculated using the bulk partition coefficients of this study (tab. 5.4) and a simple batch melting equation with 8 % melt fraction simulating a complete decarbonation for a sediment containing ca. 3 wt% CO_2. a) Comparison between our calculated compositions at the different pressures and the typical EM I OIB patterns (Weaver, 1991a; Hofmann, 1997; Lustrino and Dallai, 2003). b) Comparison between the calculated melt at 8 GPa and different ultrapotassic rocks (Gaussberg lamproites are after Murphy et al. (2002); data for the Italian kamafugites are after Peccerillo (1998) for which a contamination from continental materials (sediment pattern after Plank and Langmuir, 1998) has been postulated by the cited authors. c) Comparison between the calculated melt at 22 GPa with no perovskite in the residuum and typical EM II pattern in OIB (Weaver, 1991a). All data are normalized to primitive mantle value (Hofmann, 1988).*

5.4.2 Radiogenic isotopes and the mantle end members HIMU, EM I and II

Table 5.5: Summary of the calculated radiogenic isotops evolutions

	PM	DM	1.5Ga old sedi	8GPa melt	13GPa melt	22GPa melt	22GPa melt(pv)
Initial							
$^{87}Rb/^{86}Sr$=	0.03	0.02	[a]0.20	-	-	-	-
$^{147}Sm/^{144}Nd$=	0.32	0.21	0.13	-	-	-	-
μ=	0.13	10.00	2.00	-	-	-	-
κ=	0.53	2.70	6.30	-	-	-	-
subduction fractionation				**after 8% batch melting**			
25% U loss + 65%Pb loss							
$^{87}Rb/^{86}Sr$=	-	-	2.00	0.13	0.13	0.16	0.15
$^{147}Sm/^{144}Nd$=	-	-	0.13	0.15	0.13	0.20	0.20
μ=	-	-	4.30	6.79	7.82	58.13	57.14
κ=	-	-	8.40	9.03	8.46	5.07	5.32
At 1.5 Ga							
$^{87}Sr/^{86}Sr$=	-	-	0.7069	0.7069	0.7069	0.7069	0.7069
$^{143}Nd/^{144}Nd$=	-	-	0.5104	0.5104	0.5104	0.5104	0.5104
$^{206}Pb/^{204}Pb$=	-	-	16.2	16.2	16.2	16.2	16.2
$^{207}Pb/^{204}Pb$=	-	-	15.4	15.4	15.4	15.4	15.4
$^{208}Pb/^{204}Pb$=	-	-	35.8	35.8	35.8	35.8	35.8
Today							
$^{87}Sr/^{86}Sr$=	0.7045	0.7025	0.7112	0.7097	0.7098	0.7104	0.7102
$^{143}Nd/^{144}Nd$=	0.5126	0.5132	0.5117	0.5119	0.5117	0.5124	0.5123
$^{206}Pb/^{204}Pb$=	17.51	18.00	17.33	17.98	18.25	31.43	31.17
$^{207}Pb/^{204}Pb$=	15.36	15.43	15.49	15.56	15.58	16.82	16.79
$^{208}Pb/^{204}Pb$=	38.01	37.70	38.58	40.53	40.90	58.49	59.22
ϵNd=	0.00	10.96	-18.66	-14.41	-17.98	-4.77	-5.88

[a] *Rehkämper and Hofmann (1997) assumed a value of 0.61. We prefer to use a lower ratio due to the mixed character of our sediment.*

The isotopic composition of the primitive mantle (PM) is taken from Hofmann (1997). The depleted mantle (DM) isotope ratios at 1.5 Ga are from Rehkämper and Hofmann (1997). 1.5 Ga old sediment consists of 94 wt% pelagic sediment with an initial $^{87}Sr/^{86}Sr_i$ of 0.7074 (Rehkämper and Hofmann 1997) and 6 wt% marine carbonates with an initial $^{87}Sr/^{86}Sr_i$ of 0.706 and a Sr concentration 10 times higher than in the pelagic sediment (Mirota and Veizer 1994; Plank and Langmuir 1996). Values for the fractionation of Pb and U during subduction dehydration are in agreement with Kelley et al. (2005).

In order to test the metasomatic effect of the sediment derived highly alkaline Ca-carbonate melts on the isotopic composition of the mantle, we calculate the evolution of the different melts derived from a 1.5 Ga old sediment that consists of 94 wt% pelagic sediment with an initial $^{87}Sr/^{86}Sr_i$ of 0.7074 (Rehkamper and Hofmann, 1997) and 6 wt% marine carbonate with an initial

$^{87}Sr/^{86}Sr_i$ of 0.706 and a Sr concentration 10 times higher than in the pelagic sediment (Mirota and Veizer, 1994; Plank and Langmuir, 1998). Again we assumed a subduction related fractionation of U and Pb during dehydration prior to the melting of the sediments leading to 65 wt% Pb loss and 25 wt% U loss (Kelley et al. 2005). The isotopic evolution was calculated assuming zero time between sediment age and melting directly yielding an evolution age of 1.5 GPa for the melt reservoirs. The result of this model is summarized in table 5.5 and illustrated in figure 5.7. The isotopic compositions of the melts generated at 8 and 13 GPa after 1.5 Ga of isotopic evolution in a closed system are quite similar and comparable to the compositions of their source sediment. This reflects the only minor fractionation of the parent/daughter elements U/Pb, Th/Pb, Rb/Sr and Sm/Nd during melting at these pressures. The resulting reservoirs are then dominated by the high concentrations of U, Th, Pb, Rb, Sr, Sm, and Nd in the carbonate melts and evolve towards compositions with radiogenic $^{87}Sr/^{86}Sr$ (0.7097-0.7099) and unradiogenic $^{143}Nd/^{144}Nd$ (0.5117-0.5119) (fig. 5.7c), and with a Pb isotopy that is more radiogenic for $^{207}Pb/^{204}Pb$ (15.56-15.58) and $^{208}Pb/^{204}Pb$ (40.53-40.90) and less radiogenic for $^{206}Pb/^{204}Pb$ (17.98-18.25) than that of depleted mantle types (fig. 5.7a). When migrating into the mantle, these carbonate melts produce a mixed reservoir which fits well the EM I mantle type. The high degree of trace element enrichment in the carbonate melts, compared to the unmolten sediment source renders the physically easy-to-achieve migration of these melts into the mantle one order of magnitude more effective than a mechanical bulk mixing-process between sediments and mantle (0.1 wt% of melt has the same effect as adding 1-3 wt% of sediment). At this point, it should be emphasized that bulk mixing of carbonated pelite and mantle at $\geq$ 6 GPa (chapter 3) is not an option: assuming a near adiabatic mantle, the solidus of carbonated sediments would be overstepped by several 100 °C and thus carbonate melt melting and melt migration would be unavoidable.

Melting at 22 GPa in the presence of the CAS-phase and perovskite in the residuum produces stronger fractionation, in particular within the U-Th-Pb system, leading to isotopic compositions with different characteristics than the melts and sediments at 8 and 13 GPa. Carbonate melts at 22 GPa evolve to a strongly radiogenic Pb isotopy ($^{207}Pb/^{204}Pb$ = 16.79 - 16.82, $^{208}Pb/^{204}Pb$ = 58.50 - 59.22 and $^{206}Pb/^{204}Pb$ = 31.17 - 31.43), a more radiogenic $^{87}Sr/^{86}Sr$ (0.7102-0.7104), but less radiogenic $^{143}Nd/^{144}Nd$ (ca. 0.5123) than carbonate melts generated at 8 and 13 GPa. The mixing of such melts with a depleted mantle will create a mixture which fits very well with the EM II Nd- and Sr signature but which is slightly too radiogenic in $^{206}Pb/^{204}Pb$ for EM II.

These model calculations demonstrate that by varying the pressure of melting of carbonated clastic sediments, carbonate melts result that by mixing with a silicate mantle domain will cover the entire range of isotopic EM-like mantle signatures. Varying the deposition and melting age of the sediment, the sediment composition, and the devolatilisation history before melting, a broader range of isotopic compositions could be obtained; nevertheless, the chosen parameters are suitable for generating the EM mantle array.

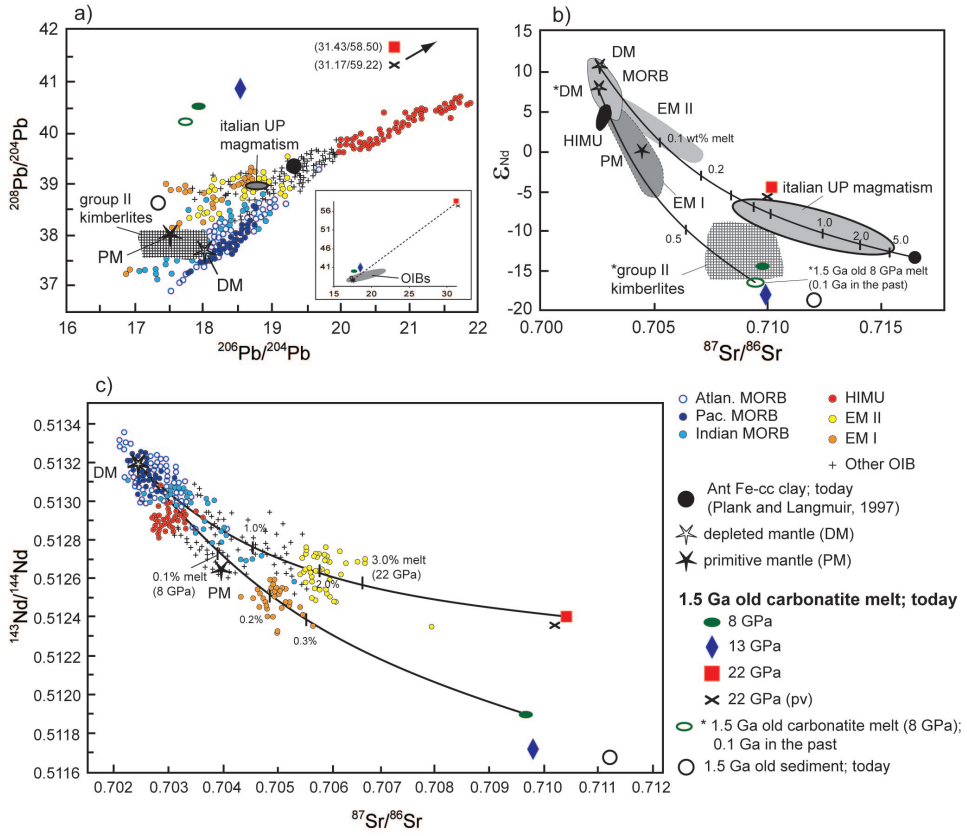

Figure 5.7: *Sr, Nd and Pb isotopic compositions of sediments and 8 % carbonate melts generated at 8, 13 and 22 GPa evolved separately for 1.5 Ga. The composition of present-day depleted mantle (DM) is from Salters and Stracke (2004) and the one for primitive mantle from Hofmann (1997). Present-day isotope composition for pelagic clays is taken from the same sediment used for the trace element composition (Plank and Langmuir, 1998). Isotopic compositions of OIB with different EM I, EM II and HIMU flavor and other MORB (Hofmann, 1997) are plotted for comparison. a) Pb isotopic compositions for sediments and carbonate melts generated at 8, 13 and 22 GPa evolved separately for 1.5 Ga compared to isotopic compositions of OIBs, today composition of Italian ultrapotassic rocks (Gasperini et al., 2002) and to the initial south African group II kimberlites (Smith, 1983; Becker and Le Roex, 2006). Note that the initial isotopic compositions of group II kimberlites (Smith, 1983 and Becker and Le Roex, 2006) and 0.1 Ga old (after 1.4 Ga evolution) *8 GPa melt plot exactly in the same field. b) Sr and Nd isotopic compositions of present-day pelagic clays and carbonate melts generated at 8 GPa evolved separately for 1.4 Ga (*8 GPa melt). Initial isotopic compositions of group II kimberlites lay on the mixing line between 0.1 Ga old depleted mantle and 0.1 ga old (after 1.4 Ga evolution) *8 GPa melt. Same behaviour is observed for the Italian ultrapotassic rocks which lay along the mixing line between present-day depleted mantle and pelagic sediments. c) Sr and Nd isotopic compositions for sediments and carbonate melts evolved separately for 1.5 Ga compared to isotopic compositions of OIBs. The addition of only minor amounts (< 2 wt%) of the generated carbonate melts to the depleted or primitive mantle can produce different domains covering a wide compositional spectrum. For details see text.*

5.4.3 Melting of re-enriched depleted mantle

The high degree of incompatible element enrichment in most alkaline magmatic suites (various OIBs, kimberlites, lamproites and other highly alkaline rocks) implies a metasomatic enrichment of the source region. The enrichment in incompatible elements (LILE, LREE) is often coupled with evidence for refractory source compositions with high Mg-number, high Ni-concentrations and low Al_2O_3 and HREE which suggest a previous depletion of the source mantle predating the metasomatic enrichment (Brey et al., 2008).

Recently Dasgupta et al. (2009) revisited trace element partitioning between garnet lherzolite and a carbonate melt at pressures of 6.6-8.6 GPa. Using their partition coefficients and a batch melting equation, we calculated the melt composition resulting from the re-melting (1.5 % melt fraction) of a depleted mantle (Salters and Stracke, 2004) previously re-enriched by 0.4 wt% of our K-rich carbonate melt generated at 8 GPa. The resulting trace element characteristics of such mantle melts are illustrated in figure 5.8 and compared with group II kimberlites from South Africa (Becker and Le Roex, 2006) and Gaussberg lamproites (Murphy et al., 2002), both showing characteristics related to the recycling of crustal material through subduction processes (Ringwood et al., 1992; McCandless, 1999; Murphy et al., 2002; Mirnejad and Bell, 2006). The primitive mantle normalized trace element concentrations of this modeled melt is almost completely congruent with group II kimberlites and the Gaussberg lamproites. The only difference is the greater HFSE-depletion in our calculated melt, which results from the characteristic inability of carbonate melts in dissolving HFSE. At higher degrees of melting, sediment melt compositions will evolve from carbonate melts to more Si-rich melts leading to an increased incompatibility of HFSE, the latter being one order of a magnitude more soluble in silicate melts than in carbonate melts (Veksler et al., 1998). The observed small discrepancies concerning some LILE including Rb and Ba could be adjusted by selecting a different initial chemical composition of the clastic sediment component (Plank and Langmuir, 1998), ours being highly depleted in Ba and enriched in Rb and Th.

The isotopical composition of group II kimberlites from South Africa shows highly radiogenic $^{87}Sr/^{86}Sr$ (0.708-0.712) and unradiogenic $^{143}Nd/^{144}Nd$ (ϵNd between -7 and -17) relative to the primitive mantle (Becker and Le Roex, 2006). The Pb isotopy (Smith, 1983) has some similarities with the calculated radiogenic composition of our 8 and 13 GPa melts generated 1.5 Ga in the past (fig. 5.7a) with slightly unradiogenic $^{206}Pb/^{204}Pb$ and radiogenic $^{207}Pb/^{204}Pb$ and $^{208}Pb/^{204}Pb$ compared to depleted mantle. The age of the South African group II kimberlites varies between 100 and 150 Ma (Becker and Le Roex, 2006) but orogenesis on the South African craton, supposedly ending subduction, dates to ca. 1 Ga (Namaqua-Natal belt of the Kibarian orogenic period; Thomas et al., 1994; Hopp et al., 2008; Lazarov et al., 2009) and to ca. 280 Ma (Permo triassic Cape Fold belt; Frimmel et al., 2001). Figure 5.7b illustrates the effect of mixing between a depleted mantle and our melt generated at 8 GPa on the Nd and Sr isotopy. Compositions have been calculated for 100 Ma old reservoirs (after 1.4 Ga evolution for the 8 GPa melt). The mixing of a depleted mantle with 0.5 to 1.0 wt% carbonate melt generated at 8 GPa fit the initial $^{87}Sr/^{86}Sr$ and ϵNd composition of group II kimberlites. These data strongly support the hypothe-

sis of a relation between group II kimberlites and lamproites with carbonate melt subduction zone metasomatism and related enrichment of a depleted mantle source region. Our model explains very well the observed trace elements abundances and isotopical characteristics of these magmas through migration of sediment derived carbonate melts into the sublithospheric depleted mantle.

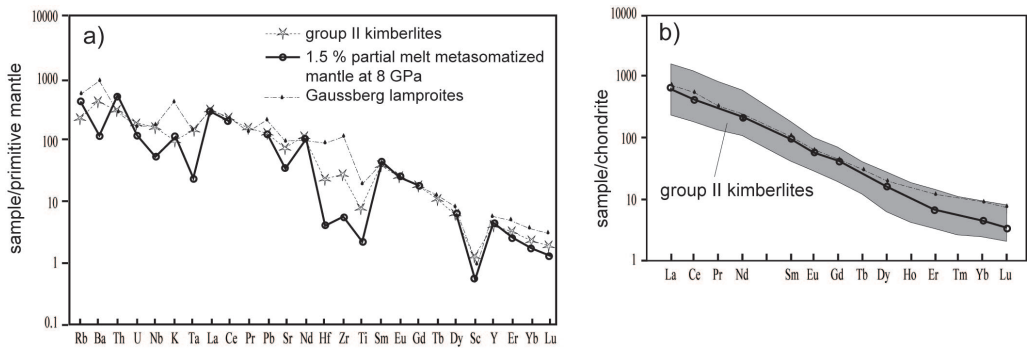

Figure 5.8: *Calculated trace elements patterns for a hypothetical melt generated from a reenriched depleted mantle using bulk partition coefficient from Dasgupta et al. (2009). 0.4 wt% of the calculated melt compositions of this study at 8 GPa has been added to a depleted mantle composition (Salters and Stracke, 2004). a) The resulting melt composition using a simple batch melting equation with 1.5% melt fraction is compared with primitive mantle normalized compositions of the South African group II kimberlites (Becker and Le Roex, 2006) and the Gaussberg lamproites (Murphy et al., 2002). Major differences are due to the carbonate melt derived bulk partition coefficients (HFSE) and to the sediment composition (LILE) which already showed a strong Ba-depletion (fig. 5.5b) (Plank and Langmuir, 1998). b) Chondrite-normalized (McDonough and Sun, 1995) REE diagram for the same hypothetical melt compared again with group II kimberlites and the Gaussberg lamproites.*

5.5 Conclusion

The partition coefficients between typical eclogite and higher pressure minerals and alkali carbonate melts measured in this study, allow for quantifying the metasomatic effect of highly enriched sediment derived carbonate melts on mantle reservoirs from 150 to 660 km depths. In the presence of cpx the calculated melts have extreme Nb/Ta ratios and their trace element characteristics matches well with many ultrapotassic rocks such as kamafugites and lamproites. Addition of small amounts of these melts to a depleted mantle followed by a later melting of this re-enriched mantle source produces liquids which perfectly match the isotopic characteristics of group II kimberlites. The parent/daughter element fractionation induced by melting of carbonated eclogitic pelites produces reservoirs having different Rb/Sr, U/Pb, Th/U and Sm/Nd ratios and also higher Sr, Nd and Pb concentrations than the unmelted sedimentary source. The isotopic evolution of these melts as separate reservoirs for relatively short periods explains, if mixed with a mantle source, the entire compositional range defined by the EM flavors of OIBs.

Chapter 6

Carbonated Pelites in the Lower Mantle

6.1 Previous work

At pressure conditions corresponding to lower mantle depths (P $>$ 23 GPa) the typical mantle assemblage consists of orthorhombic perovskite (Mg,Fe)SiO_3, cubic perovskite $CaSiO_3$ and magnesiumwüstite (Oneill and Jeanloz, 1990). The low Al_2O_3 content in this system can be incorporated into the structure of (Mg,Fe)SiO_3-perovskite and no additional Al-phase is observed (Irifune, 1994). In more Al-rich system like typical MORB or sedimentary compositions which have an Al_2O_3 content higher than ca. 15 wt%, various aluminous phases have been detected (Irifune and Ringwood, 1993; Irifune et al., 1994; Wang and Takahashi, 1999; Hirose and Fei, 2002; Litasov and Ohtani, 2005; Wu et al., 2009) . These alumina-rich phases, which have a large compositionally variability, are the CAS-phase ($CaAl_4Si_2O_{11}$, Irifune et al., 1994 and Gautron et al., 1997), the CF- and NAL-phase (Guignot and Andrault, 2004) and K-hollandite II (Sueda et al., 2004). The exact occurrence, compositions and stability of these phases with respect to pressure and temperature has yet not been completely elucidated, mainly because of the complexity of their solid solutions. The alkalines present in crustal compositions in the lower mantle conditions are stored into these alumina-rich phases. K-hollandite is the major host for potassium (up to 15 wt%), the CF-phase for sodium (up to 12 wt%) and the NAL-phase can contain large amount of both sodium and potassium (Guignot and Andrault, 2004). The carbonate found to be stable under subsolidus conditions in peridotitic and basaltic compositions at pressure between 20 and 30 GPa is magnesite ($MgCO_3$) (Litasov et al., 2008; Litasov and Ohtani, 2009; Ghosh et al., 2009; Rohrbach et al., 2009). Biellmann et al. (1993) showed through diamond-anvil experiments that magnesite is the only stable carbonate in the lower mantle at pressure to 50 GPa. In an in-situ X-ray study Isshiki et al. (2004) suggested that $MgCO_3$, could be stable down to depths corresponding to the core-mantle boundary. Ono et al. (2007) also showed that $CaCO_3$ can be stable up to 130 GPa.

Table 6.1: Mineral compositions in the second experiments DG2-BK2

DG2-BK2 30 GPa/1400 °C	Ca-pv	K-holl	NAL	mgs
SiO_2 (wt%)	47.61	62.96	15.07	0.25
TiO_2	1.64	0.15	0.94	0.01
Al_2O_3	2.58	16.73	48.90	2.65
FeO	1.91	2.06	12.62	11.65
MgO	0.44	1.02	9.33	34.83
CaO	43.44	1.89	1.40	0.46
Na_2O	0.60	2.59	4.31	1.12
K_2O	0.26	8.34	4.07	0.08
tot.	98.48	95.76	96.65	51.03
[a]Si (pfu)	0.94	3.03	1.20	0.01
Ti	0.02	0.01	0.06	0.00
Al	0.06	0.95	4.59	0.09
Fe^{3+}	0.00	0.00	0.00	0.00
Fe^{2+}	0.03	0.08	0.84	0.29
Mg	0.01	0.07	1.11	1.53
Ca	0.92	0.10	0.12	0.01
Na	0.02	0.24	0.67	0.06
K	0.01	0.51	0.41	0.00
tot.	2.02	5.00	8.99	2.00

[a] Cations calculated on the basis of 3 oxygens (Ca-pv), 8 (K-holl), 12 (NAL-phase) and 6 (mgs)

6.2 Experimental and analytical technique

The starting material used in the 2 experiments at 30 GPa at ca. 1350 °C is the nominally anhydrous bulk composition DG2 which characteristics and synthesis are fully described in the previous chapters. After the experiments made by A. Rohrbach, capsules were mounted longitudinally in epoxy resin and polished to the centre by dry polishing to avoid alkali-loss in the alkali-rich carbonates and in the quench products of the carbonate melts. The open capsules were repeatedly embedded in low viscosity resin to avoid chemical and mechanical loss of quench carbonate melts. When not analyzed, the capsules were kept in a desiccator under vacuum conditions as described in the previous chapters. Major element analyses were made with a JEOL JXA8200 electron microprobe at ETH-Zürich under the same conditions as for the experiment at pressures between 5.5 and 23.5 GPa (see chapter 2 to 5 for details).

6.2.1 Experimental Apparatus

In traditional uni-axial multi-anvil presses, maximum sample pressures are limited to 25-27 GPa, due to plastic deformation of the tungsten carbide (WC) cubes used for pressure transmission. The 10/3.5 assembly (Stewart et al., 2006) used for the experiments between 16 and 23.5 GPa of

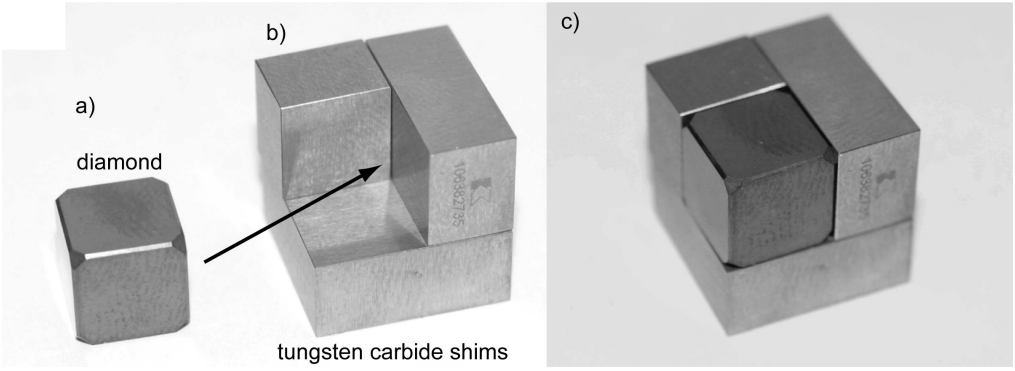

Figure 6.1: *Composite cube design of three hard metal (WC) shims (b) and a 9 mm edge length diamond cube (a), together composing a 16 mm edge length cube (c).*

this study is limited to 24 GPa. Any experiments at higher pressure using this uni-axial multi-anvil press are limited by the deviatoric stress which causes the tungsten carbide (WC) cubes to deform and diamond cubes to break. In order to perform experiments at higher pressure a method employing a true "split spher" (Kawai et al., 1970) was used. This spherical multianvil device is then compressed in an oil bath to ensure hydrostatic pressure. A detailed description of this method and its pressure calibration can be found in the supporting online material of Stewart et al. (2007). What has changed since then is the size of the diamond cubes (from 14 to 9 mm edge length) and thus the shape of the WC-pieces supporting the cubes. The reason for this is the extreme heat conductivity of diamond which becomes a fundamental problem, because it is one order of magnitude higher than for tungsten carbide. This leads to twice the electrical power/heat consumption than for the same assemblage with tungsten carbide cubes. The result is, that assembly and gaskets overheat, causing failure ("blow-outs") at T $>$ 1400 °C. For this reason the 14 mm edge length diamond cubes have been replaced by smaller diamond cubes of intermediate sizes (9 and edge length) which are then surrounded by rectangular tungsten carbide shims resulting to a composite cube of 16 mm (fig. 6.1).

6.3 Results at 30 GPa

Two experiments (DG2-BK1 and DG2-BK2) at a lower mantle pressure of 30 GPa have been run with the nominally anhydrous composition DG2 (chapter 2 tab. 2.1). The temperature of these experiments was between 1300 and 1400 °C corresponding to subsolidus conditions (fig. 3.1; chapter 3). Run durations were below 5 hours resulting in incomplete reaction in the charges, especially in the first experiments DG2-BK1 (fig. 6.2a). Nevertheless, the stable phase assemblage can be deduced from the experiments.

At the pressure of 30 GPa the garnet bearing assemblage is replaced by a perovskite bearing assemblage. In the first experiment DG2-BK1, phases coexisting along grain boundaries and most likely stable are stishovite, Ca-perovskite, FeTi-phase (perovskite?) a compositionally variable

CaO-Al_2O_3-rich phase (CAS-phase?), K-hollandite, magnesite and a Na-rich carbonate. In the second experiments DG2-BK2 Ca-perovskite coexists with stishovite, K-hollandite, magnesite and the aluminous phase NAL (tab. 6.1). In this experiment no Na-rich carbonate and CAS-phase have been observed. Simply mass balance calculations show a lack of Na in the first experiments as observed at lower pressure (see chapter 3) suggesting the presence of a Na-rich CO_2-bearing fluid phase. For the second experiments the Na-deficit is even bigger and it involves also a large quantity of CO_2 implying loss of CO_2 and Na_2O during the experiments. These observations suggest that the assemblage including Ca-perovskite, Fe-perovskite, K-hollandite, CAS-phase, stishovite, magnesite and a Na-carbonate is the stable one at 30 GPa at subsolidus conditions. Moreover, in a similar composition but with lower CO_2 content, Na-carbonate will be replaced by the NAL phase which can accommodate significant amount of sodium.

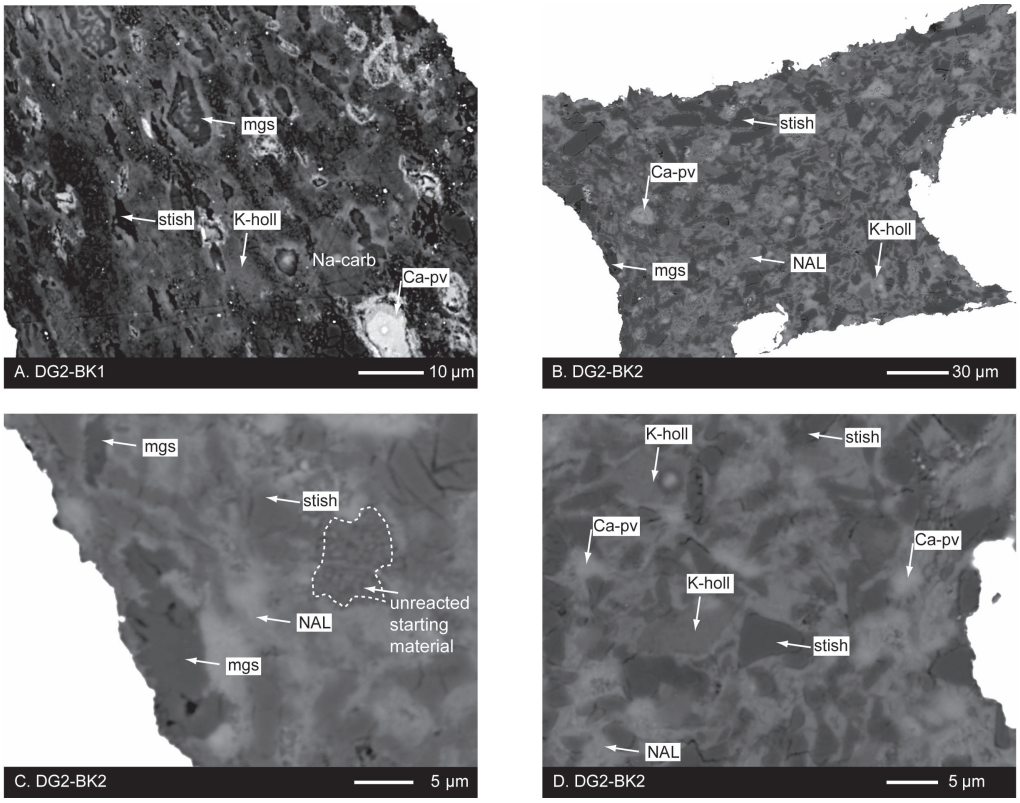

Figure 6.2: *BSE-images of run products. A: DG2-BK1; note the large amount of unreacted material and related lack of equilibrium throughout the entire capsule. B: DG2-BK2; full image of the capsule showing a better equilibrium in the second experiments at 30 GPa. C: DG2-BK2; small magnesite crystals coexisting with stishovite, NAL-phase and small patches of unreacted starting material. D: DG2-BK2; coexisting phases at 30 GPa at subsolidus are Ca-perovskite, stishovite, K-hollandite, NAL-phase and magnesite (only in C).*

The following mineral description is based on the second experiments DG2-BK2.
The *K-hollandite* crystallizing at 30 GPa shows lower potassium content (0.51 apfu) but higher

Na_2O (0.24 apfu) and CaO (0.10 apfu) contents than at lower pressures confirming a trend of increasing Na and Ca with increasing pressure (see chapter 3).

Ca-perovskite contains 1.64 wt% TiO_2, 2.58 wt% Al_2O_3 and 1.91 wt% FeO_{tot}, concentrations which are slightly higher than at 23.5 GPa. The amount of alkalis remains below 0.7 wt% with a Na_2O/K_2O wt ratio of ca. 2.

NAL-phase shows large sodium (4.31 wt%) and potassium (4.07 wt%) contents and is the phase which incorporates the highest amount of sodium. Our measured NAL-phase has a Mg# of 56.9 which is slightly lower than the Mg# of 60.6 found in a dry basaltic system by Litasov and Ohtani (2005) at 28 GPa and 1600°C.

The *magnesite* stable at 30 GPa contains 15.2 mol% of siderite, 0.8 mol% of calcite and 2 mol% of Na_2CO_3 similar to magnesites measured at 23.5 GPa for the same bulk composition.

In spite of the incomplete reaction in the charges, these preliminary experiments at 30 GPa show that no significant changes on phase assemblage occur between 24 and 30 GPa. The presence of a Na-rich CO_2-bearing fluid phase coexisting with carbonates (Na-carbonate and magnesite) suggests a similar melting reaction and melt composition as it is observed at 22 GPa (see chapter 3).

Chapter 7

Conclusions and Outlook

7.1 Summary

The purpose of this work was to understand the deep subduction and final recycling of carbonated sediments into the upper mantle and transition zone including phase relations and melting reactions. The characterization and quantification of the decarbonation process is at the bases for a good knowledge of the geochemical cycle of trace elements (U, Pb, Th, Nd, Sr, Ba, Rb, Cs, Nb, etc.), isotopes and major elements (K_2O, CO_2) enriched in sediments. Of all lithologies present in the mantle, sediments are the most exotic ones and thus the ones most easily producing geochemical anomalies observed in ocean island basalts.

Experiments have been run between 5.5 and 30 GPa at temperatures between 900 and 1850 °C on different bulk compositions also including a series of experiments dealing with the reaction between carbonate melts and peridotite at 8 and 13 GPa under different conditions of oxygen fugacity. Moreover, reverse sandwich experiments which allowed a better quantification of the melt compositions at the solidus supplied material well suited for trace elements analysis. The large amount of data produced by the many multi-anvil experiments of this study leads to numerous conclusions which can be summarized as follows:

- At pressures between 5.5 and 16 GPa, when heating towards a mantle adiabat, carbonated eclogitic pelites produce highly potassic magnesio- to ferro- dolomitic carbonate melts. The presence of jadeite in the residuum holds back Na and fractionates the K/Na ratio up to 40, thus providing a genetic link between CO_2 and potassic metasomatism of the mantle in this pressure range. At higher pressures, the breakdown of jadeite combined to an extended stability of K-hollandite towards higher temperatures leads to the generation of Na-rich carbonate melts with K/Na < 0.5.

- Comparison of the solidi for carbonated pelites with typical subduction P-T-path shows that, melting is likely to occur especially at two distinct depths: the first occasion occurs between 6-9 GPa and is related to an increased incompatibility of potassium combined with the breakdown reactions of lawsonite and phengite producing an aqueous fluid capable to

lower the solidus temperature of the flushed rocks. The second location is along the 660-km discontinuity whenever a deflection of the slab occurs and the subsequent relaxation of the isotherms within the slab automatically leading to melting.

- The low melting point, the position on the top of a stratified slab and the dynamics of subducting slabs suggest that much of the CO_2 trapped in pelitic rocks will be released within the upper mantle making carbonated pelites the most efficient in recycling CO_2, alkalis and incompatible elements back into the mantle.
- Slab derived alkaline carbonate melts undergo different reactions with the surrounding mantle depending on the local oxygen fugacity during metasomatism. Under strongly reducing deep mantle conditions, these melts can effectively be redox frozen leading to diamond nucleation.

Trace elements analyses obtained for carbonate melts and minerals including clinopyroxene, garnet, K-hollandite, CAS-phase and FeTi-perovskite suggest the following conclusions:

- In the presence of cpx, the calculated melts have extreme Nb/Ta ratio and their trace element flavor shows good matches with many ultrapotassic rocks like kamafugites and lamproites.
- Addition of small amounts of these melts to a depleted mantle followed by a successive or later melting event of the reenriched mantle source produces liquids which match pretty well the trace element and isotopic characteristics of group II kimberlites.
- The parent/daughter element fractionation induced by melting of carbonated eclogitic pelites can produce reservoirs having different Rb/Sr, U/Pb, Th/U and Sm/Nd ratios and also higher Sr, Nd and Pb concentrations than the unmelted sedimentary source. The evolution of these melts as separate reservoirs leads to a large variety of isotopic compositions.

7.2 Outlook and suggestions for future work

Recently, several studies showed that at pressures above 2-5 GPa carbonate melts can be produced at near solidus conditions by melting of a large spectrum of carbonated subducted rocks including peridotites, basalts and sediments. Considering their physical and chemical characteristics, carbonate melts are probably the most effective metasomatic agent acting in the deep mantle. The metasomatic effect that these melts have on typical mantle assemblages is poorly known, especially at high pressures. The large spectrum of possible metasomatic agents and reactions, as implied by different melt compositions, oxygen fugacities, mantle assemblages and pressures, supplies thus enough material for many further investigations also including trace element partitioning and remelting of metasomatic mantle.

The existence of stagnant slabs along the 660-km discontinuity underneath East Asia, Peru, The southwest Pacific (Tonga), the Aleutians and North America (Farallon plate) has been shown

based on global mantle tomographic models by many authors. The origin of some intraplate volcanoes has been recently connected to the presence of these stagnant slabs just underneath their source regions. The comparison of the geochemical characteristic (trace elements and isotopes) observed in these volcanoes with the typical signature of slab-derived melts produced with K-hollandite and the CAS-phase in the residuum should furnish supplementary evidence to this theory.

In this and other recent studies on carbonated rocks at pressures above 10 GPa the presence of an unquenchable alkali-rich, CO_2-bearing liquid coexisting with solid carbonates has been suggested by mass balance calculations. Up to now it is unknown, whether the appearance of (quenched) carbonate melts with increasing temperatures is in chemical continuum with the liquids at lower temperatures or whether a true carbonate solidus involving two immiscible liquids occurs. In other words, the effect of CO_2 on the supercritical behaviour of liquids in complex systems at high pressure is fully unknown.

Appendix A

High Pressure K-phase (HPK-phase) in the Hydrous Composition AM

A.1 Introduction

A.1.1 Hydrous alumina phases at pressure exceeding phengite stability

Previous studies on SiO_2-Al_2O_3-saturated compositions at similar P-T-conditions as employed in this study resulted in three hydrous phases at pressure above the phengite to K-hollandite reaction at 8-9 GPa. Ono (1998) studied average shale and continental crust compositions with 6 wt% H_2O at 6-15 GPa, 800-1400 °C and found, that in peraluminous compositions topaz-OH ($Al_2Si_4(OH)_2$, Wunder et al., 1993) forms instead of kyanite upon phengite breakdown and that near 12 GPa topaz-OH reacts to phase egg ($AlSiO_3(OH)$, Eggleton et al., 1978 and Schmidt et al., 1998). Phase egg is stable to 22 GPa in synthetic Al_2O_3-SiO_2-H_2O systems (Sano et al., 2003), nevertheless, its temperature stability in natural systems appears to be limited to 1300-1400 °C (Ono, 1998). Dobrzhinetskaya and Green (2007) confirmed the presence of K-hollandite and topaz-OH in continental crust compositions at 10-12 GPa, 1100-1300 °C. At 16-20 GPa, 1250-1300 °C, Rapp et al. (2008) obtained phase egg in a pelitic bulk composition with 8 wt% H_2O, but not in the pelite with 1 wt% H_2O. Even in the original synthesis by Eggleton et al. (1978), phase egg was only obtained from starting materials containing substantial quantities of water. At pressures higher than 20-22 GPa phase-egg decomposes into a new hydrous phase δ-AlOOH + stishovite which is then stable up to 30 GPa (Suzuki et al., 2000; Sano et al., 2004). The structure of this hydrous phase has a framework of oxygen packing similar to the $CaCl_2$ (distorted rutile) structure, containing columns of edge-sharing AlO_6 octaedra that are joined via corners (Xue et al., 2006). Ohtani et al. (2001) showed that δ-AlOOH is also stable in a CMAS model pyrolite-H_2O system at pressure between 19 and 25 GPa containing up to 8.3 wt% SiO_2 and ca. 5.5 wt% MgO which suggests coupled substitutions of the type $2Al^{3+} = Si^{4+} + Mg^{2+}$ and $Al^{3+} + H^{+} = Si^{4+}$.

In alumina-rich systems, including subducted sediments and basalts, after the breakdown of phengite, K-hollandite is the major potassium bearing phase to pressures higher than 50 GPa

(Irifune et al., 1994; Tutti et al., 2001; Sueda et al., 2004). Its structure consists of double chains of edge-sharing $Si(Al)O_6$ octaedra which share corners with other double chains forming large tunnels which host the large K-cations. Si and Al in the octahedral sites are randomly distributed and no evidence of ordering between Si and Al has been described. One of the Si(Al)-O bond distances in the highly distorted $Si(Al)O_6$ octaedra is very short (1.77 Å) similar to the Si-O distance in stishovite. A phase transformation from tetragonal to a monoclinic phase called K-hollandite II occurs at ca. 20-22 GPa (Sueda et al., 2004; Ferroir et al., 2006). This phase transition implies an increased compressibility of the structure (Ferroir et al., 2006) as well as a change of the melting curve of $KAlSi_3O_8$ hollandite (Wang and Takahashi, 1999) and some small compositional changes (Yagi et al., 1994; Wang and Takahashi, 1999).

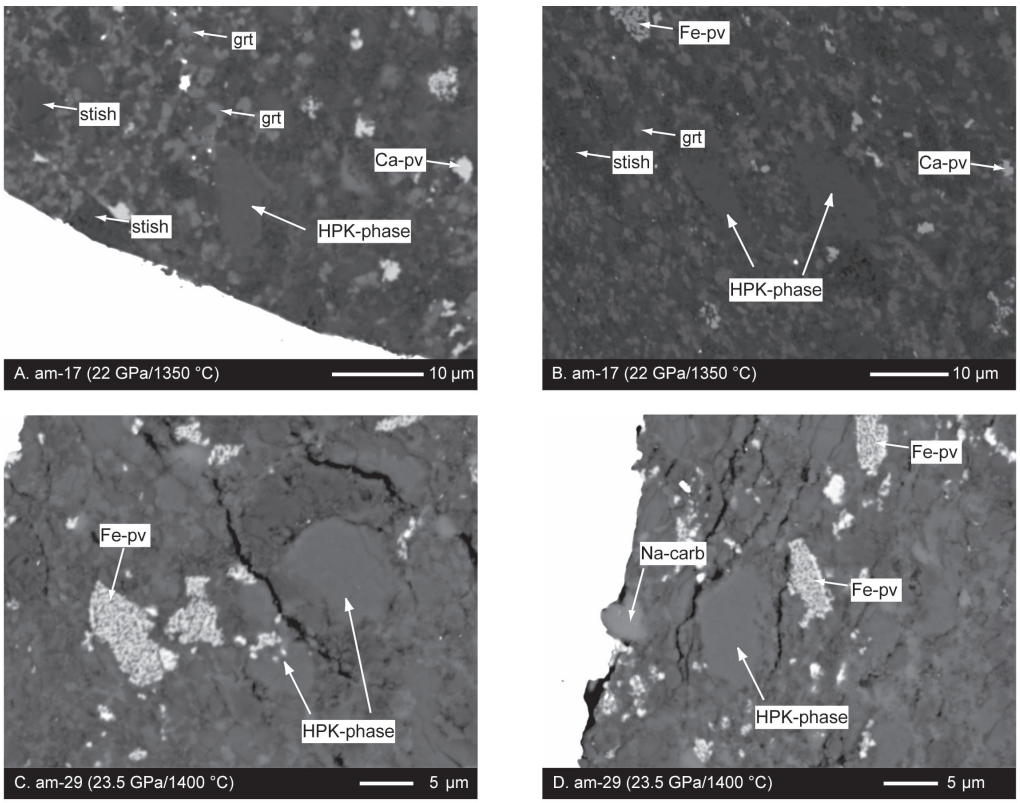

Figure A.1: *BSE-images of the new potassium HPK-phase crystallizing at 22 and 23.5 GPa at the lowest temperatures. A and B: am-17 (22 GPa/1350 °C); subsolidus assemblage with the HPK-phase coexisting with grt, Ca-pv, FeTi-pv, stishovite, corundum and Na-carbonate. C and D: am-29 (23.5 GPa/1400 °C); the HPK-phase coexists with the same phases as at 22 GPa but with larger amount of Ca- and FeTi-pv replacing garnet with increasing pressure.*

Table A.1: List of single analysis for the HPK-phase at 22 and 23.5 GPa. Mean values as well as standard deviation, variance and confidence are also given

am-17	HPK-phase													mean	stdv.	conf.	var.
SiO_2 (wt%)	59.27	53.82	57.35	47.88	55.02	50.88	52.00	52.83	54.16	52.37	49.25	56.02	54.99	53.53	3.16	0.03	10.00
TiO_2	-	-	-	-	-	-	-	-	-	-	-	-	-	-	-	-	-
Al_2O_3	24.54	33.35	24.66	35.16	27.05	31.75	31.78	28.83	30.91	30.76	34.33	25.18	25.70	29.54	3.78	0.03	14.30
FeO	0.71	1.58	0.94	2.23	1.43	2.24	1.60	1.88	1.53	1.77	2.34	1.23	0.85	1.56	0.53	0.00	0.28
MgO	0.14	0.14	0.06	0.24	0.16	0.54	0.37	0.35	0.14	0.15	0.16	0.06	0.19	0.21	0.14	0.00	0.02
CaO	0.79	0.67	2.03	1.01	0.76	1.09	0.80	0.74	0.96	0.75	0.75	0.66	0.73	0.90	0.36	0.00	0.13
Na_2O	0.19	0.25	0.18	0.23	0.30	0.23	0.20	0.16	0.25	0.23	0.11	0.19	0.24	0.21	0.05	0.00	0.00
K_2O	13.06	11.91	12.36	11.31	12.56	11.33	11.64	12.10	12.65	12.27	11.16	12.40	12.26	12.08	0.58	0.01	0.33
tot.	98.70	101.75	97.58	98.05	97.28	98.06	98.41	96.89	100.60	98.30	98.11	95.74	94.95	98.03	1.78	0.02	3.16

am-29	HPK-phase													mean	stdv.	conf.	var.
SiO_2 (wt%)	56.64	53.66	51.59	54.68	51.23	51.66								53.24	2.15	0.03	4.61
TiO_2	-	-	-	-	-	-								-	-	-	-
Al_2O_3	25.99	29.47	33.14	29.07	32.50	32.55								30.45	2.78	0.04	7.72
FeO	1.27	1.39	1.81	1.48	1.32	1.64								1.48	0.21	0.00	0.04
MgO	0.01	0.13	0.14	0.10	0.11	0.16								0.11	0.05	0.00	0.00
CaO	0.83	0.93	0.83	0.81	0.66	0.99								0.84	0.11	0.00	0.01
Na_2O	0.24	0.13	0.27	0.11	0.18	0.25								0.20	0.07	0.00	0.00
K_2O	13.60	12.76	12.13	13.60	13.21	12.23								12.92	0.65	0.01	0.43
tot.	98.57	98.48	99.91	99.86	99.21	99.48								99.25	0.62	0.01	0.38

Table A.2: Average compositions of the HPK-phase and K-hollandite

	am-17		am-29		am-26
P [GPa]/T [°C]	22/1350		23.5/1400		18/1300
	HPK-phase		HPK-phase		K-holl
SiO_2 (wt%)	53.53		53.24		65.57
TiO_2	-		-		-
Al_2O_3	29.54		30.45		19.33
FeO	1.56		1.48		0.33
MgO	0.21		0.11		0.03
CaO	0.90		0.84		0.66
Na_2O	0.21		0.20		0.55
K_2O	12.08		12.92		14.72
tot.	98.03		99.25		101.20
[a]Si (pfu)	3.00	3.15	2.96	3.11	3.00
Ti	-	-	-	-	-
Al	1.95	2.05	1.99	2.10	1.04
Fe^{3+}	0.00	0.00	0.00	0.00	0.01
Fe^{2+}	0.07	0.08	0.07	0.07	0.00
Mg	0.02	0.02	0.01	0.01	0.00
Ca	0.05	0.06	0.05	0.05	0.03
Na	0.02	0.02	0.02	0.02	0.05
K	0.86	0.91	0.92	0.96	0.86
H	1.00	0.00	1.00	0.00	
tot.	6.97	6.29	7.01	6.33	5.00

[a] Cations on the left column calculated on the basis of 9 oxygens and 1 OH-site;
the ones on the right columns on the basis of 10 oxygens.
K-holl normalized on the basis of 8 oxygens.

A.2 Results

A.2.1 Potassic and hydrous phases in subducted carbonated pelites (this study)

K-hollandite is the only potassium mineral at P $\geq$ 13 GPa and contains a few wt% of Na_2O and CaO mostly increasing with temperature and especially with pressure. In the DG2 composition (3.2 wt% bulk Na_2O) Na in K-hollandite increases steadily with pressure, while in the AM composition (2.4 wt% bulk Na_2O) Na in K-hollandite reaches a maximum at 16 GPa (0.06 Na pfu) and then remains constant with pressure. The different behaviour of sodium in the AM composition can be explained by the lower bulk Na_2O in combination with H_2O, the Na being more easily accommodated in a Na_2O-rich fluid and carbonate. Ca pfu increases in the DG2 composition from 0.03 at 13 GPa to 0.08 Ca pfu at 22 GPa. In the AM composition, Ca in K-hollandite is ca. 0.05 apfu at all pressures investigated. At 16 and partly at 18 GPa, K-hollandite in the AM composition shows a Si deficit up to 0.15-0.2 apfu at the lowest temperatures. This Si-deficit may be attributed

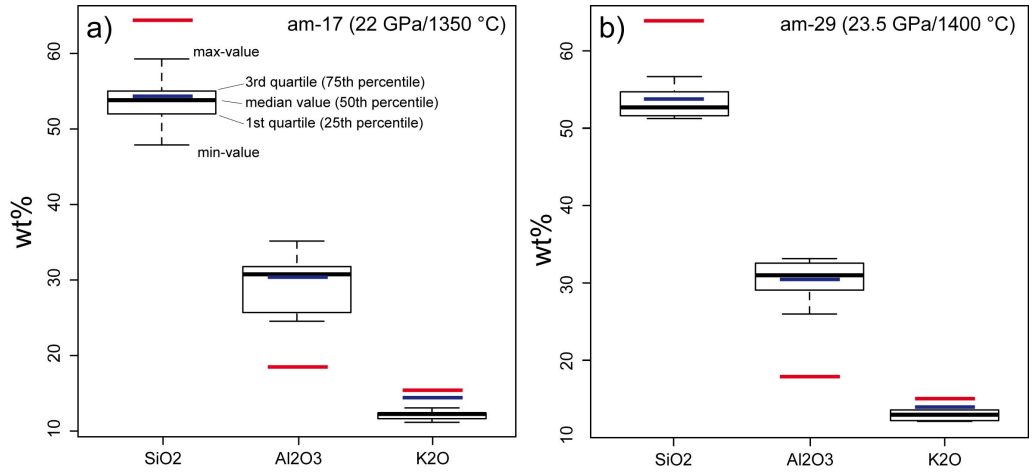

Figure A.2: *Boxplots for the measured SiO_2, Al_2O_3 and K_2O contents (wt%) in the HPK-phase at 22 GPa (a) and 23.5 GPa (b). Red and blue lines show the theoretical values for stoichiometric $KAlSi_3O_8$ (hollandite) and $KAl_2Si_3O_9(OH)$ (HPK-phase), respectively.*

to the incorporation of a small amount of hydrogen, probably due to the substitution of Si with Al + OH on the octahedral (Si^{4+}) site as it is known for stishovite (Panero et al., 2003; Panero and Stixrude, 2004; Litasov et al., 2007) and several DHMS phases.

At pressure higher than 13 GPa no hydrous phases have been detected and the H_2O previously stored in phengite in the AM bulk is likely to be present as a fluid-phase. The presence of a fluid also depends on the H-solubility of other nominally anhydrous phases (Keppler and Smyth, 2006) such as stishovite which can dissolve up to 3000 ppm H_2O through a simple substitution Si^{4+} = Al^{3+} + H^+ on the octahedral (Si^{4+}) site (Litasov et al., 2007). Nevertheless, stishovite (max. 3000 ppm H_2O), garnet (max. 1000 ppm H_2O in Mg-rich garnet), K-hollandite (max. 2000 ppm H_2O) and clinopyroxene (max. 1200 ppm H_2O in $Di_{60}Jd_{40}$, Wu et al., 2009) can only accommodate a total of max. 2000 ppm H_2O (0.2 wt% H_2O) in the AM bulk, far less than the 1.1 wt% present. Thus, the AM composition should be fluid saturated.

A.2.2 The HPK-phase at 22 and 23.5 GPa

In the hydrous AM composition at 22 and 23.5 GPa and at the lowest temperatures of 1350-1400 °C, K-hollandite was not observed but a new potassium phase (here named HPK-phase) (fig. A.1) with higher Al_2O_3 contents varying from 24.54 to 35.16 wt% and lower SiO_2 concentrations of 49.25 to 57.35 wt% (tab. A.1 and fig. A.2) yielding a K:Al:Si ratio of approximately 1:2:3 (tab. A.2). Compared to K-hollandite crystallizing in the same bulk composition but at lower pressures (13-18 GPa) this new potassium phase shows lower Na_2O and variable but higher CaO, MgO and FeO contents (tab. A.1). Totals for most of the analyses range from 95 wt% to 101 wt% with an average between 98-99 wt%, possibly indicate the presence of some hydrogen yielding an approximate formula of $KAl_2Si_3O_9(OH)$ which is simply a 1:1 mixture of K-hollandite ($KAlSi_3O_8$)

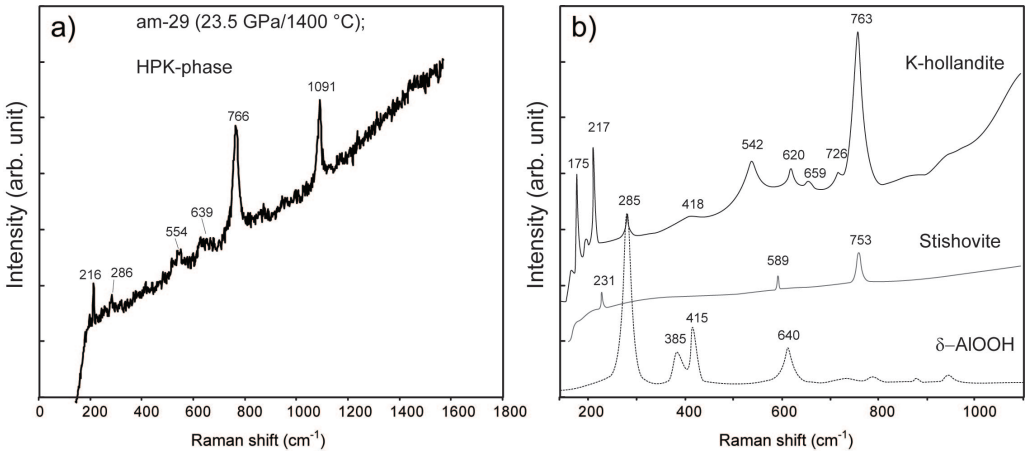

Figure A.3: *Comparison between the Raman spectra of the HPK-phase (a), K-hollandite, stishovite and that of δ-AlOOH (b).*

with AlOOH (δ-AlOOH?). The HPK-phase does not form in the dry DG2-composition, which further supports a hydrous bulk. In spite of the chemical differences concerning Si and Al, the Raman spectra (fig. A.3) is similar to the one for K-hollandite with the characteristic bands near 760 and 217 cm^{-1} (Liu and El Gorsey, 2007) suggesting some structural similarities between both potassium phases.

A.3 Interpretation and conclusions

Considering the small Si deficit in K-hollandite at 16 and 18 GPa at the lowest temperatures and the structural similarities between stishovite, AlOOH and K-hollandite allowing an Si^{4+} = Al^{3+} + H^{+} exchange, we suggest that at P $>$ 20-22 GPa after the transition to K-hollandite II, either a solid solution between K-Hollandite II and AlOOH, or a new phase exists at temperature below 1400 °C favored by the changed structural characteristics of K-hollandite II.

Appendix B

Trace Element Partitioning between Potassium rich Mg-carbonate and Carbonate Melts

In the experiment LHZ-S2a described in chapter 4 the alkali-rich carbonate melt was let to react with a lherzolitic composition (average lherzolite: Maaloe and Aoki, 1977) (tab. B.1) at 13 GPa and 1350 °C. In this experiment the lherzolite was transformed into a carbonated wehrlite consisting of grt, cpx, ol, mgs and a K_2O-rich carbonate $(K,Na)_2(Mg,Ca,Fe)(CO_3)_2$ which coexisted with a carbonate melt (fig. B.1 and chapter 4).

Table B.1: Bulk, mineral and melt major element compositions

	[a]LHZ	Bulk LHZ-S2a	K-carb LHZ-S2a 13/1350	melt LHZ-S2a 13/1350
SiO_2 (wt%)	44.23	22.53	0.04	0.26
TiO_2	0.09	0.90	0.01	0.05
Al_2O_3	2.10	2.04	0.04	0.11
FeO	8.29	8.15	1.06	2.30
MgO	42.27	24.03	16.11	10.52
CaO	1.90	12.10	3.17	20.98
Na_2O	0.32	2.68	6.28	9.99
K_2O	0.00	6.02	29.43	12.78
[b]CO_2	0.00	19.00	43.87	43.01
tot.	99.20	97.45	100.00	100.00
K_2O/Na_2O (wt%)				1.28
X^*_{Ca}			0.12	0.56
X^*_{Mg}			0.85	0.39

[a] average lherzolite after Maaloe and Aoki (1977)

[b] CO_2 content calculated by difference of 100 and the measured analytical total.

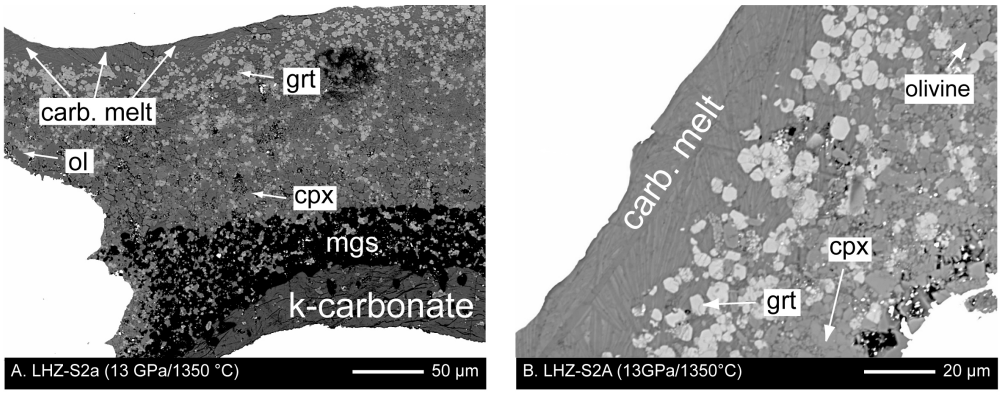

Figure B.1: *BSE-images of run products. A and B: LHZ-S2a (13 GPa/1350 °C); in the experiments using a lherzolitic composition the alkali-rich carbonate melt (top of the capsule) coexists with grt, cpx, ol, mgs and a potassium-rich carbonate.*

The potassium rich carbonate has a general formula $(K,Na)_2(Mg,Ca,Fe)(CO_3)_2$ analogue to the Na carbonates nyereite found in the Na-carbonatites of Oldoinyo-Lengai (McKie and Frankis, 1977). Pure $K_2Mg(CO_3)_2$ has been synthesized at 25 MPa, 300 °C by Simons (1983) and at 250 MPa by Taniguchi et al. (1996). It has been investigated by powder diffraction by Simons (1983) and found to be structurally analogous to nyerite. Our high pressure potassic carbonate could thus be regarded as KMg-nyerite. The melt in equilibrium with the wehrlitic assemblage is also extremely enriched in alkalis and different (lower X^*_{Mg} and higher X^*_{Ca}) from carbonate melts found to be in equilibrium with mantle peridotite at similar pressure (Dasgupta and Hirschmann, 2007; Brey et al., 2008; Ghosh et al., 2009). This carbonate melt shows an X^*_{Mg} of 0.39 and X^*_{Ca} of 0.56, much more similar to values characteristic for melts in equilibrium with basaltic compositions (Yaxley and Brey, 2004; Dasgupta et al., 2005). Nevertheless, technically spoken, the alkali-carbonate melt has only locally equilibrated with a model mantle, lowering the X^*_{Mg} of the silicate phases away from typical mantle values.

K-carbonate/carbonate melt trace element partitioning

The trace element analyses and the partition coefficients between the K-rich carbonate and carbonate melt, in equilibrium with a carbonated wehrlitic assemblage, are listed in table B.2 and are compared with Ds between magnesite and carbonate melt obtained by Dasgupta et al. (2009) (fig. B.2). Trace element analyses using a LA-ICP-MS technique have been done by the Günther Group (Prof. Detlef Günther and Kathrin Hametner: Department of Chemistry and Applied Biosciences); for details see chapter 5.

Table B.2: Trace element composition of K-carbonate and melt and resulting partition coefficients

Mineral	K-carb		melt		D(min/melt)	
run.	LHZ-S2a		LHZ-S2a		LHZ-S2a	
P[GPa]/T[°C]	13/1350		13/1350		13/1350	
	mean	stdv	mean	stdv	mean	stdv
	4/4		4/5			
Li (ppm)	14.91	5.76	97.425	39.55	0.15	0.12
Be	4.81	0.36	275.667	45.68	0.02	0.00
B	171.25	10.75	396.250	57.51	0.43	0.09
Ti	207.10	89.55	347.250	65.46	0.60	0.37
V	3.41	0.62				
Mn	72.05	7.75	151.000	24.48	0.48	0.13
Co	5.47	2.05	7.813	1.16	0.70	0.37
Ni	4.82	0.49				
Zn	7.69	0.78				
Ga	0.78	0.37				
Ge	4.44	1.14	28.800	1.26	0.15	0.05
Rb	44.10	1.68	57.900	8.85	0.76	0.15
Sr	108.75	2.06	362.750	17.75	0.30	0.02
Y	1.27	0.24	3.803	0.76	0.34	0.13
Zr	1.73	1.07	1.650	0.13	1.05	0.73
Nb	28.53	12.34	226.750	4.03	0.13	0.06
Sn	4.87	0.60				
Cs	29.65	1.65	397.500	26.19	0.07	0.01
Ba	27.98	5.25	330.000	28.13	0.08	0.02
La	3.72	0.69	240.500	7.94	0.02	0.00
Ce	4.34	0.67	155.000	11.46	0.03	0.01
Pr	3.09	0.95	102.500	2.38	0.03	0.01
Nd	4.15	1.16	73.700	13.26	0.06	0.03
Sm	2.22	0.47	34.125	4.57	0.07	0.02
Eu	1.63	0.70	20.400	7.25	0.08	0.06
Gd	1.19	0.09	28.300	1.59	0.04	0.01
Tb	1.47	0.26	11.803	1.34	0.12	0.04
Dy	1.39	0.39	22.600	2.97	0.06	0.03
Er	1.49	0.39	8.180	1.14	0.18	0.07
Yb	1.41	1.23				
Lu	1.40	0.78	3.613	0.58	0.39	0.28
Hf	1.19	0.77	1.255	0.47	0.95	0.97
Ta	3.30	1.39	4.268	0.49	0.77	0.41
Bi	3.36	0.50	0.716	0.01	4.69	0.78
Th	1.96	0.70	10.700	0.61	0.18	0.08
U	0.91	0.44	10.510	2.51	0.09	0.06

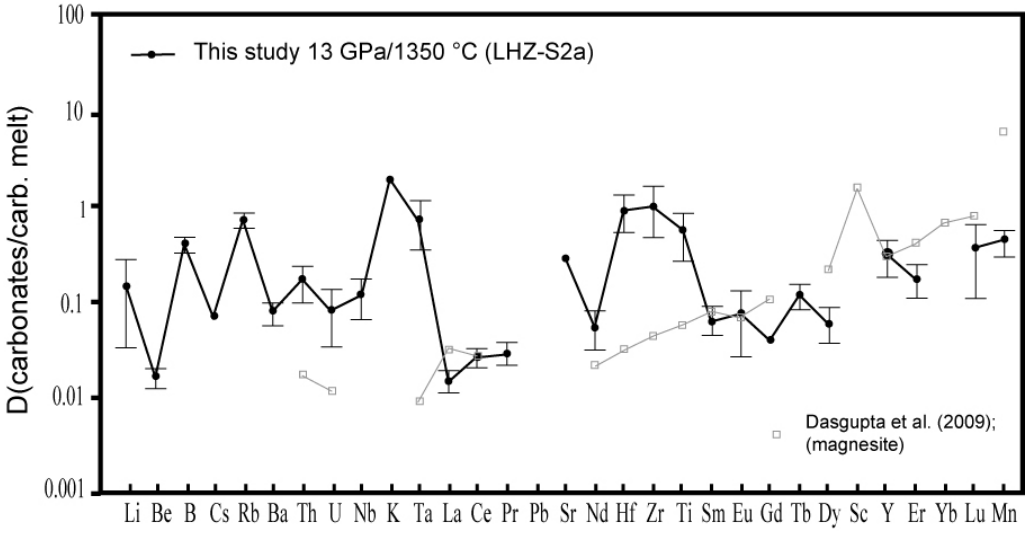

Figure B.2: *Trace element partition coefficients between K-rich carbonate and carbonate melt.*

The Ds for REEs between the K-rich carbonate and carbonate melt are comparable with the one between magnesite and melt. However, an important difference in the Ds-values for the HFSE and the LILE are observed. Partitioning coefficients for these elements are much higher in the potassium rich carbonate, by at least one order of magnitude. Similar as for other minerals presented in this study (chapter 5), D_{Ta} is higher than D_{Nb} presumably due to higher incompatibility of Ta compared to Nb in the highly alkaline carbonate melts of this study.

This KMg-nyerite will be formed in the mantle in the vicinity of the sediments or along metasomatic passage ways ("veins") which are relatively oxidized compared to average mantle. There, they could locally constitute important geochemical reservoirs, to be entrailed in mantle convection.

Appendix C

Additional Data to Chapter 2 and 3

DG1 garnet compositions

Run no.	DG1-18	DG1-9	DG1-11	DG1-19	DG1-13	DG1-8	DG1-7	DG1-15	DG1-1	DG1-6	DG1-17
P(GPa)	8	8	8	8	8	13	13	13	13	13	13
T(°C)	900	1100	1200	1300	1400	1150	1250	1400	1600	1700	1850
SiO_2	38.66	39.27	40.34	41.67	39.27	39.71	40.28	40.66	41.65	41.64	43.68
TiO_2	0.86	0.93	0.47	0.38	0.36	0.86	0.90	0.63	0.47	0.45	0.27
Al_2O_3	20.75	20.76	22.29	22.59	21.34	22.17	21.64	21.56	21.52	21.90	22.10
FeO	25.42	19.12	18.11	17.29	17.91	15.59	16.13	17.04	14.38	15.00	9.98
MgO	3.99	8.81	12.61	14.03	14.24	10.15	9.72	12.65	12.76	12.61	17.93
CaO	11.61	11.23	7.68	6.35	6.19	10.69	10.88	7.81	8.24	7.63	6.00
Na_2O	0.39	0.55	0.37	0.35	0.47	0.64	0.84	0.76	0.95	1.00	0.98
K_2O	0.08	0.10	0.06	0.28	0.22	0.02	0.01	0.02	0.14	0.06	0.09
tot.	101.76	100.77	101.93	102.94	100.00	99.83	100.39	101.13	100.11	100.27	101.04
[a]Si (pfu)	2.97	2.94	2.94	2.98	2.89	2.96	2.99	2.97	3.05	3.05	3.08
Ti	0.05	0.05	0.03	0.02	0.02	0.05	0.05	0.03	0.03	0.02	0.01
Al	1.88	1.83	1.91	1.91	1.85	1.95	1.89	1.86	1.86	1.89	1.84
Fe^{3+}	0.16	0.27	0.22	0.17	0.42	0.14	0.15	0.24	0.14	0.11	0.12
Fe^{2+}	1.47	0.93	0.88	0.87	0.69	0.84	0.86	0.80	0.74	0.80	0.47
Mg	0.46	0.98	1.37	1.50	1.56	1.13	1.08	1.38	1.39	1.38	1.88
Ca	0.95	0.90	0.60	0.49	0.49	0.85	0.87	0.61	0.65	0.60	0.45
Na	0.06	0.08	0.05	0.05	0.07	0.09	0.12	0.11	0.13	0.14	0.13
K	0.01	0.01	0.01	0.03	0.02	0.00	0.00	0.00	0.01	0.01	0.01
tot.	8.00	8.00	8.00	8.00	8.00	8.00	8.00	8.00	8.00	8.00	8.00
majorite	-0.05	-0.09	-0.10	-0.07	-0.18	-0.09	-0.08	-0.10	-0.07	-0.08	-0.05
X^*_{Mg}	0.15	0.32	0.45	0.50	0.50	0.38	0.37	0.45	0.48	0.48	0.64
X^*_{Ca}	0.33	0.32	0.21	0.17	0.18	0.30	0.31	0.22	0.23	0.22	0.16
Mg# (Fe_{tot})	22	45	55	59	59	54	52	57	61	60	76

[a] Cations calculated on the basis of 12 oxygens.

DG2 Garnet compositions

Run no.	DG2-20	DG2-31	DG2-32	DG2-30	DG2-1	DG2-5B	DG2-3	DG2-2	DG2-4	DG2-9	DG2-11	DG2-8	DG2-7
P(GPa)	5.5	5.5	5.5	6.5	8	8	8	8	8	13	13	13	13
T(°C)	1070	1125	1180	1070	900	1000	1100	1250	1400	1200	1300	1400	1600
SiO_2	38.48	38.33	39.67	37.84	40.08	39.74	39.84	41.40	40.54	40.21	40.08	41.26	41.08
TiO_2	1.19	1.54	0.44	1.04	1.25	1.44	1.11	0.93	0.71	1.11	1.54	0.92	0.79
Al_2O_3	20.30	20.57	21.85	21.30	21.27	20.65	21.44	21.90	22.00	20.66	20.99	21.86	21.59
FeO	20.59	20.51	20.61	21.06	16.83	21.27	20.57	19.37	20.63	16.91	15.98	17.23	15.82
MgO	6.17	8.58	10.03	4.78	3.34	3.51	6.71	8.49	9.43	4.00	5.09	10.01	10.37
CaO	11.18	8.31	6.75	11.68	19.90	16.48	12.72	11.13	9.05	16.41	14.99	8.53	9.49
Na_2O	0.30	0.38	0.17	0.34	0.41	0.45	0.52	0.48	0.49	0.84	1.08	0.79	0.93
K_2O	0.17	0.08	0.02	0.23	0.19	0.07	0.15	0.08	0.26	0.03	0.13	0.04	0.09
tot.	98.37	98.28	99.52	98.25	103.27	103.62	103.06	103.79	103.11	100.15	99.89	100.66	100.16
[a]Si (pfu)	3.00	2.97	3.01	2.97	2.98	2.98	2.95	3.02	2.97	3.07	3.05	3.06	3.05
Ti	0.07	0.09	0.02	0.06	0.07	0.08	0.06	0.05	0.04	0.06	0.09	0.05	0.04
Al	1.87	1.88	1.95	1.97	1.87	1.82	1.87	1.88	1.90	1.86	1.88	1.91	1.89
Fe^{3+}	0.05	0.08	0.01	0.04	0.11	0.13	0.19	0.05	0.18	0.00	0.02	0.00	0.07
Fe^{2+}	1.30	1.25	1.30	1.34	0.94	1.20	1.09	1.13	1.08	1.08	0.99	1.07	0.91
Mg	0.72	0.99	1.13	0.56	0.37	0.39	0.74	0.92	1.03	0.46	0.58	1.11	1.15
Ca	0.93	0.69	0.55	0.98	1.59	1.32	1.01	0.87	0.71	1.34	1.22	0.68	0.75
Na	0.05	0.06	0.03	0.05	0.06	0.07	0.07	0.07	0.07	0.12	0.16	0.11	0.13
K	0.02	0.01	0.00	0.02	0.02	0.01	0.01	0.01	0.02	0.00	0.01	0.00	0.01
tot.	8.00	8.00	8.00	8.00	8.00	8.00	8.00	8.00	8.00	8.00	8.00	8.00	8.00
majorite	0.01	-0.01	0.01	-0.04	-0.02	-0.01	-0.08	-0.01	-0.09	0.01	-0.04	0.00	-0.05
X^*_{Mg}	0.24	0.33	0.38	0.19	0.12	0.13	0.24	0.31	0.34	0.16	0.21	0.39	0.40
X^*_{Ca}	0.32	0.24	0.18	0.34	0.55	0.45	0.36	0.30	0.25	0.47	0.44	0.24	0.27
Mg# (Fe_{tot})	35	43	46	29	26	23	37	44	45	30	36	51	54

[a] Cations calculated on the basis of 12 oxygens.

continued

Run no.	DG2-25	DG2-27	DG2-24	DG2-26	DG2-19	DG2-17	DG2-28	DG2-13	DG2-15	DG2-29
P(GPa)	16	16	18	18	18	22	22	22	22	23.5
T(°C)	1260	1350	1200	1300	1400	1350	1400	1500	1550	1400
SiO_2	39.31	40.73	42.33	40.63	41.73	42.89	41.66	41.60	43.09	42.71
TiO_2	1.62	1.48	1.48	1.91	1.27	0.32	0.72	0.78	1.33	0.24
Al_2O_3	20.32	20.59	19.80	19.26	20.69	19.66	21.24	19.93	20.22	19.97
FeO	17.55	15.90	16.15	17.26	16.12	16.11	17.04	19.61	11.32	16.32
MgO	4.81	6.13	5.28	5.71	8.60	5.73	6.53	9.30	14.00	6.12
CaO	13.82	13.79	12.19	12.72	10.31	11.74	10.89	6.17	7.74	11.37
Na_2O	1.09	1.20	1.24	1.42	1.36	1.18	1.17	1.50	1.71	1.32
K_2O	0.03	0.01	0.05	0.09	0.04	1.15	0.36	0.08	0.09	1.34
tot.	98.55	99.84	98.50	98.99	100.11	98.78	99.61	98.96	99.50	99.38
[a]Si (pfu)	3.06	3.08	3.22	3.13	3.12	3.28	3.16	3.15	3.13	3.23
Ti	0.10	0.08	0.08	0.11	0.07	0.02	0.04	0.04	0.07	0.01
Al	1.86	1.84	1.77	1.75	1.82	1.77	1.90	1.78	1.73	1.78
Fe^{3+}	0.06	0.00	0.00	0.02	0.00	0.00	0.00	0.05	0.10	0.05
Fe^{2+}	1.08	1.00	1.03	1.09	1.01	1.03	1.08	1.19	0.59	0.99
Mg	0.56	0.69	0.65	0.71	0.96	0.65	0.74	1.05	1.52	0.69
Ca	1.15	1.12	1.04	0.94	0.83	0.96	0.88	0.50	0.60	0.92
Na	0.16	0.18	0.21	0.25	0.20	0.17	0.17	0.22	0.24	0.19
K	0.00	0.00	0.01	0.01	0.00	0.11	0.03	0.01	0.01	0.13
tot.	8.03	8.00	8.00	8.00	8.00	8.00	8.00	8.00	8.00	8.00
majorite	-0.01	-0.01	0.08	-0.01	-0.01	0.01	-0.01	-0.03	-0.04	-0.08
X^*_{Mg}	0.20	0.25	0.24	0.26	0.34	0.25	0.27	0.38	0.54	0.26
X^*_{Ca}	0.41	0.40	0.38	0.34	0.30	0.36	0.33	0.18	0.22	0.35
Mg# (Fe_{tot})	33	41	38	39	49	39	41	46	69	40

AM Garnet compositions

Run no.	am-22	am-31	am-32	am-30	am-1	am-5B	am-3	am-2	am-4	am-12	am-9	am-11	am-8	am-7
P(GPa)	5.5	5.5	5.5	6.5	8	8	8	8	8	13	13	132	13	13
T(°C)	1070	1125	1180	1070	900	1000	1100	1250	1400	1125	1200	1300	1400	1600
SiO_2	38.11	37.61	38.90	37.26	39.24	40.15	39.78	40.59	40.18	39.04	39.53	39.99	40.22	40.05
TiO_2	0.00	0.00	0.00	0.00	-	-	-	-	-	-	-	-	-	-
Al_2O_3	21.54	21.16	21.43	21.03	20.88	21.30	21.85	21.80	21.49	20.37	21.24	21.20	21.55	21.31
FeO	21.84	21.96	20.92	22.35	25.80	23.03	22.04	20.21	20.29	19.59	17.32	18.38	16.45	16.58
MgO	3.95	4.16	4.21	3.08	2.57	3.54	3.82	3.87	4.16	3.25	4.52	4.39	4.56	4.53
CaO	12.55	13.61	14.51	13.13	15.58	15.31	15.86	16.75	17.02	15.68	16.66	16.66	16.86	17.07
Na_2O	0.13	0.11	0.12	0.14	0.12	0.23	0.10	0.20	0.23	0.63	0.43	0.53	0.52	0.72
K_2O	0.18	0.15	0.07	0.66	0.21	0.52	0.07	0.21	0.15	0.11	0.05	0.12	0.05	0.06
tot.	98.30	98.75	100.16	97.64	104.39	104.08	103.51	103.62	103.53	98.67	99.75	101.28	100.23	100.32
[a]Si (pfu)	3.00	2.95	3.00	2.97	2.95	2.99	2.98	3.02	2.99	3.05	3.03	3.02	3.06	3.04
Ti	-	-	-	-	-	-	-	-	-	-	-	-	-	-
Al	2.00	1.95	1.95	1.97	1.85	1.87	1.93	1.91	1.88	1.88	1.92	1.89	1.93	1.90
Fe^{3+}	0.03	0.18	0.08	0.18	0.29	0.23	0.14	0.10	0.19	0.13	0.10	0.16	0.04	0.13
Fe^{2+}	1.40	1.26	1.27	1.30	1.33	1.21	1.24	1.16	1.07	1.15	1.01	1.00	1.00	0.92
Mg	0.46	0.49	0.48	0.37	0.29	0.39	0.43	0.43	0.46	0.38	0.52	0.49	0.52	0.51
Ca	1.06	1.14	1.20	1.12	1.25	1.22	1.27	1.33	1.36	1.31	1.37	1.35	1.37	1.39
Na	0.02	0.02	0.02	0.02	0.02	0.03	0.01	0.03	0.03	0.10	0.06	0.08	0.08	0.11
K	0.02	0.01	0.01	0.07	0.02	0.05	0.01	0.02	0.01	0.01	0.00	0.01	0.01	0.01
tot.	8.00	8.00	8.00	8.00	8.00	8.00	8.00	8.00	8.00	8.00	8.00	8.00	8.00	8.00
majorite	-0.04	-0.08	-0.03	-0.12	-0.09	-0.09	-0.04	-0.03	-0.06	-0.06	-0.04	-0.07	-0.03	-0.07
X^*_{Mg}	0.16	0.16	0.16	0.12	0.09	0.13	0.14	0.14	0.15	0.13	0.17	0.16	0.18	0.17
X^*_{Ca}	0.36	0.40	0.41	0.40	0.44	0.43	0.43	0.46	0.47	0.46	0.47	0.47	0.47	0.49
Mg# (Fe_{tot})	24	25	26	20	15	22	24	25	27	23	32	30	33	33

[a] Cations calculated on the basis of 12 oxygens.

continued

Run no.	am-25	am-27	am-24	am-26	am-19	am-17	am-28	am-13	am-15
P(GPa)	16	16	18	18	18	22	22	22	22
T(°C)	1250	1350	1200	1300	1400	1350	1400	1500	1550
SiO_2	39.53	40.01	40.10	40.30	39.75	42.49	38.80	40.42	42.03
TiO_2	-	-	-	-	-	-	-	-	-
Al_2O_3	19.97	20.89	20.46	20.99	20.88	19.58	19.58	20.37	20.31
FeO	19.14	18.76	20.19	19.48	20.39	16.37	20.37	22.60	14.73
MgO	4.01	4.18	2.91	3.91	3.42	3.89	3.11	4.56	9.38
CaO	14.77	14.69	14.24	15.08	15.54	14.71	16.32	12.24	11.74
Na_2O	0.56	0.62	0.48	0.60	0.60	0.92	0.47	0.80	1.07
K_2O	0.11	0.24	0.20	0.15	0.01	1.08	0.01	0.05	0.03
tot.	98.09	99.40	98.57	100.52	100.58	99.02	98.64	101.03	99.29
$^{\alpha}$Si (pfu)	3.10	3.10	3.15	3.08	3.05	3.27	3.04	3.08	3.14
Ti	-	-	-	-	-	-	-	-	-
Al	1.84	1.84	1.89	1.89	1.89	1.78	1.81	1.83	1.79
Fe^{3+}	0.06	0.06	0.00	0.05	0.11	0.00	0.17	0.12	0.08
Fe^{2+}	1.20	1.20	1.33	1.19	1.20	1.05	1.17	1.32	0.84
Mg	0.47	0.47	0.34	0.45	0.39	0.45	0.36	0.52	1.05
Ca	1.24	1.24	1.20	1.23	1.28	1.21	1.37	1.00	0.94
Na	0.09	0.09	0.07	0.09	0.09	0.14	0.07	0.12	0.16
K	0.01	0.01	0.02	0.01	0.00	0.11	0.00	0.00	0.00
tot.	8.00	8.00	8.00	8.00	8.00	8.00	8.00	8.00	8.00
majorite	0.00	0.00	0.06	-0.02	-0.04	0.02	-0.03	-0.04	-0.01
X^*_{Mg}	0.16	0.16	0.12	0.15	0.13	0.16	0.12	0.17	0.36
X^*_{Ca}	0.43	0.43	0.42	0.43	0.45	0.45	0.47	0.35	0.33
Mg# (Fe_{tot})	27	27	20	26	23	30	21	26	53

DG1 clinopyroxe compositions

Run no.	DG1-18	DG1-9	DG1-11	DG1-19	DG1-13	DG1-8	DG1-7	DG1-15	DG1-1	DG1-6	DG1-17
P(GPa)	8	8	8	8	8	13	13	13	13	13	13
T(°C)	900	1100	1200	1300	1400	1150	1250	1400	1600	1700	1850
SiO_2 (wt%)	59.53	57.74	59.01	58.07	56.47	57.44	57.35	58.35	57.83	56.74	58.12
TiO_2	0.17	0.16	0.23	0.27	0.21	0.06	0.11	0.11	0.10	0.08	0.07
Al_2O_3	21.27	20.27	21.36	20.44	20.22	24.30	22.85	22.04	22.18	22.70	22.78
FeO	1.93	2.12	2.72	3.69	3.35	0.56	1.86	2.98	2.20	2.20	1.86
MgO	1.75	2.50	2.87	3.52	3.48	0.86	1.01	1.59	1.80	2.24	3.87
CaO	3.44	4.19	4.60	5.00	4.51	1.25	1.48	2.21	2.61	2.92	3.72
Na_2O	10.86	9.81	9.37	9.13	6.92	13.39	12.87	12.41	12.07	11.27	9.51
K_2O	0.55	0.36	0.30	0.19	0.39	0.11	0.43	0.35	0.36	0.43	0.23
tot.	99.50	97.14	100.46	100.31	95.55	97.96	97.95	100.04	99.15	98.58	100.16
[a]Si (pfu)	2.03	2.02	2.00	1.99	2.01	1.98	1.99	2.00	1.99	1.96	1.97
Ti	0.00	0.00	0.01	0.01	0.01	0.00	0.00	0.00	0.00	0.00	0.00
Al	0.86	0.84	0.85	0.82	0.85	0.99	0.94	0.89	0.90	0.93	0.91
Fe	0.06	0.06	0.08	0.11	0.10	0.02	0.05	0.09	0.06	0.06	0.05
Mg	0.09	0.13	0.15	0.18	0.18	0.04	0.05	0.08	0.09	0.12	0.20
Ca	0.13	0.16	0.17	0.18	0.17	0.05	0.06	0.08	0.10	0.11	0.13
Na	0.72	0.67	0.62	0.61	0.48	0.89	0.87	0.82	0.81	0.76	0.62
K	0.02	0.02	0.01	0.01	0.02	0.00	0.02	0.02	0.02	0.02	0.01
tot.	3.91	3.90	3.88	3.90	3.81	3.97	3.98	3.97	3.97	3.96	3.89
Mg#(Fe_{tot}) (molar)	62	68	65	63	65	73	49	49	59	64	79
Ca-eskolaite	0.19	0.21	0.24	0.20	0.09	0.05	0.04	0.05	0.07	0.09	0.21
Jadeite	0.67	0.63	0.61	0.61	0.49	0.90	0.89	0.84	0.82	0.78	0.63
Ca-Tschermak	0.00	0.00	0.00	0.00	0.00	0.02	0.00	0.00	0.00	0.03	0.03

[a] Cations calculated on the basis of 6 oxygens.

DG2 clinopyroxe compositions

Run no.	DG2-20	DG2-31	DG2-32	DG2-30	DG2-1	DG2-5B	DG2-3	DG2-2	DG2-4	DG2-9	DG2-11	DG2-8	DG2-7	DG2-25	DG2-27
P(GPa)	5.5	5.5	5.5	6.5	8	8	8	8	8	13	13	13	13	16	16
T(°C)	1070	1125	1180	1070	900	1000	1100	1250	1400	1200	1300	1400	1600	1260	1350
SiO_2	55.54	54.96	57.15	56.23	59.67	59.32	57.99	58.68	58.78	59.81	58.88	58.20	57.46	56.94	60.02
TiO_2	0.43	0.51	0.34	0.34	0.12	0.20	0.37	0.39	0.39	0.11	0.17	0.15	0.16	0.04	0.10
Al_2O_3	17.62	19.15	20.04	20.68	23.86	21.94	21.12	20.94	21.77	24.39	24.11	23.78	22.60	23.09	23.54
FeO	3.72	3.55	3.18	2.70	1.47	2.39	2.86	3.02	3.06	1.08	1.35	1.53	1.92	1.09	1.16
MgO	3.26	3.68	3.14	2.08	1.22	2.07	2.34	3.13	2.77	0.65	0.93	1.45	1.99	0.54	0.85
CaO	6.97	6.66	5.32	4.67	2.44	4.49	5.15	6.31	5.08	1.37	2.07	2.12	3.21	0.91	1.68
Na_2O	9.02	8.57	9.51	9.90	11.11	10.05	9.50	8.61	8.00	12.10	11.74	11.50	11.33	13.71	12.36
K_2O	0.82	0.31	0.06	0.58	1.03	0.42	0.47	0.30	0.54	0.22	0.56	0.35	0.33	0.24	0.11
tot.	97.38	97.38	98.74	97.18	100.92	100.88	99.81	101.38	100.39	99.73	99.80	99.07	99.00	96.56	99.82
[a]Si (pfu)	1.99	1.96	1.99	1.99	2.00	2.00	1.99	1.98	1.99	2.01	1.99	1.99	1.98	2.00	2.02
Ti	0.01	0.01	0.01	0.01	0.00	0.01	0.01	0.01	0.01	0.00	0.00	0.00	0.00	0.00	0.00
Al	0.74	0.80	0.82	0.86	0.94	0.87	0.85	0.83	0.87	0.97	0.96	0.96	0.92	0.96	0.94
Fe	0.11	0.11	0.09	0.08	0.04	0.07	0.08	0.09	0.09	0.03	0.04	0.04	0.06	0.03	0.03
Mg	0.17	0.20	0.16	0.11	0.06	0.10	0.12	0.16	0.14	0.03	0.05	0.07	0.10	0.03	0.04
Ca	0.27	0.25	0.20	0.18	0.09	0.16	0.19	0.23	0.18	0.05	0.07	0.08	0.12	0.03	0.06
Na	0.63	0.59	0.64	0.68	0.72	0.66	0.63	0.56	0.53	0.79	0.77	0.76	0.76	0.93	0.81
K	0.04	0.01	0.00	0.03	0.04	0.02	0.02	0.01	0.02	0.01	0.02	0.02	0.01	0.01	0.00
tot.	3.96	3.93	3.91	3.93	3.91	3.89	3.90	3.88	3.84	3.90	3.92	3.92	3.94	3.99	3.91
Mg#(Fe_{tot}) (molar)	61	65	64	58	60	61	59	65	62	52	55	63	65	50	57
Ca-eskolaite	0.08	0.14	0.17	0.15	0.04	0.21	0.20	0.25	0.33	0.02	0.04	0.04	0.11	0.01	0.03
Jadeite	0.65	0.61	0.64	0.70	0.77	0.66	0.64	0.57	0.54	0.80	0.80	0.78	0.77	0.94	0.81
Ca-Tschermak	0.00	0.02	0.00	0.00	0.00	0.00	0.00	0.00	0.00	0.00	0.00	0.01	0.01	0.00	0.00

[a] Cations calculated on the basis of 6 oxygens.

AM clinopyroxe compositions

Run no.	am-22	am-31	am-32	am-30	am-1	am-5B	am-3	am-2	am-4	am-12	am-9	am-11	am-8	am-7	am-27
P(GPa)	5.5	5.5	5.5	6.5	8	8	8	8	8	13	13	13	13	13	16
T(°C)	1070	1125	1180	1100	900	1000	1100	1250	1400	1125	1200	1300	1400	1600	1350
SiO_2	57.25	54.68	56.78	56.81	61.23	58.53	58.70	59.12	59.40	58.36	58.34	59.63	57.72	57.02	59.74
TiO_2	0.00	0.00	0.00	0.00	0.00	0.00	0.00	0.00	0.00	0.00	0.00	0.00	0.00	0.00	0.00
Al_2O_3	19.70	20.18	20.81	21.64	24.92	21.95	21.20	22.42	22.17	20.79	22.78	21.78	23.19	22.51	22.27
FeO	3.48	3.42	3.41	2.80	1.15	2.65	3.05	3.08	3.15	3.70	2.32	3.25	1.76	3.04	1.45
MgO	2.39	2.33	2.28	1.45	0.47	2.27	2.14	2.09	1.90	0.35	0.61	0.74	0.98	1.32	0.58
CaO	5.20	6.95	7.23	4.51	1.13	4.27	5.91	6.33	6.03	0.97	1.33	1.62	2.60	4.12	1.37
Na_2O	10.79	8.81	8.63	9.69	11.49	10.44	9.85	8.91	8.12	13.13	12.99	12.91	12.24	10.67	12.93
K_2O	0.42	0.13	0.13	0.53	0.42	0.35	0.22	0.51	0.57	0.09	0.13	0.21	0.25	0.50	0.06
tot.	99.23	96.49	99.27	97.43	100.80	100.46	101.07	102.47	101.35	97.39	98.49	100.14	98.75	99.18	98.39
[a]Si (pfu)	2.00	1.96	1.97	1.99	2.03	1.99	1.99	1.98	2.00	2.05	2.01	2.03	1.99	1.97	2.05
Ti	0.00	0.00	0.00	0.00	0.00	0.00	0.00	0.00	0.00	0.00	0.00	0.00	0.00	0.00	0.00
Al	0.81	0.85	0.85	0.90	0.97	0.88	0.85	0.88	0.88	0.86	0.93	0.88	0.94	0.92	0.90
Fe	0.10	0.10	0.10	0.08	0.03	0.08	0.09	0.09	0.09	0.11	0.07	0.09	0.05	0.09	0.04
Mg	0.12	0.12	0.12	0.08	0.02	0.12	0.11	0.10	0.10	0.02	0.03	0.04	0.05	0.07	0.03
Ca	0.19	0.27	0.27	0.17	0.04	0.16	0.22	0.23	0.22	0.04	0.05	0.06	0.10	0.15	0.05
Na	0.73	0.61	0.58	0.66	0.74	0.69	0.65	0.58	0.53	0.89	0.87	0.85	0.82	0.72	0.86
K	0.02	0.01	0.01	0.02	0.02	0.02	0.01	0.02	0.02	0.00	0.01	0.01	0.01	0.02	0.00
tot.	3.97	3.92	3.90	3.90	3.86	3.92	3.91	3.88	3.84	3.97	3.96	3.96	3.96	3.94	3.93
Mg#(Fe_{tot}) (molar)	55	55	54	48	42	60	56	55	52	14	32	29	50	44	41
Ca-eskolaite	0.05	0.15	0.20	0.20	0.02	0.16	0.18	0.24	0.33	0.06	0.08	0.08	0.09	0.13	0.03
Jadeite	0.75	0.62	0.59	0.68	0.76	0.70	0.66	0.60	0.55	0.80	0.85	0.80	0.83	0.74	0.86
Ca-Tschermak	0.00	0.04	0.03	0.01	0.00	0.01	0.01	0.02	0.00	0.00	0.00	0.00	0.01	0.03	0.00

Normalized on the basis of 6 oxygens.

DG1 carbonate compositions

Run no.	DG1-18	DG1-18	DG1-9	DG1-11	DG1-8	DG1-8	DG1-7
P(GPa)	8	8	8	8	13	13	13
T(°C)	900	900	1100	1200	1150	1150	1250
FeO(tot) (wt%)	17.46	0.71	17.10	16.61	14.41	0.69	13.86
MgO	35.98	0.37	36.32	37.30	38.01	0.45	38.54
CaO	2.21	58.32	2.61	2.75	1.38	56.12	1.67
Na_2O	0.02	0.02	0.07	0.27	0.22	0.04	0.33
K_2O	0.04	0.23	0.09	0.44	0.01	0.02	0.04
tot.	55.71	59.65	56.19	57.36	54.03	57.32	54.44
Mg#	79	-	79	81	82	-	83
$FeCO_3$	0.21	0.01	0.20	0.19	0.17	0.01	0.16
$CaCO_3$	0.03	0.98	0.04	0.04	0.02	0.98	0.03
$MgCO_3$	0.76	0.01	0.76	0.77	0.81	0.01	0.81
$Na_2CO^{¨}_3$	0.00	0.00	0.00	0.00	0.00	0.00	0.00

Normalized on the basis of 6 oxygens.

DG2 carbonate compositions

Run no.	DG2-22	DG2-30	DG2-1	DG2-1	DG2-5B	DG2-5B	DG2-3	DG2-9	DG2-9	DG2-11	DG2-11	DG2-25	DG2-25	DG2-27	DG2-27
P(GPa)	5.5	6.5	8	8	8	8	8	13	13	13	13	16	16	16	16
T(°C)	1070	1070	900	900	1000	1000	1100	1200	1200	1300	1300	1260	1260	1350	1350
FeO_{tot} (wt%)	12.13	17.44	30.94	0.29	0.16	28.61	14.58	0.39	24.38	0.51	23.03	4.69	21.12	0.45	24.42
MgO	14.39	14.24	26.68	0.02	0.05	22.11	15.82	0.08	25.75	0.08	26.50	2.60	29.10	0.11	24.91
CaO	27.65	22.72	1.95	62.01	57.82	6.02	25.61	57.50	3.72	57.99	4.97	35.94	2.22	58.63	3.62
Na_2O	0.13	0.15	0.12	0.01	0.02	0.20	0.15	0.03	0.41	0.12	0.69	10.93	0.24	0.02	0.92
K_2O	0.18	0.30	0.11	0.09	0.02	0.20	0.25	0.07	0.03	0.07	0.08	1.22	0.02	0.04	0.08
tot.	54.48	54.84	59.79	62.41	58.06	57.15	56.41	58.08	54.30	58.77	55.27	55.36	52.70	59.25	53.95
Mg#	67	59	61	-	-	58	66	-	65	-	67	50	71	-	65
$FeCO_3$	0.17	0.24	0.38	0.00	0.00	0.38	0.19	0.01	0.32	0.01	0.30	0.07	0.28	0.01	0.33
$CaCO_3$	0.49	0.4	0.03	1.00	1.00	0.10	0.43	0.99	0.06	0.99	0.08	0.67	0.04	0.99	0.06
$MgCO_3$	0.35	0.35	0.59	0.00	0.00	0.52	0.37	0.00	0.61	0.00	0.62	0.07	0.68	0.00	0.60
Na_2CO_3	0.00	0.00	0.00	0.00	0.00	0.00	0.00	0.00	0.00	0.00	0.00	0.18	0.00	0.00	0.01

Run no.	DG2-24	DG2-24	DG2-26	DG2-26	DG2-19	DG2-17	DG2-17	*DG2-17	DG2-28	DG2-28	DG2-13	DG2-15	DG2-29	*DG2-29	DG2-29
P(GPa)	18	18	18	18	18	22	22	22	22	22	22	22	24	24	24
T(°C)	1200	1200	1300	1300	1400	1350	1350	1350	1400	1400	1500	1250	1400	1400	1400
FeO_{tot} (wt%)	11.71	6.86	15.10	6.11	18.09	16.57	6.39	0.71	6.15	17.82	19.72	8.20	7.56	0.74	10.84
MgO	37.67	3.79	29.62	4.16	34.03	36.65	4.90	0.34	5.72	35.41	33.83	40.94	4.85	0.46	37.83
CaO	1.20	36.93	2.29	35.30	1.42	0.50	35.18	37.27	34.84	0.62	0.79	0.78	34.37	35.31	1.06
Na_2O	0.76	10.54	2.14	10.23	0.62	0.40	10.64	20.77	11.04	0.25	0.50	0.48	10.87	20.99	0.76
K_2O	0.15	0.59	0.33	0.34	0.01	0.04	0.21	0.32	0.33	0.02	0.04	0.08	0.25	0.51	0.12
tot.	51.49	58.70	49.48	56.14	54.17	54.15	57.30	59.41	58.09	54.12	54.88	50.49	57.90	58.01	50.60
Mg#	85	50	78	55	77	80	58	46	62	78	75	90	53	53	86
$FeCO_3$	0.14	0.09	0.21	0.09	0.22	0.20	0.09	0.01	0.08	0.22	0.24	0.10	0.10	0.01	0.13
$CaCO_3$	0.02	0.64	0.04	0.64	0.02	0.01	0.62	0.65	0.60	0.01	0.01	0.01	0.60	0.63	0.02
$MgCO_3$	0.83	0.09	0.72	0.10	0.75	0.79	0.12	0.01	0.14	0.77	0.74	0.88	0.12	0.01	0.84
Na_2CO_3	0.01	0.17	0.03	0.17	0.01	0.01	0.17	0.33	0.17	0.00	0.01	0.01	0.17	0.34	0.01

Normalized on the basis of 6 oxygens.

* interpreted as quench product from a fluid

AM carbonate compositions

Run no.	am-22	am31	am-30	am-1	am-1	am-5B	am-3	am-12	am-12	am-9	am-25	am-25	am-27	am-27
P(GPa)	5.5	5.5	6.5	8	8	8	8	13	13	13	16	16	16	16
T(°C)	1070	1125	1070	900	900	1000	1100	1100	1100	1200	1260	1260	1350	1350
FeO_{tot} (wt%)	12.60	7.40	13.59	0.30	40.13	0.20	0.17	0.27	43.80	0.21	4.97	28.15	0.56	31.49
MgO	5.05	3.13	7.43	0.04	19.11	0.04	0.06	0.06	11.88	0.06	2.12	19.77	0.20	17.57
CaO	37.62	45.68	33.80	59.85	1.65	58.68	59.72	57.75	2.78	55.97	36.66	4.75	55.11	5.95
Na_2O	0.10	0.09	0.15	0.02	0.09	0.03	0.03	0.03	0.61	0.01	10.91	0.84	0.04	0.68
K_2O	0.39	0.24	0.36	0.25	0.29	0.03	0.08	0.08	0.07	0.10	0.95	0.04	0.15	0.15
tot.	55.76	56.54	55.32	60.46	61.26	58.98	60.07	58.20	59.13	56.35	55.60	53.54	56.07	55.83
Mg#	42	44	49	-	46	-	38	-	33	-	43	56	-	50
$FeCO_3$	0.18	0.10	0.19	0.00	0.53	0.00	0.00	0.00	0.64	0.00	0.07	0.40	0.01	0.44
$CaCO_3$	0.69	0.82	0.61	1.00	0.03	1.00	1.00	0.99	0.05	0.00	0.68	0.09	0.98	0.11
$MgCO_3$	0.13	0.08	0.19	0.00	0.45	0.00	0.00	0.00	0.31	1.00	0.05	0.50	0.01	0.44
Na_2CO_3	0.00	0.00	0.00	0.00	0.00	0.00	0.00	0.00	0.00	0.00	0.18	0.01	0.00	0.01

Run no.	am-24	am-24	am-26	am-26	am-19	am-19	am-17	am-28	am-28	am-13	am-29
P(GPa)	18	18	18	18	18	18	22	22	22	22	23.5
T(°C)	1200	1200	1300	1300	1400	1400	1350	1400	1400	1500	1400
FeO_{tot}	5.80	34.13	5.44	29.15	6.85	0.48	3.48	6.31	34.23	29.76	4.15
MgO	2.05	16.34	3.15	21.24	2.44	0.20	6.21	3.08	15.41	24.09	5.43
CaO	37.53	1.68	34.45	1.58	36.05	57.93	38.56	36.00	7.75	1.63	38.26
Na_2O	10.95	0.29	10.11	0.20	10.99	0.02	11.04	10.65	2.14	0.54	10.26
K_2O	0.83	0.43	1.22	0.40	1.11	0.04	0.42	1.05	0.26	0.07	0.37
tot.	57.16	52.88	54.37	52.57	57.44	58.67	59.70	57.09	59.78	56.08	58.47
Mg#	39	46	51	56	39	-	76	47	45	59	70
$FeCO_3$	0.08	0.52	0.08	0.42	0.10	0.01	0.05	0.09	0.46	0.39	0.06
$CaCO_3$	0.68	0.03	0.65	0.03	0.65	0.99	0.64	0.65	0.13	0.03	0.65
$MgCO_3$	0.05	0.44	0.08	0.54	0.06	0.00	0.14	0.08	0.37	0.57	0.13
Na_2CO_3	0.18	0.01	0.17	0.00	0.18	0.00	0.17	0.17	0.03	0.01	0.16

Normalized on the basis of 6 oxygens.

DG2/AM CAS-phase and perovskite compositions

	CAS-phase						**perovskite**									
Run no.	am-28	am-13	am-15	DG2-28	DG2-13	DG2-15	am-17	am-28	Dg2-29	am-17	am-28	DG2-17	DG2-28	DG2-17	DG2-28	Dg2-29
P(GPa)	22	22	22	22	22	22	22	23.5	23.5	22	23.5	22	22	22	22	23.5
T(°C)	1400	1500	1550	1400	1500	1550	1300	1400	1400	1300	1400	1300	1400	1300	1400	1400
SiO_2 (wt%)	33.59	37.58	39.73	35.00	36.13	34.87	54.91	54.68	50.17	34.95	34.02	50.29	24.19	4.09	5.24	34.31
TiO_2	-	-	-	1.27	1.16	1.41	-	-	0.17	-	-	0.10	27.47	28.91	38.87	1.61
Al_2O_3	45.41	45.49	42.53	46.94	45.95	47.02	0.96	0.92	0.25	1.48	1.43	0.15	0.74	6.79	8.035	1.40
FeO_{tot}	5.60	2.60	2.11	1.87	1.98	1.56	1.21	1.81	0.32	56.29	57.59	0.26	0.22	53.41	40.238	59.14
MgO	0.20	0.26	0.11	0.23	0.44	0.35	2.31	3.06	0.10	0.83	0.39	0.06	0.04	0.99	1.913	0.40
CaO	12.65	11.75	10.31	11.96	10.89	11.44	35.13	33.15	46.16	0.34	0.33	46.62	40.88	0.61	0.60	0.38
Na_2O	0.21	0.40	0.39	0.50	0.72	0.56	0.04	0.10	0.31	0.11	0.06	0.12	0.93	0.64	1.01	0.14
K_2O	1.38	2.12	3.93	1.54	1.95	1.76	0.05	0.13	0.13	0.05	0.05	0.09	0.21	0.38	0.41	0.04
tot.	99.03	100.20	99.11	99.31	99.21	98.96	94.61	93.86	97.61	94.04	93.86	97.69	94.68	95.83	96.31	97.41
[a]Si (apfu)	2.21	2.40	2.56	2.25	2.32	2.25	1.12	1.12	0.99	0.82	0.80	0.99	0.53	0.10	0.13	0.78
Ti	-	-	-	0.06	0.06	0.07	-	-	0.00	-	-	0.00	0.45	0.53	0.70	0.03
Al_{tot}	3.52	3.42	3.23	3.56	3.48	3.57	0.02	0.02	0.01	0.04	0.04	0.00	0.02	0.19	0.23	0.04
Fe^{3+}	0.00	0.00	0.00	0.00	0.00	0.00	0.00	0.00	0.01	0.33	0.36	0.00	0.00	0.59	0.18	0.35
Fe^{2+}	0.31	0.14	0.11	0.10	0.11	0.08	0.02	0.03	0.00	0.77	0.77	0.00	0.00	0.49	0.62	0.77
Mg	0.02	0.02	0.01	0.02	0.04	0.03	0.07	0.09	0.00	0.03	0.01	0.00	0.00	0.04	0.07	0.01
Ca	0.89	0.80	0.71	0.82	0.75	0.79	0.77	0.73	0.98	0.01	0.01	0.99	0.95	0.02	0.02	0.01
Na	0.03	0.05	0.05	0.06	0.09	0.07	0.00	0.00	0.01	0.00	0.00	0.00	0.04	0.03	0.05	0.01
K	0.12	0.17	0.32	0.13	0.16	0.14	0.00	0.00	0.00	0.00	0.00	0.00	0.01	0.01	0.01	0.00
tot.	7.10	7.00	7.01	7.00	7.01	7.01	2.00	2.00	2.00	2.00	2.00	2.00	2.00	2.00	2.00	2.00

[a] Cations calculated on the basis of 11 oxygens for the CAS-phase and on the basis of 3 oxygens for perovskites.

DG2 K-hollandite compositions

Run no.	DG2-9	DG2-11	DG2-25	DG2-27	DG2-24	DG2-26	DG2-19	DG2-17	DG2-28	DG2-13	DG2-15	DG-29
P(GPa)	13	13	16	16	18	18	18	22	22	22	22	23.5
T(°C)	1200	1300	1260	1350	1200	1300	1400	1350	1400	1500	1550	1400
SiO_2 (wt%)	65.18	63.72	63.75	64.78	66.22	63.39	64.62	61.62	63.52	65.17	64.33	61.49
TiO_2	0.29	0.50	0.19	0.33	0.31	0.25	0.24	0.17	0.21	0.05	0.22	0.12
Al_2O_3	18.29	19.26	17.76	18.11	16.33	18.57	18.96	18.11	17.54	19.97	18.23	18.22
FeO	0.40	0.58	0.33	0.25	0.44	0.35	0.32	0.77	0.61	0.11	0.17	0.62
MgO	0.09	0.18	0.08	0.09	0.16	0.04	0.07	0.29	0.15	0.06	0.10	0.06
CaO	0.59	1.16	0.53	0.33	0.60	0.54	0.51	1.58	0.95	0.79	0.72	1.40
Na_2O	0.29	0.49	0.46	0.49	0.92	1.33	0.87	1.17	1.11	1.83	0.93	1.08
K_2O	14.33	13.54	14.49	15.37	14.56	14.37	14.67	13.12	14.72	12.37	14.28	13.87
tot.	99.46	99.42	97.58	99.76	99.54	98.83	100.26	96.83	98.81	100.36	98.98	96.87
[a]Si (pfu)	3.05	2.98	3.03	3.01	3.09	2.95	2.98	2.94	2.97	2.99	3.00	2.93
Ti	0.01	0.02	0.01	0.01	0.01	0.01	0.01	0.01	0.01	0.00	0.01	0.00
Al	1.01	1.06	1.00	0.99	0.90	1.02	1.03	1.02	0.97	1.08	1.00	1.02
Fe^{3+}	0.00	0.00	0.00	0.00	0.00	0.01	0.00	0.00	0.02	0.00	0.00	0.02
Fe^{2+}	0.02	0.02	0.01	0.01	0.02	0.00	0.01	0.03	0.00	0.00	0.01	0.00
Mg	0.01	0.01	0.01	0.01	0.01	0.00	0.01	0.02	0.01	0.00	0.01	0.00
Ca	0.03	0.06	0.03	0.02	0.03	0.03	0.03	0.08	0.05	0.04	0.04	0.07
Na	0.03	0.04	0.04	0.04	0.08	0.12	0.08	0.11	0.10	0.16	0.08	0.10
K	0.85	0.81	0.88	0.91	0.87	0.85	0.86	0.80	0.88	0.72	0.85	0.84
tot.	5.00	5.00	5.00	5.00	5.00	5.00	5.00	5.00	5.00	5.00	5.00	5.00
$CaAl_2Si_2O_8$ (An)	0.03	0.06	0.03	0.02	0.03	0.03	0.03	0.08	0.05	0.04	0.04	0.07
$NaAlSi_3O_8$ (Alb)	0.03	0.05	0.05	0.05	0.08	0.12	0.08	0.11	0.10	0.18	0.09	0.10
$KAlSi_3O_8$	0.94	0.89	0.93	0.94	0.88	0.85	0.89	0.81	0.86	0.78	0.88	0.83

[a] Cations calculated on the basis of 8 oxygens.

AM K-hollandite compositions

Run no.	am-12	am-9	am-11	am-8	am-25	am-27	am-24	am-26	am19	am-28	am-13	am-15
P(GPa)	13	13	13	13	16	16	18	18	18	22	22	22
T(°C)	1125	1200	1300	1400	1250	1350	1200	1300	1400	1400	1500	1550
SiO_2 (wt%)	63.21	65.36	64.23	65.37	58.81	62.53	66.51	65.57	65.86	63.58	65.46	63.62
TiO_2	-	-	-	-	-	-	-	-	-	-	-	-
Al_2O_3	18.47	19.56	19.60	19.64	19.35	19.42	18.51	19.33	19.25	18.57	19.98	19.24
FeO	0.62	0.28	0.71	0.26	0.75	0.34	0.75	0.33	0.31	1.01	0.24	0.51
MgO	0.05	0.01	0.14	0.02	0.06	0.04	0.07	0.03	0.02	0.00	0.03	0.05
CaO	0.58	0.43	1.11	0.69	1.10	0.95	1.05	0.66	0.62	0.72	1.03	1.10
Na_2O	0.41	0.28	0.48	0.42	0.65	0.61	0.43	0.55	0.54	0.37	0.47	0.51
K_2O	15.56	14.80	14.31	13.39	14.05	14.66	14.88	14.72	14.28	15.38	12.92	13.16
tot.	98.90	100.71	100.57	99.78	93.68	98.54	102.20	101.20	100.89	99.64	100.13	98.19
[a]Si (pfu)	2.96	3.01	2.96	3.04	2.86	2.93	3.02	3.00	3.03	2.96	3.04	3.01
Ti	-	-	-	-	-	-	-	-	-	-	-	-
Al	1.02	1.06	1.06	1.08	1.11	1.07	0.99	1.04	1.04	1.02	1.09	1.07
Fe^{3+}	0.20	0.01	0.03	0.01	0.03	0.01	0.03	0.01	0.01	0.03	0.01	0.02
Fe^{2+}	0.00	0.00	0.00	0.00	0.00	0.00	0.00	0.00	0.00	0.00	0.00	0.00
Mg	0.00	0.00	0.01	0.00	0.00	0.00	0.00	0.00	0.00	0.00	0.00	0.00
Ca	0.03	0.02	0.05	0.03	0.06	0.05	0.05	0.03	0.03	0.04	0.05	0.06
Na	0.04	0.03	0.04	0.04	0.06	0.06	0.04	0.05	0.05	0.03	0.04	0.05
K	0.93	0.87	0.84	0.80	0.87	0.88	0.86	0.86	0.84	0.91	0.76	0.79
tot.	5.00	5.00	5.00	5.00	5.00	5.00	5.00	5.00	5.00	5.00	5.00	5.00
$CaAl_2Si_2O_8$ (An)	0.03	0.02	0.06	0.04	0.06	0.05	0.05	0.03	0.03	0.04	0.06	0.06
$NaAlSi_3O_8$ (Alb)	0.04	0.03	0.05	0.04	0.06	0.06	0.04	0.05	0.05	0.03	0.05	0.05
$KAlSi_3O_8$	0.93	0.95	0.90	0.92	0.88	0.90	0.91	0.91	0.91	0.93	0.89	0.89

[a] Cations calculated on the basis of 8 oxygens.

AM Phengite and HPK-phase compositions

	phengite									**HPK-phase**	
Run no.	b AM-23	AM-19	AM-03	AM-08	ME-109	AM-15	am-22	am-1	Run no.	am-17	am-29
P(GPa)	2.5	2.5	3.7	3.7	5	5	5.5	8	P(GPa)	22	23.5
T(°C)	850	900	900	950	1000	1050	1070	900	T(°C)	1350	1400
SiO_2 (wt%)	46.61	46.80	48.77	48.18	48.07	51.33	51.53	54.83	SiO_2 (wt%)	53.53	53.24
TiO_2	-	-	-	-	-	-	-	-	TiO_2	0.00	0.00
Al_2O_3	32.73	32.35	30.57	31.12	29.11	27.27	24.53	21.74	Al_2O_3	29.54	30.45
FeO	3.41	1.63	2.63	2.76	3.93	2.64	3.97	2.69	FeO	1.56	1.48
MgO	1.84	1.94	1.99	1.86	2.35	3.11	1.68	2.34	MgO	0.21	0.11
CaO	0.11	0.14	0.05	0.08	0.11	0.16	0.41	1.48	CaO	0.90	0.84
Na_2O	0.48	0.60	0.33	0.26	0.25	0.01	0.08	0.05	Na_2O	0.21	0.20
K_2O	10.12	9.66	10.50	10.47	11.24	10.72	11.12	13.51	K_2O	12.08	12.92
H_2Ocalculated	4.46	4.42	4.47	4.46	4.41	4.49	4.36	4.47			
tot.	99.77	97.55	99.29	99.19	99.48	99.73	97.68	101.10	tot.	98.03306154	99.25
[a] Si (pfu)	3.13	3.18	3.27	3.24	3.27	3.43	3.55	3.68	[a] Si (pfu)	3.00	2.96
Ti	-	-	-	-	-	-	-	-	Ti	-	-
Al(IV)	0.87	0.82	0.73	0.76	0.73	0.57	0.45	0.32	Al	1.95	1.99
Al(VI)	1.72	1.77	1.69	1.71	1.60	1.57	1.54	1.39	Fe^{3+}	0.00	0.00
Fe_{tot}	0.19	0.09	0.15	0.16	0.22	0.15	0.23	0.15	Fe^{2+}	0.07	0.07
Mg	0.18	0.20	0.20	0.19	0.24	0.31	0.17	0.23	Mg	0.02	0.01
Ca	0.01	0.01	0.00	0.01	0.01	0.01	0.03	0.11	Ca	0.05	0.05
Na	0.06	0.08	0.04	0.03	0.03	0.00	0.01	0.01	Na	0.02	0.02
K	0.87	0.84	0.90	0.90	0.97	0.91	0.98	1.15	K	0.86	0.92
tot.	7.04	6.98	6.99	6.99	7.07	6.96	6.95	7.05	tot.	5.97	5.98
									H	1.00	1.00
$X_{Mg}(Fe_{tot})$ (molar)	0.49	0.68	0.57	0.55	0.52	0.68	0.43	0.61			
Octahedral vacancy	0.90	0.94	0.96	0.95	0.94	0.97	1.06	1.22			

[a] Cations calculated on the basis of 11 oxygens and o the basis of 9 oxygens for the new HPK-Phase.

[b] Phengites from experiments at P $\leq$ 5 GPa are from Thomsen and Schmidt (2008b)

Appendix D

Additional Data to Chapter 5

garnet and clinopyroxene compositions

grt	am-S3b 8/1100	DG2-S1a 8/1350	am-S4b 13/1220	DG2-S2a 13/1350	am-S6a 22/1500	DG2-S5a 22/1500	cpx	am-S3b 8/1100	DG2-S1a 8/1350	am-S4b 13/1220	DG2-S2a 13/1350
SiO_2 (wt%)	38.22	40.07	39.02	39.77	42.07	40.15	SiO_2 (wt%)	56.38	56.72	56.33	57.32
TiO_2	0.00	0.79	0.00	1.70	0.00	1.44	TiO_2	0.00	0.34	0.00	0.30
Al_2O_3	21.03	21.59	19.85	20.66	19.65	18.78	Al_2O_3	20.11	19.82	19.06	22.29
FeO	16.95	14.45	16.91	14.96	19.30	17.07	FeO	2.56	2.23	2.95	1.48
MgO	2.89	8.14	3.96	7.23	7.96	9.59	MgO	2.13	3.42	2.22	1.31
CaO	18.41	14.18	16.54	13.68	7.44	7.25	CaO	5.55	7.25	4.05	2.68
Na_2O	0.16	0.38	0.65	1.00	1.51	2.00	Na_2O	9.91	7.79	11.66	12.09
K_2O	0.59	0.12	0.15	0.27	0.41	0.02	K_2O	0.87	1.03	0.41	0.37
tot.	98.25	99.72	97.09	99.27	98.34	96.29	tot.	97.51	98.60	96.70	97.83
[a]Si (pfu)	2.99	3.01	3.07	3.01	3.22	3.10	[b]Si (pfu)	1.99	1.98	2.01	1.99
Ti	0.00	0.04	0.00	0.10	0.00	0.08	Ti	0.00	0.01	0.00	0.01
Al	1.94	1.91	1.84	1.84	1.77	1.71	Al	0.84	0.82	0.80	0.91
Fe^{3+}	0.17	0.04	0.13	0.11	0.06	0.22					
Fe^{2+}	0.94	0.87	0.98	0.84	1.17	0.88	Fe	0.08	0.07	0.09	0.04
Mg	0.34	0.91	0.46	0.82	0.91	1.10	Mg	0.11	0.18	0.12	0.07
Ca	1.54	1.14	1.39	1.11	0.61	0.60	Ca	0.21	0.27	0.15	0.10
Na	0.02	0.06	0.10	0.15	0.22	0.30	Na	0.68	0.53	0.81	0.81
K	0.06	0.01	0.02	0.03	0.04	0.00	K	0.04	0.05	0.02	0.02
tot.	8.00	8.00	8.00	8.00	8.00	8.00	tot.	3.95	3.89	4.00	3.96
Mg#	23.10	50.40	29.40	46.40	42.10	50.50	Mg#	60	73	57	61
majorite	-0.09	-0.01	-0.04	-0.06	-0.05	-0.12	jadeite	0.72	0.57	0.80	0.82
pyrope	0.10	0.28	0.13	0.23	0.19	0.24	Al4	0.01	0.02	0.00	0.01
almandine	0.29	0.27	0.27	0.24	0.25	0.19	Al6	0.83	0.79	0.80	0.91
grossular	0.47	0.35	0.39	0.32	0.13	0.13					
X^*_{Mg}	0.12	0.31	0.16	0.30	0.34	0.43					

[a] Cations calculated on the basis of 12 oxygens.

[b] Cations calculated on the basis of 6 oxygens.

K-hollandite, CAS-phase and carbonate compositions

	am-S4b	DG2-S2a	am-S6a	DG2-S5a		am-S6a	DG2-S5a	trace 4		am-S4b	am-S4b	DG2-S5a
K-Holl	13/1220	13/1350	22/1500	22/1500	CAS-phase	22/1500	22/1500	22/1500	carbonates	13/1220	13/1220	22/1500
SiO_2 (wt%)	63.27	62.77	62.49	60.95	SiO_2 (wt%)	35.11	32.56	34.53	SiO_2 (wt%)	0.00	0.00	0.00
TiO_2	0.00	0.98	0.00	0.56	TiO_2	0.00	1.51	1.68	TiO_2	0.00	0.00	0.02
Al_2O_3	17.82	18.65	17.93	17.80	Al_2O_3	45.65	42.59	45.46	Al_2O_3	1.23	0.01	1.25
FeO	0.19	0.35	0.26	0.23	FeO	2.21	1.94	2.34	FeO	24.85	0.33	17.50
MgO	0.00	0.05	0.18	0.00	MgO	0.36	0.36	0.35	MgO	23.30	0.05	34.01
CaO	0.23	0.66	1.13	1.04	CaO	11.55	11.01	11.09	CaO	5.96	57.96	0.75
Na_2O	0.35	0.44	1.30	1.38	Na_2O	0.80	0.96	0.93	Na_2O	0.82	0.00	0.86
K_2O	15.39	15.70	14.13	13.85	K_2O	1.55	1.66	1.68	K_2O	0.07	0.08	0.01
									CO_2			
tot.	97.23	99.61	97.41	95.82	tot.	97.24	92.59	98.07	tot.	56.21	58.43	54.42
[a]Si (pfu)	3.01	2.92	2.95	2.93	[b]Si (pfu)	2.29	2.24	2.24	X^*_{Ca}	0.10	1.00	0.01
Ti	0.00	0.03	0.00	0.02	Ti	0.00	0.08	0.08	X^*_{Mg}	0.56	0.00	0.77
Al	1.00	1.02	1.00	1.01	Al	3.51	3.45	3.48				
					Fe^{3+}	0.12	0.11	0.12				
Fe_{tot}	0.01	0.01	0.01	0.01	Fe^{2+}	0.00	0.00	0.01				
Mg	0.00	0.00	0.01	0.00	Mg	0.03	0.04	0.03				
Ca	0.01	0.03	0.06	0.05	Ca	0.81	0.81	0.77				
Na	0.03	0.04	0.12	0.13	Na	0.10	0.13	0.12				
K	0.93	0.93	0.85	0.85	K	0.13	0.15	0.14				
tot.	5.00	5.00	5.00	5.00	tot.	7.00	7.00	7.00				
Ca-holl	0.01	0.03	0.06	0.05								
Na-Holl	0.03	0.04	0.12	0.12								
K-holl	0.96	0.93	0.83	0.82								

[a] Cations calculated on the basis of 8 oxygens.

[b] Cations calculated on the basis of 11 oxygens.

Trace element compositions of garnet

Mineral	grt									
run.	am-S3b		DG2-S1a		am-S4b		DG2-S2a		DG2-S5a	
P[GPa]/T[°C]	8/1100		8/1350		13/1220		13/1350		22/1500	
	mean	stdv	mean	stdv	mean	stdv	mean	stdv	mean	stdv
	[α]6/7		4/7		5/5		2/2		4/4	
Li (ppm)	20.200	3.00			17.500	1.23			3.210	0.21
Be					125.000	16.42	527.000	21.45		
B									86.700	19.46
Sc	135.200	30.05	125.525	23.48	202.000	4.46	194.000	12.45	697.250	59.14
V	94.767	36.39	95.250	12.63	132.160	28.58	247.000	13.46	191.750	31.69
Cr					741.000	12.45			235.500	8.63
Mn	548.667	116.88	573.000	19.00	560.600	6.65	461.000	15.64	530.750	20.42
Co	150.250	12.00	150.000	14.00	177.780	56.88	61.200	5.74	101.475	6.51
Ni	60.767	9.52	173.650	21.63					21.450	4.88
Zn	251.400	14.20	150.000	1.23	187.500	6.16	513.000	34.58	169.825	32.14
Ga	87.633	5.30	64.175	17.26	182.800	5.00	97.500	24.75	112.700	18.11
Ge	322.800	41.36	0.000		279.500	12.45	301.000	16.54	86.075	11.21
Rb									2.730	0.88
Sr	4.250	0.55	0.000		8.235	0.65	8.200	1.60	8.400	0.24
Y	35.167	5.88	31.400	2.65	62.680	13.11	30.500	3.66	68.075	8.77
Zr	31.830	9.12	22.167	3.91	90.920	19.03	67.050	6.60	337.500	52.14
Nb			1.550	0.06	11.385	1.12	34.800	5.47	8.115	1.37
Cd					106.000	12.12				
Sn					83.600	5.09				
Cs			1.420	0.06	6.770	0.89	12.300	1.26	1.475	0.08
Ba	38.000	2.14	21.950	21.95					10.395	1.79
La	1.790	0.09	0.795	0.09	2.710	0.45	2.850	0.90	2.765	0.46
Ce					5.150	1.12			1.126	0.09
Pr			0.775	0.08	3.065	1.75			0.769	0.07
Nd					10.300	1.46			2.700	0.18
Sm	8.000	3.52	10.000	0.89	18.733	6.12				
Eu	7.260	1.12	15.250	1.05	22.800	1.74	4.510	0.37	7.458	0.59
Gd	12.900	3.68	22.200	0.79	56.700	2.45	59.300	4.60	10.038	1.24
Tb	9.567	1.14	11.565	2.92	41.160	9.98	26.600	4.60	22.700	4.20
Dy	31.000	5.41	9.760	1.64	54.375	11.17			46.975	6.38
Er	48.183	11.23	52.450	7.65	72.200	4.57	60.000	5.68	101.800	10.85
Yb	79.783	5.62	108.850	25.08	116.520	6.80	205.000	9.46	241.750	25.34
Lu	102.05	21.457	89.375	10.575	126	15.668	114.5	10.579	269	34.185
Hf	32.6	11.23	3.02	0.32	81.44	3.154	111	19.15	393.25	52.134
Ta			1.95	0.56					0.3805	0.051
Pb	3.585	1.902	0		7.205	0.745			0.298	0.123
Bi					2.9	0.88			0.555	0.318
Th	0.224	0.05	1.033	0.069	2.45	0.874				
U	0.552	0.043	1.413	0.094	1.284	0.478			0.473	0.049

uncertainties are one standard deviation with respect to the mean

[α] x/y should be understand as x spots analyzed and data od y spots used for determining the average concentration

Trace element compositions of cpx, K-holl, CAS-phase and perovskite

Mineral	cpx		K-holl				CAS				Fe(Ti)pv	
run.	DG2-S1a		am-S4b		am-S6a		am-S6a		trace 4		DG2-S5a	
P[GPa]/T[°C]	8/1350		13/1220		22/1500		22/1500		22/1500		22/1500	
	mean	stdv	mean	stdv	mean	stdv	mean	stdv	mean	stdv	mean	stdv
	15/17		6/7		3/3		5/6		4/5		3/4	
Li (ppm)	98.433	6.654	15.090	7.502			36.267	34.346				
Be	37.333	11.135	47.700	12.460					260.000	186.676		
B	92.700	2.658	12.250	1.400							50.500	71.418
Sc	101.000	11.220									457.667	95.631
V	89.408	4.326	12.502	3.506	47.200	4.510	124	8.602	189	63.242	1776.667	73.711
Cr			103.333	3.235			1340	183.848	1250	254.558	1595	176.777
Co	37.092	2.687	0.608	0.037	5.450	3.210					137.333	27.099
Ni	304.067	78.692	0.799	0.025							129.000	18.385
Zn	129.700	5.698	13.575	1.325					97.800	5.650	1012.667	403.288
Ga	92.500	18.071	27.067	4.408	46.867	1.405	423.400	71.027	289.750	52.829	270.000	31.321
Ge			609.000	98.393			230.000	9.650			272.333	56.871
Rb			8.873	1.853	34.100	5.930			7.170	1.320	7.970	1.400
Sr	2.843	1.210	24.667	1.693	102.600	13.486	160.600	3.362	177.800	17.456	21.500	3.111
Y	2.958	0.870	0.634	0.06	1.235	1.747	22.675	7.223	28.280	12.269	19.133	10.501
Zr	3.850	0.970	3.998	1.325			8.745	2.199	16.350	5.728	2440	122.882
Nb	2.728	0.897	5.852	0.987	8.100	2.088	15.200	2.944	46.175	16.418	3240	209.523
Cs	5.085	0.987	16.117	2.366	12.457	4.289			32.500	10.607	13.525	5.056
Ba			18.083	1.548	212.667	72.700	83.200	61.943	47.667	32.581	39.900	4.243
La	0.370	0.180	4.833	0.754	121.900	94.646	686.000	120.849	528.000	246.417	30.033	20.170
Ce	1.458	0.987	2.227	0.818	6.110	1.697	145.200	23.371	131.200	16.529	5.515	4.575
Pr	0.948	0.643	1.589	0.897	4.600	1.240	138.600	34.195	121.140	25.892	3.860	0.300
Nd	14.500	2.650	1.780	0.598			160.000	34.180	130.000	35.079	8.000	0.600
Sm	3.125	0.840	1.747	0.597	21.300	2.340	109.975	20.442	117.360	75.399	16.900	4.243
Eu	3.768	1.265	1.193	0.458	2.455	3.472	86.380	18.127	94.960	20.197	5.735	2.949
Gd	4.300	0.874	1.649	0.137			125.267	53.493	62.150	41.621	7.500	10.607
Tb	2.517	0.699	0.496	0.088	2.130	0.030	65.820	17.594	51.520	19.295	11.060	5.572
Dy	4.767	2.450	1.580	0.798			67.220	53.487	60.350	9.900	36.500	2.700
Er	20.550	9.657	0.555	0.079			31.267	22.415	22.533	3.855	36.900	15.839
Yb	7.979	4.135	0.816	0.047					9.500	13.435	73.667	16.974
Lu	4.803	0.570	0.692	0.048			14.350	0.636	8.820	3.711	54.933	17.676
Hf	12.720	1.365	4.717	1.214	2.650	0.840	14.300	1.210	11.065	7.686	2686.667	411.380
Ta	2.010	0.875			1.195	0.545			3.725	5.268	56.467	15.282
Pb	0.990	0.240	11.860	1.997	3.960	1.120	10.410	9.603	18.900	1.570	2.120	0.500
Th	0.835	0.248	0.969	0.079	0.780	1.103	43.440	11.694	42.300	4.021	2.563	3.244
U	1.555	0.987	1.009	0.067			29.360	7.901	34.560	11.901	5.907	2.857

Trace element compositions of carbonate melts

run.	am-S3b		DG2-S1a		am-S4b		DG2-S2a		am-S6a		DG2-S5a	
P[GPa]/T[°C]	8/1100		8/1350		13/1220		13/1350		22/1500		22/1500	
	mean	stdv	mean	stdv	mean	stdv	mean	stdv	mean	stdv	mean	stdv
	6/7		*5/6*		*4/6*		*5/7*		*6/6*		*4/4*	
Li (ppm)	78.2	45.3	41.1	10.1	81.5	22.0	81.4	13.1	50.43	6.5	48.1	1.6
Be	425.7	218.5	180.0	67.9	445.0	271.5	131.8	28.0	102.20	17.8	114.4	12.3
B	246.9	19.3	92.8	17.5	233.0	12.4	101.5	20.8	95.18	7.7	75.4	7.7
Sc	105.5	16.4	70.6	10.9	85.8	16.8	59.2	1.9	35.40	0.8	46.3	1.2
Ti	5810.0	759.7	20480.0	1071.0	171.3	88.0	11950.0	331.7	64.40	11.1	3312.5	81.8
V	98.4	23.1	69.8	9.7	106.9	31.5	82.2	4.0	42.88	1.4	39.0	0.8
Mn	164.8	24.9	175.0	14.7	198.5	77.7	193.5	5.8	255.25	4.0	205.8	6.2
Co	69.0	13.0	59.1	3.2	72.4	6.3	76.0	4.5	29.05	1.9	38.4	1.5
Ni	70.4	4.4	125.0	17.2	51.8	2.2	55.3	6.7	20.20	2.5	20.3	2.0
Zn	253.0	75.5	67.7	20.7	164.5	54.3	125.5	11.6	52.88	9.5	357.5	187.8
Ga	56.8	9.5	17.3	4.4	23.1	6.2	26.9	1.9	5.27	0.5	7.8	0.9
Ge	47.4	7.0	11.0	3.7			10.3	4.2	3.42	0.9	3.8	0.9
Rb	57.8	7.1	83.3	6.4	38.5	10.0	38.9	2.1	14.00	0.7	15.8	0.6
Sr	306.8	49.9	271.0	13.2	204.5	60.7	212.3	3.3	88.73	1.6	102.2	4.0
Y	135.3	18.0	130.6	6.5	146.5	47.2	114.3	2.1	74.43	2.8	79.5	2.5
Zr	198.0	21.8	172.4	10.7	255.3	97.3	121.0	5.3	74.25	2.3	45.2	1.8
Nb	529.8	50.4	342.2	17.0	614.5	98.3	270.5	2.9	164.25	4.5	122.5	4.7
Sn	15.0	0.4	1.2	1.0	4.5	1.0			5.82	0.2		
Cs	370.7	8.3	236.8	22.2	421.5	47.3	208.0	7.7	143.75	6.9	152.8	5.9
Ba	302.3	87.0	201.6	15.7	306.0	48.3	148.0	3.8	93.83	2.4	77.4	3.8
La	192.7	21.5	159.0	4.6	257.0	91.4	129.3	5.4	1390.00	29.4	330.5	12.4
Ce	170.3	15.2	144.4	8.3	190.8	76.4	112.5	3.5	43.05	1.3	61.2	2.5
Pr	146.5	23.9	131.8	6.3	178.3	67.9	99.7	0.9	41.33	0.9	54.3	1.7
Nd	134.0	31.0	137.6	15.2	177.3	65.6	96.1	4.4	42.73	3.2	57.4	1.6
Sm	147.5	40.5	145.2	23.5	192.5	62.4	123.3	6.7	62.20	5.0	72.5	2.5
Eu	156.2	14.7	154.0	10.1	165.9	56.3	113.0	5.0	61.28	1.1	71.8	1.7
Gd	160.2	27.9	138.2	13.6	175.0	75.6	107.2	11.5	62.53	1.3	70.6	5.6
Tb	139.7	20.1	139.0	7.7	151.7	60.0	112.0	3.2	71.03	1.9	73.2	2.7
Dy	154.2	25.8	163.4	14.8	159.3	49.2	126.8	7.2	80.70	4.9	90.5	4.9
Er	113.6	24.2	108.8	4.4	95.6	12.3	97.2	7.1	60.80	3.2	77.0	3.5
Yb	124.8	7.5	128.8	14.2	148.7	67.0	110.5	7.2	81.55	2.8	88.3	3.5
Lu	102.6	13.7	104.2	6.6	118.6	35.0	95.9	1.3	69.33	2.7	78.0	1.5
Hf	153.7	35.0	151.8	9.8	181.6	42.2	100.5	6.1	40.43	2.9	31.0	1.9
Ta			0.2	0.0	2.0	0.1	0.3	0.1	1.29	0.1	0.8	0.0
Pb	206.2	30.3	3.6	0.5	75.8	3.3	3.5	0.7	1.75	0.2	0.5	0.2
Th	57.0	5.4	43.6	2.7	86.8	6.0	33.1	2.0	13.18	0.4	18.2	0.7
U	48.4	8.3	42.1	2.05	72.6	16.6	29.9	1.5	18.55	1.3	19.6	0.5

Mineral/melt partitioning coefficients

Mineral	grt									
run.	am-S3b		DG2-S1a		am-S4b		DG2-S2a		DG2-S5a	
P[GPa]/T[°C]	8/1100		8/1350		13/1220		13/1350		22/1500	
	mean		mean		mean		mean		mean	
Li	0.258	0.188			0.187	0.064			0.067	0.007
Be					0.262	0.194	3.998	1.012		
B									1.150	0.375
Sc	1.282	0.484	1.778	0.606	2.015	0.440	3.280	0.318	15.059	1.674
Ti	0.284	0.080	0.193	0.031	1.768	1.013	0.601	0.024	2.111	0.309
V	0.963	0.596	1.365	0.371	1.084	0.554	3.004	0.309	4.923	0.912
Co	2.177	0.582	2.539	0.376	2.203	0.896	0.805	0.123	2.641	0.274
Ni	0.863	0.189	1.389	0.364					1.058	0.345
Zn	0.994	0.353	2.215	0.696	1.001	0.363	4.088	0.652	0.475	0.339
Ga	1.544	0.350	3.714	1.947	6.605	1.941	3.631	1.179	14.500	4.086
Ge	6.817	1.881					29.359	13.634	22.430	8.325
Rb									0.173	0.062
Sr	0.014	0.004			0.036	0.013	0.039	0.008	0.082	0.005
Y	0.260	0.078	0.240	0.032	0.381	0.202	0.267	0.037	0.856	0.137
Zr	0.161	0.064	0.129	0.031	0.320	0.189	0.554	0.079	7.467	1.447
Nb			0.005	0.000	0.016	0.004	0.129	0.022	0.066	0.014
Cs			0.006	0.001	0.014	0.003	0.059	0.008	0.010	0.001
Ba	0.126	0.043	0.109	0.117					0.134	0.030
La	0.009	0.002	0.005	0.001	0.009	0.005	0.022	0.008	0.008	0.002
Ce					0.024	0.015			0.018	0.002
Pr			0.006	0.001	0.015	0.015			0.014	0.002
Nd					0.052	0.027			0.047	0.004
Sm	0.054	0.039	0.069	0.017	0.086	0.056				
Eu	0.046	0.012	0.099	0.013	0.123	0.051	0.040	0.005	0.104	0.011
Gd	0.081	0.037	0.161	0.021	0.295	0.140	0.553	0.102	0.142	0.029
Tb	0.068	0.018	0.083	0.026	0.246	0.157	0.238	0.048	0.310	0.069
Dy	0.201	0.069	0.060	0.015	0.303	0.156			0.519	0.099
Er	0.424	0.189	0.482	0.090	0.673	0.129	0.617	0.103	1.323	0.201
Yb	0.639	0.083	0.845	0.288	0.718	0.365	1.855	0.206	2.737	0.396
Lu	0.994	0.341	0.858	0.156	0.939	0.393	1.194	0.126	3.448	0.504
Hf	0.212	0.121	0.020	0.003	0.408	0.111	1.105	0.258	12.696	2.459
Ta			11.437	6.853					0.473	0.073
Pb	0.017	0.012			0.086	0.013			0.564	0.418
Th	0.004	0.001	0.024	0.003	0.025	0.011				
U	0.011	0.003	0.034	0.004	0.016	0.010			0.024	0.003

mineral/melt partitioning coefficients

Mineral	cpx		K-holl				K-carb		CAS				Fe(Ti)pv	
run.	DG2-S1a		am-S4b		am-S6a		LHZ-S2a		am-S6a		trace 4		DG2-S5a	
P[GPa]/T[°C]	8/1350		13/1220		22/1500		13/1350		22/1500		22/1500		22/1500	
	mean		mean		mean		mean		mean		mean		mean	
Li	2.393	0.750	0.161	0.124			0.153	0.121	0.719	0.774				
Be	0.207	0.140	0.100	0.087			0.017	0.004			2.171	1.736		
B	0.999	0.217	0.056	0.009			0.432	0.090					0.670	1.016
Sc	1.431												9.885	2.326
Ti	0.031	0.028	0.204	0.141			0.596	0.370			4.517	1.495	60.881	8.522
V	1.282	0.241	0.103	0.059	1.101	0.142			2.892	0.297	9.120	3.385	45.614	2.802
Co	0.628	0.080	0.008	0.001	0.188	0.123	0.699	0.365					3.574	0.847
Ni	2.433	0.963	0.011	0.001									6.363	1.531
Zn	1.915	0.670	0.072	0.031							2.020	0.253	2.833	2.616
Ga	5.353	2.412	0.978	0.420	8.897	1.166			80.380	21.613	43.214	11.282	34.738	8.237
Ge							0.154	0.046	67.350	21.094			70.966	31.918
Rb			0.198	0.093	2.436	0.553	0.762	0.145			0.384	0.089	0.505	0.108
Sr	0.010	0.005	0.107	0.039	1.156	0.172	0.300	0.020	1.810	0.070	2.198	0.279	0.210	0.039
Y	0.023	0.008	0.004		0.017	0.024	0.335	0.131	0.305	0.109	0.364	0.166	0.241	0.140
Zr	0.022		0.014	0.010			1.051	0.727	0.118	0.033	0.757	0.290	53.982	4.844
Nb	0.008	0.003	0.008	0.003	0.049	0.014	0.126	0.057	0.093	0.020	0.255	0.094	26.449	2.731
Cs	0.021	0.006	0.034	0.009	0.087	0.034	0.075	0.009			0.181	0.062	0.089	0.037
Ba			0.053	0.013	2.267	0.834	0.085	0.023	0.887	0.683	0.477	0.330	0.515	0.080
La	0.002		0.017	0.009	0.088	0.070	0.015	0.003	0.494	0.097	0.521	0.253	0.091	0.064
Ce	0.010	0.007	0.011	0.008	0.142	0.044	0.028	0.006	3.373	0.648	3.733	0.622	0.090	0.078
Pr	0.007	0.005	0.008	0.008	0.111	0.032	0.030	0.010	3.354	0.902	3.568	0.892	0.071	0.008
Nd	0.105		0.009	0.006			0.056	0.026	3.745	1.077	3.654	1.176	0.139	0.014
Sm	0.022		0.008	0.005	0.342	0.065	0.065	0.022	1.768	0.470	2.135	1.448	0.233	0.067
Eu	0.024	0.010	0.006	0.005	0.040	0.057	0.080	0.063	1.410	0.321	1.677	0.391	0.080	0.043
Gd	0.031	0.009	0.009	0.004			0.042	0.006	2.003	0.898	1.078	0.778	0.106	0.159
Tb	0.018	0.006	0.003	0.002	0.030	0.001	0.125	0.036	0.927	0.273	0.809	0.335	0.151	0.082
Dy	0.029		0.009	0.007			0.062	0.025	0.833	0.713	0.791	0.158	0.403	0.052
Er	0.189	0.096	0.005	0.001			0.182	0.073	0.514	0.396	0.429	0.086	0.480	0.228
Yb	0.062	0.039	0.005	0.003							0.158	0.228	0.834	0.225
Lu	0.046	0.008	0.005	0.002			0.388	0.278	0.207	0.017	0.189	0.085	0.704	0.240
Hf	0.084	0.014	0.024	0.012	0.066	0.025	0.946	0.970			1.647	1.279	86.737	18.581
Ta	11.789	8.810			0.928	0.475	0.772	0.414			3.170	4.878	70.210	20.251
Pb	0.275		0.142	0.030	2.262	0.857			5.945	6.054	55.547	19.726	4.009	2.263
Th	0.019	0.007	0.010	0.001	0.059	0.086	0.183	0.076	3.297	0.988	4.143	0.517	0.141	0.184
U	0.037	0.025	0.013	0.004			0.086	0.063	1.583	0.535	2.140	0.770	0.302	0.154

calculated melt compositions

P[GPa]	8	13	22	22 pv
Sc (ppm)	14.61	155.00		
Ti	3.68	1.51	0.54	0.15
V	140.62	121.36	42.13	22.28
FeO	9.58	10.66	9.30	7.67
Co	27.19	42.39	28.71	26.32
Ni	65.28	87.67	161.58	93.26
Zn	86.38	81.71	146.51	123.71
Rb	840.60	682.41	147.97	145.06
Sr	2442.76	1911.47	345.42	353.16
Y	167.22	152.71	73.22	79.17
Zr	889.92	553.82	51.69	23.97
Nb	111.95	91.30	71.70	6.17
Cs	87.22	76.65		
Ba	2312.43	2202.91	367.60	360.68
La	596.56	562.66	304.57	306.28
Ce	1126.01	1118.97	190.40	203.18
Nd	383.71	416.06	85.07	90.67
Sm	91.73	87.34	27.05	28.00
Eu	18.83	18.81	6.77	7.17
Gd	65.02	39.59	25.23	26.64
Dy	49.86	38.77	20.22	20.79
Er	14.01	12.62	7.01	7.53
Yb	10.47	7.33	3.76	4.11
Lu	1.34	1.26	0.45	0.50
Hf	25.67	11.42	0.91	0.44
Ta	0.12	0.15	0.93	0.17
Pb	83.38	75.05	2.91	3.00
Th	167.02	162.10	27.93	29.76
U	8.08	8.37	2.41	2.45

Melt composition calculated with a batch melting equation using the bulk partition coefficients established in chapter 5 and a melt fraction of 0.08 (8 wt% melting).

Bibliography

Adam, J., Green, T., 2001. Experimentally determined partition coefficients for minor and trace elements in peridotite minerals and carbonatitic melt, and their relevance to natural carbonatites. European Journal of Mineralogy 13, 815-827.

Agashev, A.M., Pokhilenko, N.R., Takazawa, E., McDonald, J.A., Vavilov, M.A., Watanabe, I., Sobolev, N.V., 2008. Primary melting sequence of a deep ($>$ 250 km) lithospheric mantle as recorded in the geochemistry of kimberlite-carbonatite assemblages, Snap Lake dyke system, Canada. Chemical Geology 255, 317-328.

Aizawa, Y., Tatsumi, Y., Yamada, H., 1999. Element transport by dehydration of subducted sediments: Implication for arc and ocean island magmatism. Island Arc 8, 38-46.

Akaogi, M., Ito, E., Navrotsky, A., 1989. Olivine-modified spinel-spinel transitions in the system $MgSiO_4$-$FeSiO_4$-calorimetric measurements, thermochemical calculation, and geophysical application. Journal of Geophysical Research-Solid Earth and Planets 94, 15671-15685.

Alt, J.C., Teagle, D.A.H., 1999. The uptake of carbon during alteration of ocean crust. Geochimica Et Cosmochimica Acta 63, 1527-1535.

Arima, M., Kozai, Y., Akaishi, M., 2002. Diamond nucleation and growth by reduction of carbonate melts under high-pressure and high-temperature conditions. Geology 30, 691-694.

Avanzinelli, R., Lustrino, M., Mattei, M., Melluso, L., Conticelli, S., 2009. Potassic and ultrapotassic magmatism in the circum-Tyrrhenian region: Significance of carbonated pelitic vs. pelitic sediment recycling at destructive plate margins. Lithos 113, 213-227.

Ballhaus, C., 1993. Redox states of lithospheric and asthenospheric upper-mantle. Contributions to Mineralogy and Petrology 114, 331-348.

Becker, M., Le Roex, A.P., 2006. Geochemistry of South African on- and off-craton, Group I and Group II kimberlites: Petrogenesis and source region evolution. Journal of Petrology 47, 673-703.

Biellmann, C., Gillet, P., Guyot, F., Peyronneau, J., Reynard, B., 1993. Experimental-evidence for carbonate stability in the earth's lower mantle. Earth Planet. Sci. Lett. 118, 31-41.

Blundy, J., Dalton, J., 2000. Experimental comparison of trace element partitioning between clinopyroxene and melt in carbonate and silicate systems, and implications for mantle metasomatism. Contributions to Mineralogy and Petrology 139, 356-371.

Blundy, J., Wood, B., 1994. Prediction of crystal-melt partition-coefficients from elastic-moduli. Nature 372, 452-454.

Blundy, J.D., Falloon, T.J., Wood, B.J., Dalton, J.A., 1995. Sodium partitioning between clinopyroxene and silicate melts. Journal of Geophysical Research-Solid Earth 100, 15501-15515.

Bonatti, E., Emiliani, C., Ferrara, G., Honnorez, J., Rydell, H., 1974. Ultramafic-carbonate breccias from equatorial mid-atlantic ridge. Marine Geology 16, 83-102.

Brand, U., Tazawa, J., Sano, H., Azmy, K., Lee, X.Q., 2009. Is mid-late Paleozoic ocean-water chemistry coupled with epeiric seawater isotope records? Geology 37, 823-826.

Brenan, J.M., Watson, E.B., 1991. Partitioning of trace-elements between carbonate melt and clinopyroxene and olivine at mantle P-T conditions. Geochimica Et Cosmochimica Acta 55, 2203-2214.

Brey, G.P., Bulatov, V.K., and, Girnis, A.V., 2009. Influence of water and fluorine on melting of carbonated peridotite at 6 and 10 GPa. Lithos 112, 249-259.

Brey, G.P., Bulatov, V.K., Girnis, A.V., Lahaye, Y., 2008. Experimental melting of carbonated peridotite at 6-10 GPa. Journal of Petrology 49, 797-821.

Buob, A., Luth, R.W., Schmidt, M.W., Ulmer, P., 2006. Experiments on $CaCO_3$-$MgCO_3$ solid solutions at high pressure and temperature. American Mineralogist 91, 435-440.

Campbell, A.J., Danielson, L., Righter, K., Seagle, C.T., Wang, Y., Prakapenka, V.B., 2009. High pressure effects on the iron-iron oxide and nickel-nickel oxide oxygen fugacity buffers. Earth Planet. Sci. Lett. 286, 556-564.

Canil, D., Scarfe, C.M., 1990. Phase-Relations in Peridotite + CO_2 Systems to 12 GPa - Implications for the Origin of Kimberlite and Carbonate Stability in the Earths Upper Mantle. Journal of Geophysical Research-Solid Earth and Planets 95, 15805-15816.

Cartigny, P., Harris, J.W., Javoy, M., 2001. Diamond genesis, mantle fractionations and mantle nitrogen content: a study of delta C-13-N concentrations in diamonds. Earth Planet. Sci. Lett. 185, 85-98.

Cartigny, P., 2005. Stable isotopes and the origin of diamond. Elements 1, 79-84.

Chakhmouradian, A.R., 2006. High-field-strength elements in carbonatitic rocks: Geochemistry, crystal chemistry and significance for constraining the sources of carbonatites. Chemical Geology 235, 138-160.

Chauvel, C., Hofmann, A.W., Vidal, P., 1992. HIMU EM - The french-polynesian connection. Earth Planet. Sci. Lett. 110, 99-119.

Coleman, R.G., Lee, D.E., Beatty, L.B., Brannock, W.W., 1965. Eclogites and eclogites - their differences and similarities. Geological Society of America Bulletin 76, 483-491.

Coe, N., Le Roex, A., Gurney, J., Pearson, D.G., Nowell, G., 2008. Petrogenesis of the Swartruggens and Star Group II kimberlite dyke swarms, South Africa: constraints from whole rock geochemistry. Contributions to Mineralogy and Petrology 156, 627-652.

Coltorti, M., Bonadiman, C., Hinton, R.W., Siena, F., Upton, B.G.J., 1999. Carbonatite metasomatism of the oceanic upper mantle: Evidence from clinopyroxenes and glasses in ultramafic xenoliths of Grande Comore, Indian Ocean. Journal of Petrology 40, 133-165.

Connolly, J.A.D., 2005. Computation of phase equilibria by linear programming: A tool for geodynamic modeling and its application to subduction zone decarbonation. Earth Planet. Sci. Lett. 236, 524-541.

Corgne, A., Wood, B.J., 2002. $CaSiO_3$ and $CaTiO_3$ perovskite-melt partitioning of trace elements: Implications for gross mantle differentiation. Geophysical Research Letters 29, 39-53.

Dalton, J.A., Wood, B.J., 1993. The Composition of Primary Carbonate Melts and their Evolution through Wallrock Reaction in the Mantle. Earth Planet. Sci. Lett. 119, 511-525.

Dalton, J.A., Presnall, D.C., 1998. Carbonatitic melts along the solidus of model lherzolite in the system CaO-MgO-Al_2O_3-SiO_2-CO_2 from 3 to 7 GPa. Contributions to Mineralogy and Petrology 131, 123-135.

Dasgupta, R., Hirschmann, M.M., 2006. Melting in the Earth's deep upper mantle caused by carbon dioxide. Nature 440, 659-662.

Dasgupta, R., Hirschmann, M.M., 2007a. Effect of variable carbonate concentration on the solidus of mantle peridotite. American Mineralogist 92, 370-379.

Dasgupta, R., Hirschmann, M.M., 2007b. A modified iterative sandwich method for determination of near-solidus partial melt compositions. II. Application to determination of near-solidus melt compositions of carbonated peridotite. Contributions to Mineralogy and Petrology 154, 647-661.

Dasgupta, R., Hirschmann, M.M., Smith, N.D., 2007a. Partial melting experiments of peridotite CO_2 at 3 GPa and genesis of alkalic ocean island basalts. Journal of Petrology 48, 2093-2124.

Dasgupta, R., Hirschmann, M.M., Smith, N.D., 2007b. Water follows carbon: CO_2 incites deep silicate melting and dehydration beneath mid-ocean ridges. Geology 35, 135-138.

Dasgupta, R., Hirschmann, M.M., Dellas, N., 2005. The effect of bulk composition on the solidus of carbonated eclogite from partial melting experiments at 3 GPa. Contributions to Mineralogy and Petrology 149, 288-305.

Dasgupta, R., Hirschmann, M.M., Stalker, K., 2006. Immiscible transition from carbonate-rich to silicate-rich melts in the 3 GPa melting interval of eclogite plus CO_2 and genesis of silica-undersaturated ocean island lavas. Journal of Petrology 47, 647-671.

Dasgupta, R., Hirschmann, M.M., Withers, A.C., 2004. Deep global cycling of carbon constrained by the solidus of anhydrous, carbonated eclogite under upper mantle conditions. Earth Planet. Sci. Lett. 227, 73-85.

Dasgupta, R., Hirschmann, M.M., McDonough, W.F., Spiegelman, M., Withers, A.C., 2009. Trace element partitioning between garnet lherzolite and carbonatite at 6.6 and 8.6 GPa with applications to the geochemistry of the mantle and of mantle-derived melts. Chemical Geology 262, 57-77.

Dawson, J.B., The mantle and crust-mantle relationship, in: J. Kornprobst, (Ed), Kimberlites II, Elsevier, Amsterdam, 1984, pp. 289-294.

Deines, P., Harris, J.W., Gurney, J.J., 1991. The carbon isotopic composition and nitrogen-content of lithospheric and asthenospheric diamonds from the Jagersfontein and Koffie-fontein kimberlite, South-Africa. Geochimica Et Cosmochimica Acta 55, 2615-2625.

Dixon, J., Clague, D.A., Cousens, B., Monsalve, M.L., Uhl, J., 2008. Carbonatite and silicate melt metasomatism of the mantle surrounding the Hawaiian plume: Evidence from volatiles, trace elements, and radiogenic isotopes in rejuvenated-stage lavas from Niihau, Hawaii. Geochemistry Geophysics Geosystems 9.

Dobrzhinetskaya, L.F., Green, H.W., 2007. Experimental studies of mineralogical assemblages of metasedimentary rocks at Earth's mantle transition zone conditions. Journal of Metamorphic Geology 25, 83-96.

Dobson, D.P., Jones, A.P., Rabe, R., Sekine, T., Kurita, K., Taniguchi, T., Kondo, T., Kato, T., Shimomura, O., Urakawa, S., 1996. In-situ measurement of viscosity and density of carbonate melts at high pressure. Earth Planet. Sci. Lett. 143, 207-215.

Domanik, K.J., Holloway, J.R., 1996. The stability and composition of phengitic muscovite and associated phases from 5.5 to 11 GPa: Implications for deeply subducted sediments. Geochimica Et Cosmochimica Acta 60, 4133-4150.

Domanik, K.J., Holloway, J.R., Experimental synthesis and phase relations of phengitic muscovite from 6.5 to 11 GPa in a calcareous metapelite from the Dabie Mountains, China, International Workshop on UHP Metamorphism and Exhumation, Stanford, California, 1998, pp. 51-77.

Eggleton, R.A., Boland, J.N., Ringwood, A.E., 1978. High-pressure synthesis pf a new aluminium silicate - $Al_5Si_5O_{17}(OH)$. Geochemical Journal 12, 91-194.

Eisele, J., Sharma, M., Galer, S.J.G., Blichert-Toft, J., Devey, C.W., Hofmann, A.W., 2002. The role of sediment recycling in EM-1 inferred from Os, Pb, Hf, Nd, Sr isotope and trace element systematics of the Pitcairn hotspot. Earth Planet. Sci. Lett. 196, 197-212.

Duan, Y.H., Zhao, D.P., Zhang, X.K., Xia, S.H., Liu, Z., Wang, F.Y., Li, L., 2009. Seismic structure and origin of active intraplate volcanoes in Northeast Asia. Tectonophysics 470, 257-266.

Falloon, T.J., Green, D.H., 1989. The solidus of carbonated, fertile peridotite. Earth Planet. Sci. Lett. 94, 364-370.

Falloon, T.J., Green, D.H., O'Neill, H.S., Hibberson, W.O., 1997. Experimental tests of low degree peridotite partial melt compositions: implications for the nature of anhydrous near-solidus peridotite melts at 1 GPa. Earth Planet. Sci. Lett. 152, 149-162.

Faure, G., 2000. Origin of Igneous Rocks: The Isotopic Evidence, Springer, Berlin.

Ferroir, T., Onozawa, T., Yagi, T., Merkel, S., Miyajima, N.H., Nishiyama, N., Irifune, T., Kikegawa, T., 2006. Equation of state and phase transition in $KAlSi_3O_8$ hollandite at high pressure. American Mineralogist 91, 327-332.

Foley, S., 1992. Vein-plus-wall-rock melting mechanism in the lithosphere and the origin of potassic alkaline magmas. Lithos 28, 435-453.

Foley, S.F., 2008. Rejuvenation and erosion of the cratonic lithosphere. Nature Geoscience 1, 503-510.

Foley, S.F., Yaxley, G.M., Rosenthal, A., Buhre, S., Kiseeva, E.S., Rapp, R.P., and, Jacob, D.E., 2009. The composition of near-solidus melts of peridotite in the presence of CO_2 and H_2O between 40 and 60 kbar. Lithos 112, 274-283.

Francis, D., Patterson, M., 2009. Kimberlites and aillikites as probes of the continental lithospheric mantle. Lithos 109, 72-80.

Freestone, I.C., Hamilton, D.L., 1980. The role of liquid immiscibility in the genesis of carbonatites - an experimentsl-study. Contributions to Mineralogy and Petrology 73, 105-117.

French, B.M., 1971. Stability relations of siderite ($FeCO_3$) in system Fe-C-O. American Journal of Science 271, 37-78.

Frimmel, H.E., Folling, P.G., Diamond, R., 2001. Metamorphism of the Permo-Triassic Cape Fold Belt and its basement, South Africa. Mineralogy and Petrology 73, 325-346.

Frost, D.J., McCammon, C.A., 2008. The redox state of Earth's mantle. Annual Review of Earth and Planetary Sciences 36, 389-420.

Fukao, Y., Obayashi, M., Nakakuki, T., 2009. Stagnant Slab: A Review. Annual Review of Earth and Planetary Sciences 37, 19-46.

Fukao, Y., Widiyantoro, S., Obayashi, M., 2001. Stagnant slabs in the upper and lower mantle transition region. Reviews of Geophysics 39, 291-323.

Gaffney, A.M., Blichert-Toft, J., Nelson, B.K., Bizzarro, M., Rosing, M., Albarede, F., 2007. Constraints on source-forming processes of West Greenland kimberlites inferred from Hf-Nd isotope systematics. Geochimica Et Cosmochimica Acta 71, 2820-2836.

Gasparik, T., 1996. Diopside-jadeite join at 16-22 GPa. Physics and Chemistry of Minerals 23, 476-486.

Gasparik, T., 2000. Evidence for immiscibility in majorite garnet from experiments at 13-15 GPa. Geochimica Et Cosmochimica Acta 64, 1641-1650.

Gasparik, T., Litvin, Y.A., 2002. Experimental investigation of the effect of metasomatism by carbonatic melt on the composition and structure of the deep mantle. Lithos 60, 129-143.

Gasperini, D., Blichert-Toft, J., Bosch, D., Del Moro, A., Macera, P., Albarede, F., 2002. Upwelling of deep mantle material through a plate window: Evidence from the geochemistry of Italian basaltic volcanics. Journal of Geophysical Research-Solid Earth 107.

Gautron, L., Fitz Gerald, J.D., Kesson, S.E., Eggleton, R.A., Irifune, T., 1997. Hexagonal Ba-ferrite: a good model for the crystal structure of a new high-pressure phase $CaAl_4Si_2O_{11}$? Physics of the Earth and Planetary Interiors 102, 223-229.

Genge, M.J., Jones, A.P., Price, G.D., 1995. An infrared and raman-study of carbonate glasses - implications for the structure of carbonatite magmas. Geochimica Et Cosmochimica Acta 59, 927-937.

Ghosh, S., Ohtani, E., Litasov, K.D., Terasaki, H., 2009. Solidus of carbonated peridotite from 10 to 20 GPa and origin of magnesiocarbonatite melt in the Earth's deep mantle. Chemical Geology 262, 17-28.

Girnis, A.V., Bulatov, V.K., Lahaye, Y., Brey, G.P., 2006. Partitioning of trace elements between carbonate-silicate melts and mantle minerals: Experiment and petrological consequences. Petrology 14, 492-514.

Green, T.H., Adam, J., 2003. Experimentally-determined trace element characteristics of aqueous fluid from partially dehydrated mafic oceanic crust at 3.0 GPa, 650-700 degrees C. European Journal of Mineralogy 15, 815-830.

Green, T.H., Adam, J., Sie, S.H., 1992. Trace-element partitioning between silicate minerals and carbonatite at 25 kbar and application to mantle metasomatism. Mineralogy and Petrology 46, 179-184.

Green, D.H., Wallace, M.E., 1988. Mantle metasomatism by ephermal carbonatite melts. Nature 336, 459-462.

Guignot, N., Andrault, D., 2004. Equations of state of Na-K-Al host phases and implications for MORB density in the lower mantle. Physics of the Earth and Planetary Interiors 143, 107-128.

Guillong, M., Hametner, K., Reusser, E., Wilson, S.A., Gunther, D., 2005. Preliminary characterisation of new glass reference materials (GSA-1G, GSC-1G, GSD-1G and GSE-1G) by laser ablation-inductively coupled plasma-mass spectrometry using 193 nm, 213 nm and 266 nm wavelengths. Geostandards and Geoanalytical Research 29, 315-331.

Gunther, D., Frischknecht, R., Heinrich, C.A., Kahlert, H.J., 1997. Capabilities of an Argon Fluoride 193 nm excimer laser for laser ablation inductively coupled plasma mass spectrometry microanalysis of geological materials. Journal of Analytical Atomic Spectrometry 12, 939-944.

Guzmics, T., Kodolanyi, J., Kovacs, I., Szabo, C., Bali, E., Ntaflos, T., 2008. Primary carbonatite melt inclusions in apatite and in K-feldspar of clinopyroxene-rich mantle xenoliths hosted in lamprophyre dikes (Hungary). Mineralogy and Petrology 94, 225-242.

Hacker, B.R., 2008. H_2O subduction beyond arcs. Geochemistry Geophysics Geosystems 9.

Hacker, B.R., Abers, G.A., Peacock, S.M., 2003. Subduction factory - 1. Theoretical mineralogy, densities, seismic wave speeds, and H_2O contents. Journal of Geophysical Research-Solid Earth 108.

Hahm, D., Hilton, D.R., Cho, M., Wei, H., Kim, K.R., 2008. Geothermal He and CO_2 variations at Changbaishan intra-plate volcano (NE China) and the nature of the sub-continental lithospheric mantle. Geophysical Research Letters 35.

Hammouda, T., 2003. High-pressure melting of carbonated eclogite and experimental constraints on carbon recycling and storage in the mantle. Earth Planet. Sci. Lett. 214, 357-368.

Hammouda, T., Laporte, D., 2000. Ultrafast mantle impregnation by carbonatite melts. Geology 28, 283-285.

Hammouda, T., Moine, B.N., Devidal, J.L., Vincent, C., 2009. Trace element partitioning during partial melting of carbonated eclogites. Physics of the Earth and Planetary Interiors 174, 60-69.

Harlow, G.E., 1997. K in clinopyroxene at high pressure and temperature: An experimental study. American Mineralogist 82, 259-269.

Harlow, G.E., Davies, R., 2004. Status report on stability of K-rich phases at mantle conditions. Lithos 77, 647-653.

Hauri, E.H., Shimizu, N., Dieu, J.J., Hart, S.R., 1993. Evidence for hotspot-related carbonatite metasomatism in the oceanic upper-mantle. Nature 365, 221-227.

Hermann, J., Spandler, C.J., 2008. Sediment melts at sub-arc depths: An experimental study. Journal of Petrology 49, 717-740.

Hirose, K., Shimizu, N., van Westrenen, W., Fei, Y.W., 2004. Trace element partitioning in Earth's lower mantle and implications for geochemical consequences of partial melting at the core-mantle boundary. Physics of the Earth and Planetary Interiors 146, 249-260.

Hirose, K., Fei, Y.W., 2002. Subsolidus and melting phase relations of basaltic composition in the uppermost lower mantle. Geochimica Et Cosmochimica Acta 66, 2099-2108.

Hirschmann, M.M., 2000. Mantle solidus: Experimental constraints and the effects of peridotite composition, composition, Geochem. Geophys. Geosyst., 1(10).

Hirschmann, M.M., Aubaud, C., Withers, A.C., 2005. Storage capacity of H_2O in nominally anhydrous minerals in the upper mantle. Earth Planet. Sci. Lett. 236, 167-181.

Hofmann, A.W., 1988. Chemical differentiation of the earth - the relationship between mantle, continental-crust, and oceanic-crust. Earth Planet. Sci. Lett. 90, 297-314.

Hofmann, A.W., 1997. Mantle geochemistry: The message from oceanic volcanism. Nature 385, 219-229.

Hofmann, A.W., White, W.M., 1982. Mantle plume from ancient oceanic crust. Earth Planet. Sci. Lett. 57, 421-436.

Hopp, J., Trieloff, M., Brey, G.P., Woodland, A.B., Simon, N.S.C., Wijbrans, J.R., Siebel, W., Reitter, E., 2008. Ar-40/Ar-39-ages of phlogopite in mantle xenoliths from South African kimberlites: Evidence for metasomatic mantle impregnation during the Kibaran orogenic cycle. Lithos 106, 351-364.

Irifune, T., 1994. Absence of an aluminous phase in the upper part of the earths lower mantle. Nature 370, 131-133.

Irifune, T., Ringwood, A.E., 1993. Phase-transformations in subducted oceanic-crust and buoyancy relationships at depths of 600-800 km in the mantle. Earth Planet. Sci. Lett. 117, 101-110.

Irifune, T., Ringwood, A.E., Hibberson, W.O., 1994. Subduction of continental-crust and terrigenous and pelagic sediments - an experimental study. Earth Planet. Sci. Lett. 126, 351-368.

Irifune, T., Sekine, T., Ringwood, A.E., Hibberson, W.O., 1986. The eclogite-garnetite transformation at high-pressure and some geophysical implications. Earth Planet. Sci. Lett. 77, 245-256.

Irving, A.J., Wyllie, P.J., 1975. Subsolidus and Melting Relationships for Calcite, Magnesite and Join $CaCO_3$-$MgCO_3$ to 36 Kb. Geochimica Et Cosmochimica Acta 39, 35-53.

Ishibashi, K., Hirose, K., Sata, N., Ohishi, Y., 2008. Dissociation of CAS phase in the uppermost lower mantle. Physics and Chemistry of Minerals 35, 197-200.

Isshiki, M., Irifune, T., Hirose, K., Ono, S., Ohishi, Y., Watanuki, T., Nishibori, E., Takata, M., Sakata, M., 2004. Stability of magnesite and its high-pressure form in the lowermost mantle. Nature 427, 60-63.

Jackson, M.G., Dasgupta, R., 2008. Compositions of HIMU, EM1, and EM2 from global trends between radiogenic isotopes and major elements in ocean island basalts. Earth Planet. Sci. Lett. 276, 175-186.

Johnson, K.T.M., Dick, H.J.B., Shimizu, N., 1990. Melting in the oceanic upper mantle - an ion microprobe study of diopsides in abyssal peridotites. Journal of Geophysical Research-Solid Earth and Planets 95, 2661-2678.

Kamenetsky, M.B., Sobolev, A.V., Kamenetsky, V.S., Maas, R., Danyushevsky, L.V., Thomas, R., Pokhilenko, N.P., Sobolev, N.V., 2004. Kimberlite melts rich in alkali chlorides and carbonates: A potent metasomatic agent in the mantle. Geology 32, 845-848.

Kato, T., Ohtani, E., Ito, Y., Onuma, K., 1996. Element partitioning between silicate perovskites and calcic ultrabasic melt. Physics of the Earth and Planetary Interiors 96, 201-207.

Katsura, T., Tsuchida, Y., Ito, E., Yagi, T., Utsumi, W., Akimoto, S., 1991. Stability of magnesite under the lower mantle conditions. Proceedings of the Japan Academy Series B-Physical and Biological Sciences 67, 57-60.

Kawamoto, T., Hervig, R.L., Holloway, J.R., 1996. Experimental evidence for a hydrous transition zone in the early Earth's mantle. Earth Planet. Sci. Lett. 142, 587-592.

Kelley, K.A., Plank, T., Farr, L., Ludden, J., Staudigel, H., 2005. Subduction cycling of U, Th, and Pb. Earth Planet. Sci. Lett. 234, 369-383.

Keppler, H., Smyth, J.R., 2006. Water in nominally anhydrous minerals, Mineralogical Society of America, Chantilly, Virginia.

Kerrick, D.M., Connolly, J.A.D., 2001. Metamorphic devolatilization of subducted marine sediments and the transport of volatiles into the Earth's mantle. Nature 411, 293-296.

Kessel, R., Schmidt, M.W., Ulmer, P., Pettke, T., 2005a. Trace element signature of subduction-zone fluids, melts and supercritical liquids at 120-180 km depth. Nature 437, 724-727.

Kessel, R., Ulmer, P., Pettke, T., Schmidt, M.W., Thompson, A.B., 2005b. The water-basalt system at 4 to 6 GPa: Phase relations and second critical endpoint in a K-free eclogite at 700 to 1400 degrees C. Earth Planet. Sci. Lett. 237, 873-892.

Kincaid, C., Sacks, I.S., 1997. Thermal and dynamical evolution of the upper mantle in subduction zones. Journal of Geophysical Research-Solid Earth 102, 12295-12315.

Klein-BenDavid, O., Izraeli, E.S., Hauri, E., Navon, O., 2007. Fluid inclusions in diamonds from the Diavik mine, Canada and the evolution of diamond-forming fluids. Geochimica Et Cosmochimica Acta 71, 723-744.

Klein-BenDavid, O., Logvinova, A.M., Schrauder, M., Spetius, Z.V., Weiss, Y., Hauri, E.H., Kaminsky, F.V., Sobolev, N.V., Navon, O., High-Mg carbonatitic microinclusions in some Yakutian diamonds-a new type of diamond-forming fluid. Lithos 112, 648-659.

Klemme, S., Vanderlaan, S.R., Foley, S.F., Gunther, D., 1995. Experimentally determined trace and minor element partitioning between clinopyroxene and carbonatite melt under upper-mantle conditions. Earth Planet. Sci. Lett. 133, 439-448.

Kohara, S., Badyal, Y.S., Koura, N., Idemoto, Y., Takahashi, S., Curtiss, L.A., Saboungi, M.L., 1998. The structure of molten alkali carbonates studied by neutron diffraction and ab initio calculations. Journal of Physics-Condensed Matter 10, 3301-3308.

Komabayashi, T., Omori, S., Maruyama, S., 2004. Petrogenetic grid in the system MgO-SiO_2-H_2O up to 30 GPa, 1600 degrees C: Applications to hydrous peridotite subducting into the Earth's deep interior. Journal of Geophysical Research-Solid Earth 109.

Konzett, J., Fei, Y.W., 2000. Transport and storage of potassium in the Earth's upper mantle and transition zone: an experimental study to 23 GPa in simplified and natural bulk compositions. Journal of Petrology 41, 583-603.

Konzett, J., Ulmer, P., 1999. The stability of hydrous potassic phases in lherzolitic mantle - An experimental study to 9 center dot 5 GPa in simplified and natural bulk compositions. Journal of Petrology 40, 629-652.

Korsakov, A.V., Hermann, J., 2006. Silicate and carbonate melt inclusions associated with diamonds in deeply subducted carbonate rocks. Earth Planet. Sci. Lett. 241, 104-118.

Lauterbach, S., McCammon, C.A., van Aken, P., Langenhorst, F., Seifert, F., 2000. Mossbauer and ELNES spectroscopy of (Mg,Fe)(Si,Al)O_3 perovskite: a highly oxidised component of the lower mantle. Contributions to Mineralogy and Petrology 138, 17-26.

Lazarov, M., Brey, G.P., Weyer, S., 2009. Time steps of depletion and enrichment in the Kaapvaal craton as recorded by subcalcic garnets from Finsch (SA). Earth Planet. Sci. Lett. 279, 1-10.

Leinenweber, K., Linton, J., Navrotsky, A., Fei, Y., Parise, J.B., 1995. High-pressure perovskites on the join $CaTiO_3$-$FeTiO_3$. Physics and Chemistry of Minerals 22, 251-258.

Le Roex, A.P., Bell, D.R., Davis, P., 2003. Petrogenesis of group I kimberlites from Kimberley, South Africa: Evidence from bulk-rock geochemistry. Journal of Petrology 44, 2261-2286.

Litasov, K., Ghosh, S., Ohtani, E., Solidus of carbonated peridotite and basalt to 33 GPa with implication to origin of kimberlite- and carbonatite-like melts in the deep mantle, 9th International Kimberlite Conference, Frankfurt, Germany, 2008.

Litasov, K.D., Kagi, H., Shatskly, A., Ohtani, E., Lakshtanov, D.L., Bass, J.D., Ito, E., 2007. High hydrogen solubility in Al-rich stishovite and water transport in the lower mantle. Earth Planet. Sci. Lett. 262, 620-634.

Litasov, K.D., Ohtani, E., 2005. Phase relations in hydrous MORB at 18-28 GPa: implications for heterogeneity of the lower mantle. Physics of the Earth and Planetary Interiors 150, 239-263.

Litasov, K.D., Ohtani, E., 2009. Solidus and phase relations of carbonated peridotite in the system CaO-Al_2O_3-MgO-SiO_2-Na_2O-CO_2 to the lower mantle depths. Physics of the Earth and Planetary Interiors 177, 46-58.

Liu, L.G., El Gorsey, A., 2007. High-pressure phase transitions of the feldspars, and further characterization of lingunite. International Geology Review 49, 854-860.

Litasov, K.D., Kagi, H., Shatskly, A., Ohtani, E., Lakshtanov, D.L., Bass, J.D., Ito, E., 2007. High hydrogen solubility in A1-rich stishovite and water transport in the lower mantle. Earth Planet. Sci. Lett. 262, 620-634.

Longerich, H.P., Jackson, S.E., Gunther, D., 1996. Laser ablation inductively coupled plasma mass spectrometric transient signal data acquisition and analyte concentration calculation. Journal of Analytical Atomic Spectrometry 11, 899-904.

Lustrino, M., Dallai, L., 2003. On the origin of EM-I end-member. Neues Jahrbuch Fur Mineralogie-Abhandlungen 179, 85-100.

Luth, R.W., 2001. Experimental determination of the reaction aragonite plus magnesite = dolomite at 5 to 9 GPa. Contributions to Mineralogy and Petrology 141, 222-232.

Luth, R.W., 1995. Potassium in pyroxenes at high pressure. EOS Transactions, American geophysical Union 76, F711.

Luth, R.W., 1997. Experimental study of the system phlogopite-diopside from 3.5 to 17 GPa. American Mineralogist 82, 1198-1209.

Maaloe, S., Aoki, K.I., 1977. Major element composition of upper mantle estimated from composition of lherzolites. Contributions to Mineralogy and Petrology 63, 161-173.

McCammon, C.A., Ross, N.L., 2003. Crystal chemistry of ferric iron in (Mg, Fe)(Si,Al)O_3 majorite with implications for the transition zone. Physics and Chemistry of Minerals 30, 206-216.

McCandless, T.E., Kimberlites: mantle expressions of deep-seated subduction, in: J.J. in Gurney, Gurney, J.L., Pascoe, M.D. and Richardson, S.H., (Ed), Proceedings of the 7th International Kimberlite Conference, Volume 2, Red Roof Publishers, Cape Town, South Africa, 1999, pp. 545-549.

McDonough, W.F., Sun, S.S., 1995. The composition of the earth. Chemical Geology 120, 223-253.

McKie, D., Frankis, E.J., 1977. Nyerereite - new volcanic carbonate mineral from Oldoinyo-Lengai Tanzania. Zeitschrift Fur Kristallographie 145, 73-95.

Meyer, H.O.A., Inclusions in diamonds, in: P.H. Nixon, (Ed), Mantle Xenolits, Wiley, Chischester, 1987, pp. 501-523.

Mirnejad, H., Bell, K., 2006. Origin and source evolution of the Leucite Hills lamproites: Evidence from Sr-Nd-Pb-O isotopic compositions. Journal of Petrology 47, 2463-2489.

Mirota, M.D., Veizer, J., 1994. Geochemistry of precambrian carbonates .6. aphebian albanel formations, Quebec, Canada. Geochimica Et Cosmochimica Acta 58, 1735-1745.

Mitchell, R.H., 1995. Kimberlites. Mineralogy, Geochemistry, and Petrology, Plenum Press, New York and London.

Mitchell, R.H., Carbonatites and carbonatites and carbonatites, Joint Annual Meeting of the Geological-Association-of-Canada/Mineralogical-Association-of-Canada, Mineralogical Assoc Canada, Halifax, CANADA, 2005, pp. 2049-2068.

Molina, J.F., Poli, S., 2000. Carbonate stability and fluid composition in subducted oceanic crust: an experimental study on H_2O-CO_2-bearing basalts. Earth Planet. Sci. Lett. 176, 295-310.

Morishima, H., Kato, T., Suto, M., Ohtani, E., Urakawa, S., Utsumi, W., Shimomura, O., Kikegawa, T., 1994. The phase-boundary between alpha-Mg_2SiO_4 and beta-$MgSiO_4$ determined by insitu X-ray-observation. Science 265, 1202-1203.

Morlidge, M., Pawley, A., Droop, G., 2006. Double carbonate breakdown reactions at high pressures: an experimental study in the system CaO-MgO-FeO-MnO-CO_2. Contributions to Mineralogy and Petrology 152, 365-373.

Munker, C., 1998. Nb/Ta fractionation in a Cambrian arc back arc system, New Zealand: source constraints and application of refined ICPMS techniques. Chemical Geology 144, 23-45.

Murphy, D.T., Collerson, K.D., Kamber, B.S., 2002. Lamproites from Gaussberg, Antarctica: Possible transition zone melts of Archaean subducted sediments. Journal of Petrology 43, 981-1001.

Nichols, G.T., Wyllie, P.J., Stern, C.R., 1994. Subduction zone-melting of pelagic sediments constrained by melting experiments. Nature 371, 785-788.

Niida, K., Green, D.H., 1999. Stability and chemical composition of pargasitic amphibole in MORB pyrolite under upper mantle conditions. Contributions to Mineralogy and Petrology 135, 18-40.

Ohtani, E., Litasov, K., Suzuki, A., Kondo, T., 2001. Stability field of new hydrous phase, delta-AlOOH, with implications for water transport into the deep mantle. Geophysical Research Letters 28, 3991-3993.

Ohtani, E., Litasov, K., Hosoya, T., Kubo, T., Kondo, T., 2002. Water transport into the deep mantle and formation of a hydrous transition zone. Physics of the Earth and Planetary Interiors 143, 255-269.

Okamoto, K., Maruyama, S., 2004. The eclogite-gametite transformation in the MORB+H_2O system. Physics of the Earth and Planetary Interiors 146, 283-296.

Oneill, B., Jeanloz, R., 1990. Experimental petrology of the lower mantle - a natural peridotite taken to 54 GPa. Geophysical Research Letters 17, 1477-1480.

Ono, S., 1998. Stability limits of hydrous minerals in sediment and mid-ocean ridge basalt compositions: Implications for water transport in subduction zones. Journal of Geophysical Research-Solid Earth 103, 18253-18267.

Ono, S., Yasuda, A., 1996. Compositional change of majoritic garnet in a MORB composition from 7 to 17 GPa and 1400 to 1600 degrees C. Physics of the Earth and Planetary Interiors 96, 171-179.

Ono, S., Kikegawa, T., Ohishi, Y., 2007. High-pressure transition of $CaCO_3$. American Mineralogist 92, 1246-1249.

Othman, D.B., White, W.M., Patchett, J., 1989. The geochemistry of marine sediments, island arc magma genesis, and crust-mantle recycling. Earth Planet. Sci. Lett. 94, 1-21.

Palyanov, Y.N., Shatsky, V.S., Sobolev, N.V., Sokol, A.G., 2007. The role of mantle ultrapotassic fluids in diamond formation. Proceedings of the National Academy of Sciences of the United States of America 104, 9122-9127.

Panero, W.R., Benedetti, L.R., Jeanloz, R., 2003. Transport of water into the lower mantle: Role of stishovite. Journal of Geophysical Research-Solid Earth 108.

Panero, W.R., Stixrude, L.P., 2004. Hydrogen incorporation in stishovite at high pressure and symmetric hydrogen bonding in delta-AlOOH. Earth Planet. Sci. Lett. 221, 421-431.

Peacock, S.M., Thermal structure and metamorphic evolution of subducting slab, in: J. Eiler, (Ed), Inside the Subduction Factory 138, American Geophysical Union, Washington, DC, 2003, pp. 7-22.

Peccerillo, A., 1998. Relationships between ultrapotassic and carbonate-rich volcanic rocks in central Italy: petrogenetic and geodynamic implications. Lithos 43, 267-279.

Peccerillo, A., 2005. Plio-Quaternary Volcanism in Italy, Springer-Verlag, Berlin.

Peccerillo, A., Poli, G., Serri, G., 1988. Petrogenesis of orenditic and kamafugitic rocks from central Italy. Canadian Mineralogist 26, 45-65.

Philipp, R.W., Phasenbeziehungen im System MgO-H_2O-CO_2-NaCl. Ph.D. dissertation, ETH, Zürich, 1998.

Pilet, S., Baker, M.B., Stolper, E.M., 2008. Metasomatized lithosphere and the origin of alkaline lavas. Science 320, 916-919.

Plank, T., Langmuir, C.H., 1998. The chemical composition of subducting sediment and its consequences for the crust and mantle. Chemical Geology 145, 325-394.

Poli, S., Schmidt, M.W., 2002. Petrology of subducted slabs. Annual Review of Earth and Planetary Sciences 30, 207-235.

Presnall, D.C., Gudfinnsson, G.H., Walter, M.J., 2002. Generation of mid-ocean ridge basalts at pressures from 1 to 7 GPa. Geochimica Et Cosmochimica Acta 66, 2073-2090.

Prouteau, G., Maury, R.C., Sajona, F.G., Cotten, J., Cotten, J.L., 2000. Behavior of Niobium, Tantalum and other high field strength elements in adakites and related lavas from The Philippines. Island Arc 9, 487-498.

Rapp, R.P., Irifune, T., Shimizu, N., Nishiyama, N., Norman, M.D., Inoue, J., 2008. Subduction recycling of continental sediments and the origin of geochemically enriched reservoirs in the deep mantle. Earth Planet. Sci. Lett. 271, 14-23.

Rapp, R.P., Watson, E.B., 1995. Dehydration melting of metabasalt at 8.32 kbar - implication for continental growth and crust-mantle recycling. Journal of Petrology 36, 891-931.

Rehkamper, M., Hofmann, A.W., 1997. Recycled ocean crust and sediment in Indian Ocean MORB. Earth Planet. Sci. Lett. 147, 93-106.

Ringwood, A.E., Kesson, S.E., Hibberson, W., Ware, N., 1992. Origin of kimberlites and related magmas. Earth Planet. Sci. Lett. 113, 521-538.

Rohrbach, A., Ballhaus, C., Golla-Schindler, U., Ulmer, P., Kamenetsky, V.S., Kuzmin, D.V., 2007. Metal saturation in the upper mantle. Nature 449, 456-458.

Rohrbach, A., Schmidt, M.W., Ballhaus, C., 2009. Carbonate stability in the Earth's lower mantle and redox melting across the 660 km discontinuity. Geochimica et cosmochimica acta 73, A1113-A1113.

Ryabchikov, I.D., Brey, G., Kogarko, L.N., Bulatov, V.K., 1989. Partial melting of carbonated peridotite at 50-kbar. Geokhimiya 3-9.

Salters, V.J.M., Stracke, A., 2004. Composition of the depleted mantle. Geochemistry Geophysics Geosystems 5.

Sano, A., Ohtani, E., Kubo, T., Funakoshi, K., 2003. In situ X-ray observation of decomposition of hydrous aluminum silicate $AlSiO_3OH$ and aluminum oxide hydroxide d-AlOOH at high pressure and temperature. Journal of physics and chemistry of solidus 65, 1547-1554.

Schmidt, M.W., Finger, L.W., Angel, R.J., Dinnebier, R.E., 1998. Synthesis, crystal structure, and phase relations of $AlSiO_3OH$, a high-pressure hydrous phase. American Mineralogist 83, 881-888.

Schmidt, M.W., Poli, S., 1998. Experimentally based water budgets for dehydrating slabs and consequences for arc magma generation. Earth Planet. Sci. Lett. 163, 361-379.

Schmidt, M.W., Poli, S., Comodi, P., Zanazzi, P.F., 1997. High-pressure behavior of kyanite: Decomposition of kyanite into stishovite and corundum. American Mineralogist 82, 460-466.

Schmidt, M.W., Ulmer, P., 2004. A rocking multianvil: Elimination of chemical segregation in fluid-saturated high-pressure experiments. Geochimica Et Cosmochimica Acta 68, 1889-1899.

Schmidt, M.W., Vielzeuf, D., Auzanneau, E., 2004. Melting and dissolution of subducting crust at high pressures: the key role of white mica. Earth Planet. Sci. Lett. 228, 65-84.

Shannon, R.D., 1976. Revised effective ionic-radii and systematic studies of interatomic distances in halides and chalcogenides. Acta Crystallographica Section A 32, 751-767.

Shimizu, N., Pokhilenko, N.P., Boyd, F.R., Pearson, D.G., Geochemical characteristics of mantle xenoliths from Udachnaya kimberlite pipe, 6th International Kimberlite Conference, Novosibirsk, Russia, 1995, pp. 194-205.

Simons, P.Y., Dachille, F., 1967. Structure of TiO_2 II a high-pressure phase of TiO_2. Acta Crystallographica 23, 334-341.

Simons, B., 1983. Crystal data for synthetic $K_2Mg(CO_3)_2$. Journal of Applied Crystallography 16, 143-143.

Singh, J., Johannes, W., 1996. Dehydration melting of tonalites. 1. Beginning of melting. Contributions to Mineralogy and Petrology 125, 16-25.

Smith, C.B., 1983. Pb, Sr and Nd isotopic evidence for sources of southern african cretaceous kimberlites. Nature 304, 51-54.

Sobolev, N.V., Logvinova, A.M., Zedgenizov, D.A., Seryotkin, Y.V., Yefimova, E.S., Floss, C., Taylor, L.A., Mineral inclusions in microdiamonds and macrodiamonds from kimberlites of Yakutia: a comparative study, 8th International Kimberlite Conference, Victoria, CANADA, 2003, pp. 225-242.

Spandler, C., Yaxley, G., Green, D.H., Rosenthal, A., 2008a. Phase relations and melting of anhydrous k-bearing eclogite from 1200 to 1600 degrees C and 3 to 5 GPa. Journal of Petrology 49, 771-795.

Spandler, C., Yaxley, G., Green, D.H., Scott, D., 2010. Experimental phase and melting relations of metapelite in the upper mantle: implications for the petrogenesis of intraplate magmas. Contributions to Mineralogy and Petrology DOI: 10.1007/s00410-010-0494-2.

Stachel, T., 2001. Diamonds from the asthenosphere and the transition zone. European Journal of Mineralogy 13, 883-892.

Stachel, T., Harris, J.W., 2008. The origin of cratonic diamonds - Constraints from mineral inclusions. Ore Geology Reviews 34, 5-32.

Stewart, A.J., Schmidt, M.W., van Westrenen, W., Liebske, C., 2007. Mars: A new core-crystallization regime. Science 316, 1323-1325.

Stewart, A.J., van Westrenen, W., Schmidt, M.W., Melekhova, E., Effect of gasketing and assembly design: a novel 10/3.5mm multi-anvil assembly reaching perovskite pressures, Fall Annual Meeting of the American-Geophysical-Union, San Francisco, CA, 2006, pp. 293-299.

Stracke, A., Hofmann, A.W., Hart, S.R., 2005. FOZO, HIMU, and the rest of the mantle zoo. Geochemistry Geophysics Geosystems 6.

Sudo, A., Tatsumi, Y., 1990. Phlogopite and K-amphibole in the upper mantle - implication for magma genesis in subduction zones. Geophysical Research Letters 17, 29-32.

Sueda, Y., Irifune, T., Nishiyama, N., Rapp, R.P., Ferroir, T., Onozawa, T., Yagi, T., Merkel, S., Miyajima, N., Funakoshi, K., 2004. A new high-pressure form of $KAlSi_3O_8$ under lower mantle conditions. Geophysical Research Letters 31.

Sui, J.L., Fan, Q.C., Liu, J.Q., Guo, Z.F., 2007. Mantle heterogeneity beneath Changbaishan volcanic province: evidence from geochemical study on trace elements and isotopes. Acta Petrologica Sinica 23, 1512-1520.

Susaki, J., Akaogi, M., Akimoto, S., Shimomura, O., 1985. Garnet-perovskit transformation in $CaGeO_3$ - insitu X-ray measurements using synchrotron radiation. Geophysical Research Letters 12, 729-732.

Suzuki, A., Ohtani, E., Kamada, T., 2000. A new hydrous phase delta-AlOOH synthesized at 21 GPa and 1000 degrees C. Physics and Chemistry of Minerals 27, 689-693.

Sweeney, R.J., 1994. Carbonatite melt compositions in the earths mantle. Earth Planet. Sci. Lett. 128, 259-270.

Sweeney, R.J., Prozesky, V., Przybylowicz, W., 1995. Selected trace and minor element partitioning between peridotite minerals and carbonatite melts at 18-46 kbar pressure. Geochimica Et Cosmochimica Acta 59, 3671-3683.

Sweeney, R.J., Green, D.H., Sie, S.H., 1992. Trace and minor element partitioning between garnet and amphibole and carbonatitic melt. Earth Planet. Sci. Lett. 113, 1-14.

Taniguchi, T., Dobson, D., Jones, A.P., Rabe, R., Milledge, H.J., 1996. Synthesis of cubic diamond in the graphite-magnesium carbonate and graphite-$K_2Mg(CO_3)_2$ systems at high pressure of 9-10 GPa region. Journal of Materials Research 11, 2622-2632.

Taura, H., Yurimoto, H., Kato, T., Sueno, S., 2001. Trace element partitioning between silicate perovskites and ultracalcic melt. Physics of the Earth and Planetary Interiors 124, 25-32.

Taylor, W.R., Green, D.H., 1988. Measurement of reduced peridotite-C-O-H solidus and implications for redox melting of the mantle. Nature 332, 349-352.

Thibault, Y., Edgar, A.D., Lloyd, F.E., 1992. Experimental investigation of melts from a carbonated phlogopite lherzolite - implications for metasomatism in the continental lithospheric mantle. American Mineralogist 77, 784-794.

Thomas, R.J., Agenbacht, A.L.D., Cornell, D.H., Moore, J.M., 1994. The Kibarian of southern Africa - Tectonic evolution and metallogeny. Ore Geology Reviews 9, 131-160.

Thomsen, T.B., 2006. Micas in carbonate-saturated pelites: The transformation from biotite to phengite, melting and melt geochemistry. Ph.D. dissertation, ETH, Zürich, 2006.

Thomsen, T.B., Schmidt, M.W., 2008a. The Biotite to Phengite Reaction and Mica-dominated Melting in Fluid Carbonate-saturated Pelites at High Pressures. Journal of Petrology 49, 1889-1914.

Thomsen, T.B., Schmidt, M.W., 2008b. Melting of carbonated pelites at 2.5-5.0 GPa, silicate-carbonatite liquid immiscibility, and potassium-carbon metasomatism of the mantle. Earth Planet. Sci. Lett. 267, 17-31.

Tomlinson, E.L., Jones, A.P., Harris, J.W., 2006. Co-existing fluid and silicate inclusions in mantle diamond. Earth Planet. Sci. Lett. 250, 581-595.

Tsuno, K., Dasgupta, R., 2010. Melting phase relation of anhydrous, carbonated pelitic-eclogite at 2.5-3 GPa and deep cycling of sedimentary carbon. Contrib. Min. Petrol. submitted.

Tsuruta, K., Takahashi, E., 1998. Melting study of an alkali basalt JB-1 up to 12.5 GPa: behavior of potassium in the deep mantle. Physics of the Earth and Planetary Interiors 107, 119-130.

Turner, S., Foden, J., 2001. U, Th and Ra disequilibria, Sr, Nd and Pb isotope and trace element variations in Sunda arc lavas: predominance of a subducted sediment component. Contributions to Mineralogy and Petrology 142, 43-57.

Tutti, F., Dubrovinsky, L.S., Saxena, S.K., Carlson, S., 2001. Stability of $KAlSi_3O_8$ hollandite-type structure in the earth's lower mantle conditions. Geophysical Research Letters 28, 2735-2738.

Ulmer, P., Trommsdorff, V., 1995. Serpentine stability to mantle depths and subduction-related magmatism. Science 268, 858-861.

Ulmer, P., Sweeney, R.J., 2002. Generation and differentiation of group II kimberlites: Constraints from a high-pressure experimental study to 10 GPa. Geochimica Et Cosmochimica Acta 66, 2139-2153.

van Achterbergh, E., Griffin, W.L., Ryan, C.G., O'Reilly, S.Y., Pearson, N.J., Kivi, K., Doyle, B.J., 2002. Subduction signature for quenched carbonatites from the deep lithosphere. Geology 30, 743-746.

van Achterbergh, E., Griffin, W.L., Ryan, C.G., O'Reilly, S.Y., Pearson, N.J., Kivi, K., Doyle, B.J., Melt inclusions from the deep Slave lithosphere: implications for the origin and evolution of mantle-derived carbonatite and kimberlite, 8th International Kimberlite Conference, Victoria, CANADA, 2003, pp. 461-474.

van Keken, P.E., Kiefer, B., Peacock, S.M., 2002. High-resolution models of subduction zones: Implications for mineral dehydration reactions and the transport of water into the deep mantle. Geochemistry Geophysics Geosystems 3.

van Westrenen, W., Draper, D.S., 2007. Quantifying garnet-melt trace element partitioning using lattice-strain theory: new crystal-chemical and thermodynamic constraints. Contributions to Mineralogy and Petrology 154, 717-730.

Veksler, I.V., Petibon, C., Jenner, G.A., Dorfman, A.M., Dingwell, D.B., 1998. Trace element partitioning in immiscible silicate-carbonate liquid systems: An initial experimental study using a centrifuge autoclave. Journal of Petrology 39, 2095-2104.

Vervoort, J.D., Blichert-Toft, J., 1999. Evolution of the depleted mantle: Hf isotope evidence from juvenile rocks through time. Geochimica Et Cosmochimica Acta 63, 533-556.

Wallace, M.E., Green, D.H., 1988. An experimental-determination of primary carbonatite magma composition. Nature 335, 343-346.

Walter, M.J., Bulanova, G.P., Armstrong, L.S., Keshav, S., Blundy, J.D., Gudfinnsson, G., Lord, O.T., Lennie, A.R., Clark, S.M., Smith, C.B., Gobbo, L., 2008. Primary carbonatite melt from deeply subducted oceanic crust. Nature 454, 622-630.

Wang, W., Sueno, S., 1996. Discovery of a NaPx-En inclusion in diamond: possible transition zone origin. Mineral. J. 18, 9-16.

Wang, W.Y., Gasparik, T., 2000. Evidence for a deep-mantle origin of a NaPX-EN inclusion in diamond. International Geology Review 42, 1000-1006.

Wang, W.Y., Gasparik, T., 2001. Metasomatic clinopyroxene inclusions in diamonds from the Liaoning province, China. Geochimica Et Cosmochimica Acta 65, 611-620.

Wang, W.Y., Takahashi, E., 1999. Subsolidus and melting experiments of a K-rich basaltic composition to 27 GPa: Implication for the behavior of potassium in the mantle. American Mineralogist 84, 357-361.

Weaver, B.L., 1991a. The origin of ocean island basalt end-member compositions - trace-element and isotopic constraints. Earth Planet. Sci. Lett. 104, 381-397.

Weaver, B.L., 1991b. Trace-element evidence for the origin of ocean-island basalts. Geology 19, 123-126.

Wood, B.J., Blundy, J.D., 1997. A predictive model for rare earth element partitioning between clinopyroxene and anhydrous silicate melt. Contributions to Mineralogy and Petrology 129, 166-181.

Wu, Y., Fei, Y.W., Jin, Z.M., Liu, X.Y., 2009. The fate of subducted Upper Continental Crust: An experimental study. Earth Planet. Sci. Lett. 282, 275-284.

Wunder, B., Rubie, D.C., Ross, C.R., Medenbach, O., Seifert, F., Schreyer, W., 1993. Synthesis, stability, and properties of $Al_2SiO_4(OH)_2$ - a fully hydrated analog of topaz. American Mineralogist 78, 285-297.

Wyllie, P.J., 1988. Magma genesis, plate-tectonics, and chemical differentiation of the earth. Reviews of Geophysics 26, 370-404.

Wyllie, P.J., and, Sekine, T., 1982. The Formation of Mantle Phlogopite in Subduction Zone Hybridization. Contrib. Min. Petrol. 79, 375-380.

Xue, X.Y., Kanzaki, M., Fukui, H., Ito, E., Hashimoto, T., 2006. Cation order and hydrogen bonding of high-pressure phases in the Al_2O_3-SiO_2-H_2O system: An NMR and Raman study. American Mineralogist 91, 850-861.

Yagi, T., Akimoto, S.I., 1976. Direct determination of coesite-stishovite transition by insitu X-ray measurements. Tectonophysics 35, 259-270.

Yasuda, A., Fujii, T., Kurita, K., 1994. Melting phase-relations of an anhydrous midocean ridge basalt from 3 to 20 GPa - Implications for the behaviour of subducted oceanic-crust in the mantle. Journal of Geophysical Research-Solid Earth 99, 9401-9414.

Yaxley, G.M., Brey, G.P., 2004. Phase relations of carbonate-bearing eclogite assemblages from 2.5 to 5.5 GPa: implications for petrogenesis of carbonatites. Contributions to Mineralogy and Petrology 146, 606-619.

Yaxley, G.M., Green, D.H., 1994. Experimental Demonstration of Refractory Carbonate-Bearing Eclogite and Siliceous Melt in the Subduction Regime. Earth Planet. Sci. Lett. 128, 313-325.

Yong, W.J., Dachs, E., Withers, A.C., Essene, E.J., 2006. Heat capacity and phase equilibria of hollandite polymorph of $KAlSi_3O_8$. Physics and Chemistry of Minerals 33, 167-177.

Zhai, S.M., Ito, E., 2008. Phase relations of $CaAl_4Si_2O_{11}$ at high-pressure and high-temperature with implications for subducted continental crust into the deep mantle. Physics of the Earth and Planetary Interiors 167, 161-167.

Zhang, J., Li, B., Utsumi, W., Liebermann, R.C., 1996. In situ X-ray observations of the coesite stishovite transition: Reversed phase boundary and kinetics. Physics and Chemistry of Minerals 23, 1-10.

Zhao, D.P., Lei, J.S., Tang, R.Y., 2004. Origin of the Changbai intraplate volcanism in Northeast China: Evidence from seismic tomography. Chinese Science Bulletin 49, 1401-1408.

Zhao, D.P., Tian, Y., Lei, J.S., Liu, L.C., Zheng, S.H., 2009. Seismic image and origin of the Changbai intraplate volcano in East Asia: Role of big mantle wedge above the stagnant Pacific slab. Physics of the Earth and Planetary Interiors 173, 197-206.

Aknowledgments

First I would like to thank Prof. Dr. Max W. (yes!! like George...) Schmidt who gave me the oppurtunity to spend 4 years of my life as PhD student at the Institute of Mineralogy and Petrology (IMP) at the ETH. Thanks for the freedom you have given me and for discussions and corrections of this thesis. Also thanks to Stefano Poli and Gerhard Brey, who hopefully appreciate to be included in my list of co-supervisors, and for being so kind to come to Zürich. I am also grateful to Prof. Detlef Günther and Kathrin Hametner (The Günther Group: Trace Element and Micro Analysis) at the Department of Chemistry and Applied Biosciences for the LA-ICP-MS analysis and data-evaluation.

A special thank goes also to all the people who helped me in the different labs and with the various technical instruments and machines: Christian, Arno (thanks for the 30 GPa experiments) and Elena with the multi-anvil, Ettore and Maarten with piston-cylinder, Davide with the Raman and Eric (Gazzella Turbata) with the Microprobe and SEM. Thanks to Ettore for being THE PC-support with a magic touch, to Pulmi for the numerous good advices, to all the technicians of the institute (Bruno, Urs, Andreas), and to Lydia who was taking care of most of my duties as crushing room assistant.

Many thanks goes to my IMP-girls for the funny time at lunch or at the bequem: Angelika, Esther, Tamar(r)a and Ute!...ok, if I have to. . . , thanks also to all aspirant or already doctors (male) who shared with me part of my IMP-life.

A huge thank goes to the Ticino Brass Band with Paola, Stefania, Erica, Monica, Gal, Sweety, Pippo, Claudio, Bona, Omar, Auro and also the pseudo-ticines Christoph “tüt a post?”. The last few months have been quite stressful for me, but fortunately there have been always somebody in my office able to put a smile on my face. Thank you Gal, thank you Ettore, and thank you Rohit (the word for today is...“atrezzo da giardino”), thank you Tobîas...it has been a pleasure!

Da ultimo vorrei ringraziare la mia famiglia per il sostegno e l’aiuto che sempre hanno saputo darmi. Grazie mam, grazie pà, grazie fratellino (a ghe in bal un trasloc fö par Züric se te se mia cosa fa). Ah già quasi dimenticavo...grazie ALE per l’immensa pazienza, l’aiuto con LateX e per la squisita trota salmonata ;-) (bacio)...

P.S.: Is there anyone who wants to join for a short excursion and a relaxing night at the Bivacco Vaninetti?... Aduig ocrop Lag!

Zurigo, aprile 2010 Daniele Grassi